Institut für Theoretische Physik
Fakultät Mathematik und Naturwissenschaften
Technische Universität Dresden

Epithelial Mechanics in 3D
– how form follows force –

Dissertation

zur Erlangung des akademischen Grades
Doctor rerum naturalium
(Dr. rer. nat.)

vorgelegt von

Silvanus Alt

geboren am 09.09.1987 in Torgau

Max-Planck-Institut für
Physik komplexer Systeme
Dresden

The Francis Crick Institute
London

Eingereicht am
15.03.2016

Erster Gutachter

Prof. Dr. Frank Jülicher

Zweiter Gutachter

Prof. Dr. Stephan Grill

Acknowledgements

First and foremost I want to thank Guillaume Salbreux for his patient guidance and supervision. Guillaume contributed a great lot to the research carried out for this dissertation, and to my personal scientific development. Also, I want to thank Professor Frank Jülicher for granting me the chance to pursue my PhD under his supervision in the great environment of the group of Biological Physics, which he built at the Max Planck Institute for the Physics of Complex Systems. Frank played a crucial part in the development of the projects, and I am grateful for many encouraging, and insightful discussions. Guillaume's and Frank's curiosity, attention to detail and deep knowledge, mixed with creativity and brilliance, have been and will continue to be a great example for me. Without them this work would not have been possible.

During my PhD I have had the chance to work with several great Biologists, from whom I could learn many a thing about the beauty and complexity of Biology. For that I am grateful to Anne Classen and Christina Bielmeier, Christian Dahmann, Liyuan Sui and Daiki Umetsu, Matteo Rauzi and Hendrik Messal, and many more for all the insightful discussions, and exciting projects we started together.

I want to thank my colleagues and friends from the MPI PKS Dresden for an amazing time, many deep discussions about Physics and the world and the vivid, friendly atmosphere in this great scientific place: André Scholich, Christoph Weber, Matthias Merkel, Gary Klindt, Steffen Werner, Vijaykumar Krishnamurthy, Jochen Schneider, Amitabha Nandi, Anna Erzberger, Marko Popovic, Pawel Romanczuk, Johannes Baumgart and many more. It was a pleasure working with you.

Furthermore I want to thank my colleagues from the Crick Institute London, namely Poulami Ganguly, Jasper Bathmann, Silvia Grigolon, and Marc de Gennes for making my stay in London worthwhile.

I am especially grateful to André Scholich for taking the time and patience to proofread the whole of my thesis and contributing many critical comments. Also Jasper Bathmann, Pragya Srivastava and Silvia Grigolon supported me through this difficult process by providing useful comments on the draft.

Most importantly, I am deeply indebted to my grand-grandmother Oma Ur, my grandparents, my parents, my sister Nicole, my girlfriend Miriam, and all my friends for being my inexhaustible source of support and backup.

Abstract

Complex deformations of simple epithelia play a fundamental role during the morphogenesis of humans and animals. The shape of an epithelium is determined by the balance of mechanical stresses generated inside the cells and external mechanical forces. To shed light on this interplay of 3D shape and mechanics we develop and introduce the 3D Vertex Model for simple epithelia. In this model the epithelial shape is characterised by an apical and basal network of 3D vertices determining the corresponding cell outlines. Mechanical stresses are assumed to arise from the volume control of cells, as well as from tensions that act along apical, basal and lateral interfaces between cells and along their apical and basal surfaces. In addition, external mechanical forces, such as compression and the attachment of the tissue to an underlying basement membrane, are taken into account.

We thus show how the shape of epithelia, ranging from squamous to columnar, depends on the external forces and the active tensions generated inside the cells, and we identify different buckling regimes of epithelia subjected to external compression. Starting from the 3D Vertex Model we derive elastic moduli of epithelia, and relate the model to a coarse grained continuum theory where epithelia are represented as thin elastic sheets. After discussing flat epithelia we study the equilibrium shapes of spherical epithelia surrounding a compressible fluid. These mechanical models for epithelial deformations in 3D are then applied to study two important processes in the morphogenesis of the fruit fly *Drosophila*. By combing physical modelling and biological experiments, we demonstrate that cyst formation in the imaginal wing disc epithelium is mechanically driven by increased tensions along the apical and lateral interfaces between differently fated cells. Using the newly developed theoretical framework we verify that the observed cyst shapes result from a buckling of clones due to the compression exerted by the contractile boundary. Cyst formation is a general response to interrupted transcriptional expression and signalling patterns, and we argue that increased interface contractility around misspecified clones constitutes a novel error correction mechanism through the extrusion of small aberrant clones from the tissue. In the last part of the thesis we present a new minimal mechanical for ventral furrow formation. Making use of the 3D Vertex Model and the corresponding continuum theory, we show that mesodermal constriction is sufficient to initiate the furrowing. We argue that this new perspective on ventral furrow formation can help elucidate recent experimental findings, which cannot be explained by means of established mechanical models.

We conclude this thesis by offering an outlook into possible future applications of the developed methods towards a better understanding of 3D epithelial mechanics.

Kurzzusammenfassung

Die mechanische Verformung von einlagigen Epithelien in komplexe Organe spielt eine wichtige Rolle in der Entwicklung von der befruchteten Eizelle zum ausgewachsenen Individuum bei Menschen und Tieren. In der vorliegenden Arbeit entwickeln und analysieren wir neue Modelle und Ansätze, um das komplexe Zusammenspiel von Form und Mechanik von Epithelien in Raum und Zeit zu verstehen.

Wir entwickeln ein neuartiges 3D Vertex Modell, das Epithelien durch Netzwerke von apikalen und basalen Vertices beschreibt, die Schnittstellen zwischen drei oder mehr benachbarten Zellen repräsentieren. Der Zellinnendruck und durch den Aktin-Kortex erzeugte Spannungen entlang von Zelloberflächen führen im Zusammenspiel mit Kräften, die von außen auf das Gewebe wirken, zur Verformung des Gewebes. Anhand unseres Modells zeigen wir auf, wie die vielfältigen Formen von Platten- bis Zylinderepithelien von den aktiv erzeugten Spannungen in den Zellen und externen Kräften abhängen.

Im Anschluss stellen wir eine kontinuierliche Theorie für die Mechanik von einlagigen Epithelien vor, und nutzen das 3D Vertex Modell um die charakterisierenden effektiven Elastitizätsmodule eines Epithels in Abhängigkeit von den zellulären Kräften herzuleiten. Schließlich wenden wir die entwickelten Theorien zur Erforschung zweier wichtiger Prozesse in der Morphogenese der Fruchtfliege *Drosophila melanogaster* an.

Wir zeigen, dass die Entstehung von Zysten in den Imaginalscheiben der Fruchtfliegenlarve auf mechanischen Spannungen beruht, die entlang der Grenzflächen zwischen genetisch unterschiedlichen Zellgruppen erzeugt werden. Wir demonstrieren in Theorie und Experiment, dass dieser Effekt einen mechanischen Korrekturmechanismus für Epithelien darstellt, da er zum Ausschluss von fehlerhaften differenzierten Zellen aus dem Gewebe führen kann, und so dazu beiträgt die Homogenität gesunder Gewebe zu erhalten.

Im letzten Teil der Dissertation präsentieren wir einen neuen physikalischen Mechanismus, der der Invagination der Mesoderm in den ersten Stadien der Entwicklung von *Drosophila* zugrunde liegt. Durch die Anwendung des 3D Vertex Modells und der entsprechenden Kontinuumstheorie für die Mechanik von Epithelien zeigen wir, dass die Kontraktion der Mesoderm und die Krümmung des Embryo eine wichtige Rolle spielen, um diesen ersten Schritt der Gastrulation einzuleiten. Unsere Forschung eröffnet neue Perspektiven im Hinblick auf den Prozess der Gastrulation, und wirft Licht auf experimentelle Erkenntnisse, die im Rahmen der zahlreichen bestehenden Modelle nicht erklärt werden konnten.

Ein Ausblick auf die vielfältigen Anwendungsmöglichkeiten der im Rahmen der Promotion entwickelten Methoden schließt die vorliegende Arbeit ab.

Contents

1 Introduction **1**

1.1 Motivation and overview 1

1.2 The fruit fly *Drosophila melanogaster* 2

1.3 Epithelial tissues 6

1.4 Prerequisites of cell and epithelial mechanics 8

1.5 Mechanical models of simple epithelia 11

1.5.1 Vertex models for epithelial mechanics 11

1.5.2 Continuum models 16

1.5.3 Bridging the scales between vertex and continuum models 16

2 3D description of epithelial mechanics **19**

2.1 A 3D Vertex Model for epithelial mechanics 19

2.1.1 The 3D Vertex Model representation of simple epithelia 20

2.1.2 Work function and resulting forces 22

2.1.3 Topological transitions 26

2.1.4 Boundary conditions 29

2.1.5 Minimising the work function 30

2.1.6 The limit of the Apical 3D Vertex Model 32

2.2 Coarse grained properties of hexagonally packed epithelia 33

2.2.1 A coarse grained description of flat epithelia 33

2.2.2 Coarse grained mechanical material properties of epithelia 34

2.2.3 Cell shape control in flat epithelia 41

2.2.4 Stability of flat epithelia subject to external tension or compression 45

2.2.5 Coarse grained material properties of epithelia in the Apical 3D Vertex Model 48

2.3 Simple epithelia on a sphere 49

2.4 Numerical study of mechanically homogeneous tissues 52

2.4.1 Shear and bulk moduli 52

- 2.4.2 Preferred curvature . . . 55
- 2.4.3 Bending modulus . . . 56
- 2.4.4 Equilibrium aspect ratios . . . 57
- 2.4.5 Epithelial buckling in simulations . . . 58
- 2.4.6 Spherical epithelia . . . 59
- 2.5 Summary . . . 62

3 Cyst Formation in the wing imaginal disc of *Drosophila* 63

- 3.1 The biology of cyst formation . . . 64
  - 3.1.1 Cell fate misspecification and cyst formation . . . 65
  - 3.1.2 Inverse cysts . . . 67
  - 3.1.3 Actin accumulation at clone boundaries . . . 68
  - 3.1.4 Clone shape quantifications . . . 70
- 3.2 The mechanics of cyst formation . . . 72
  - 3.2.1 The boundary contraction mechanism . . . 72
  - 3.2.2 Cysts are buckled clones . . . 73
  - 3.2.3 Cyst formation in the 3D Vertex Model . . . 78
  - 3.2.4 Relating the coarse grained theory and the 3D Vertex Model . . . 84
- 3.3 The function of the contractile boundary mechanism . . . 86
  - 3.3.1 Loss of small misspecified clones . . . 86
  - 3.3.2 Cyst formation and cancer . . . 87
- 3.4 Summary . . . 90

4 Ventral furrow formation through sagittal contraction 93

- 4.1 Introduction . . . 93
  - 4.1.1 The nuts and bolts of mesoderm invagination . . . 94
  - 4.1.2 Mechanical models of ventral furrow formation . . . 98
- 4.2 The sagittal contraction mechanism . . . 100
  - 4.2.1 Sagittal contraction in the Apical 3D Vertex Model . . . 102
  - 4.2.2 A continuum model for sagittal contraction . . . 105
  - 4.2.3 Bridging the scales between the continuous and the discrete model . 110

4.3 Outlook . . . 113
4.4 Summary . . . 114

5 Conclusions 115

5.1 Two complementary approaches to 3D epithelial mechanics . . . 115
5.2 Applications . . . 116
5.2.1 Shapes and stability of simple epithelia . . . 116
5.2.2 Cyst formation . . . 116
5.2.3 Ventral furrow formation by a sagittal contraction mechanism . . . 117
5.3 Outlook . . . 118

Appendices

Appendix A Introduction 123

A.1 List of vertex models for epithelial mechanics 123

Appendix B The 3D Vertex Model 125

B.1 The implementation 125

B.1.1 Obtaining the cell volume and surface areas from the vertex positions 125

B.1.2 Forces acting on the periodic box 126

B.1.3 Initial tissue configurations 127

B.2 Mechanical Properties 129

B.2.1 Geometrical quantities of regular hexagonal tissues 129

B.2.2 Parametrisation of curved tissues 129

B.2.3 Mechanical properties of epithelia in the Apical 3D Vertex Model . 130

B.3 Mechanical parameters in 3D Vertex Model simulations 135

B.3.1 Simulation parameters for 3D Vertex Model simulations of homogeneous, planar tissues 135

B.3.2 Simulation parameters for simulations of homogeneous, spherical epithelia 135

Appendix C Cyst Formation 137

C.1 Buckling instability of a spherical clone under compression 137

C.1.1 Details of the parameter search 139

C.1.2 Parameter variation for cyst simulations in the 3D Vertex Model . . 140

Appendix D Ventral furrow formation through sagittal contraction 143

D.1 Solving the stress equation on a sphere 143

D.1.1 Differential geometry of the sphere 143

D.1.2 Constitutive equations and force balance 145

D.1.3 Solving the force balance equations 145

D.1.4 Spherical harmonics 147

D.1.5 Deformations resulting from small perturbations in the active tension 149

D.1.6 Mode-wise comparison of Apical 3D Vertex Simulations and analytical calculations 151
D.2 The vitelline membrane in the 3D Vertex Model 155

CHAPTER 1

Introduction

1.1 Motivation and overview

Cells are the smallest independently self-replicating functional building blocks of any organism, and each adult human consists of as many as $\sim 4 \times 10^{13}$ cells [1]. The emergence of the observed complexity and diverse behaviours at the level of an organism from the genetic information stored in the DNA inside a fertilised egg is astonishing. This autonomous developmental process, termed *morphogenesis*, has a multitude of steps involving orchestrated growth, deformation and reorganisation of cells. It is driven by mechanical stresses generated inside the cells, which are regulated by chemical signalling and mechanical cues imposed by the environment. A major part of morphogenesis involves the deformation, flow and reorganisation of 2D sheets of cells, called *simple epithelia*.

The aim of present thesis is to understand the complex shape changes of epithelial tissues during morphogenesis. Note that the underlying biochemical processes, while playing an important role in generating and regulating the mechanical effects, are not the focus of this thesis. The central theme is instead the interplay between the mechanical stresses generated inside the cells and the shape of the epithelia. To characterise the epithelial shape we introduce a new 3D Vertex Model for the mechanics of simple epithelia that takes into account the full 3D structure of the tissue. After studying the resulting equilibrium shapes of cells in flat and spherical epithelia, we derive an effective continuum theory that represents the epithelium as a thin elastic sheet with bulk, shear and bending modulus. Then we bridge the scales between the two approaches by establishing the relationships between the respective mechanical parameters.

In the remainder of the thesis make use of the advantages of the 3D Vertex Model and the corresponding coarse-grained continuum theory to understand two morphogenetic processes in the development of the fruit fly *Drosophila melanogaster*: the *cyst formation* in the wing imaginal disc, and the *ventral furrow formation* in the early stages of gastrulation.

In SECTIONS 1.2 and 1.3 of the present chapter we introduce the biological system, *Drosophila melanogaster*, that serves as the model organism in this thesis. We then discuss the basics of simple epithelia and of cell mechanics that are prerequisites for the construction of the 3D Vertex Model of epithelial mechanics in SECTION 1.4. A description of existing vertex models and continuum theories for epithelial mechanics follows in SECTION 1.5.

In CHAPTER 2 we introduce the 3D Vertex Model for epithelial mechanics, and derive coarse grained mechanical properties on the level of the tissue that emerge from cellular mechanics. In CHAPTER 3 we then apply the model to the *Drosophila* wing imaginal disc and show how a mechanical boundary effect around misspecified cells leads either to the formation of cysts, or the extrusion of small cell clusters. In CHAPTER 4 we study the process of mesoderm invagination at the beginning of gastrulation, and suggest a new perspective on its mechanical drivers. We conclude the thesis by summarising our main findings and suggesting further directions of research.

1.2 The fruit fly *Drosophila melanogaster*

In addition to providing a generic theoretical framework for epithelial mechanics in 3D, the biological focus of this thesis will be the mechanics of developmental processes in the embryogenesis of *Drosophila melanogaster* (in the following referred to as *Drosophila*). The present section gives a brief overview of the fruit fly species and its developmental process.

While being unaware of the paramount importance of the *Drosophila* in research, most people are frequently confronted with this cosmopolitan insect in their daily life; often it can be found hoovering over a glass of wine on a warm summer evening, or populating a bowl of fruits in search for yeast, its primary food. It belongs to the taxonomic order of *dipterans*, like the common house fly and the blowfly, but it is smaller and weighs about 1mg. The male of the fly, shown in FIG. 1.1a, is smaller than the female and has a black abdomen, which resulted in the name addition '*melanogaster*'.

The fruit fly has been studied intensively since the beginning of the 20th century, after it was brought to the attention of the general scientific community by the genetic studies of Thomas Morgan Hunt in 1910 [2, 3]. FIG. 1.1b shows an illustration of one of his early crossing experiments. Ever since *Drosophila* has gained importance as a model organism to study morphogenesis, cell biology, genetical pathways and tissue mechanics, to name just a few. It was soon found that all higher organisms use similar genetic systems, and although the morphology of, for instance, humans and the fruit fly is very different many processes on the level of cells and tissues are surprisingly similar.

The advantages of using fruit flies in experiments are manifold: they are easy to maintain, have a short generation time of about 10 days at room temperature in which they produce a large number of progenies, and it is easy to distinguish males and females which facilitates genetic crossing. Also, it was found that the redundancy of genes in the fruit fly is much smaller compared to genetic redundancy in mammals, which makes it significantly easier to identify the function of genes [4]. In a big collective effort, the fruit fly's entire genome of about 13,600 genes has been sequenced and a variety of tools of genetical manipulation has been designed, making *Drosophila* a very attractive model to study developmental processes [5].

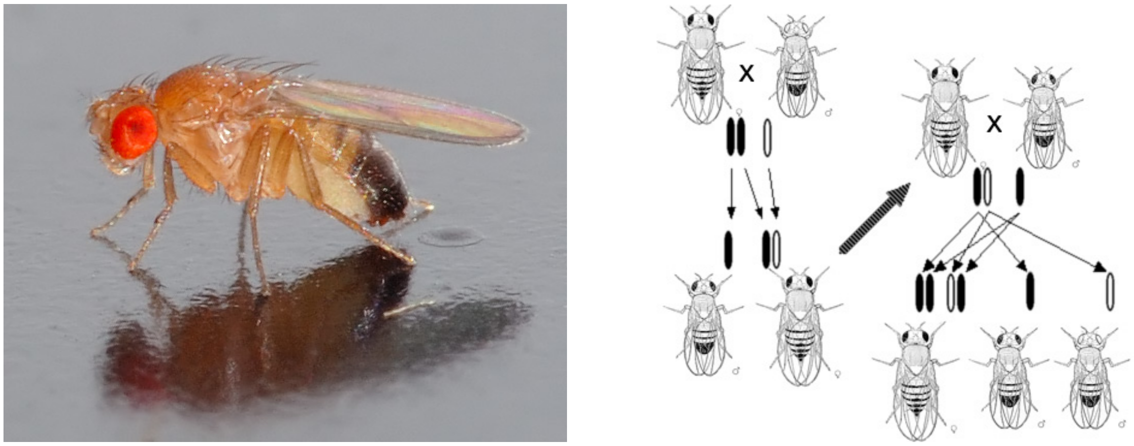

(a) The adult fruit fly *Drosophila* **(b)** Early crossing experiments by TH Morgan [3].

Figure 1.1: The morphogenesis and genetics of the fruit fly *Drosophila melanogaster* have been studied since the beginning of the 20th century, following the seminal research of Thomas Hunt Morgan.

Embryonic development

The morphogenesis of *Drosophila*, as outlined in Fig. 1.2a, is the sequence of morphological events by which the fertilised egg develops into a fully-grown adult fly. After fertilisation of the oocyte the embryo undergoes 12 to 13 rounds of rapid DNA replications until approximately 5,000 to 6,000 nuclei are dispersed in the so called *blastocoel*, which is filled with the fluid yolk. By the end of the 8th round of replication most nuclei have migrated to the surface surrounding the embryo. Approximately after the 13th round of nuclear division, cellularisation takes place and a cell membrane is established around the single nuclei, dividing the cytoplasm from the yolk. At this stage the embryo is called *blastula* and the cells form a simple epithelium, called *blastoderm*, that surrounds the blastocoel. Shortly after completion of cellularisation, the process of *gastrulation* sets in, during which the simple blastula is transformed into a trilaminar *gastrula* in which the three germ layers *endoderm*, *mesoderm* and *ectoderm* are separated. Gastrulation happens through a well coordinated sequence of morphological deformations, including *ventral furrow formation*, *germ-band extension* and *endoderm invagination* [6]. Ventral furrow formation and its mechanical drivers will be discussed in more depth in Chapter 4. After completion of gastrulation the embryo hatches from the surrounding cuticle as a larva. At this developmental stage the progenitors of all external body parts of the fly are embedded inside the larva as *imaginal discs* as shown in Fig. 1.2b. These imaginal discs are *simple epithelia* (cf. Section 1.3) that initially consist of as few as 20 cells and grow 1000-fold, while undergoing complex deformations during the larval and pupal development. About 10 days after the egg lay the young *Drosophila* concludes its embryonic development and starts its adult life as a full functioning insect.

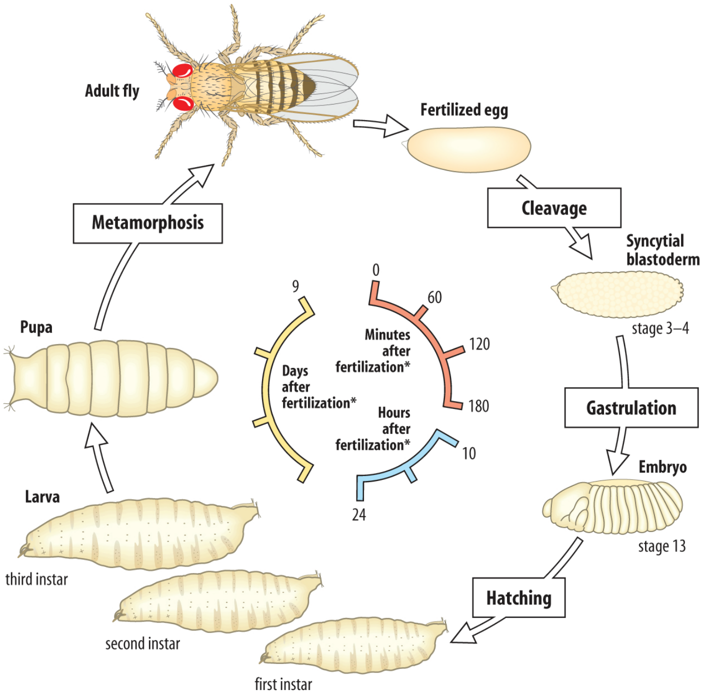
Adult fly
Fertilized egg
Cleavage
Syncytial blastoderm
stage 3–4
Gastrulation
Embryo
stage 13
Hatching
first instar
second instar
third instar
Larva
Pupa
Metamorphosis
0
60
120
180
Minutes after fertilization*
10
24
Hours after fertilization*
9
Days after fertilization*

(a) *Drosophila* morphogenesis from a fertilised egg to the adult fly (from [7]).

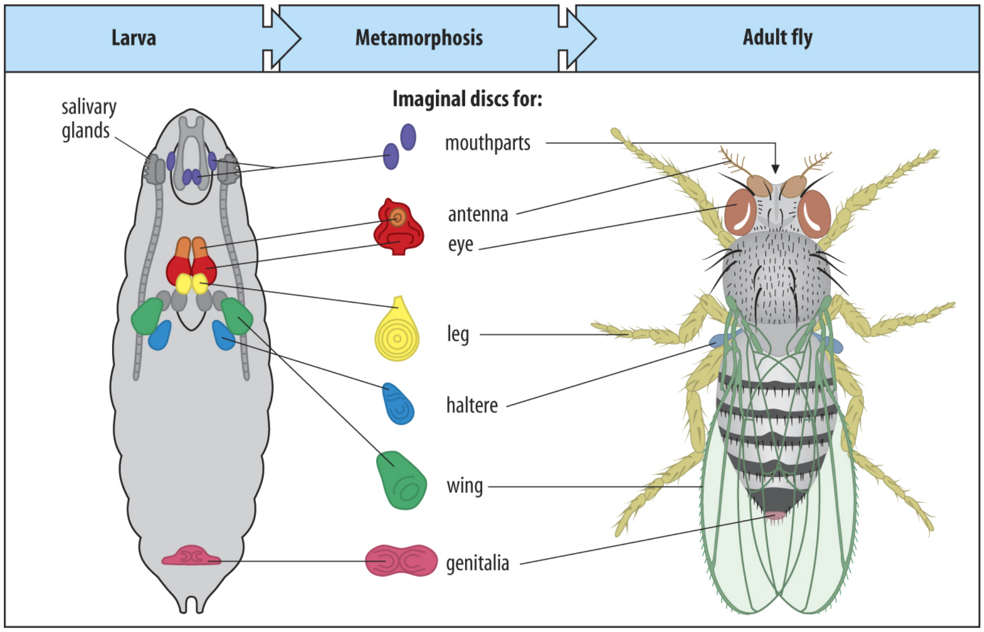
Larva
Metamorphosis
Adult fly
salivary glands
Imaginal discs for:
mouthparts
antenna
eye
leg
haltere
wing
genitalia

(b) Imaginal discs of *Drosophila* during its larval stage develop into the the corresponding external body part of the insect (adapted from [7]).

Figure 1.2: The development of *Drosophila* from a fertilised egg into the full-grown insect in the course of 10 days, in a sequence of highly coordinated morphogenetic events.

1.3 Epithelial tissues

A tissue is defined to be a group of cells of common origin that forms a separate entity inside an organism and carries out specific functions. Tissues are classified into four major classes with common features and functionality: connective tissues, muscle tissues, nerve tissues and finally epithelial tissues, which are of special importance for this thesis. Cells in epithelial tissues are arranged in a two dimensional array and coupled to their neighbouring epithelial cells by adhesion molecules along their so called lateral cell surfaces (Fig. 1.3). Epithelial cells have a well-maintained apical-basal polarity that is established through differences in protein distribution along the cell membrane. This apical-basal polarity allows for distinct mechanical features of the cells' apical and basal surfaces. Basally the cells secrete a layer of cross-linked structure proteins, such as Collagen IV, Lamin and Perlican, called basement membrane or extracellular matrix (ECM), which will be discussed in Section 1.4.

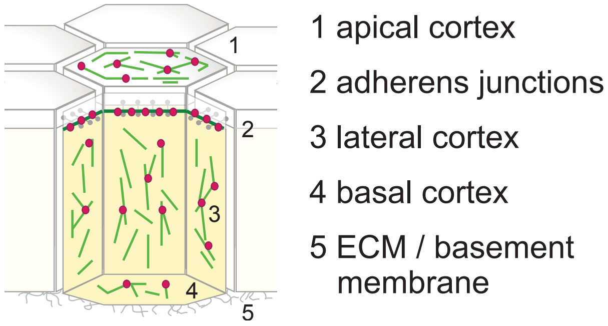

Figure 1.3: An illustration of cells in a typical simple epithelium. The cells are laterally coupled to their neighbours by adhesion proteins, which are especially prominent along the apical adherens junctions. The cells have an apical, basal and lateral actin cortex and are basally bound by integrins to a basement membrane.

Two types of epithelia can be distinguished depending on their connection to the underlying ECM: epithelia are called simple, if each cell is in direct contact with the underlying basement membrane (Fig. 1.4), or stratified if instead the cells in the epithelium are organised into layers. The focus of this thesis is on simple epithelia, and therefore in the following 'simple epithelium' and 'epithelium' will be used interchangeably. Simple epithelia have crucial functions both in morphogenesis and in the later adult life of all animals, where they line the cavities and surfaces of blood vessels and organs throughout the body. During embryogenesis many complex organs such as the heart in mammals [8] and the wing in *Drosophila* develop from a simple epithelium consisting of less than 50 cells. In adult animals, epithelia are mostly found in organs where secretion, absorption and filtration occur, because these processes are facilitated by the structure of the epithelia [9].

Simple epithelia are found in a variety of shapes and are classified depending on their cells' aspect ratio - one can distinguish *squamous* epithelia (found in lungs, heart, blood vessels), *cuboidal* epithelia (found in kidney and glands) and *columnar* epithelia (found in bronchi, uterus, bladder, intestines). It is also this range of different shapes that allows epithelial tissues to account for a broad range of functionality, such as protection, secretion, absorption, filtration and sensing [9]. Possible mechanisms by which epithelia are able to control their shape are discussed in Section 2.2.3.

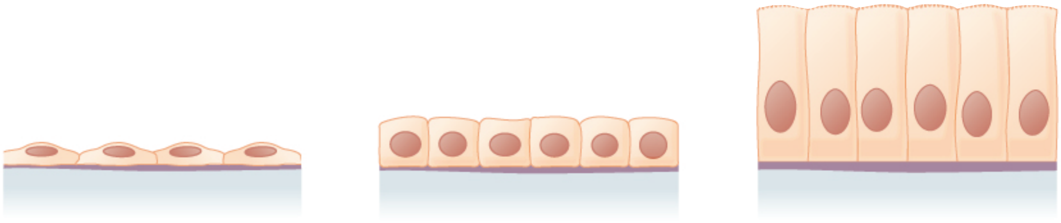

(a) Squamous *(lung, heart, blood vessels)*

(b) Cuboidal *(kidneys, glands)*

(c) Columnar *(bronchi, bladder, intestines)*

Figure 1.4: Simple epithelia can be classified by their aspect ratio, which allows them to fulfil a variety of functions in higher animals [9]. All images are adapted from `http://cnx.org/content/col11496/1.6/`

.

1.4 Prerequisites of cell and epithelial mechanics

The mechanics of simple epithelia has fascinated scientists for more than a century, which is partly due to their apparently simple 2D arrangement and regular features. In the famous book "On Growth and Form" in the early 20th century, D'Arcy Wentworth Thompson explained how tensions generated inside epithelia can explain the hexagonal packing of cells [10], and since that time many great contributions have been made towards the understanding of the 2D arrangement of cells in epithelia [11, 12]. To understand the deformations of epithelia from a mechanical point of view one needs to take into account how cells are mechanically coupled to each other and their environment, which tensions are actively generated inside the cells and which external forces are applied onto the epithelium.
In the present section we review some key aspects of cell and epithelial mechanics that will form the basis of the 3D Vertex Model introduced later on.

Tension generation inside the cell cortex

The cell cortex, or actin cytoskeleton, in animal cells is a thin, cross linked layer of actin filaments directly underneath the plasma membrane. Myosin motors actively generate tensions inside the meshwork under the consumption of chemical energy stored in adenosine triphosphate, by sliding actin filaments with respect to each other [13, 14]. The structure of the cortex, its dynamics and how tensions are generated have been scrutinised in the past decades and while great advances have been made, many details still remain poorly understood.

The cortex thickness is estimated to range in thickness from $\sim$100 nm in *Dictyostelium discoideum* to $\sim$190 nm in HeLa cells [15, 16]. The structure of the cortex is complex and highly dynamic, as its constituents are undergoing constant turnover on timescales ranging from a few seconds to minutes. There exists a plethora of actin binding proteins that couple actin to other actin filaments, to the membrane and membrane binding proteins, and to other cytoskeletal structures, such as microtubules and intermediate filaments [17]. In many epithelial cells the cortex is thicker along the apical cell surfaces, but it is also covering the cells' lateral and basal surfaces.

Through micropipette aspiration and atomic force microscopy, the cortical tensions have been estimated to be in the range of $\sim$30 pN/μm in blood granulocytes [18, 19], through $\sim$300-400 pN/μm in fibroblasts [20, 21] to 1500-4000 pN/μm in *Dictyostelium* [22, 23]. Due to the coupling of the cortex to the cell membrane and neighbouring cells the tensions generated inside the cortex can lead to the deformation of the cells and the surrounding tissue. Therefore, the cell cortex plays an important role in stabilising the cells' shape, but also in cell motility and cell division.

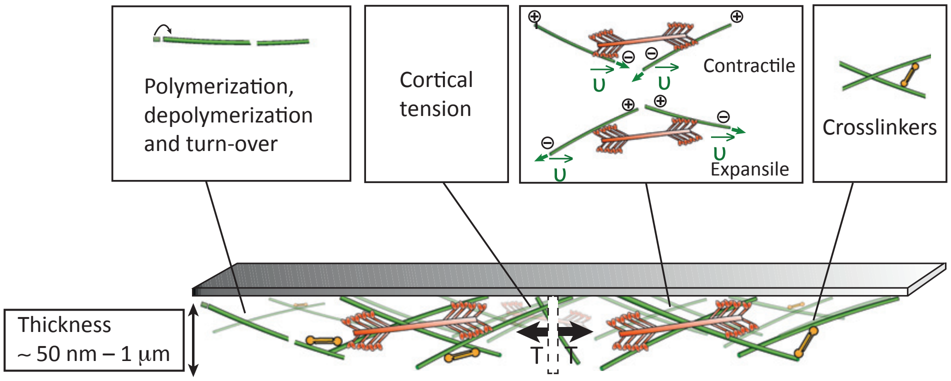

Figure 1.5: The actin cortex is made of actin filaments that are coupled by cross linkers. Myosin II motors shear the filaments with respect to each other and generate an effective tension T inside the cortex. Because the cortex is tightly coupled to the cell membrane, it plays a significant role in cell mechanics and cell shape changes. Image adopted from [14].

Volume conservation in cells

It has been shown in various experimental studies for different tissues and organisms that cells are very well able to maintain a constant volume, even if they are exposed to mechanical stresses [24, 25, 26]. It is however not well understood how this volume regulation is achieved. One discussed possibility is that the cell membrane, which is a selectively permeable phospholipid bilayer surrounding the cell volume, regulates the in- and out-flux of water by the generation of osmotic stress and can thereby act as a control mechanism []. In addition, the crowding of cells by cell organelles and elastic structures confined inside the cells, such as the nucleus or microtubuli, could also contribute to an effective volume conservation of the cells through steric hindrance.

The basement membrane

The basement membrane is a specialised form of ECM and lies as a dense sheet-like structure of 50-100 nm in thickness underneath the basal surface of epithelia [27] (see also schematics in Fig. 1.3). It is a network of extracellular molecules secreted by epithelial cells that provides them with mechanical and biochemical support. Among all of its constituents Collagen IV is the most abundant as it comprises about 50% of the proteins of the basement membrane [27], thus providing it with its main structural features [28]. Integrins are transmembrane proteins that play a crucial role in binding the basement membrane to the epithelium, as they link the Collagen to the actin cytoskeleton inside the cells [29, 30]. Several studies found that disturbing integrin activity or cleaving ECM components leads to significant deformations of the wing imaginal disc [31, 28, 32], suggesting a crucial mechanical role of the basement membrane during the fly's development.

1.5 Mechanical models of simple epithelia

In physical terms, cells and biological tissues are best described as complex, active materials. In living systems chemically stored energy can be transformed into active tensions, leading to motion and deformation inside the system. Interesting phenomena in these materials are happening on length scales ranging from a few nanometer (DNA transcription) to several centimetres (muscle contraction) and meters (information transport through axons), and on time scales ranging from a few microseconds (protein folding) to years (ageing). Consequently no unified model is applicable to the whole range of phenomena involving living matter, but instead the appropriate model has to be chosen or tailored depending on the question being asked.

Simple epithelia, introduced in Section 1.3, are an important example of a complex living material. They are composed of cells of different types, which themselves are made of a plethora of complex cell organelles. Simple epithelia can actively and autonomously deform due to active tensions, which are generated inside the cells under constant hydrolysation of adenosine triphosphate, as explained in Section 1.4. The field of epithelial mechanics aims to understand the fundamental principles of epithelial deformations on the length scales of cells, which is why it is reasonable to assume that the sub-cellular mechanical details can be submerged into effective parameters on the length scales equal or larger than the typical size of cells.

Existing models of epithelial mechanics can be classified according to the chosen geometrical description and their underlying mechanical assumptions into the following groups: vertex models, continuous models, cellular Potts models, immersed boundary models, spheroid models, sub-cellular element models and more. The following Sections 1.5.1 and 1.5.2 give a brief overview of the definitions, properties and previous applications of vertex models and continuum models for epithelial mechanics, respectively.

1.5.1 Vertex models for epithelial mechanics

Vertex models for tissue mechanics have been around for a long time, and have been successfully applied to study a variety of developmental processes [33, 34, 35]. In the present section we give an overview of the geometrical and mechanical representation of epithelia in vertex models, and illustrate some of their applications. For an overview for studies that used the model and the corresponding applications please refer to the table A.1 in the appendix.

In existing vertex models, epithelia are described by a network of vertices that define the

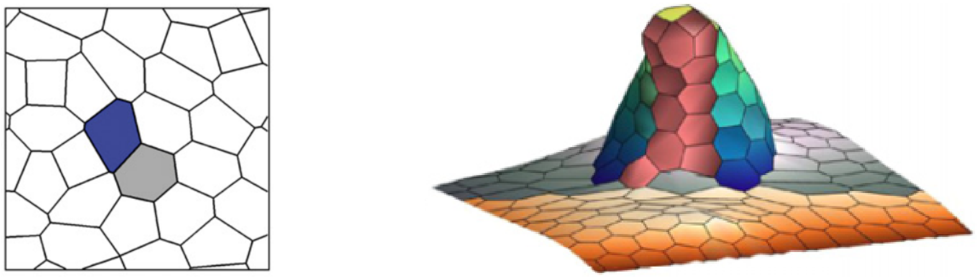

(a) 2D apical vertex model [35] **(b)** 3D apical vertex model [45]

Figure 1.6: Apical vertex models describe the tissue through the network of apical cell shapes. In 2D models, the apical surfaces are confined in a plane, whereas in 3D models the apical tissue surface is not necessarily flat and described by a 2D manifold in 3D space. The images are adapted from the respective publications.

polygonal apical cell surfaces. In the following these models will be referred to as 'apical vertex models, in order to differentiate them from models that also take into account the basal geometry of the tissue. Whereas in the original studies the tissue surface was confined in a 2D plane [35, 36, 37, 38, 39, 40, 41, 42, 43, 44], recent models represent the apical tissue surface by a 2D manifold in 3D space to study non-planar tissue configurations [45, 46, 47]. In addition to vertex positions also the topology of the network plays a crucial role and is allowed to change over time by means of cell division, cell extrusion and cell-neighbour exchange [35].

Forces in vertex models are acting to displace the vertices, and cell shape changes are due to movements of the vertices and topological changes of the cell network. The forces derive from an effective mechanical work function, which is a function of the vertex positions and the network topology. The detailed form of the work function depends on the underlying assumptions regarding the mechanical stresses generated inside the cells, and the forces acting onto the tissue.

In the model introduced by Farhadifar and colleagues in [35], cells are assumed to exhibit an elasticity of their apical areas, resulting from the volume elasticity of the cells and a constant cell height. Also line tensions acting along the apical bonds connecting the cells have been taken into account, together with a perimeter elasticity experienced by the cells. The resulting work function was consequently defined as:

$$E = \sum_{\alpha} \frac{K_\alpha}{2}(A_\alpha - A_\alpha^{(0)})^2 + \sum_{<i,j>} \Lambda_{ij} l_{ij} + \sum_{\alpha} \frac{\Gamma_\alpha}{2} P_\alpha^2, \tag{1.1}$$

where K_α denotes the 2D bulk modulus of cell α, A_α denotes its current area, $A_\alpha^{(0)}$ denotes its preferred area, P_α denotes its current apical perimeter and Γ_α denotes its perimeter elasticity; the line tension acting along bond $< i, j >$ with length l_{ij} is given by Λ_{ij}.

Later models allowed a dependency of the mechanical parameters on additional fields such as the protein distribution inside the cells [38, 43]. In the 3D version of the apical vertex model by Murisic et al. [46], an additional bending term was introduced to penalise local curvature of the tissue.

Once the tissue's effective work function W is defined, the force $\mathbf{F}_i$ acting on vertex i with position $\mathbf{X}_i$ is given by the derivative of the work function with respect to vertex movements:

$$\mathbf{F}_i = -\frac{\partial W}{\partial \mathbf{X}_i}. \tag{1.2}$$

A tissue configuration is a stable mechanical equilibrium if the forces on all vertices vanish, and any small deviation from the configuration results in a restoring force. Therefore mechanical equilibria correspond to local minima of the energy function W.

Two fundamentally different approaches to simulate the dynamics of epithelia have been implemented in vertex models. In the quasi-static approach, the network dynamics arise from variations over time in the mechanical parameters describing the tissue. The tissue is assumed to relax instantly to the 'closest' mechanical equilibrium after each incremental change of the mechanical properties, which thereby set the dynamics. The relaxation to the closest mechanical equilibrium can be efficiently implemented using high-dimensional minimisation methods, like the gradient or the conjugate gradient method. Note that the definition of 'closest' depends on the method used to identify the subsequent minima, and in specific cases different methods might lead to different dynamics. For a brief account of advantages and shortcomings of the quasistatic approximation please refer to the dissertation of D. Staple [48].

In the second approach to vertex dynamics, the vertices are assumed to experience an effective friction force depending on their velocity that has to be balanced by the current force acting on the vertex due to unbalanced tensions. In this approach inertial forces are assumed to be negligible. For vertex i, experiencing a friction η_i, the force balance equation then reads:

$$\eta_i \frac{d\mathbf{X}_i}{dt} = \mathbf{F}_i. \tag{1.3}$$

This first order differential system can be solved numerically for a given initial tissue configuration, using for instance a Runge-Kutta scheme. Previously the friction coefficient η_i has been considered to be constant and to represent a simple drag force for a vertex being pulled through a viscous medium, but in general it could also depend on the tissue state as suggested in [48], in which case η_i could also be a matrix. This method could specifically take into account the viscous dissipation resulting from deformations of the different elements of the tissue, such as bond lengths and surface areas.

Several variations of the original vertex model have been derived from the presented design principles, to address different research questions. The 2D versions have been applied to flat epithelia to study different aspects of the in-plane shape of the cells as a function of the mechanical stresses. They have been successfully applied with minor modifications to study cell packing [35, 39], cell sorting [37, 44], system size control [40, 42], cell migration [41], wound healing [36], tissue patterning [43] and the interplay between cell polarity and tissue mechanics [38]. These phenomenons have been studied in various organisms, such as the fruit fly, mouse, zebrafish and frog. FIG. 1.7 shows images of simulation results of the 2D apical vertex model from a selection of the aforementioned publications. Osterfield and colleagues were the first to propose the extension of the 2D vertex model to study the morphogenesis of the respiratory appendages on eggshells of *Drosophila*, FIG. 1.8a. They account for out of plane deformations of epithelia [45] by representing them as triangulated 2D manifolds in 3D, but used the same work function as 1.1. The purely theoretical study [46] used a 3D version of the apical vertex model to analyse the buckling behaviour of an apical surface subjected to compression (FIG. 1.8b). Monier et al. used a 3D apical vertex model in [47] to study the epithelial folding of the developing leg disc in *Drosophila*. The leg disc epithelium was described by the apical network of cell shapes. Instead the cells were assigned an effective volume elasticity that replaced the area elasticity introduced in [35] (FIG. 1.8c).

Underlying assumptions and limitations of apical vertex models

All apical vertex models described above necessarily make the simplification that the epithelial geometry can be effectively described through the apical network of cells. The basis of this assumption is that the basal tissue shape does not play a role in the studied system, or, alternatively, can be effectively adsorbed in the apical representation. While this approximation is valid in the case of flat epithelia, where the apical and basal cell network are very similar, it is not in general the case for deformed, non-planar epithelia. It has been shown in recent experiments that significant contractile stresses are also acting along the basal cell surfaces and along lateral cell interfaces that can lead to significant tensions acting outside the apical plane of the tissue. For instance, differences in apical and basal tensions can lead to the generation of local torques which cannot be accounted for by the purely apical description of epithelia. Furthermore, in most apical vertex models

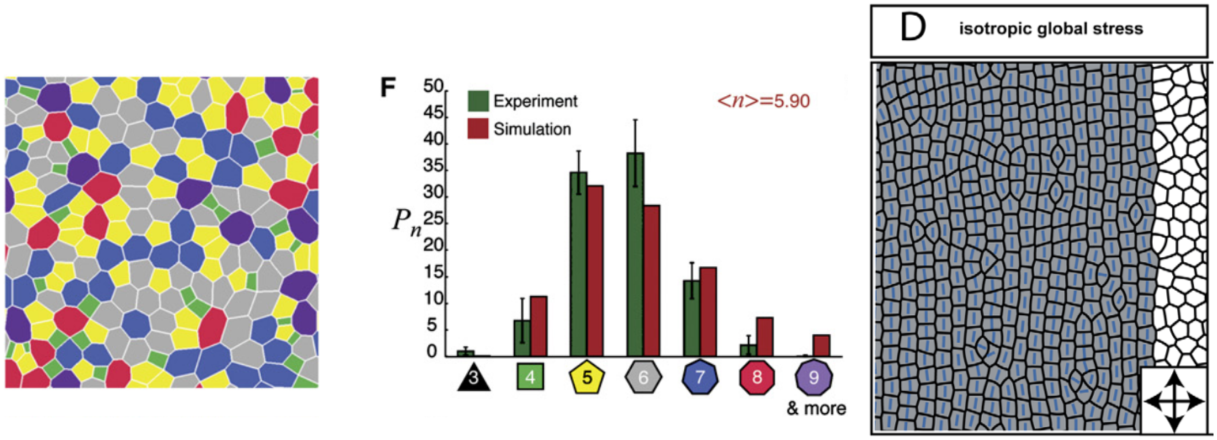

(a) Cell shape distribution [35] **(b)** Tissue patterning [43]

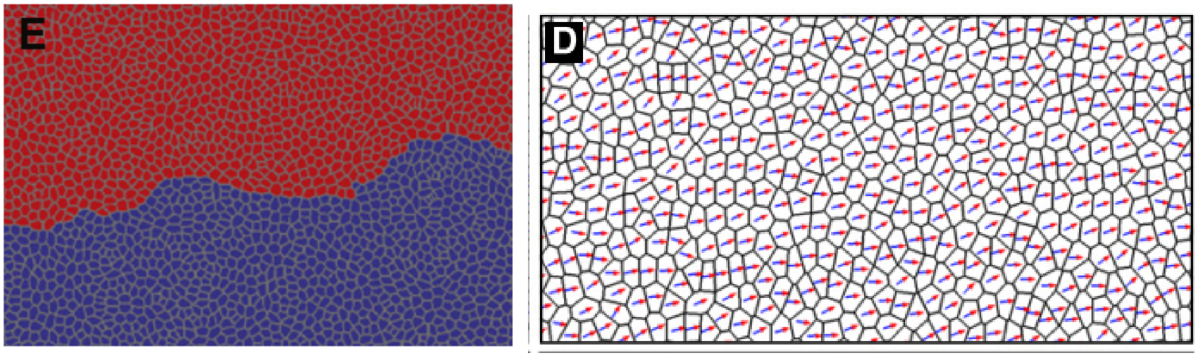

(c) Interface mechanics [44] **(d)** Planar cell polarity [38]

Figure 1.7: Images showing 2D apical vertex model simulation results from studies of various phenomena in developing epithelia in different organisms. The images are adapted from the respective publications.

the assumption is made that the cells experience an elasticity of the apical cell surfaces, resulting from the volume elasticity of cells and a fixed height of the tissue. Yet, what sets the height of the tissue in the first place, and how the effective area elasticity relates to the cells' mechanical properties lies outside the explanatory powers of the existing frameworks.

While apical vertex models are therefore well suited models to explain the 2D arrangement of cells in planar epithelial tissues, a different model is required to describe complex 3D epithelial deformations. Furthermore, also in the case of flat epithelia existing models do not give account for the full 3D cell shapes, and the origin of the preferred cell area and cell height.

To research these open questions we develop in present thesis a new mechanical model of epithelial mechanics, which accounts for both the apical and the basal shapes of the cells: the 3D Vertex Model.

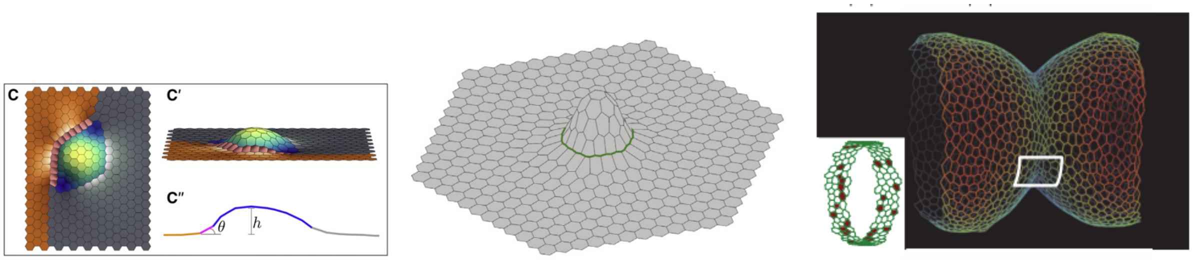

(a) Appendage formation [45] **(b)** Tissue buckling [46] **(c)** Fold formation [47]

Figure 1.8: Apical vertex models in 3D have been applied to study out-of-plane deformation of epithelia in different developmental contexts. The images are adapted from the respective publications.

1.5.2 Continuum models

Whereas simple epithelia in vertex models are modelled to consist of discrete cellular units, in continuum approaches they are regarded as continuous materials. These descriptions do not depend on the exact shape of the cells in the epithelium, and they are valid only on length scales larger than the typical length scale of cells. The idea to represent a tissue as a continuum material dates back to Malcolm S. Steinberg and colleagues, who described a cellular aggregate as a visco-elastic fluid in a series of publications in the early 1960s [49, 50, 51]. In these studies the *Differential adhesion hypothesis* was put forward, stating that the sorting of different cell types can be understood as the unmixing of two liquids with different surface tensions, similar to the separation of oil in water. Although these ideas were initially developed to explain properties of bulk tissues, similar ideas have been applied to simple epithelia in order to explain the straightening of the compartment boundaries in the imaginal wing disc of *Drosophila* [52, 44, 37]. Depending on the tissue properties and on the time-scales considered, tissues in continuous models have been described as purely elastic, purely viscous or as visco-elastic materials. Whereas Steinberg and coworkers successfully modelled aggregates of cells as viscous or visco-elastic fluids [51], cells organised into epithelia are coupled more strongly through adhesion molecules and can often be described more accurately as elastic or visco-elastic materials. More recently, theories of complex active visco-elastic fluids have been developed, which have been applied in 2D to study biological materials and tissues [53, 54, 55, 56, 52, 57].

1.5.3 Bridging the scales between vertex and continuum models

Continuum models and vertex models can be regarded as complementary in several aspects and the simultaneous use of the two frameworks can provide several advantages as we will highlight in this section.

In continuum models the underlying microscopic parameters are submerged into coarse-grained parameters featuring in the constitutive equations. If the epithelium is represented as a thin elastic sheet, the relevant mechanical parameters describe the response of the tissue to in-plane deformations, namely its bulk and the shear moduli, its preferred curvature and its response to bending deformations, namely the bending modulus. Different underlying microscopic models can give rise to identical continuum representations, which makes the continuum approach less dependent on the microscopic model. Depending on the experimental system, it might be possible to mechanically probe the coarse grained mechanical parameters, for instance by exposing the tissue to bulk and shear deformations and measure the response. However, how the coarse grained mechanical parameters depend on the stresses generated inside the cells is not immediately clear. Continuum models of mechanical systems have the advantage that they can be solved analytically in generic limits. They can be used for instance to predict buckling behaviour of epithelia, and to estimate the deformations of epithelia resulting from small mechanical perturbations. This analytical approach can therefore serve as a tool to identify key parameters that play a crucial role in the specifically studied process. Due to their construction continuum models cannot account for the detailed shapes of the epithelium and the cells, since they are valid only on the length scale of several cells. Furthermore, obtaining solutions of the continuum equations to obtain equilibrium epithelial shapes far from the linear regime of perturbations is analytically very challenging, and can normally only be achieved through advanced numerical routines.

Vertex models of tissue mechanics often feature a greater number of parameters than continuum models, but they directly reflect stresses generated on the level of the cells. These tensions can be inferred experimentally by locally probing the cell properties, for instance through laser ablation experiments or by measuring local concentrations of motor-molecules. The bigger number of mechanical parameters and degrees of freedom often makes vertex models less generic and more complicated to treat than continuum models. However, there exist powerful computational frameworks that allow to solve the constitutive equations for the dynamical behaviour and the equilibrium tissue shapes even for strong perturbations away from homogeneous tissue shapes. The obtained results also take into account non-linearities of the system, which can be much harder to study in continuum frameworks. Furthermore vertex models can account for more details of cell shapes and local deformations, which can then be directly compared to experimental observations.

Both discussed approaches have therefore complimentary advantages, which makes their combination a powerful tool to study and understand the mechanics of complex morphogenetic events. The connection between vertex model simulations and a continuum theory has been made by Staple et al. in [39] where the authors derived the effective coarse grained shear and bulk modulus of a model tissue as a function of the apical area and perimeter elasticity in the 2D apical vertex model. In [46] Murisic and coauthors derived the effective bending modulus of the tissue from their apical 3D vertex model. They then analysed theoretically the buckling behaviour of a tissue under compression in simulations and in their continuum theory and showed that both approaches yield the same results.

In present thesis we show the correspondence between microscopic parameters of the 3D Vertex Model and a continuum approach of epithelial deformations. Then we go beyond this theoretical approach and combine the developed tools to study two concrete processes in the morphogenesis of *Drosophila*. The continuum model is used to identify key features that account for the qualitative behaviour of the studied mechanisms and to develop a physical intuition of the influence of the coarse grained parameters. 3D Vertex Model simulations are then used to obtain the resulting detailed tissue shapes, which are quantitatively matched with the experimental observations. At each step we show that the continuum theory and the 3D Vertex Model simulations yield the same results in the limits of the continuum calculations, thereby demonstrating the consistency of the two approaches.

CHAPTER 2

3D description of epithelial mechanics

The complex 3D shapes of epithelia are determined by the interplay of pressures and tensions generated inside the cells, and by external forces that are exerted onto the tissue. We argued in Section 1.5.1 that the existing vertex models of epithelial mechanics, while yielding a good description of many flat epithelia, are not suited to account for many complex 3D morphogenetic processes. In the present chapter a new 3D Vertex Model for epithelial mechanics is introduced and analysed, which also takes into account stresses that are not generated inside the apical cell surfaces. Thereby we aim to provide a new tool for the effective study of morphological events that involve the complex deformations of simple epithelia in three dimensions.

The introduction of the 3D Vertex Model in Section 2.1 is organised into three parts focussing on the different aspects of geometry, the mechanical work function and topological changes. After defining the model, we derive the effective bulk modulus, shear modulus and bending modulus of flat homogeneous epithelia in Section 2.2.1. Then we show how epithelial equilibrium height and cell density is controlled by tensions generated inside the cells, and external tensions. External tensions can lead to the buckling of flat epithelia, which we will study in Section 2.2.4. After focussing on flat homogeneous epithelia we move on to spherical epithelia surrounding a compressible liquid in Section 2.3, and study their equilibrium properties both analytically and by means of 3D Vertex Model simulations. In Section 2.4, the final part of the chapter, we show the consistency of the 3D Vertex Model simulations with the coarse graining approach by comparing the analytically predicted and the numerically obtained mechanical moduli and tissue properties.

2.1 A 3D Vertex Model for epithelial mechanics

In this section we introduce the mechanical hypotheses and geometrical formulation of the 3D Vertex Model and important details of its implementation, such as topological transitions and the identification of equilibrium tissue shapes. We start by describing the geometrical representation of the epithelial cells through apical and basal vertices in 2.1.1. Then the effective mechanical work function of the model is introduced in 2.1.2, and it is shown forces and equilibrium configurations can be obtained from the work funcion.

Finally we introduce of topological transitions and show how cell division, T1 transition and cell extrusion are taken into account in the framework of the 3D Vertex Model.

2.1.1 The 3D Vertex Model representation of simple epithelia

Simple epithelia in the 3D Vertex model are represented by a set $\mathcal{V}$ of vertices marking the common apical and basal points of three or more cells. The assumption is made that two cells are adjacent basally if they are adjacent apically, hence enforcing that the apical and basal networks of vertices and bonds have the same topology (Fig. 2.1a). Therefore the tissue is completely described by the topology of the apical network together with the apical and basal vertex positions, called $\mathbf{X}_a^i$ and $\mathbf{X}_b^i$ respectively for each vertex $i \in \mathcal{V}$. Each edge of the network corresponds to a cell-cell interface, describing common apical, lateral and basal contacts between cells. Straight lines between apical positions of adjacent vertices represent the apical cell outlines, and the same holds respectively for their basal counterparts. Lateral bonds are lines connecting the apical and basal positions of each vertex. Each cell α is represented by a set of M^α vertices as shown in Fig. 2.1b. The apical surface of cell α is given by the surface enclosed by the vertex positions $(\mathbf{X}_a^{\alpha,i})_{i=1}^{M^\alpha}$, and the corresponding basal surface by $(\mathbf{X}_b^{\alpha,i})_{i=1}^{M^\alpha}$. Any lateral surface $i, j \in \mathcal{V}$ common to two cells, is defined by the surface enclosed by the apical and basal vertex positions

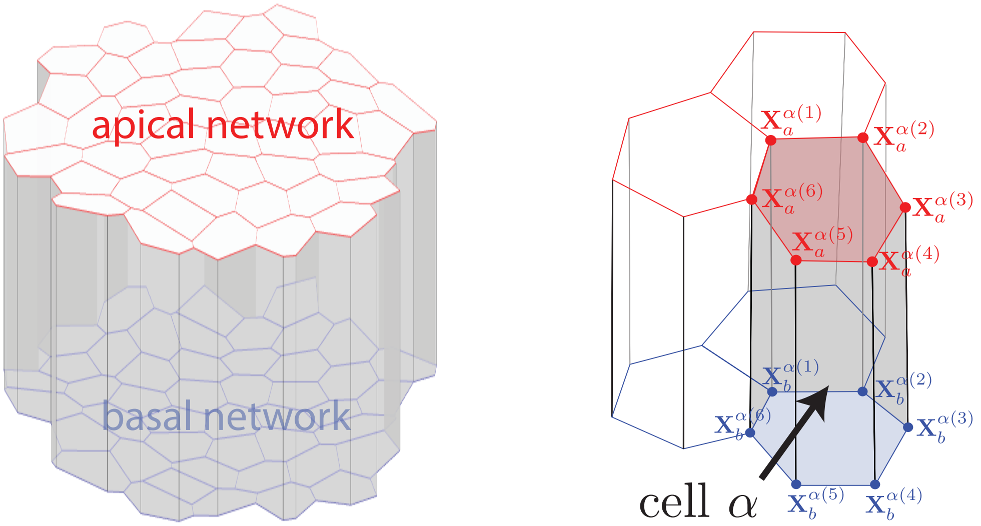
apical network
basal network
$\mathbf{X}_a^{\alpha(1)}$
$\mathbf{X}_a^{\alpha(2)}$
$\mathbf{X}_a^{\alpha(3)}$
$\mathbf{X}_a^{\alpha(4)}$
$\mathbf{X}_a^{\alpha(5)}$
$\mathbf{X}_a^{\alpha(6)}$
$\mathbf{X}_b^{\alpha(1)}$
$\mathbf{X}_b^{\alpha(2)}$
$\mathbf{X}_b^{\alpha(3)}$
$\mathbf{X}_b^{\alpha(4)}$
$\mathbf{X}_b^{\alpha(5)}$
$\mathbf{X}_b^{\alpha(6)}$
cell α

(a) Tissues are modelled by an apical and basal network of cells with the same topology.

(b) Cell α is represented by a set of vertices $1, .., 6$ and their apical and basal positions.

Figure 2.1: The representation of epithelial cells in the 3D Vertex Model through networks of apical and basal vertices that represent the intersection of three or more cells.

$(\mathbf{X}_a^i \rightarrow \mathbf{X}_b^i \rightarrow \mathbf{X}_b^j \rightarrow \mathbf{X}_a^j)$.

Because positions of vertices constituting a surface are not enforced to be coplanar, the

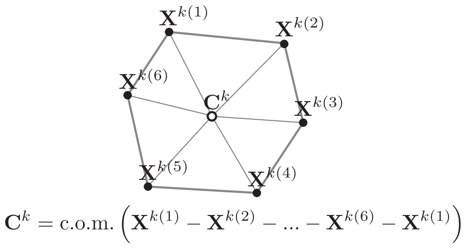
$\mathbf{X}^{k(1)}$
$\mathbf{X}^{k(2)}$
$\mathbf{X}^{k(6)}$
$\mathbf{C}^k$
$\mathbf{X}^{k(3)}$
$\mathbf{X}^{k(5)}$
$\mathbf{X}^{k(4)}$
$\mathbf{C}^k = \text{c.o.m.}\left(\mathbf{X}^{k(1)} - \mathbf{X}^{k(2)} - \ldots - \mathbf{X}^{k(6)} - \mathbf{X}^{k(1)}\right)$

Figure 2.2: All surfaces confining cells in the 3D Vertex Model are triangulated, and are defined by the triangles connecting their vertices and the centre of mass of their circumference given in Eq. 2.1.

surfaces enclosing the cell have to be defined. Let k be an apical, basal or lateral surface with its contour line defined by the path through the N^k vertex positions ($\mathbf{X}^{k(1)} \rightarrow \mathbf{X}^{k(2)} \rightarrow \ldots \rightarrow \mathbf{X}^{k(N_k)} \rightarrow \mathbf{X}^{k(N^k+1)} = \mathbf{X}^{k(1)}$). The associated centre of mass $\mathbf{C}^k$ of surface k is then defined as the centre of mass of the contour line

$$\mathbf{C}^k = \frac{\sum_{i=1}^{N^k} |\mathbf{X}^{k(i)} - \mathbf{X}^{k(i+1)}| \frac{\mathbf{X}^{k(i)} + \mathbf{X}^{k(i+1)}}{2}}{\sum_{i=1}^{N^k} |\mathbf{X}^{k(i)} - \mathbf{X}^{k(i+1)}|}. \tag{2.1}$$

The centre of mass $\mathbf{C}^k$ is used to generate a triangulation of the interface k, by joining the centre to all vertices belonging to the interface as shown in Fig. 2.2. A cell α that is given by M^α vertices, is therefore a polyhedron which is fully enclosed by 6 M^α triangular faces, of which M^α triangles each form the apical and the basal cell surface and 4 M^α triangles form the cell's lateral interface that connect it to other cells.

Geometrically the tissue consists of 4 different structures with different dimensions: a set of vertices $\mathcal{V}$ (corresponding to apical and basal points of intersection of three or more cells), a set of lines $\mathcal{L}$ (corresponding to bonds between cells), a set of surfaces $\mathcal{S}$ (corresponding to apical and basal cell surfaces, and lateral cell interfaces) and a set of polyhedrons $\mathcal{C}$ (corresponding to cell volume). The relevant geometrical quantities of the tissue are therefore the positions of the vertices, the lengths of the lines, the areas of the surfaces and the volumes of the polyhedrons, which can all be derived from the positions of the vertices.

2.1.2 Work function and resulting forces

In the 3D Vertex Model forces act to displace vertices in the model epithelium. These forces are derived from a virtual work, based on the tensions generated inside the epithelium and external mechanical constraints, which have been described in SECTION 1.4. For clarity the differential virtual work δW is therefore written as the sum of the work exerted within the epithelium δW_i and outside the epithelium δW_e:

$$\delta W = \delta W_i + \delta W_e. \tag{2.2}$$

In the following we discuss the detailed form of the internal and external work contributions.

Internal forces

The differential of the internal virtual work reads

$$\delta W_i = \sum_{\alpha \in \mathcal{C}} -P^\alpha \delta V^\alpha + \sum_{k \in \mathcal{S}} T^k \delta A^k + \sum_{\lambda \in \mathcal{L}} \Lambda^\lambda \delta l^\lambda, \tag{2.3}$$

where, as described above, $\mathcal{C}$ is the list of all cells, $\mathcal{S}$ is the list of all surfaces and $\mathcal{L}$ is the list of all bonds in the tissue. The volume of cell α, the surface area of interface k and the length of the bond λ are respectively given by V^α, A^k, and l^λ. P^α denotes the pressure acting in cell α, T^k denotes the surface tension on interface k, and Λ^λ denotes the line tension acting on the line λ. Note that all mechanical parameters can be functions of the current state of the tissue.

Surface tensions T^k are thought to arise from the active actomyosin cortical cytoskeleton, where contractility of myosin molecular motors in the surface actin network leads to the establishment of a surface tension (FIG. 2.3a, SECTION 1.4). We assume that surface tensions act throughout the apical and basal cell surfaces, as well as along the lateral cell interfaces and that they are homogeneous on all triangles of each of these interfaces. Note that the tensions need not be independent of the current area of the surface, but the surfaces could exhibit elastic properties where the tension depends explicitly on the area of the surface (i.e. $T^k = T^k(A^k)$). Line tensions are thought to arise from actin cables forming along the apical and basal perimeter of cells (FIG. 2.3b).

Cells are assumed to be able to maintain a preferred volume, as described in SECTION 1.4. We make an expansion of the cells' pressure around the preferred volume and only take into account the linear contribution:

$$P^\alpha = -K^\alpha (V^\alpha - V_0^\alpha), \tag{2.4}$$

where V_0^α is the preferred cell volume of cell α and the proportionality constant K_α is its bulk elastic modulus (FIG. 2.3c).

All considered internal differential work functions δW_i in this thesis can be derived from an actual work function W_i by:

$$\delta W_i = \sum_{\alpha \in \mathcal{C}} \frac{\partial W_i}{\partial V^\alpha} \delta V^\alpha + \sum_{k \in \mathcal{S}} \frac{\partial W_i}{\partial A^k} \delta A^k + \sum_{\lambda \in \mathcal{L}} \frac{\partial W_i}{\partial l^\lambda} \delta l^\lambda, \tag{2.5}$$

and the pressure P^α, surface tensions T^k, and line tensions Λ^λ are consequently defined by:

$$P^\alpha = -\frac{\partial W_i}{\partial V^\alpha} \tag{2.6}$$

$$T^k = \frac{\partial W_i}{\partial A^k} \tag{2.7}$$

$$\Lambda^\lambda = \frac{\partial W_i}{\partial l^\lambda}. \tag{2.8}$$

In the case of constant line and surface tensions along all lines and surfaces, and a cell pressure given through Eq. 2.4, integrating the differential work function yields the internal work function:

$$W_i = \sum_{\alpha \in \mathcal{C}} \frac{K^\alpha}{2} (V^\alpha - V_0^\alpha)^2 + \sum_{k \in \mathcal{S}} T^k A^k + \sum_{\lambda \in \mathcal{L}} \Lambda^\lambda l^\lambda. \tag{2.9}$$

External forces acting on the epithelium

In addition to the internally generated tensions we take into account two sources of external force: an external in-plane surface tension acting on the area of the tissue (FIG. 2.3e) and a term representing constrains imposed by attachment to and constraints imposed by the ECM (FIG. 2.3d). The external variation of the virtual work then reads

$$\delta W_e = \sum_{i \in \mathcal{V}} k^i z_b^i \delta z_b^i - T_{ext} \delta A^{tot}, \tag{2.10}$$

where the shortest euclidean distance of the basal position of vertex i to the ECM is denoted z_b^i, and the total tissue surface area is denoted A^{tot}. The spring modulus k^i

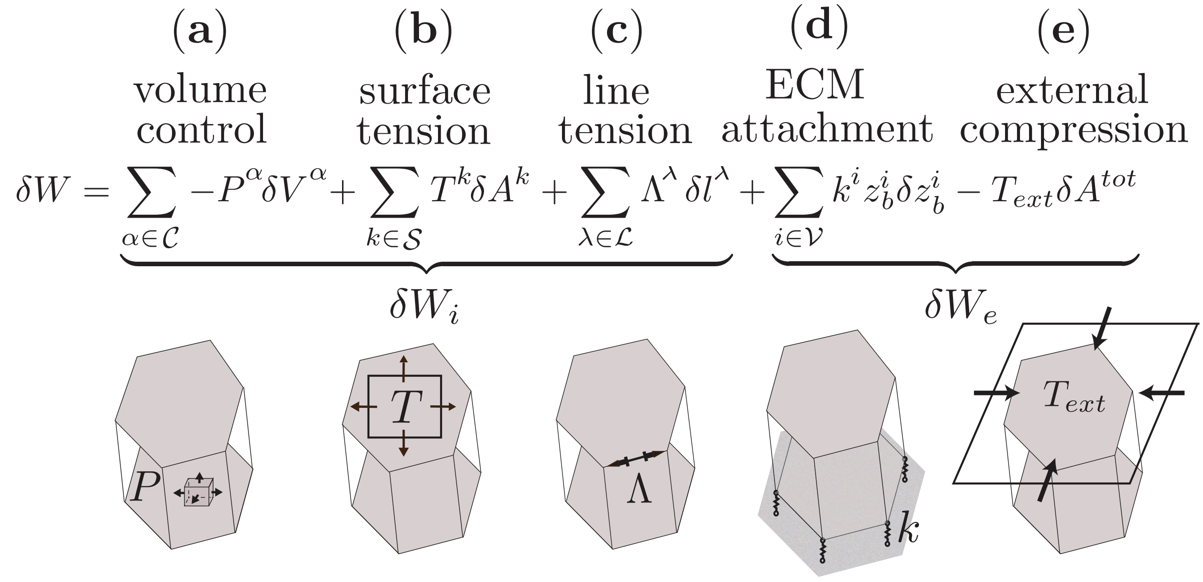
(a)
volume control
(b)
surface tension
(c)
line tension
(d)
ECM attachment
(e)
external compression
$\delta W = \underbrace{\sum_{\alpha\in\mathcal{C}} -P^{\alpha}\delta V^{\alpha} + \sum_{k\in\mathcal{S}} T^{k}\delta A^{k} + \sum_{\lambda\in\mathcal{L}} \Lambda^{\lambda}\,\delta l^{\lambda}}_{\delta W_i} + \underbrace{\sum_{i\in\mathcal{V}} k^{i} z_b^{i}\delta z_b^{i} - T_{ext}\delta A^{tot}}_{\delta W_e}$
P
T
Λ
k
T_{ext}

Figure 2.3: The differential mechanical work function of the tissue includes cell pressure, surface and line tensions acting along the cell outlines, an elastic attachment to the underlying ECM and the compression of the tissue. All mechanical parameters can be function of the current state of the tissue, which for instance allows for elastic behaviour of cell surfaces.

represents elastic bonds attaching the tissue to the extracellular matrix, and it is non-zero only for basal vertices as the apical tissue does not form connections to the ECM. Analogously to the internal differential work function, also the external differential work function δW_e can be integrated to yield a work function W_e which is defined by:

$$\delta W_e = \sum_{i\in\mathcal{V}} \frac{\partial W_e}{\partial z_b^i}\delta z_b^i + \frac{\partial W_e}{\partial A^{tot}}\delta A^{tot}. \tag{2.11}$$

Thus, for the case of constant external tension T_{ext} the integrated external work function reads:

$$W_e = \sum_{i\in\mathcal{V}} \frac{k^i}{2}(z_b^i)^2 - T_{ext}A^{tot}. \tag{2.12}$$

Resulting forces acting on vertices

Summing up all internal and external contributions give rise to a total differential form of the work function, which is shown together with a schematic in Figure (2.3). The forces

$\mathbf{F}_a^i$ and $\mathbf{F}_b^i$ acting on the apical and basal positions of vertex $i \in \mathcal{V}$ are defined through the infinitesimal change of the mechanical work under vertex displacement:

$$\mathbf{F}_a^i = -\frac{\delta W}{\delta \mathbf{X}_a^i} \tag{2.13}$$

$$\mathbf{F}_b^i = -\frac{\delta W}{\delta \mathbf{X}_b^i}. \tag{2.14}$$

Apical vertices experience forces due to surface tensions of the adjacent apical cell surfaces and lateral interfaces, due to line tensions of the connected bonds and due to volume pressure of the adjacent cells. Basal vertices in addition are also subject to forces due to the ECM attachment.

If the work function can be integrated, the forces can be obtained through differentiation of this internal work:

$$\mathbf{F}_a^i = -\frac{\partial W}{\partial \mathbf{X}_a^i} \tag{2.15}$$

$$\mathbf{F}_b^i = -\frac{\partial W}{\partial \mathbf{X}_b^i}. \tag{2.16}$$

Note that the centres of mass of the surfaces are not taken as degrees of freedom (cf. Eq. 2.1), but have to be considered in the calculation of the forces acting on the single vertices. To clarify this, we note that the virtual work introduced in Eq. 2.2 is a function of the positions of the vertices and centres of mass, $\delta\bar{W}(\{\mathbf{X}^i\}, \{\mathbf{C}^k\})$. As the centres of mass depend on vertex positions through Eq. 2.1, the virtual work in Eq. 2.15 can be obtained from

$$\delta W(\{\mathbf{X}^i\}) = \delta\bar{W}(\{\mathbf{X}^i\}, \{\mathbf{C}^k(\mathbf{X}^i)\}), \tag{2.17}$$

and the whole expression for the force on any vertex i reads

$$\mathbf{F}^i = -\frac{\delta\bar{W}}{\delta \mathbf{X}^i} - \sum_{k=1}^{M} \frac{\delta\bar{W}}{\delta \mathbf{C}^k}\frac{\partial \mathbf{C}^k}{\partial \mathbf{X}^i}, \tag{2.18}$$

where the sum is taken over all surfaces k. Note that $\partial\mathbf{C}^k/\partial\mathbf{X}^i \neq \mathbf{0}$ only if the vertex i is a part of surface k.

Mechanical equilibria in the 3D Vertex Model

Let again $\{\mathbf{X}^i\}$ be the state of the tissue in the 3D Vertex Model, describing the vertex positions and the tissue topology. This state corresponds to a mechanical equilibrium state if the sum of the internal and external forces acting on all vertices balance

$$\mathbf{F}_a^i(\{\mathbf{X}^i\}) = \mathbf{F}_b^i(\{\mathbf{X}^i\}) = \mathbf{0} \;\; \forall i \in \mathcal{V}. \tag{2.19}$$

If the differential mechanical work function is derived from a mechanical work function, which is always the case in this thesis, any equilibrium state $\mathcal{E}$ corresponds to a local extremum of the integrated work function W. A mechanical equilibrium is stable if it corresponds to a minimum of the work function and unstable otherwise. In simulations the equilibrium configurations can therefore be obtained by the minimisation of the work function W with respect to the position of the vertices.

2.1.3 Topological transitions

In addition to changes in the position of the vertices, we also allow for simultaneous topological transitions of the apical and basal networks. These topological changes accounted for in the model, namely T_1 transitions and cell division, are described in this subsection. Note that, while not required for this thesis, also cell extrusions can be implemented in the model to account for apoptotic or mechanically driven removal of cells from the epithelium.

$\mathbf{T_1}$ transitions

T_1 transitions are topological transitions that represent the exchange of cell neighbours. T1 transitions occur through the shrinkage of the interface in between two cells and the expansion of a new interface between two cells which were previously not in contact.

We impose here that T_1 topological transitions must occur both on the apical and the basal side, such that both networks maintain the same topology. In the implementation of the 3D Vertex Model, a T_1 transition occurs if the apical and the basal length of an edge e fall under the threshold length l^{T1} and the forces acting on the vertices of the edge tend to further reduce the apical and basal length of the edge (Fig. S4A). In the exemplary illustration the edge e, common to cells 2 and 4, is then replaced by a single fourfold vertex. This new vertex can be replaced by a new bond, connecting the cells 2 and 4 which were previously unconnected. To decide if this topological transition is performed, a hypothetic new bond $e^{1,3}$ is introduced between the two cells 1 and 3, with the direction of the apical/basal edge obtained by connecting the apical/basal cell centres of the other two cells. The apical and basal cell centres of cell α are denoted $\mathbf{M}_a^\alpha$ and $\mathbf{M}_b^\alpha$ respectively. We denote $\mathbf{F}_a^2$ and $\mathbf{F}_a^4$ the forces acting on the apical vertices of the hypothetic edge e which are part of cell 2 and 4, and $\mathbf{F}_b^2$ and $\mathbf{F}_b^4$ the respective forces on the basal vertices. The

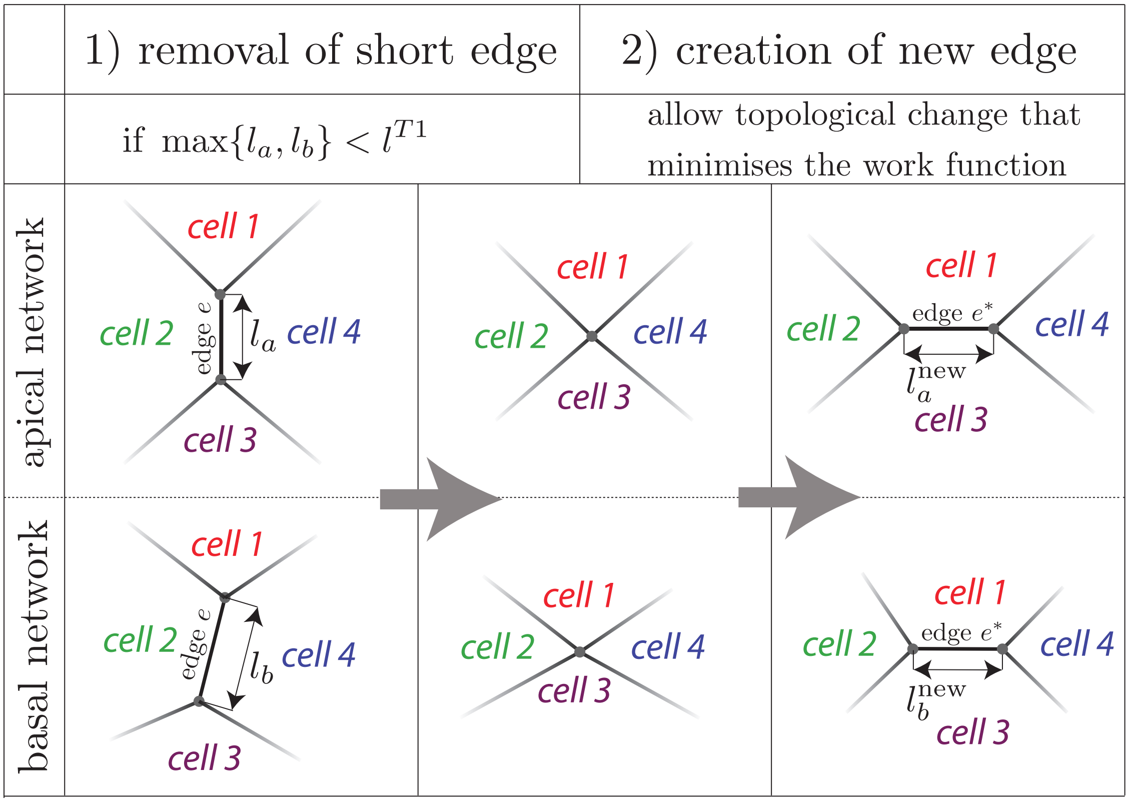
1) removal of short edge
2) creation of new edge
if $\max\{l_a, l_b\} < l^{T1}$
allow topological change that minimises the work function
apical network
basal network
cell 1
cell 2
cell 3
cell 4
edge e
l_a
l_b
edge e^*
l_a^{new}
l_b^{new}

Figure 2.4: If the apical and basal length of an edge e, named l_a and l_b, are shorter than the threshold l^{T1} this edge gets removed from the tissue, resulting in a new 4-fold vertex (step 1). This vertex can then be replaced in two topologically distinct ways by a new edge, and the energetically more favourable replacement will take place and give rise to a new edge e^* with apical and basal lengths l_a^{new} and l_b^{new} (step 2).

separating forces for the hypothetic edge $e^{1,3}$ are given by the projection of the force on the opening direction:

$$f_a^{1,3} = (\mathbf{F}_a^2 - \mathbf{F}_a^4) \cdot \frac{\mathbf{M}_a^2 - \mathbf{M}_a^4}{|\mathbf{M}_a^2 - \mathbf{M}_a^4|} \tag{2.20}$$

$$f_b^{1,3} = (\mathbf{F}_b^2 - \mathbf{F}_b^4) \cdot \frac{\mathbf{M}_a^2 - \mathbf{M}_a^4}{|\mathbf{M}_a^2 - \mathbf{M}_a^4|} \tag{2.21}$$

$$f^{1,3} = f_a^{1,3} + f_b^{1,3}. \tag{2.22}$$

The hypothetic edge $e^{1,3}$ is allowed to open if both apical and basal opening forces are positive $f_a^{1,3} > 0, f_b^{1,3} > 0$. The newly established edge is assigned the initial apical and basal lengths l_a^{new} and l_b^{new}. The topology remains unchanged and the fourfold vertex is conserved if the formation of the new edge is unfavourable.

Cell divisions

In cell divisions one cell is replaced by two daughter cells that inherit the mother cell's mechanical properties. The division of a cell is implemented by placing two new additional vertices n_1 and n_2 on two distinct edges of the cell's circumference (shown in FIG. 2.5). These vertices, with apical positions $\mathbf{X}_a^{n1}$ and $\mathbf{X}_a^{n2}$, and basal positions $\mathbf{X}_b^{n1}$ and $\mathbf{X}_b^{n2}$, split both two edges into two new edges each, and are then connected by a new edge $< n_1, n_2 >$ that divides the cell α into two daughter cells α_1 and α_2. The choice on which edges to place the two new vertices could be random, or made on the basis of geometrical arguments or mechanical arguments and depends on the underlying model of cell division. For instance one could perform the division perpendicular to the axis of elongation or just choose a random orientation of the axis of cell division.

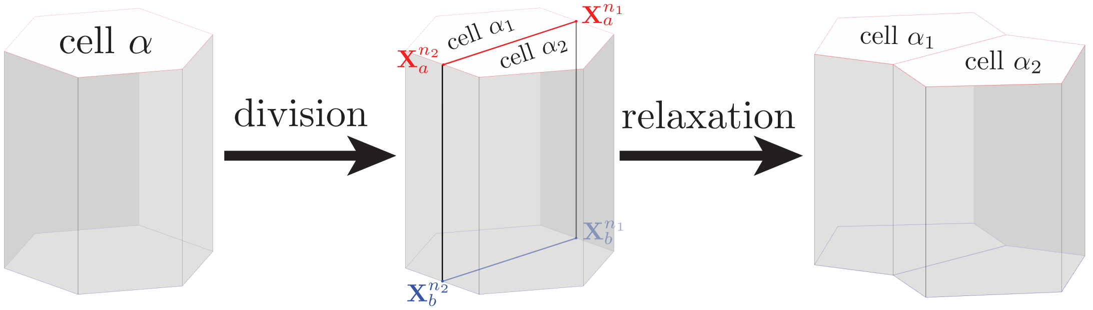

Figure 2.5: Cell α is divided into two daughter cells α_1 and α_2, by the placement of two new vertices n_1 and n_2 on the circumference of the cell and the consequent establishment of a new edge between the two vertices.

2.1.4 Boundary conditions

In the framework of the 3D Vertex Model, tissues can be modelled that are subjected to very different boundary conditions. These include periodic boundary conditions, free boundary conditions, and non-periodic tissues without a free boundary that are topologically equivalent to a sphere. Examples of the three cases are shown in FIG. 2.6.

Note that if a tissue is periodic in one direction of space in the model and in simulations, it needs not necessarily be periodic in a second direction of space. This way we can also account for tissues shaped like infinite tubes, which are periodic only along the elongation of the tubes (simulations not shown). In the case of periodic boundary conditions, the size of the periodic box adds an additional degree of freedom which needs to be accounted for in the identification of the forces and the mechanical equilibrium configurations. The details will be explained in the following subsection.

Periodic boundary conditions

In the case of periodic boundary conditions the vertex positions are constrained to remain inside a periodic box in $x-$ and $y-$direction and are unconstrained to move in $z-$direction, i.e. $\mathbf{X} \in ([0, L_x], [0, L_y], \mathbb{R})$ and the size of the periodic box $L_x \times L_y$ adds additional degrees of freedom. The positions of all vertices in the box are affinely rescaled when the lengths L_x and L_y are modified: under a change of tissue size $L_x \to L_x + \delta L_x$, $L_y \to L_y + \delta L_y$ every vertex position $\mathbf{X}$ changes according to

$$\mathbf{X} \to \begin{pmatrix} \frac{L_x+\delta L_x}{L_x} & 0 & 0 \\ 0 & \frac{L_y+\delta L_y}{L_y} & 0 \\ 0 & 0 & 1 \end{pmatrix} \mathbf{X}. \tag{2.23}$$

For the tissue to be in mechanical equilibrium the forces on the system size also have to be balanced, giving rise to two additional force balance equations:

$$\frac{\delta W}{\delta L_x} = \frac{\delta W_{int}(L_x, L_y)}{\delta L_x} - T_{ext} L_y = 0 \tag{2.24}$$

$$\frac{\delta W}{\delta L_y} = \frac{\delta W_{int}(L_x, L_y)}{\delta L_y} - T_{ext} L_x = 0. \tag{2.25}$$

Analytical expressions for the forces on the periodic box are derived in APPENDIX B.1.2.

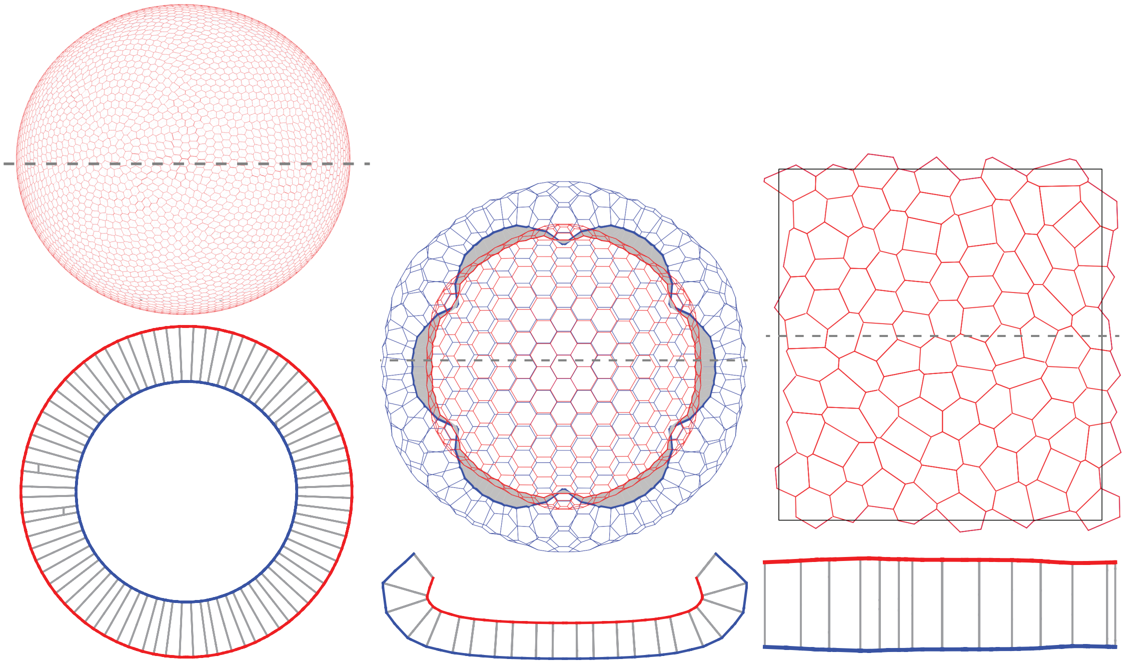

(a) Spherical topology **(b)** Free boundaries **(c)** Periodic box

Figure 2.6: Three different boundary conditions in the 3D Vertex Model. In (c) the tissue is confined in a periodic box, whereas in (a) and (b) the tissues are free to extend in all directions.

2.1.5 Minimising the work function

The identification of configurations of tissues in mechanical equilibrium can be done either by solving the system of ODE using a standard solver, or by minimising the work function using optimisation tools. The simulations studied in this thesis were done by means of minimisation methods, which are described in this section.

Mechanical equilibria of epithelial shapes for given mechanical properties are been obtained by initiating the tissue to a starting configuration (see Appendix B.1.3) and consequently iterating the tissue shape until it corresponds to a local minimum of the work function. For a fixed tissue topology this minimisation has been implemented by means of the Polak-Ribiére conjugate gradient algorithm [58]. The algorithm starts with a first step, in which the work function is minimised along its current gradient using Brent's method. In the following steps the work is then always minimised along the conjugate gradient of the previous step. The algorithm terminates and the tissue is assumed to have reached a local minimum, once the norm of the gradient of the work function is smaller than a preset threshold, or once the work done between successive points is lower than a predefined

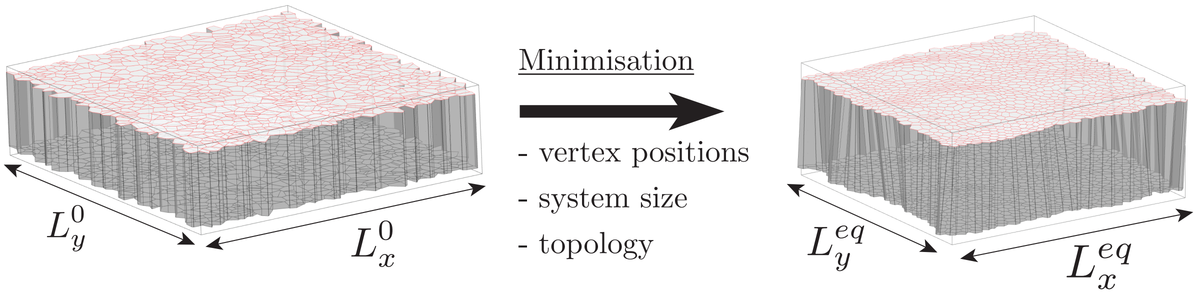

(a) Minimisation of a flat periodic tissue, in a periodic box with box sizes L_x and L_y.

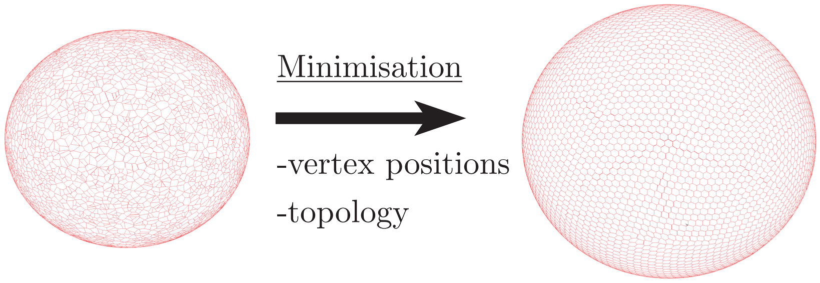

(b) Minimisation of an epithelium tissue on a sphere - note that the system size is not an additional parameter, but the size of the sphere is set only by the position of the vertices.

Figure 2.7: Initial configuration and equilibrium configuration of a periodic and a spherical tissue. The equilibrium is found by minimising the work function with respect to vertex positions and tissue topology. If the tissue is periodic the work is also minimised with respect to the size of the periodic box.

threshold. Once the work has been minimised with respect to vertex positions, the tissue is allowed to undergo T1 transitions as described in Fig. 2.4. After all allowed T1 transitions have taken place the work function is again minimised. The tissue is mechanically equilibrated once all forces vanish and there are no more T1 transitions possible. The succession of tissue states in the course of the minimisation can be seen as a pseudo-dynamics of the relaxation process, but for the analysis of the real dynamical properties of the tissue deformation the introduction of a viscous friction would be required. In this thesis we are only studying properties of mechanically equilibrated shapes of tissues. Whether a tissue is in equilibrium does not depend on the detailed structure of the friction, and therefore friction is not discussed in detail here. Note however that the choice of the dynamics or the chosen minimisation algorithm might influence the local minimum that is reached from a certain initial tissue configuration.

In Appendix B.1.3 it is described how random and ordered configurations of periodic tissues have been derived in this thesis as starting configurations simulations. Fig. 2.7 shows two such initial random configurations of epithelia which were obtained by Voronoi tessellations around randomly placed points in a plane and on a sphere. The images on the right show the mechanical equilibrium configurations of the corresponding epithelium that were obtained by minimising the work function with respect to vertex positions and with respect to the tissue topology. In the flat case shown in Fig. 2.7b, the work function has also been minimised with respect to the size of the periodic box.

2.1.6 The limit of the Apical 3D Vertex Model

The Apical 3D Vertex Model is a limit of the full 3D Vertex Model, where the tissue is completely described by the geometry of the apical tissue surface, and corresponds therefore to the 3D apical vertex models discussed in Section 1.5.1. The model is used in this thesis to represent tissues where all tensions are generated in the apical plane of the tissue, and the basal geometry of the cells does not play a role. This assumption is reasonable for tissues, where the cells are not completely closed or are not able to control their volume. Consequently the cells cannot generate a volume pressure but instead experience an apical area elasticity. All forces are acting on the apical vertices, and the work function is completely determined by the apical vertex positions:

$$W^{2D} = \sum_{\alpha \in \mathcal{C}} \frac{K_\alpha^{2D}}{2} (A_\alpha - A_\alpha^0)^2 + \sum_{\lambda \in \mathcal{L}} \Lambda_\lambda l_\lambda + T_{ext} A^{tot}. \tag{2.26}$$

Cells are denoted by α, and their apical area A_α is assumed to behave elastically around their preferred area A_α^0 with area elasticity K_α^{2D}. Lines λ have a length l_λ and experience a tension Λ_λ. This mechanical model has been used in Chapter 4 as a model for the *Drosophila* blastula, and describes for instance an epithelium where the cells are not completely closed or where all forces are generated along the apical cell surfaces.

2.2 Coarse grained properties of hexagonally packed epithelia

2.2.1 A coarse grained description of flat epithelia

In the following we will describe a planar epithelium as a 2D elastic material and derive its coarse grained mechanical properties such as the generated tension and the bulk and shear modulus as a function of the mechanical parameters of the 3D Vertex Model.
If a tissue is in mechanical equilibrium all internally generated stresses σ^0_{ij} are balanced by external tensions σ^e_{ij}:

$$\sigma^0_{ij} = \sigma^e_{ij}. \tag{2.27}$$

The stress generated inside the tissue depends on the locally averaged in-plane deformation tensor of the cells u^0_{ij} and the initial tissue height h^0. The stress response of the tissue to deviations from the initial in-plane deformation $u^0_{ij} \to u^0_{ij} + \delta u_{ij}$ is used to characterise the mechanical tissue properties.
The change in the exerted stress described by the 2D stress tensor $\sigma_{ij} - \sigma^0_{ij} = \delta\sigma_{ij}$ relates to the 2D deformation tensor δu_{ij} according to Hooke's Law for isotropic materials:

$$\delta\sigma_{ij} = 2\mu(\delta u_{ij}) + \lambda(\delta u_{ll})\delta_{ij}. \tag{2.28}$$

The two material parameters λ and μ, respectively, are the so called first and second Lamé parameter. The strain tensor can be split into the sum of a diagonal matrix and its traceless part, representing separately the change in average cell area and the change in average cell elongation:

$$\begin{aligned}\delta u_{ij} &= \frac{1}{2}(\delta u_{ll})\delta_{ij} + \left((\delta u_{ij}) - \frac{1}{2}(\delta u_{ll})\delta_{ij}\right) & (2.29)\\ &= \frac{1}{2}(\delta u_{ll})\delta_{ij} + (\delta\tilde{M}_{ij}). & (2.30)\end{aligned}$$

Then the stress can be rewritten

$$\delta\sigma_{ij} = 2\mu(\delta\tilde{M}_{ij}) + (\lambda+\mu)(\delta u_{ll})\delta_{ij}, \tag{2.31}$$

where μ represents the tissues shear modulus and the bulk modulus is consequently given by $K = \lambda + \mu$. If the tissue is under isotropic external stresses $\sigma^e_{ij} = T_{ext}\delta_{ij}$, also the internal stresses have to be isotropic in equilibrium and the cells are in average in an isotropic shape that is described by the cell density ρ denoting the number of cells per unit area. The internally generated isotropic tension ζ only depends on this cell density:

$$\sigma^0_{ij} = \zeta(\rho)\delta_{ij}. \tag{2.32}$$

From Eq. 2.27 follows that the equilibrium cell density ρ_0 is defined by $\zeta(\rho_0) = T_{ext}$, and the resulting stresses for small deformations around the equilibrium cell density read

$$\sigma_{ij} = \zeta(\rho_0)\delta_{ij} + 2\mu(\delta\tilde{M}_{ij}) + K(\delta u_{ll})\delta_{ij}. \tag{2.33}$$

A pure bulk deformation $B_{ij}(u)$ of the tissue with scaling factor u is defined through

$$\delta u_{ij} = B_{ij}(u) = u\delta_{ij}. \tag{2.34}$$

A pure shear deformation is a deformation under which the area of the cells is conserved but the cells are stretched. The pure shear deformation $S_{ij}(\epsilon)$ with shearing factor ϵ can be written as

$$\delta u_{ij} = S_{ij}(\epsilon) = \begin{pmatrix} \epsilon & 0 \\ 0 & (1+\epsilon)^{-1} - 1 \end{pmatrix} \tag{2.35}$$

$$= \begin{pmatrix} \epsilon & 0 \\ 0 & -\epsilon + \mathcal{O}(\epsilon^2) \end{pmatrix}. \tag{2.36}$$

Using these definitions the bulk and shear modulus can then be obtained by separately considering pure bulk and shear deformations and obtaining the tissue's response for small deformations u and ϵ. For an isotropic material the elastic moduli read:

$$K = \lim_{u\to 0} \frac{\partial \sigma_{xx}}{\partial u} = \lim_{u\to 0} \frac{\partial \sigma_{yy}}{\partial u} \tag{2.37}$$

$$\mu = \lim_{\epsilon\to 0} \frac{1}{2}\frac{\partial \sigma_{xx}}{\partial \epsilon} = \lim_{\epsilon\to 0} -\frac{1}{2}\frac{\partial \sigma_{yy}}{\partial \epsilon}. \tag{2.38}$$

2.2.2 Coarse grained mechanical material properties of epithelia

In the following we will derive the coarse grained elastic moduli of an epithelium and the effective tension it exerts on its surrounding, starting from the mechanical stresses considered in the 3D Vertex Model. We assume that the cells are mechanically homogeneous and arranged in a regular hexagonal packing. The tissue is enclosed in a periodic box aligned along the x- and y-axis with respective extensions L_x and L_y, and it is described by the in-plane shape of the cells through the cell elongation tensor u_{ij}, and the cell height h. The chosen parametrisation of the flat periodic cell arrangement is shown in FIG. 2.8.

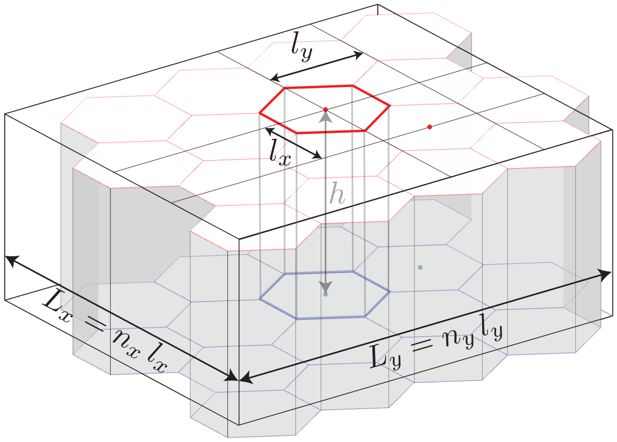

Figure 2.8: The regular hexagonal tissue is parametrised by the cells' in-plane extension l_x and l_y, as well as by the tissue height h, it is periodic and consists of $n_x \times n_y$ cells.

The epithelium consists of n_x cells along the x-direction and n_y cells along the y-direction. The apical and basal surfaces of the cells are identical hexagons and are described by their in-plane extensions l_x and l_y, and the cells' apical to basal distance is given by their height h. The epithelium Ω has a total volume of $L_x \times L_y \times h$ and the 2D cell density reads $\rho = (n_x n_y)/(L_x L_y)$. All cells are assumed to be equal in their apical and basal surface areas ($A_a = A_b = A$), in their lateral interface areas A_l, their perimeters ($P_a = P_b = P$) and their volume V. These geometrical quantities are given in terms of the parametrisation (l_x, l_y, h) in APPENDIX B.2.1.

Active tension generated by a homogenous piece of flat tissue

If all cells α in a piece of tissue Ω have the same apical surface tension T_a, basal surface tension T_b, lateral surface tension T_l, apical line tension Λ_a, basal line tension Λ_b, preferred volume V_0 and volume elasticity K_{3D}, the work function of a piece of tissue Ω can be rewritten by:

$$W_\Omega = \sum_{\alpha\in\Omega} \Big(\frac{K_{3D}}{2}(V^\alpha - V_0)^2 + T_a A_a^\alpha + T_b A_b^\alpha + \frac{T_l}{2} A_l^\alpha + \frac{\Lambda_a}{2} P_a^\alpha + \frac{\Lambda_b}{2} P_a^\alpha \Big) - T_{ext} L_x L_y \tag{2.39}$$

$$= n_x n_y \Big(\frac{K_{3D}}{2}(Ah - V_0)^2 + T_s A + \frac{T_l}{2} A_l + \frac{\Lambda_s}{2} P_s \Big) - T_{ext} n_x n_y A, \tag{2.40}$$

where we introduced the sum of the apical and basal surface tensions $T_s = T_a + T_b$ and line tensions $\Lambda_s = \Lambda_a + \Lambda_b$.

We assume that the forces acting on the cell height h are balanced and consequently

$$\frac{\partial W}{\partial h} = 0, \tag{2.41}$$

which couples the tissue height to the cell density ρ:

$$h(\rho) = V_0 \rho - 3^{1/4}\sqrt{2}\frac{T_l}{K_{3D}}\rho^{3/2}. \tag{2.42}$$

Note that $h(\rho) < 0$ for $\rho > \left(\frac{V_0 K_{3D}}{3^{1/4}\sqrt{2}T_l}\right)^2$, implying that beyond this critical cell density the cells collapse to zero volume. In the limit of infinite cellular bulk modulus $K_{3D} \to \infty$ the height will vary to ensure that the cells are always at their preferred volume.

The active tension exerted by a piece of tissue with cell density ρ and cell height h reads:

$$\zeta(\rho, h) \equiv \frac{\partial W}{\partial \rho^{-1}}(\rho, h) \tag{2.43}$$

$$= T_s + \frac{3^{1/4}}{\sqrt{2}}\sqrt{\rho}(\Lambda_s + T_l h) + K_{3D}h^2(\frac{1}{\rho} - \frac{V_0}{h}). \tag{2.44}$$

Now we assume that the cell height is equilibrated and impose relation 2.42, to find the following tension exerted by a piece of tissue, which only depends on the average cell density:

$$\boxed{\zeta(\rho) = T_s + \frac{3^{1/4}}{\sqrt{2}}\sqrt{\rho}(\Lambda_s - T_l V_0 \rho) + \sqrt{3}\frac{T_l^2}{K_{3D}}\rho^2} \tag{2.45}$$

Force balance requires that internal tensions are balanced by the external tension and for the equilibrium cell density ρ_0 it reads:

$$\zeta(\rho_0, h(\rho_0)) = T_{ext}. \tag{2.46}$$

Eq. 2.46 will be used in SECTION 2.2.3 to derive the equilibrium aspect ratios of flat epithelia. The graphs in FIG. 2.9 show how the active tension exerted by the tissue depends on the cell density. For infinite bulk modulus ($K_{3D} \to \infty$) there exists a unique cell density ρ^* where the tension exerted by the tissue is zero; for a cell density above the threshold the tissue exerts compressive stresses, whereas the tissue is tensile for lower cell densities (FIG. 2.9a). If the cell volume is not constrained, the behaviour becomes more

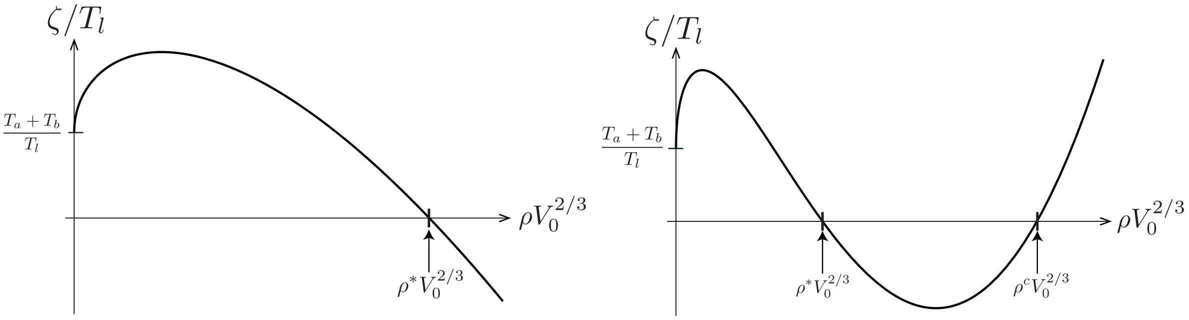

(a) Constrained cell volume **(b)** Finite volume elasticity

Figure 2.9: Normalised isotropic tension ζ/T_l generated in the hexagonally packed tension as a function of the normalised cell density $\rho V_0^{2/3}$

complex and a second (unstable) equilibrium configuration ρ^c arises. The resulting force balance conditions and equilibrium cell densities for given external tensions will be studied in SECTION 2.2.3.

Bulk and shear modulus

The bulk modulus of a tissue describes its resistance to the change in cell density, whereas its shear modulus describes its resistance to shear deformations at constant cell density (cf. SECTION 2.2.1). To obtain these quantities we again assume that the cell height h is always equilibrated and therefore h can be replaced by the expression given in Eq. 2.42. Then the stresses in $x-$ and $y-$ direction as a function of the cell sizes read respectively:

$$\sigma_{xx}(l_x, l_y) = T_s + \frac{1}{l_y}\left(\Lambda_s - \frac{\sqrt{3}}{2}\frac{T_l V_0}{l_x^2}\right) \tag{2.47}$$

$$\sigma_{yy}(l_x, l_y) = T_s + \frac{1}{l_x}\left(\frac{\sqrt{3}}{2}\Lambda_s - \frac{T_l V_0}{l_y^2}\right). \tag{2.48}$$

A pure bulk deformation corresponds to an isotropic expansion in $x-$ and $y-$direction, and for the parametrisation given in FIG. 2.8 it is equivalent to an isotropic rescaling of the cells $l_x \to l_x(1+u)$, $l_y \to l_y(1+u)$, as shown in FIG. 2.10a. The 2D bulk modulus of the tissue according to Eq. 2.37 is given by

$$\boxed{K = \frac{3^{1/4}}{2^{3/2}}\sqrt{\rho}(3\rho T_l V_0 - \Lambda_s) - 2\sqrt{3}\frac{T_l^2}{K_{3D}}\rho^2}. \tag{2.49}$$

The pure 2D shear deformation of a tissue is equivalent to the rescaling $l_x \to (1+\epsilon)l_x$ and $l_y \to (1-\epsilon)l_y$, as is shown in Fig. 2.10b. Using definition Eq. 2.38 we find the following expression for the 2D shear modulus of the hexagonally packed tissue:

$$\boxed{\mu = \frac{3^{1/4}}{2^{3/2}}\sqrt{\rho}\,(\Lambda_s + T_l V_0 \rho) - \frac{\sqrt{3}}{2}\frac{T_l^2}{K_{3D}}\rho^2} \tag{2.50}$$

In Section 2.4.1 we obtain the numerical values of the shear modulus in simulations for the hexagonally packed and for the disordered tissue, and compare them to the analytical prediction given above.

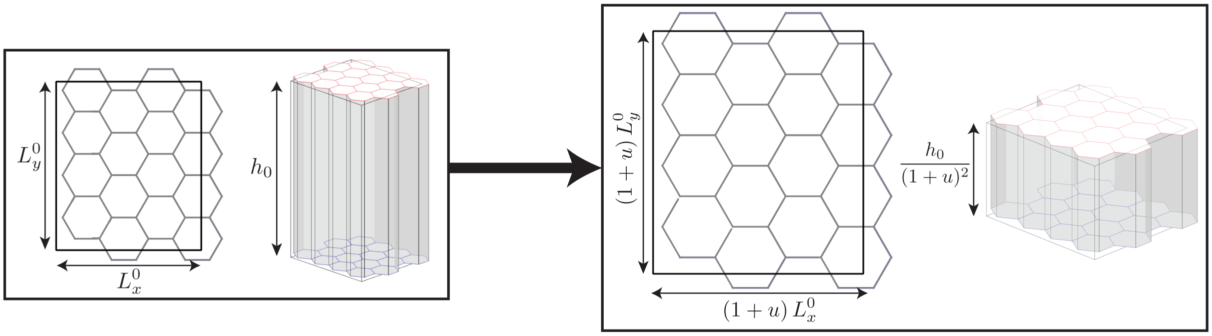

(a) Pure bulk deformation with scaling factor u. Note that the scaling induces a change in tissue height.

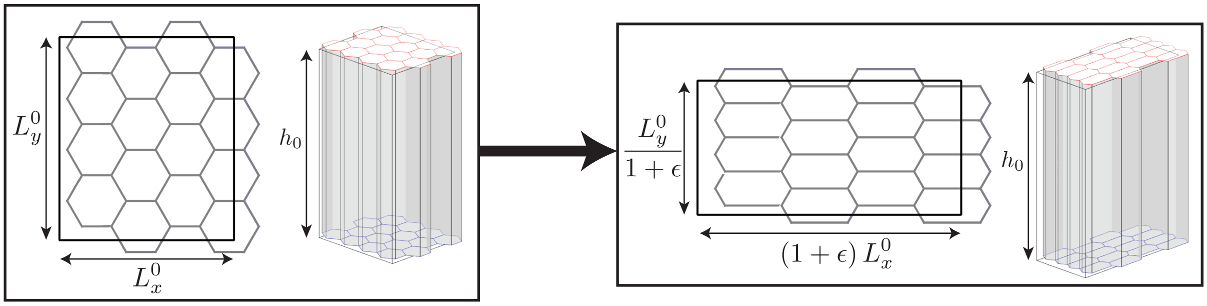

(b) Pure shear deformation with shearing factor ϵ

Figure 2.10: Bulk and shear deformations of a regular, hexagonally packed tissue.

Bending modulus and preferred curvature

In the previous sections we analysed the properties of flat epithelia, assuming them to be periodic and hexagonally packed. In this section we maintain the focus on hexagonally packed tissues, but will allow for the tissue to curve. This way we derive the effective bending modulus of the epithelial tissues, as well as their preferred curvature arising from differences in the apical and basal tensions.

The work function for a piece of tissue Ω is given in Eq. 2.39. If again all cells are assumed to have the same shape, the corresponding energy density $w = W_\Omega \rho / N_\Omega$ can be written:

$$w = \rho \left(\frac{K_{3D}}{2}(V - V^0)^2 + T^a A^a + T^b A^b + \frac{T^l}{2} A^l + \frac{\Lambda^a}{2} P^a + \frac{\Lambda^b}{2} P^b \right). \tag{2.51}$$

with N_Ω the number of cells within the piece of tissue Ω. We restrict ourselves to cells with apical and basal surfaces being regular hexagons as shown in Fig. 2.11. The energy density $w(h, R_a, R_b)$ can then be reexpressed in terms of the cell height h and apical and basal radii R_a and R_b. The apical, basal and lateral surface areas, apical and basal perimeters and cell volume can indeed be related to h, R_a, R_b through the relations given in Appendix B.2.2. We consider the limit $K_{3D} \to \infty$ where the cell volume V is constrained to be equal to the reference volume V_0. The energy density $w(\rho, C, V_0)$ can then be written in terms of the cell density ρ, the total tissue curvature C and the reference volume V_0 through the following change of variables (Fig. 2.11):

$$\rho = \frac{4}{(\sqrt{A^a} + \sqrt{A^b})^2} = \frac{8}{3\sqrt{3}(R_a + R_b)^2} \tag{2.52}$$

$$C = \frac{4(R_b - R_a)}{(R_a + R_b)h} \tag{2.53}$$

$$V_0 = \frac{\sqrt{3}}{2} h \left(R_a^2 + R_b^2 + R_a R_b \right). \tag{2.54}$$

For small curvature C, the energy density w can be expanded in powers of curvature:

$$w(\rho, C, V_0) \simeq w_0(\rho, V_0) - \kappa C_0 C + \frac{\kappa}{2} C^2, \tag{2.55}$$

where the bending modulus of the tissue κ and the preferred curvature C_0 are functions of ρ, V_0 and the tissue line and surface tensions. The effective bending modulus of the tissue

κ is therefore given by

$$\kappa = \left.\frac{\partial^2 w}{\partial C^2}\right|_{C=0} \tag{2.56}$$

$$\boxed{\kappa = \frac{T^a + T^b}{8} V_0^2 \rho^2 + \frac{\sqrt{2}}{8 \cdot 3^{3/4}} T_l V_0 \sqrt{\rho} \left(\sqrt{3} - V_0^2 \rho^3 \right)} \tag{2.57}$$

and the preferred curvature of the tissue reads

$$\boxed{C_0 = \frac{V_0\, \rho}{2\kappa} \left((T_a - T_b) + \frac{3^{1/4}}{\sqrt{2}} \sqrt{\rho} (\Lambda_a - \Lambda_b) \right)} \tag{2.58}$$

Note that κ can become negative for sufficiently large ρ, in which case the cells prefer to wedge and the flat tissue shape ceases to be a stable equilibrium anymore even in the case of identical apical and basal tensions. In Sections 2.4.2 and 2.4.3 we determine the preferred curvature and the bending modulus of the cells in simulations and compare the results to the expressions given above.

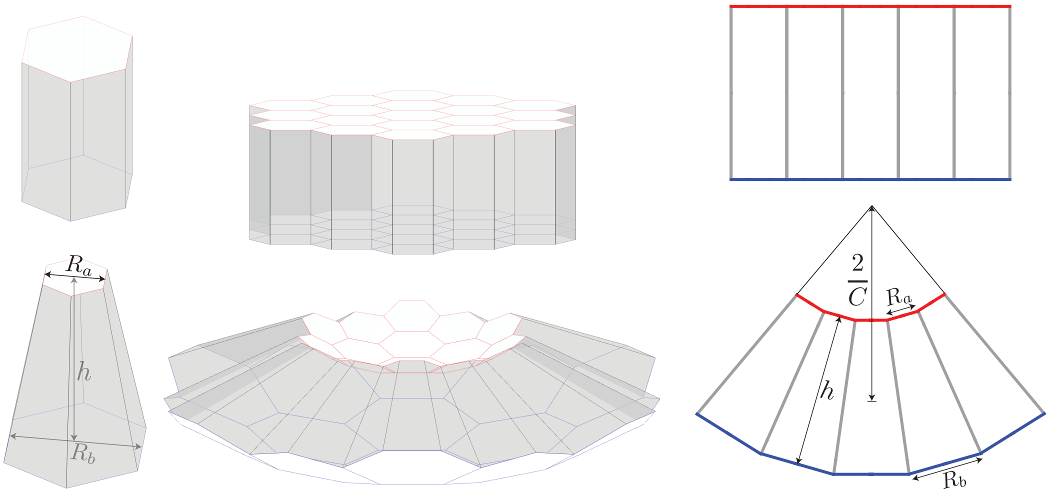

Figure 2.11: A flat and a curved simple epithelium, shown in 3D and in cross section. The cells are described by their apical and basal radii R_a and R_b and their height. The local curvature is given by $C = \frac{4}{h} \frac{R_b - R_a}{R_a + R_b}$.

2.2.3 Cell shape control in flat epithelia

In this section we discuss the equilibrium shapes of a mechanically homogeneous, hexagonally packed tissue under isotropic external tension, which are determined by the force balance Eq. 2.45. The epithelium is enforced to be flat, and therefore only the sum of the apical and basal tension matters ($T_s = T_a + T_b, \Lambda_s = \Lambda_a + \Lambda_b$). It is characterised completely by its cell height h and cell density ρ, and we introduce the dimensionless aspect ratio of the cells $\beta = h\sqrt{\rho}$ describing the cell shape. If $\beta \simeq 1$, the cells are cuboidal whereas $\beta \gg 1$ corresponds to a columnar cell shape, and $\beta \ll 1$ to squamous cells (FIG. 2.12c). For a given cell density ρ_c the force acting on the cell density is given by

$$f_\rho(\rho_c) = -\frac{\partial W}{\partial \rho}|_{\rho_c}. \tag{2.59}$$

Assuming that the height h is equilibrated, which is enforced by condition 2.42, and using the work function 2.9, the expression simplifies to

$$f_\rho(\rho_c) = \sqrt{3}\frac{T_l^2}{K_{3D}} + \frac{T_s - T_{ext}}{\rho_c^2} + \frac{3^{1/4}}{\sqrt{2}}\frac{\Lambda_s}{\rho_c^{3/2}} - \frac{3^{1/4}}{\sqrt{2}}\frac{T_l V_0}{\sqrt{\rho_c}}. \tag{2.60}$$

If we assume a friction that acts on the cell density ρ with a friction coefficient $\alpha(\rho) > 0$, we obtain the dynamical equation for the change of the cell density over time

$$\alpha(\rho_c)\frac{d\rho}{dt}|_{\rho_c} = f_\rho(\rho_c). \tag{2.61}$$

A stable equilibrium ρ_0 of the dynamical system is characterised by

$$f_\rho(\rho_0) = 0 \text{ and } (\partial_\rho f_\rho)(\rho_0) < 0. \tag{2.62}$$

Limit of infinite bulk modulus

If the bulk modulus dominates ($K_{3D} \to \infty$) and the cells have a constrained cell volume, the equilibria and their stability depend on two normalised parameters: the difference of internal and external surface tension $(T_{ext} - T_s)/T_l$, and the normalised line tensions, $\Lambda_s/(T_l {V_0}^{1/3})$ respectively. The corresponding parameter space shown in FIG. 2.12a dissociates into three qualitatively distinct regions:

1. $T_{ext} \leq T_s$ - **blue region**
   one stable equilibrium (ρ_0, h_0)

2. $T_{ext} \in [T_s, T_s + \frac{\sqrt{2}}{3\sqrt[4]{3}}\frac{\Lambda_s}{\sqrt[3]{V_0}})$ - **yellow region**
   in addition to the stable equilibrium (ρ_0, h_0), there exist initial cell densities for which the tissue stretches to infinity $(\rho \to 0, h \to 0)$

3. $T_{ext} \geq T_s + \frac{\sqrt{2}}{3\sqrt[4]{3}}\frac{\Lambda_s}{\sqrt[3]{V_0}}$ - **green region**
   the tissue stretches to infinity $(\rho \to 0, h \to 0)$ regardless of the initial cell density

In the case of additional zero line tensions $\Lambda_s = 0$, an equilibrium only exists if $T_{ext} < T_s$ and the corresponding equilibrium aspect ratio is the ratio of the external and the internal tensions:

$$\beta_0 = \frac{\sqrt{2}}{3^{1/4}}\frac{T_s - T_{ext}}{T_l}. \tag{2.63}$$

If on the other hand $T_{ext} = T_s$ the epithelium's equilibrium aspect ratio is given by

$$\beta_0 = \left(\frac{\Lambda_s}{T_l V_0^{1/3}}\right)^{3/2}. \tag{2.64}$$

In Fig. 2.12b the equilibrium cell density ρ_0 is plotted for fixed line tension as function of the externally applied tension.

Limit of zero line tensions

Now we consider the case of an epithelium with zero line tensions $\Lambda_s = 0$ and finite bulk modulus $K_{3D} < \infty$, which leaves the two dimensionless parameters describing the volume elasticity $K_{3D}/(T_l V_0^{4/3})$ and the difference of external and internal surface tensions $(T_{ext} - T_s)/T_l$. Fig. 2.13a shows the phase space of equilibrium tissue shapes as a function of these two normalised parameters. There exist three qualitatively distinct parameter regions:

1. $T_{ext} < T_s - \frac{9\sqrt{3}}{1024}\frac{(K_{3D})^3 V_0^4}{T_l^2}$ - **green region**
   the cells collapse to a point $(h \to 0,\ \rho \to 0)$

2. $T_{ext} \in [T_s - \frac{9\sqrt{3}}{1024}\frac{(K_{3D})^3 V_0^4}{T_l^2}, T_s)$ - **yellow region**
   in addition to a stable equilibrium (ρ_0, h_0), there exist initial cell densities for which the cells collapse to a point $(h \to 0,\ \rho \to 0)$

3. $T_{ext} > T_s$ - **blue region**
   depending on the initial cell density the tissue stretches to infinity $(\rho \to 0)$ or the cells collapse to a point $(h \to 0,\ \rho \to 0)$

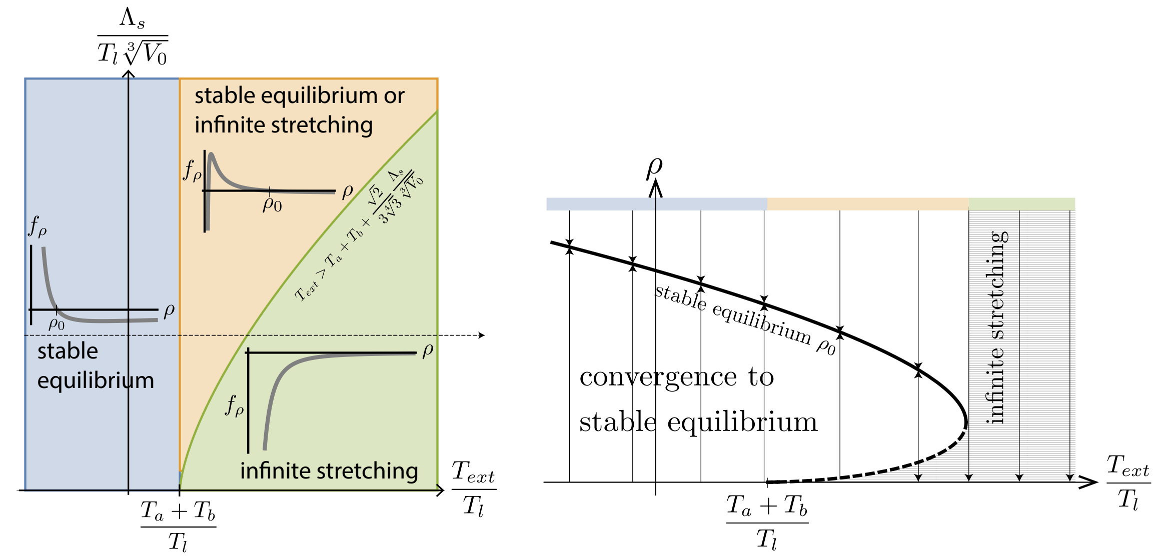
$\frac{\Lambda_s}{T_l \sqrt[3]{V_0}}$
stable equilibrium or infinite stretching
f_ρ
ρ_0
ρ
$T_{ext} > T_a + T_b + \frac{\sqrt{2}}{3\sqrt[3]{3}} \frac{\Lambda_s}{\sqrt[3]{V_0}}$
stable equilibrium
infinite stretching
$\frac{T_a + T_b}{T_l}$
$\frac{T_{ext}}{T_l}$
ρ
stable equilibrium ρ_0
convergence to stable equilibrium
infinite stretching

(a) Phase space of equilibria for constrained volume (no free parameters).

(b) Equilibrium cell density as a function of the external tension for fixed line tension, for $\Lambda_s = T_l V_0^{1/3}$

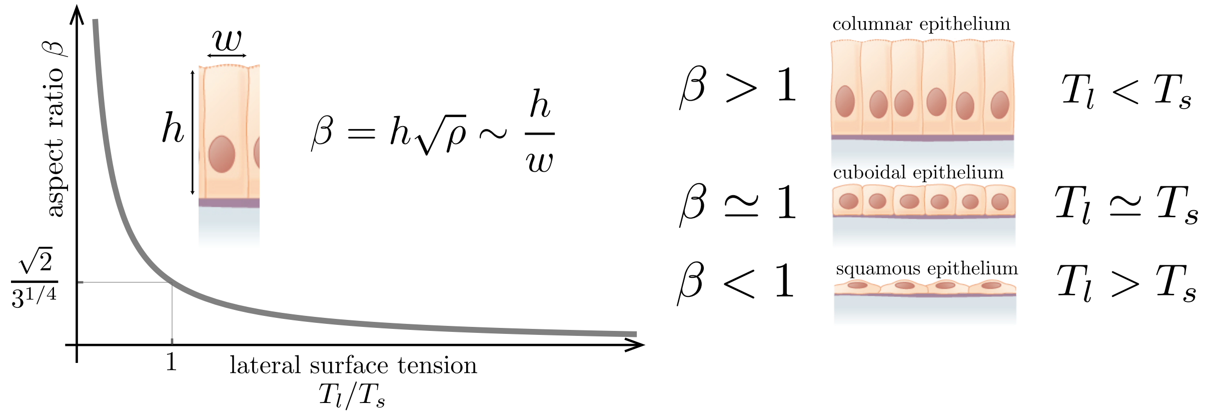

(c) Plot of the cells' aspect ratio as a function of the ratio of lateral surface tension T_l and total surface tension $T_s = T_a + T_b$ in the absence of external tension, for infinite bulk modulus and zero line tensions (Eq. 2.63). If the lateral surface tension is weak the cells take a columnar shape, and if it is high they become squamous.

Figure 2.12: If the cells volume is fixed the equilibrium cell shapes are a function of the external tension exerted on the tissue and the line tensions generated in the cells. If the external tension weaker than the apical and basal surface tensions, the tissue will always converge to a unique equilibrium shape.

In the absence of line tension the epithelium therefore only has a stable equilibrium shape for $T_{ext} \in [T_s - \frac{9\sqrt{3}}{1024}\frac{(K_{3D})^3 V_0^4}{T_l^2}, T_s)$. The dependency of the equilibrium cell density ρ_0 on the external tensions T_{ext} in these limits is shown in FIG. 2.13b.

FIG. 2.12c shows how the cells' aspect ratio depends on the forces generated along the apical surfaces of the cells, if the cells have a fixed volume and line tensions are zero.

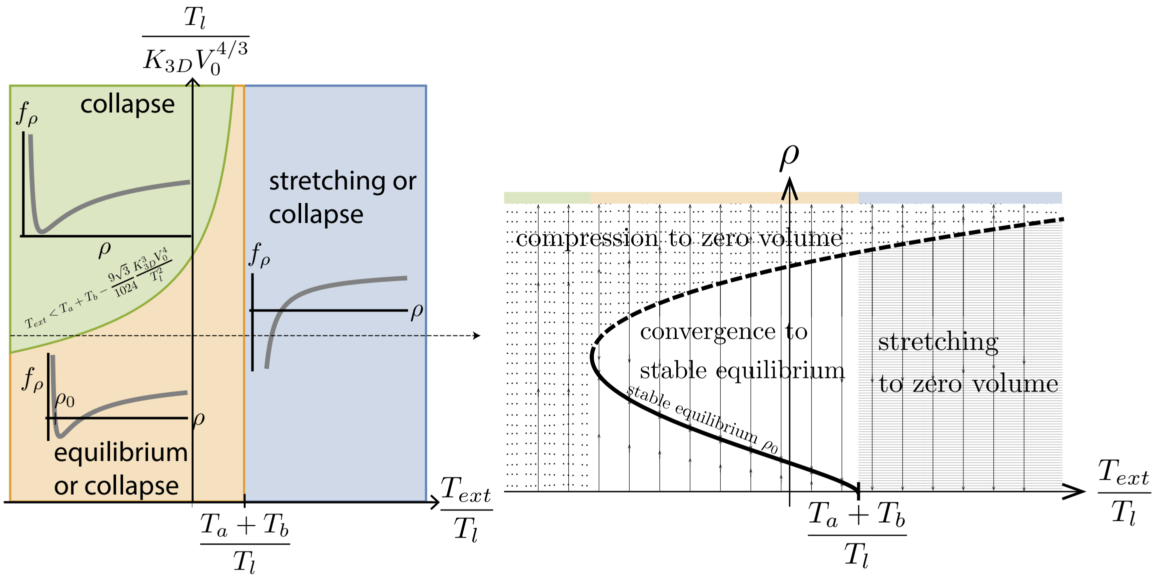
$\frac{T_l}{K_{3D}V_0^{4/3}}$
collapse
f_ρ
ρ
$T_{ext} < T_a + T_b - \frac{9\sqrt{3}}{1024}\frac{K_{3D}^3 V_0^4}{T_l^2}$
stretching or collapse
f_ρ
ρ
f_ρ
ρ_0
ρ
equilibrium or collapse
$\frac{T_a+T_b}{T_l}$
$\frac{T_{ext}}{T_l}$
ρ
compression to zero volume
convergence to stable equilibrium
stable equilibrium ρ_0
stretching to zero volume
$\frac{T_a+T_b}{T_l}$
$\frac{T_{ext}}{T_l}$

(a) Full phase space of equilibria for zero line tension.

(b) Equilibrium cell density as a function of the external tension for $T_l = K_{3D}V_0^{4/3}$.

Figure 2.13: Equilibrium shapes of a hexagonally packed epithelium with zero line tensions $\Lambda_s = 0$

2.2.4 Stability of flat epithelia subject to external tension or compression

In this section we study the stability of flat epithelia that are attached by springs to an underlying ECM and subjected to external compression. We focus on the limit of infinite bulk modulus $K_{3D} \to \infty$, and thus the remaining relevant parameters are the sum of the apical and basal surface tensions T_s and the line tension Λ_s, the lateral surface tension T_l, the preferred cell volume V_0, the external tension T_{ext} and the attachment stiffness of the vertices k_v. After normalisation with units of length $V_0^{1/3}$ and energy this leaves four dimensionless parameters that can be varied independently.

To discuss the stability of the flat tissue we proceed as follows: we use a continuum theory of epithelial tissues to derive a stability criterion of an epithelium under compression, which depends on the effective bending modulus and attachment stiffness. These coarse grained mechanical parameters are then reexpressed with 3D Vertex Model parameters as derived in SECTION 2.2.2, to derive the tissue's stability as a function of the tensions generated inside the cells.

In CHAPTER 3 we develop a continuum description of epithelia as a thin elastic sheet with a bending modulus κ that is attached to the underlying ECM with an attachment stiffness k and under an effective tension ζ. In SECTION 3.2.2 we show that the following criterion ensures the stability for a homogeneous tissue:

$$\kappa q^4 + \zeta q^2 + k > 0 \tag{2.65}$$

where $\mathbf{q}$ are Fourier modes describing the deformation and $q = |\mathbf{q}|$. In the limit of an infinite epithelium the criterion for a tissue to be stable becomes

$$\zeta > -2\sqrt{\kappa(\rho)k(\rho)}, \tag{2.66}$$

which puts an upper bound on the compression a tissue can experience before it starts to buckle. The coupling to the ECM in the 3D Vertex Model is represented by springs with spring constant k_v. In a regular hexagonal packing there are six vertices per cell, each of them being shared between three neighbouring cells, which gives rise to the following coarse grained parameter k of ECM attachment:

$$k = \frac{6}{3}\frac{k_v}{A^\alpha} = 2k_v\rho. \tag{2.67}$$

In Eq. 2.57 we gave the effective bending modulus κ of the epithelium and showed that it can be negative for certain choices of mechanical parameters, in which case the cells start to wedge spontaneously. Therefore another criterion for the flat tissue to be stable reads:

$$\kappa(\rho_0) = \frac{T^s}{8} V_0^2 \rho_0^2 + \frac{\sqrt{2}}{8 \cdot 3^{3/4}} T_l V_0 \sqrt{\rho_0} \left(\sqrt{3} - V_0^2 \rho_0^3 \right) > 0 \tag{2.68}$$

The equilibrium cell density ρ_0 depends on the external tension T_{ext}, which thereby also controls the bending modulus. If this criterion is fulfilled, the stability of the epithelium with respect to buckling is ensured by:

$$T_{ext} > -2\sqrt{\kappa(\rho_0) k(\rho_0)} \tag{2.69}$$

This shows that a nonzero attachment stiffness to the ECM is required to ensure the stability of an infinite tissue under compression.

Furthermore, we showed in section 2.2.3, that a stable equilibrium cell density only exists under the condition

$$T_{ext} < T_s + \frac{\sqrt{2}}{3\sqrt[4]{3}} \frac{\Lambda_s}{\sqrt[3]{V_0}}. \tag{2.70}$$

Taken together, the criteria 2.68, 2.69 and 2.70 ensure the existence and the stability of the flat equilibrium shape. The FIGS. 2.14a-2.14c show stability diagrams of flat epithelia for different sets of mechanical parameters, as a function of the normalised external tension T_{ext}/T_l. These parameter spaces have up to four distinct regimes configurations, depending on the stability criteria that are violated. In the white region the tissue is stretched to infinite size, since criterion 2.70 is violated. In the green region of the parameter space, all criteria 2.68-2.70 are fulfilled and there exists a stable flat configuration - a typical configuration is shown in the right column in FIG. 2.14d. In the beige region the tissue has a positive bending modulus at equilibrium cell density, but it buckles due to the compression. The tissue start to undergo long wavelength undulations as shown in the second column in FIG. 2.14d. In the blue region the tissue is even further compressed, the bending modulus becomes negative and the cells wedge spontaneously. The undulations in this case occur on the length scale of cells, as shown in the first column of FIG. 2.14d. FIG. 2.14c shows the stability phase plot of the tissue as a function of the external compression T_{ext} and the line tension Λ_s for fixed $k/T_l = 0.1$ and $(T_a + T_b)/T_l = 1$. In SECTION 2.4.5 we determine the stability of a hexagonal packed tissue in simulations numerically and show that the analytical predicted buckling transitions closely match the ones in simulations.

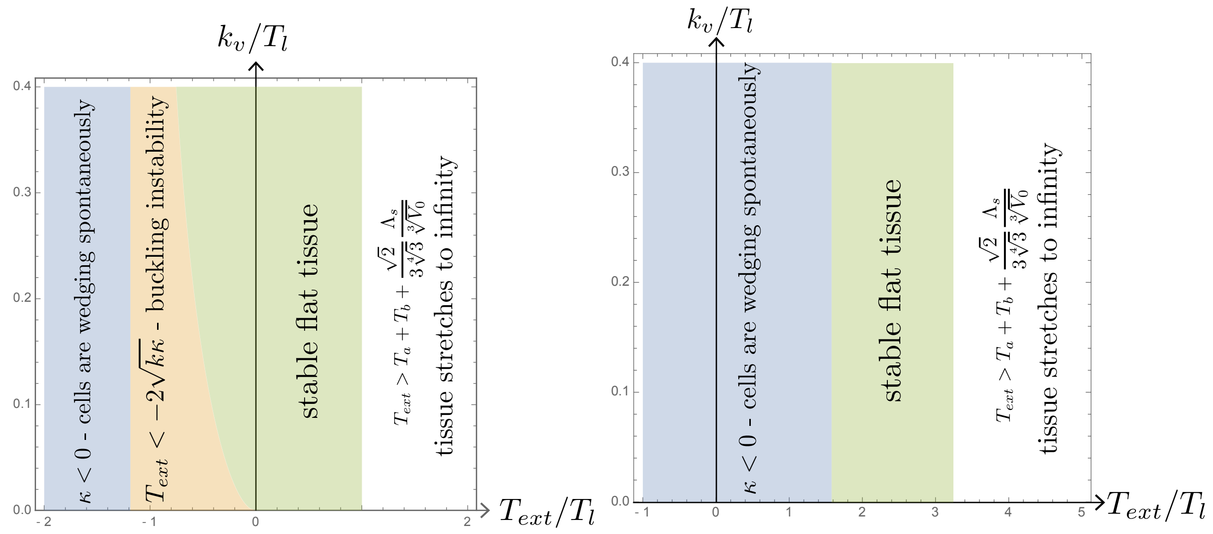

(a) $\Lambda_s = 0$, $T_s = 1$ **(b)** $\Lambda_s/(T_l V_0^{1/3}) = 2.2$, $T_s = 1$

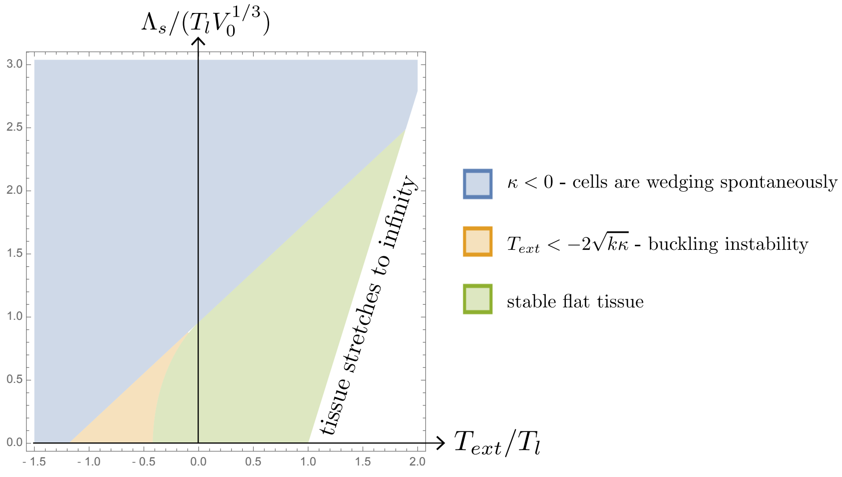

(c) $k_v/T_l = 0.1$, $T_s/T_l = 1$

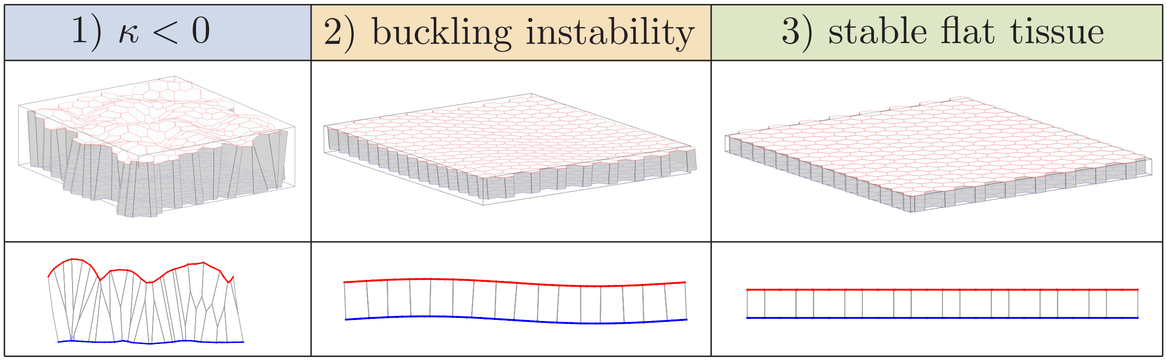
1) $\kappa < 0$
2) buckling instability
3) stable flat tissue

(d) Exemplary tissue shapes for the three distinct regions of the parameter space.

Figure 2.14: Stability of a flat tissue under compression. FIGURES 2.14a - 2.14c show phase plots for different fixed parameters which are given below the respective figure, and FIG. 2.14d shows examples of the different regions in 3D Vertex Model simulations.

2.2.5 Coarse grained material properties of epithelia in the Apical 3D Vertex Model

In this section the generated tensions, the bulk and shear modulus and the equilibrium shapes of homogeneous, hexagonally packed epithelium in the Apical 3D Vertex Model are derived. As defined in Section 2.1.6 cells in this purely apical model have zero volume elasticity, no basal and lateral tensions, but do experience apical surface elasticity. The internal work function for a tissue consisting of N identical cells reads accordingly:

$$W = N\left(\frac{K_{2D}}{2}(A-A_0)^2 + \frac{\Lambda}{2}P\right). \tag{2.71}$$

where each cell has the apical area A and perimeter P, all line tensions are given by Λ and the area elasticity is set by the preferred area A_0 and the cellular bulk modulus K_{2D}.

The tension generated by such a tissue, and its bulk and shear modulus can be derived analogously to Section 2.2.2. In this section only the respective expressions will be given, and for the details of the calculations and illustrations please refer to Appendix B.2.3.

The isotropic tension, the bulk modulus and the shear modulus of the tissue read:

$$\boxed{\begin{aligned} \zeta(\rho) &= K_{2D}\left(\frac{1}{\rho} - A^0\right) + \frac{3^{1/4}}{\sqrt{2}}\Lambda\sqrt{\rho} && (2.72)\\ K(\rho) &= \frac{K_{2D}}{\rho} - \frac{3^{1/4}}{2^{3/2}}\Lambda\sqrt{\rho} && (2.73)\\ \mu(\rho) &= \frac{3^{1/4}}{2^{3/2}}\Lambda\sqrt{\rho} && (2.74)\end{aligned}}$$

An equilibrium cell density ρ_0 is defined by $T_{ext} = \zeta(\rho_0)$ and only exists if the tissue is under sufficiently strong tension

$$T_{ext} > \frac{3^{7/6}}{2^{5/2}}(K_{2D}\Lambda^2)^{1/3} - K_{2D}A_0, \tag{2.75}$$

and otherwise the tissue collapses towards an infinite cell density. The corresponding phase space for the existence of an equilibrium cell density in terms of the only two dimensionless parameters $T_{ext}/(K_{2D}A_0)$ and $\Lambda/(K_{2D}A_0^{3/2})$ is shown in the Appendix in Fig. B.4.

The given results are used to relate Apical 3D Vertex Model simulations and the emergent continuum theory in Chapter 4.

2.3 Simple epithelia on a sphere

In the previous sections we focussed on the analysis of the mechanical properties and stability of flat tissues. In what follows, we study the properties of an epithelium surrounding a cavity, which is filled with a compressible fluid. The cavity has a volume V^y, a preferred volume V_0^y and the pressure generated by the fluid is given by $P^y = K^y(V_0^y - V^y)$. An illustration is shown in FIG. 2.15.

The effective internal work function of an epithelium (given in Eq. 2.9), and the external contribution W_e coming from the pressure generated inside the circular cavity, read as a sum over all cells $\mathcal{C}$:

$$W_e = \frac{K^y}{2}(V^y - V_0^y)^2 \tag{2.76}$$

$$W_i = \sum^{\alpha} \Big(\frac{K_c}{2}(V^\alpha - V_0)^2 + T_a A_a^\alpha + T_b A_b^\alpha + \frac{T_l}{2} A_l^\alpha + \frac{\Lambda_a}{2} P_a^\alpha + \frac{\Lambda_b}{2} P_b^\alpha\Big) \tag{2.77}$$

$$W = W_i + W_e, \tag{2.78}$$

where K_{3D} denotes the bulk modulus and V_0 the reference volume of all cells, T_a and T_b denote the apical and basal surface tensions, Λ_a and Λ_b denote the apical and basal line tensions. A_a^α and A_b^α denote the apical and basal cell surfaces, and P_a^α and P_b^α denote the respective perimeters of cell α.

Let the radius of the sphere be R and the tissue be made of N_c cells: then the curvature of the tissue is small on the length scale of cells, if $\sqrt{\rho}R \gg 1$. Since $\sqrt{\rho}R \sim \sqrt{N_c}$ this is true for large cell numbers, in which the local equilibrium tissue shapes can be close to a hexagonal packing of cells. In this limit of large cell numbers the apical and basal cell surfaces of the cells can consequently be approximated by identical regular hexagons. Therefore, the only degrees of freedom left are the height of the tissue h and the radius of the sphere R, as shown schematically in FIG. 2.15a. Furthermore we assume that the cell height relaxes quickly compared to the tissue radius, which gives an explicit relation $h = h(R)$ and makes the sphere's radius R the only degree of freedom in the following considerations. Henceforth the equilibrium sphere radius R_{eq} is determined by force balance

$$\frac{dW_i}{dR}\Big|_{R_{eq}} = -\frac{dW_e}{dR}\Big|_{R_{eq}}. \tag{2.79}$$

This equation can be solved numerically to obtain the unique equilibrium radius of the sphere and the resulting equilibrium height of the cells as a function of the mechanical parameters and the number of cells forming the tissue.

In SECTION 2.2.2 we obtained the tissue's effective surface tension γ, bending modulus κ

and preferred curvature C_0 by expanding the work function around its equilibrium in area and curvature. The application of this continuum approach yields the expansion of the internal work function:

$$\frac{dW_i}{dR} \simeq \frac{\partial W_i}{\partial A}\frac{dA}{dR} + \frac{\partial W_i}{\partial C}\frac{dC}{dR} \tag{2.80}$$

$$\simeq \gamma\frac{dA}{dR} + \kappa(C - C_0)A\frac{dC}{dR}. \tag{2.81}$$

By rewriting the force balance condition 2.79 one obtains the following approximate criterion for the equilibrium tissue radius R_{eq}:

$$P(R_{eq}) \simeq \frac{2\gamma(R_{eq})}{R_{eq}} + \frac{2\kappa(R_{eq})}{R_{eq}^2}(R_{eq} - \frac{2}{R_{eq}}), \tag{2.82}$$

where γ, κ and C_0 depend on the cell density (cf. SECTION 2.2.2) and are therefore functions of R. Relation 2.82 hence shows how the law of Laplace has to be corrected in order to account for the additional bending stiffness and the preferred curvature of the tissue.

In SECTION 2.4.6 we show for different sets of parameters how the radius of the sphere depends on the difference and the sum in apical and basal tensions in the epithelium, and compare the analytical predictions to the results obtained in 3D Vertex Model simulations.

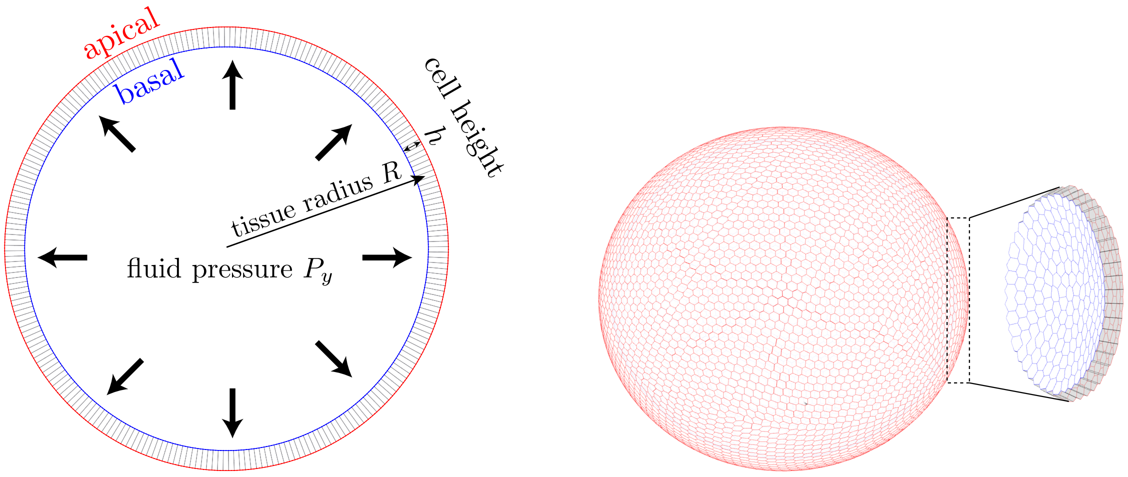

(a) Cross section and parametrisation. **(b)** 3D view on the epithelium.

Figure 2.15: A full 3D epithelium packed on a sphere. The mean radius of the tissue is R and the average height of the cells is h.

Spherical epithelia in the Apical 3D Vertex Model

Now we study the case of a Apical 3D Vertex Model epithelium confined on a sphere, analogously to the previous study of full 3D epithelia. The tissue surrounds a weakly compressible fluid that exerts a pressure onto the epithelium, and if the tissue is under tension the spherical equilibrium shape can be parameterised by the radius of the sphere R. An illustration for such a tissue made of 5000 cells is shown in Fig. 2.16, and its work function which is a sum of the internal work given in Eq. 2.26 and the contribution from the compressible fluid reads

$$W = \sum_{\alpha} \left(\frac{K_{2D}}{2} (A^{\alpha} - A_0)^2 + \frac{\Lambda}{2} P^{\alpha} \right) + \frac{K_y}{2} (V^y - V_0^y)^2. \tag{2.83}$$

The enclosed fluid has the volume V^y, a reference volume V_0^y and an effective bulk modulus K^y. All cells have the same preferred apical area A_0 and area elasticity K_{2D}, and all lines experience the tension Λ. The area and perimeter of cell α are given by A_{α} and P_{α} respectively.All cells are approximated to have the same regular hexagonal shape, which makes the work a function of the sphere's radius only. Force balance equations for the equilibrium radius R_{eq} gives rise to the Law of Laplace, where the surface tension ζ generated by the tissue has to be balanced by the fluid pressure P^y:

$$\zeta(\rho(R_{eq})) = \frac{P^y(R_{eq}) R_{eq}}{2}. \tag{2.84}$$

The isotropic tension generated by the tissue $\zeta(\rho)$ was given in Eq. B.26. In Section 2.4.6 we compare equilibrium radii obtained from simulations and from Eq. 2.84 for different mechanical parameter sets.

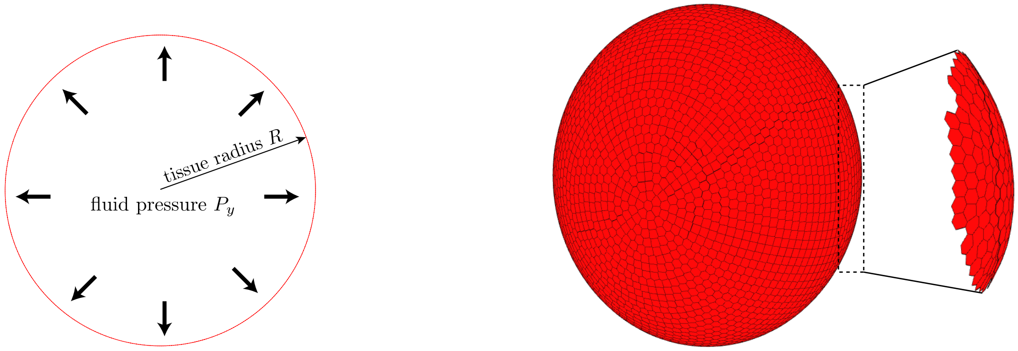

(a) Tissue cross section.

(b) 3D view of the epithelium.

Figure 2.16: An epithelium in the Apical 3D Vertex Model made of 5000 cells packed on a sphere, with R being the radius of the epithelium.

2.4 Numerical study of mechanically homogeneous tissues

The focus of the previous sections were equilibrium shapes, tissue stability and emergent coarse grained mechanical properties of tissues as a function of the tensions generated inside the tissue. In present section the same parameters will be measured numerically in simulations, and compared to the analytical predictions. This serves as a consistency check for the simulations and the continuum model, and shows that the applied coarse graining and the approximations were appropriate.

2.4.1 Shear and bulk moduli

Eq. 2.49 gives the effective bulk modulus of an epithelium represented in the 3D Vertex Model, which was derived by assuming a regular hexagonal packing of the cells. In this section we obtain the bulk modulus numerically in simulations for different mechanical parameters, and compare the results for regular and disordered starting configurations of epithelia to the analytical predictions. To quantify the bulk modulus in simulations, the tissue was relaxed to its equilibrium shape from 1) randomly obtained and 2) regular starting configurations. Then the periodic box was isotropically scaled by $(L_x, L_y) \to (uL_x, uL_y)$, which is shown for the case of a regular packing in Fig. 2.10a. The size of the periodic box was fixed, and the energy was minimised with respect to the vertex positions. Finally change in the stresses imposed by the tissue on the periodic box $\delta\sigma_{xx}$ and $\delta\sigma_{yy}$ were obtained as described in Appendix B.1.2 and the numerical bulk modulus was calculated for small u through:

$$K = \frac{1}{4u} \left(\delta\sigma_{xx} + \delta\sigma_{yy} \right). \tag{2.85}$$

Fig. 2.17 shows a plot of the numerically obtained bulk moduli of ordered and disordered tissues for varying lateral surface tension T_l and external tension T_{ext}. The graphs show the very good agreement between analytical prediction of the bulk modulus derived from assuming a hexagonal packing, and the numerically obtained bulk modulus. In the case of the regular hexagonal packing, the relative difference is negligible and within the numerical precision, but also in the case of the disordered tissue the maximal relative difference between simulations and predictions was still less than 1%. These results suggest that the analytically derived bulk modulus is a very good approximation even for unordered tissues.

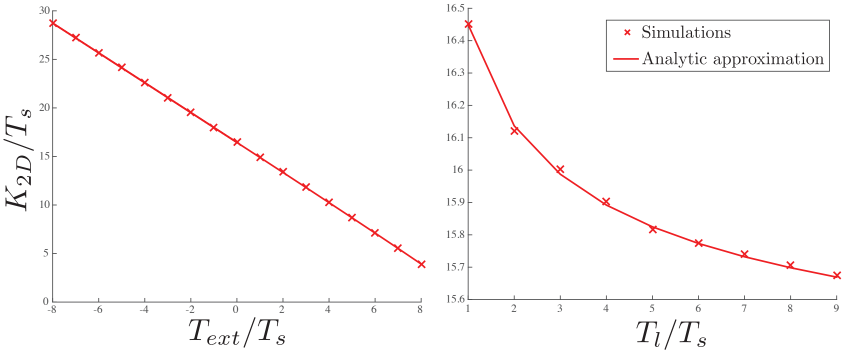

(a) Regular hexagonal tissue

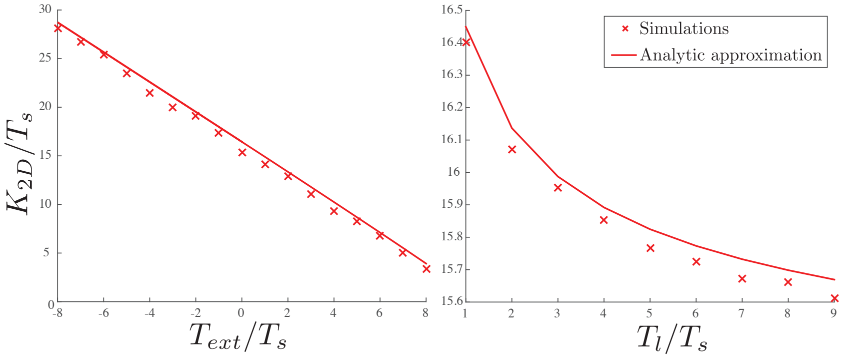

(b) Randomly initialised tissue

Figure 2.17: Numerically obtained bulk modulus K_{2D} in simulations for varying external tension T_{ext} and lateral surface tension T_l, starting from an initially hexagonally packed tissue and a disordered tissue made of 256 cell. The results compare very well to the analytical prediction given in Eq. 2.49, which was obtained for a hexagonally packed tissue. Remaining parameters are given in B.1(A) for the left plots, and in (B) for the right plots).

As described in Section 2.2.2, the shear modulus describes the linear response an epithelium to a shear deformation. In simulations it was measured directly by rescaling the periodic by a shear deformation ϵ box as shown in Section 2.10b, relaxing the epithelium to the equilibrium vertex positions for fixed system size and measuring the resulting change in stresses $\delta\sigma_{xx}$ and $\delta\sigma_{yy}$ along the boundaries of the periodic box. Then the corresponding mean shear modulus μ was obtained through

$$\mu = \frac{1}{2\epsilon}\left(\delta\sigma_{xx} - \delta\sigma_{yy}\right), \tag{2.86}$$

for an infinitesimal scaling factor ϵ. This way we obtained the numerical shear moduli for regular and hexagonal tissues consisting of 16×16 cells and compared the values to the analytical prediction given in Eq. 2.50. The graphs in FIG. 2.18 show the shear modulus obtained analytically and in simulations for varying external tension T_{ext} and for varying lateral surface tension T_l.

In the case of the regular hexagonal packing the relative maximal difference between analytical predictions and simulations was on the order of 10^{-5}, well within the limits of numerical precision. This shows the consistency of the analytical derivation of the shear modulus of a hexagonally packed tissue and the implementation of the simulation tool. The shear modulus for relaxed tissues which started from a disordered configuration was found to be constantly higher than the predicted shear modulus for a regular tissue, but as in the numerical estimate for the bulk modulus also here the maximal error was smaller than 1%, indicating that the given expression for the purely hexagonal tissue is also a good approximation of the shear modulus of disordered tissues.

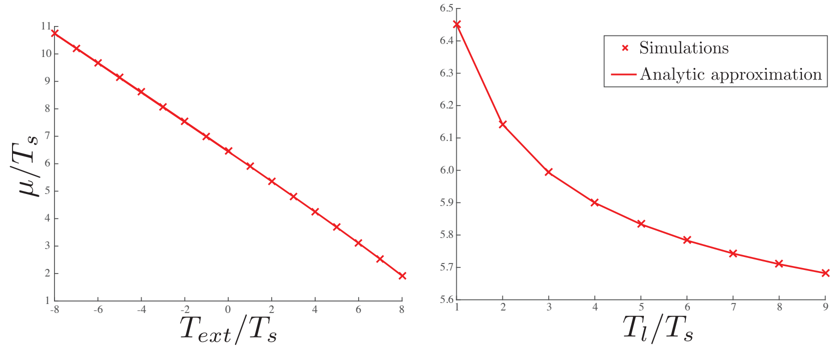

(a) Regular hexagonal tissue

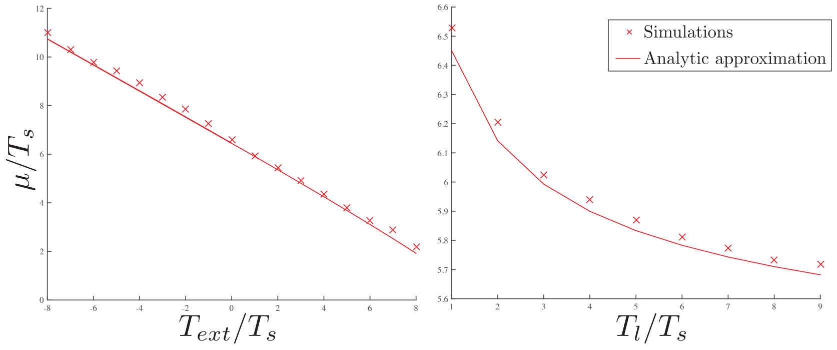

(b) Randomly initialized tissue

Figure 2.18: Numerically derived shear moduli in simulations for varying external tension T_{ext} and lateral surface tension T_l, starting from an initially hexagonally packed tissue and a disordered tissue made of 256 cells. The results compare very well to the analytical prediction given in Eq. 2.50, which was obtained for a hexagonally packed tissue. Remaining parameters are given in B.1(C) (left plots) and (D) (right plots).

2.4.2 Preferred curvature

The analytical calculations in SECTION 2.2.2 predicted a spontaneous curvature C_0 of the epithelium (given in Eq. 2.58) that result from differences in the apical and the basal tensions.

We tested the predictions in simulations by removing the periodic boundary conditions and analysing the equilibrium shape of the cells as a function of the difference in surface tensions $T_a - T_b$ and of the line tensions $\Lambda_a - \Lambda_b$. In the case of hexagonal cells, the total local curvature as a function of the apical and basal areas, A_a^α and A_b^α respectively, and the cell height h^α can be written

$$C^\alpha = \frac{4}{h^\alpha}\frac{\sqrt{A_a^\alpha} - \sqrt{A_a^\alpha}}{\sqrt{A_a^\alpha} + \sqrt{A_b^\alpha}}, \tag{2.87}$$

which is used in the following as an approximation of the cells' curvature in simulations. The resulting curvature of a single hexagonal cell as a function of differences in apical and basal tensions are shown in the plots in FIG. 2.19. We found a good agreement between simulations and the predicted curvature 2.58 for small differences in apical and basal tensions, whereas increasing nonlinearities lead to increasing deviation between prediction and simulations for larger tension differences.

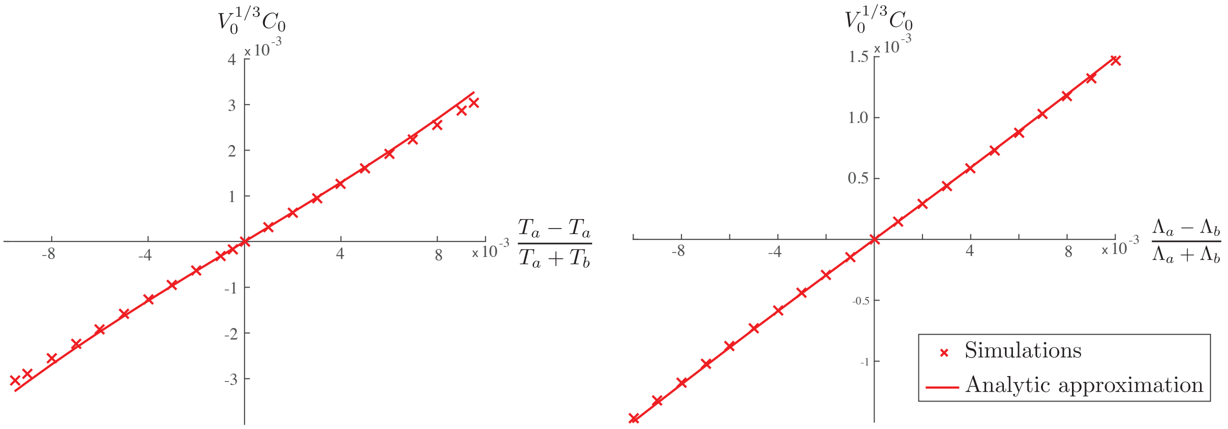

Figure 2.19: Effective tissue curvature as a function of difference in apical and basal line and surface tensions, compared to the prediction 2.58 obtained by the linear theory. Remaining parameters are given in B.1(E) for the left plot, and in (F) for the right plot.

2.4.3 Bending modulus

In Section 2.2.2 we analytically obtained the bending modulus of hexagonal cells, and in this section we compare this value to the numerically obtained bending modulus from 3D Vertex Model simulations. The bending modulus of a cell in simulations can be numerically obtained by measuring the mechanical response to the application of an infinitesimal curvature of a cell. The obtained normalised bending moduli are shown in Fig. 2.20 for varying lateral surface tension in Fig. 2.20a and for varying apical and basal line tension in Fig. 2.20b.

The analytical predictions and the results from simulations match very well in the numerical limits, as shown in Fig. 2.20. The graphs show also the transition point $\kappa = 0$, beyond which the symmetric cells become internally unstable and take spontaneously a wedged shape, for the case of $\kappa < 0$.

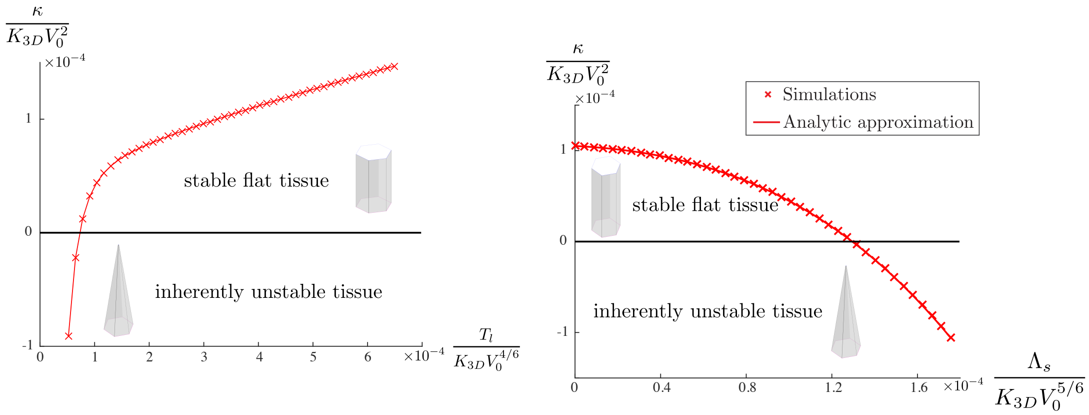

(a) Varying normalised lateral surface tension T_l for $\Lambda_a = \Lambda_b = 0$

(b) Varying normalised apical and basal line tension Λ_s for

Figure 2.20: Normalised bending modulus κ obtained in simulations as a function of the mechanical parameters, compared to analytical predictions. Remaining parameters are given in B.1(G) for the graph in 2.20a and in (H) for the graph in 2.20b.

2.4.4 Equilibrium aspect ratios

In this section we compare equilibrium shapes of flat epithelia in the 3D Vertex Model to the analytical predictions given in Section 2.2.3. Simulations were run starting from two periodic tissues made of 256 cells of which one was regularly packed, and the other was created by a 2D Voronoi tessellation as described in Appendix B.1.3. In Fig. 2.21 the resulting average cell densities and cell heights are shown together with the analytical prediction for varying total line and surface tensions. In the case of the regular hexagonal packing, the maximal relative difference between analytical predictions and simulations was on the order of 10^{-7}, meaning that the analytical and numerical predictions match very well in the limit of the numerical precision. In the case where tissues were randomly initialised tessellation, they did not converge to a perfectly hexagonally packed equilibrium shape but a slightly unordered equilibrium shape. One example of an equilibrium tissue configuration obtained from a random initial tissue configuration is shown in the right column of Fig. 2.21. Also in the case of the imperfect packing the simulated equilibrium cell shapes were close to the analytically predicted values.

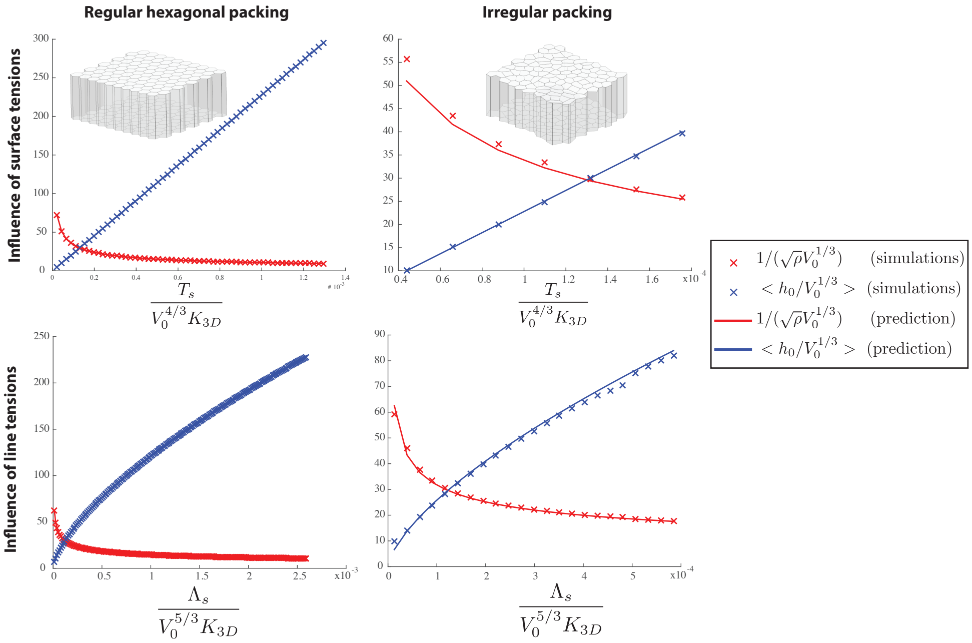

Figure 2.21: Normalised height and cell density of equilibrium tissue shapes in 3D Vertex Model simulations, as a function of the sum of the apical and basal surface and line tensions, $T_s = T_a + T_b$ and $\Lambda_s = \Lambda_a + \Lambda_b$ respectively. The simulations were run starting from a regular packing (left column) and from an irregular packing (right) and show a good agreement of simulations and analytical predictions. Remaining parameters are given in B.1(I) for the upper plots, and in (J) for the lower plots.

2.4.5 Epithelial buckling in simulations

In SECTION 2.2.4 we analysed the stability of a hexagonally packed epithelium under external compression and showed that there exist two fundamentally different regions of instability. In one region of instability the intrinsic bending modulus of the cells became negative $\kappa < 0$, and in the one the tissue buckled to reduce its total area on the cost of local bending despite the positive bending modulus. In this section we will numerically test the stability of a tissue in simulations depending on the normalised attachment stiffness $k_v/(T_l V_0^{-2/3})$ and the external tension T_{ext}/T_l, and compare the results to the analytical predictions. Simulations were run starting from a tissue consisting of $32 \times 32 = 1024$ cells. The tissue was relaxed to its equilibrium cell density, a small Gaussian noise was applied to all vertex positions and then the tissue was relaxed to the next equilibrium. To identify buckling, the variance of the z-coordinates of all apical vertices was used as a measure for the deviation of the tissue from the flat shape. For decreasing negative tension T_{ext} (i.e. for increasing compression) a sharp transition occurred in the deviation from the flat tissue shape when the variance jumped from the order of $10^{-5}V_0^{2/3}$ to being greater than $10^{-3}V_0^{2/3}$ which corresponds to a slight curvature of the tissue. Therefore, in simulations a tissue was classified as 'buckled' if this variance was greater than $10^{-3}V_0^{2/3}$ and stable otherwise. The results are shown in FIG. 2.22, which at the same time shows the analytically obtained buckling threshold taking into account the finite size of the periodic tissue. To take into account the finite size of the tissue the analytical criterion (given in 2.66) has been applied for all allowed modes $\mathbf{q} \in \{(i\frac{2\pi}{L_x}, j\frac{2\pi}{L_x})|i,j = 1,2,...\}$ with $q = |\mathbf{q}|$, and L_x and L_y, with $L_x > L_y$ are the sizes of the periodic box:

$$\kappa > 0 \text{ and} \tag{2.88}$$

$$\kappa q^4 + \zeta q^2 + k > 0 \tag{2.89}$$

FIG. 2.22 shows the good agreement between the analytical prediction and the buckling transition observed in simulations. An exemplary simulation result for a stable tissue is shown in the third column of FIG. 2.14d; the second row of the same figure shows a typical example for a slightly buckled tissue.

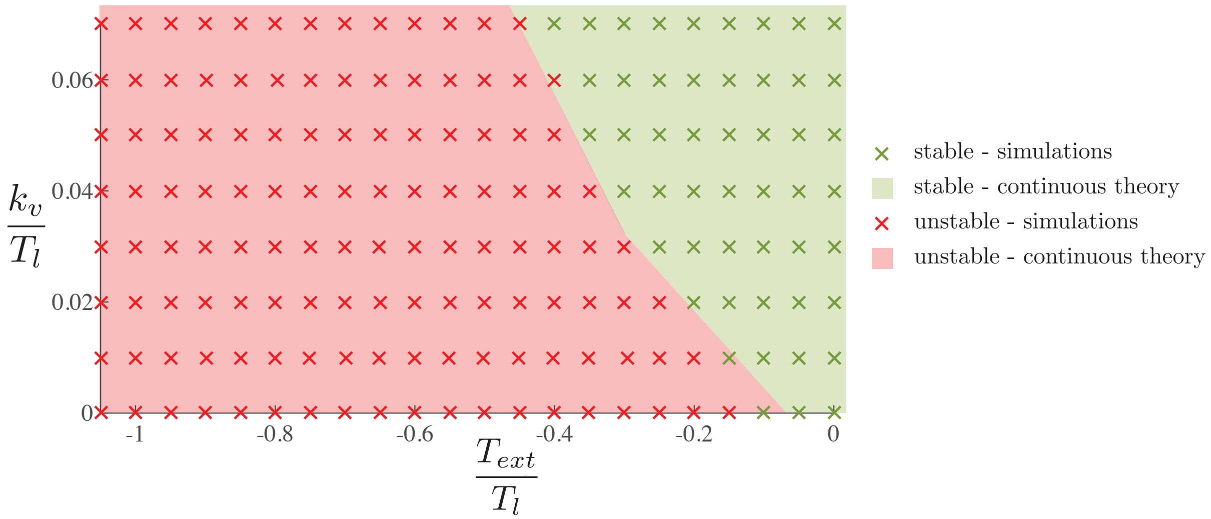

Figure 2.22: Stability diagram of a hexagonally packed tissue of $32 \times 32 = 1024$ cells in simulation under external compression as a function of the normalised attachment stiffness $k_v/(T_l V_0^{-2/3})$ and external tension T_{ext}/T_l. The remaining mechanical parameters are specified in B.1(K). The comparison to the analytical predictions of buckling of a thin sheet attached to the underlying substrate with the same coarse grained elastic properties show a great agreement of the two approaches.

2.4.6 Spherical epithelia

In Section 2.3 we introduced the spherical arrangement of an epithelium confined on a sphere, with pressure acting on the basal side of the tissue facing the cavity. Here we present equilibrium tissue shapes obtained in 3D Vertex Model simulations for varying mechanical parameters and we compare the results to the analytical approximations given in Section 2.3. To show the influence of the difference between apical and basal surface tensions on the equilibrium radius of the resulting sphere, we fix all other parameters and vary only the relative difference in surface tension $\frac{T_a - T_b}{T_a + T_b}$ at fixed total surface tensions $T_a + T_b$. The total tension generated in the tissue remains constant, but the difference in apical and basal tensions induces a non-zero preferred curvature of the tissue, which in turn is reflected in a difference of the tissue radii.

In Fig. 2.23 we show the tissue radius obtained in simulations, together with the predictions derived in Section 2.3. The simulations were started from a random tissue configuration of 2000 cells on a sphere, which was generated as explained in Appendix B.1.3 and then relaxed to the equilibrium shape. It is noteworthy that in all shown simulations the overall tissue shape remained close to a sphere, justifying the description of the geometry by the tissue radius R only. The normalisation constant R_0 was chosen to be the preferred radius

of the cavity, i.e. $R_0 = \left(\frac{3}{4\pi} V_0^y\right)^{1/3}$.
The analytical prediction I was obtained by numerically solving the full force balance Eq. 2.79 for R, and analytical prediction II was obtained by solving the linearised version using the preferred curvature and the bending modulus given in Eq. 2.82. The curves show that an increase in total surface tension $T_a + T_b$ decreases the preferred radius. Also they demonstrate that an increase in apical surface tension relatively to the basal surface tension induces a preferred curvature opposite to the curvature of the sphere and hence tends to decrease the curvature of the tissue. The good agreement between the obtained equilibrium shapes and the solution of force balance equation 2.79 justify the approximations made in the coarse grained theory.

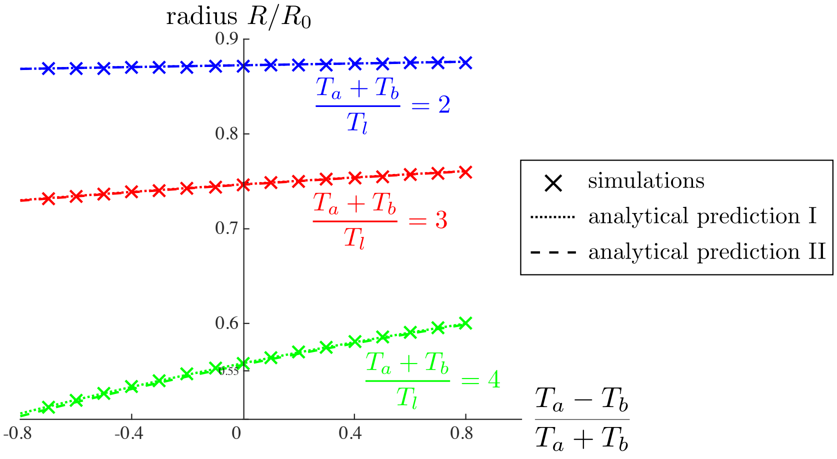

Figure 2.23: Simulations of a 3D tissue surrounding a compressible volume, where the normalised equilibrium radii of the epithelium is plotted as a function of the difference $\frac{T_a - T_b}{T_a + T_b}$ in apical and basal tensions generated inside the tissue for fixed total surface tensions $T_a + T_b$. The analytical predictions I and II have been derived from the numerical solution of the force balance Eq. 2.79, and the linearised theory 2.82, respectively. The remaining mechanical parameters are specified in the appendix in B.3.2.

The Apical 3D Vertex Model on a sphere

Here we simulate the equilibrium shapes of a tissue in the Apical 3D Vertex Model (c.f. section 2.1.6) surrounding a compressible fluid, and compare them to the analytical considerations discussed in Section 2.3. An analytical prediction for the tissue's radius can be obtained by numerically solving the analytical force balance equation 2.84 for R, which makes the assumption of a regular hexagonal packing of cells on the sphere. Mechanical parameters are the compressibility of the volume surrounded by the sphere, which is described by the preferred volume V_0^y (with preferred radius $R_0^y = \sqrt[3]{3/(4\pi)V_0^y)}$) and the bulk elasticity K_y. All bonds experience a tension Λ and the cells exhibit a volume elasticity K_{2D} around their preferred area A_0, and the respective work function is given in Eq. 2.83. Simulations were run starting from a random packing of 5,000 cells on a sphere and relaxed to the next equilibrium for the given set of parameters. The resulting equilibrium radius of the sphere in simulations is plotted in Fig. 2.24. These plots show the good match between the results of the coarse grained theory and simulations, confirming that also the simulated tissue obeys the Law of Laplace.

This test taken together with all previously discussed tests in Section 2.4 indicate a very good quantitative agreement between the introduced coarse grained theory and the results obtained in 3D Vertex Model simulations.

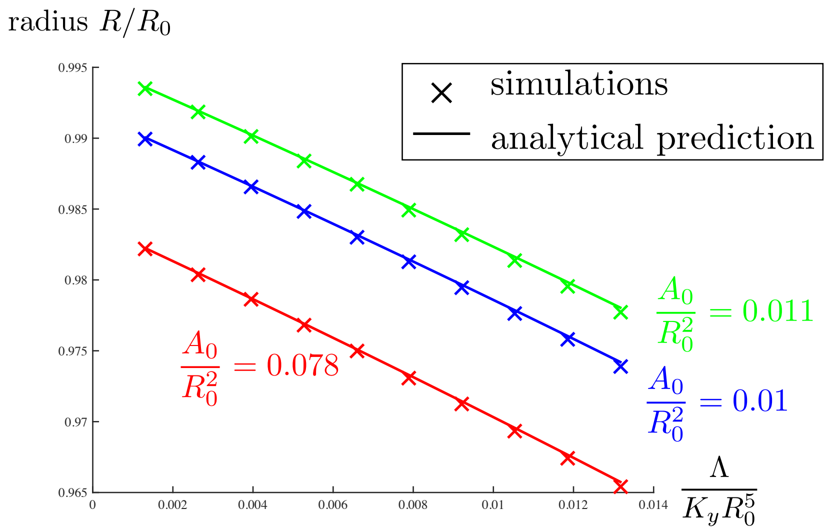

Figure 2.24: Normalised equilibrium radius of a 5000 cell epithelium in the Apical 3D Vertex Model, as a function of the preferred cell area A_0 and the line tension Λ. The results have been obtained in simulations in the 3D Vertex Model and analytically from Eq. 2.84 by assuming a hexagonal packing. The remaining mechanical parameters are specified in the appendix in B.3.2.

2.5 Summary

In present chapter we introduced a novel 3D Vertex Model for simple epithelia where cells are represented as laterally connected polyhedrons, and the tissue is completely described by apical and basal networks of vertices in 3D. Mechanically we took into account active tensions acting along all lines and surfaces of the tissue, and volume elasticity of the cells. We showed how epithelia can be basally coupled to a basement membrane, and external tensions can be applied on the tissue to account for possible constraints imposed by the environment. We then derived how the tissue's aspect ratio depends on the mechanical tissue parameters. Thereby we present a possible mechanism for cells to control their shape, which allows them to transit between columnar, cuboidal and squamous shapes by regulating the active tensions along different interfaces.

We then showed how to map the 3D Vertex Model to a continuum theory, where the tissue is represented by a 2D thin elastic sheet with bulk modulus, shear modulus, bending modulus and preferred curvature. Assuming a hexagonal packing we then derived all these coarse grained mechanical properties as a function of the mechanical stresses generated inside the cells. To confirm the validity of the coarse graining we tested analytical predictions in simulations, by numerically probing the tissues around their mechanical equilibria. We found a very good agreement between predictions and simulations even in the case of topologically disordered tissues, showing the consistency of the 3D Vertex Model simulations and the continuum theory in the studied limits.

We derived analytical stability criteria for flat tissues under compression, and found two interesting regimes where the tissue's equilibrium shapes are not flat. In one case, the tissue has a positive bending modulus and buckles due to the applied compression, giving rise to a buckling on long length scales. Interestingly, we also identified a second regime where the cells intrinsically lose their stability and individually undergo a transition towards a wedge shape. Again simulations confirmed the analytical predictions. Finally we studied the case of simple epithelia confined on a sphere surrounding a compressible fluid. We showed how equilibrium tissue shapes in this setup depend on the mechanical parameters, and a comparison of analytical predictions and simulations showed a match within high accuracy.

The 3D Vertex Model together with the introduced continuous framework provide a powerful tool to understand the shapes of epithelia as a consequence of the forces generated inside and acting onto the tissue. We will use the two approaches and their interplay in the CHAPTERS 3 and 4 to gain a deeper understanding of two fundamental morphogenetic processes.

CHAPTER 3

Cyst Formation in the wing imaginal disc of *Drosophila*

Epithelial cysts are clusters of cells that bulge out and eventually form a closed cavity underneath the epithelium. In humans, 85% of cancers are of epithelial origin and human epithelial tumours are often characterised by the presence of cysts, which have been proposed to progress into metastatic stages of cancer [59, 60, 61, 62, 63]. While the presence of cysts has severe consequences for epithelial tissue function, the cellular and physical mechanisms that promote the emergence of these structures are poorly understood. In the following chapter we combine experiments and physical modelling of epithelial mechanics to elucidate the mechanical drivers of cyst formation in the *Drosophila* imaginal wing disc.

The work presented in this chapter been done in close collaboration with Christina Bielmeier and Anne Classen from the Ludwig-Maximilians-Universität München and all experimental images shown in the chapter have been acquired by members of the Classen group. The results are published in [64].

We start by discussing the experimental observations obtained by our collaborators in SECTION 3.1. We show that the formation of cysts in the wing imaginal disc is a very general response to fate misspecification of patches of cells inside the epithelium (3.1.1). Then we demonstrate that also small wildtype clones can be induced to form cysts (3.1.2), that actin accumulates at the smoothening interface between differently fated cells (3.1.3 & 3.1.4), and that the shape of the clone depends on the number of misspecified cells in the clone (3.1.4).

Based on these observations we suggest a mechanism that drives cyst formation by a contractile boundary compressing misspecified clones, and we use a combination of 3D Vertex Model simulations and the continuum theory to study the detailed implications of the contractile boundary mechanism. Using a continuum theory for simple epithelia we show that cyst formation can be understood as a buckling instability of misspecified clones that experience size dependent compression due to the boundary contraction (3.2.2). The conclusion that cyst formation should be restricted to an intermediate clone size was confirmed in experiments. Then we use 3D Vertex Model simulations to go beyond the linear stability analysis, and show that the experimental measurements of clone shapes as a function of the clone size can be explained by a three-fold increase in apical line and lateral surface tension around misspecified clones (3.2.3). In Section 3.2.4 we relate the parameters of the 3D Vertex Model and the continuum model, and show the predictive consistency of the two models.

Simulations in the 3D Vertex Model suggested that the pressure exerted by the contractile boundary would also lead to the apical extrusion of small clones. And indeed, a statistical analysis revealed that small clones are removed from the tissue early after they are induced to take a different fate (3.3.1). Therefore we show how the contractile boundary mechanism could act as a potential tumour suppression mechanism by removing cells and small patches of cells expressing misspecified or even cancerous transcription factors (3.3.2).

3.1 The biology of cyst formation

One of the best studied epithelial tissues is the wing imaginal disc in the *Drosophila* larva, which develops into the full grown wing of the adult fly (cf. Section 1.2). As shown in Fig. 3.1, the wing disc is a two-sided simple epithelium that is topologically equivalent to a sphere. One side of the epithelium consists of elongated, columnar cells whereas the other side is the so called *peripodial membrane* and consists of stretched out, squamous cells. In this chapter we will focus on the columnar pouch region of the epithelium, which is divided by folds from the neighbouring hinge region as shown in Fig. 3.1.

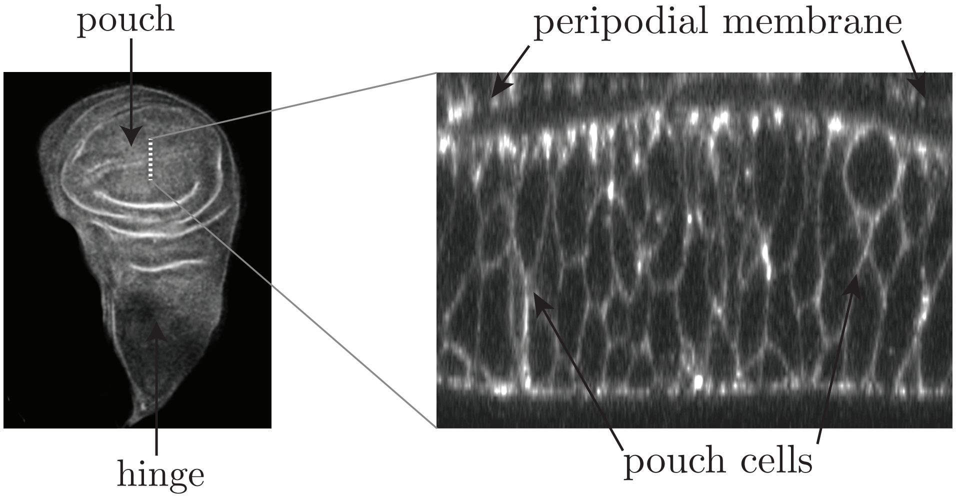

Figure 3.1: The wing imaginal disc of the *Drosophila* and its structure. Images show actin staining and have been taken by C. Bielmeier.

3.1.1 Cell fate misspecification and cyst formation

Posterior sex combs (*Psc*) and *Suppressor of zeste 2* (*Su(z)2*) are redundantly acting tumour suppressor genes in the *Drosophila* wing disc. They encode Polycomb proteins, which epigenetically silence cell-fate-specifying transcription factors during development and restrain proliferation by repressing JAK/STAT and Notch signaling. Our collaborators used a mitotic recombination system (FLP/FRT) coupled to a heat-shock promoter, to trigger the mosaic repression of both *Psc* and *Su(z)2* (in short *Psc-Su(z)2*) in randomly distributed cells of the imaginal wing disc, by a temporal temperature increase of the fly larvas to 37° C. The misspecified cells (i.e. the cells without *Psc-Su(z)2* expression) were additionally labelled by GFP, and their number was determined by the length of the heat-shock. We found that 30 h after mitotic recombination, clones where *Psc-Su(z)2* was repressed retracted from the apical surface of wing imaginal discs and by 54 h almost all clones formed cyst-like structures locating to the basal side of the epithelium (Fig. 3.2). By 102 h, many *Psc-Su(z)2* clones completely resolved contacts with wild type cells and gave rise to persistent, proliferating cysts encapsulating an apical lumen (data not shown).

The transcription factor *Psc-Su(z)2* represses a variety of other cell fate specifying transcription factors, such as *forkhead* (*fkh*), *lozenge* (*lz*) and *Abdominal-B* (*AbdB*). The overexpression of any of these genes alone in patches of cells led to the formation of cysts. We wanted to test whether cysts are specific to transcription factors silenced by *Psc/Su(z)2*, or to cell-fate misspecification in general. Through extensive genetical experiments, our collaborators revealed that cyst formation in imaginal discs represents a very general response to cell fate misspecification or perturbed signalling pathways and is driven by differences between misspecified cells and surrounding wild type cells. Table 3.1 summarises all transcription factors and signaling pathways which have been found to give rise to cysts if misexpressed (in the case of transcription factors) or impaired (in the case of signaling pathways).

Whereas for instance *Psc-Su(z)2* is homogeneously expressed throughout in the wing disc, some transcription factors, such as *homothorax* (*hth*) or *vestigial* (*vg*), display a typical expression pattern. While the repression of *Psc-Su(z)2* led to the formation of cysts everywhere in the wing disc, the overexpression of *hth* and *vg* led to the position-dependent formation of cysts in regions where their expression is normally low (data shown in [64]). Similarly, the perturbation of signalling pathways induced cyst formation depending on the local endogenous activation of the signalling pathway (Fig. 3.3).

Collectively, these observations emphasise that cyst formation in imaginal discs represents a surprisingly general response to cell-fate misspecification and is driven by relative fate differences between misspecified and surrounding wild-type cells

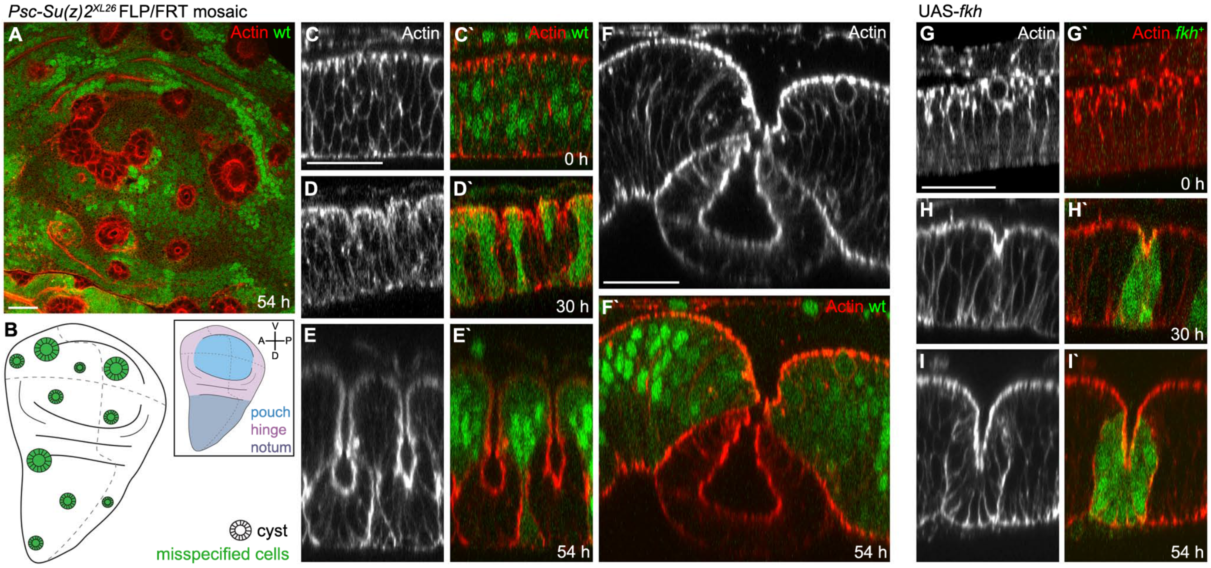
Psc-Su(z)2XL26 FLP/FRT mosaic
A
Actin wt
54 h
B
V
A
P
D
pouch
hinge
notum
cyst
misspecified cells
C
Actin
C`
Actin wt
0 h
D
D`
30 h
E
E`
54 h
F
Actin
F`
Actin wt
54 h
UAS-fkh
G
Actin
G`
Actin fkh+
0 h
H
H`
30 h
I
I`
54 h

Figure 3.2: The genes *Psc-Su(z)2* and *forkhead* (*fkh*) are not normally expressed in the wing disc, and overexpression leads to the formation of cysts regardless of the clone's initial position (A,B). The clones start out from a flat state (C,C',G,G') and successively retract from the apical surface of the tissue, forming cysts in the course of the next 30 to 100 hours (D-E,H-I).

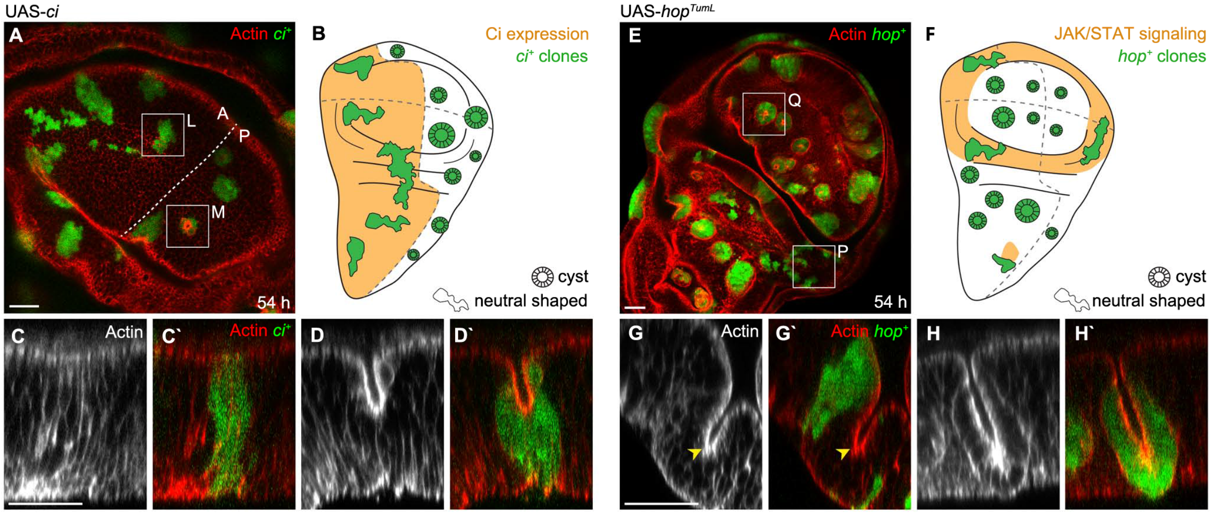
UAS-ci
A
Actin ci+
L
A
P
M
54 h
B
Ci expression
ci+ clones
cyst
neutral shaped
UAS-hopTumL
E
Actin hop+
Q
P
54 h
F
JAK/STAT signaling
hop+ clones
cyst
neutral shaped
C
Actin
C`
Actin ci+
D
D`
G
Actin
G`
Actin hop+
H
H`

Figure 3.3: Aberrantly induced Hh signalling (through *ci*) and of JAK-STAT signaling (through *hop*) led to the formation of cysts only in regions, where the signalling pathways are not endogenously active.

TF/signaling pathway	**position dependent**	**tissue**	**tested in**
Psc-Su(z)2	No	WID	this study, [65, 66]
eyeless	No	WID	this study
forkhead	No	WID, EID	this study
Abdominal-B	No	WID,EID	this study
lozenge	No	WID	this study
Ultrabithorax	No	WID, EID	this study
homothorax	Yes	WID	this study, [67, 68]
vestigial	Yes	WID, EID	this study, [67, 69, 70]
Ras	Yes	WID	this study, [61, 71, 72]
wg signaling (*arm*)	Yes	WID	this study, [70, 73]
Hh signaling (*ci*)	Yes	WID	this study, [72]
Dpp signaling (*tkv*)	Yes	WID	this study, [74, 75, 70]
JAK-STAT signaling (*hop*)	Yes	WID	this study

Table 3.1: Overview of transcription factors or signaling pathways, which were found to give rise to cysts if overexpressed or impaired, showing the generality of cystic phenotypes as response to clonal misregulation. The first column shows the misexpressed transcription factors (TF) and the compromised signaling pathways, which were found to give rise to cysts. The second column indicates if the clonal phenotype depends on the position in the disc. In all cases of positional dependency the transcription factor is normally expressed in a pattern inside the disc, or the endogeneous activation of the signaling pathway varies across the disc, and the disruption of these pattern led to the formation of cysts. The 'tissue' column indicates if cyst formation was observed in the wing imaginal disc (WID), the eye imaginal disc (EID), or both. The last column indicates in which studies cyst-like phenotypes have been observed; the table also includes studies in which we noticed cyst-related clone phenotypes that were not described as cysts in the study itself, such as round clones, smooth clones, apical retraction or invagination. Note that the overview might not be complete but includes only studies that came to our attention.

3.1.2 Inverse cysts

To observe cell-autonomous shape changes in misspecified cells more directly, our collaborators generated wing discs where the majority of cells ectopically expressed the cell fate specifying transcription factors, by increasing the duration of the heat shock. While, for instance, *fkh*-expressing cells retained their columnar shape early after the heat shock, Fig. 3.4A shows that instead the remaining small clusters of wild type cells retracted from the apical surface and formed cysts. Cyst formation of small wild-type clones was also induced by tissue wide overexpression of *AbdB*, *Ubx* or *ey* (Fig. 3.4B). Similarly, broad activation of the Shh/Hh-signalling pathway also gave rise to wild type cysts, however, only in the posterior compartment where *Shh/Hh*-signalling is normally low. These observations indicate that cyst formation is not driven cell-autonomously by misspecified cells, but is driven instead by locally generated forces arising due to the apposition of differently fated cell populations.

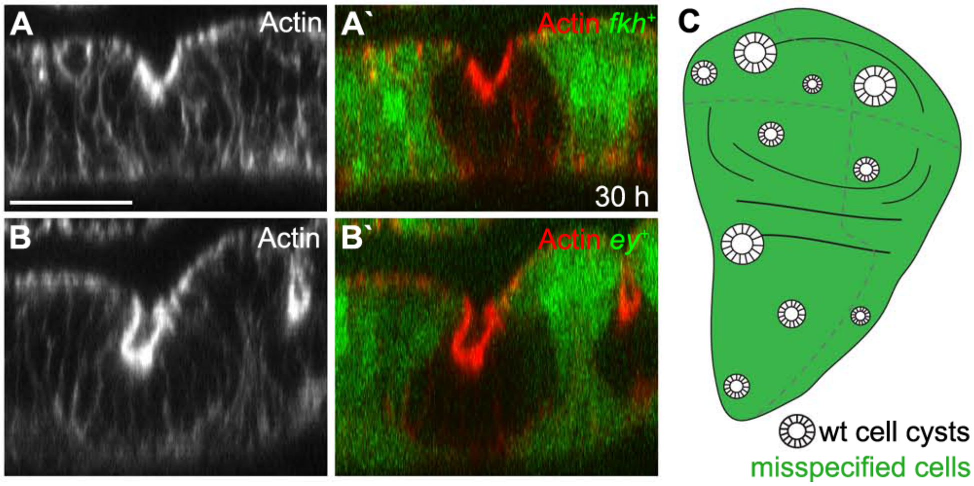

Figure 3.4: If most of the cells in the imaginal wing disc ectopically express transcription factors, such as *fkh* or *ey*, the wild type clones surrounded by misspecified cells bulge out and form (inverse) cysts.

3.1.3 Actin accumulation at clone boundaries

Following the previous observations we hypothesised that cysts form through a mechanism acting at the interface between misspecified cell and wild type cell (MWI), where the difference between the cells can be read out. Our collaborators thus performed an extensive analysis of adhesion and cytoskeletal markers at cellular interfaces during cyst formation. At early stages of cyst formation, levels of cell adhesion or cell polarity markers at interfaces between *fkh*-expressing or *Psc-Su(z)2* mutant cells were not consistently different to interfaces between wild type cells. We did, however, find that actin enriched at apical surfaces in invaginating misspecified cells as well as in invaginating wild type cells, likely as a result of apical constriction during early stages of cyst formation (compare FIGURES 3.2H and 3.4).

We next focused on the microscopical properties of the interfaces between two differently fated cell populations and compared them to the interfaces between wild-type and mutant cells. FIG. 3.5b shows that at early and late stages of cyst formation, the average actin intensity between wild-type cells and between *fkh*-expressing cells is similar. Previous studies have described apical actin cable formation around misspecified cell populations [76, 37, 77]. In agreement with these observations, FIGS. 3.5a and 3.5b show that actin levels at MWI adherens junctions of *fkh*-expressing clones were in average increased by 30%, even when a subpopulation of clones had not yet undergone invagination at 30 h after clone induction. Importantly, we found that in addition, filamentous actin was enriched by 40% at the entire basolateral MWI interface. We observed a similar enrichment of actin at the basolateral MWI of *ey*-expressing clones. FIG. 3.5b also shows that increased actin enrichment at the MWI persisted until the late stages of cyst formation (54 h after clone induction) when cysts were fully invaginated. Importantly, actin also enriched at MWI interfaces when wild type cells formed cysts (data not shown). From these observation we drew the conclusion that actin enrichment at the MWI, rather than cell-autonomous changes in misspecified or wild type cells, is a defining feature of early and late stages of cyst formation. Note that the resolution of a confocal microscope did not allow to distinguish, if the increase in actin intensity at the MWI was due to an increase in actin inside the cortices of the wildtype cells, the cortices of misspecified cells or to similar extents in both cortices.

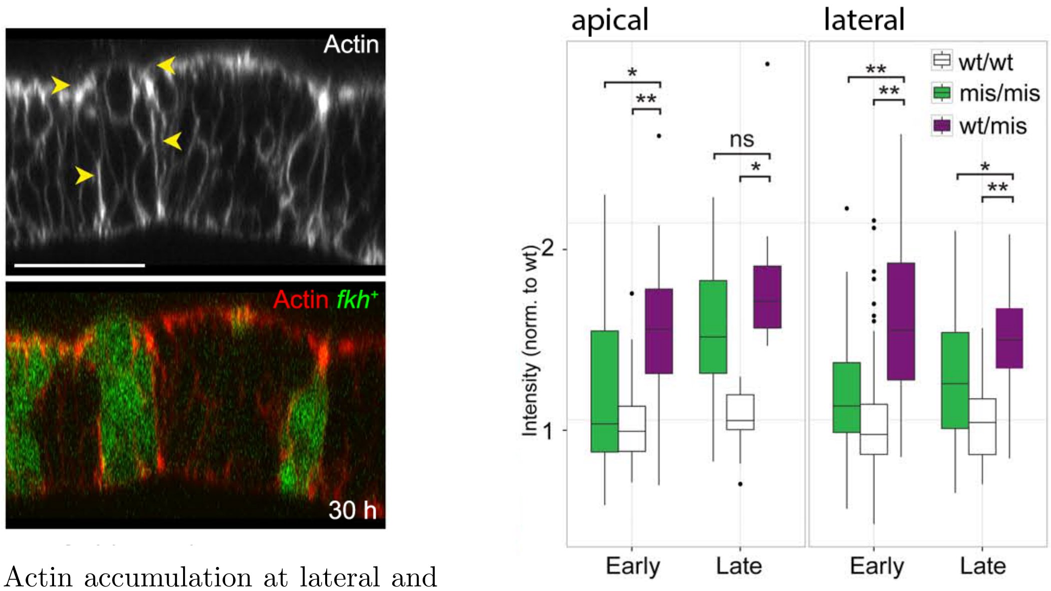

(a) Actin accumulation at lateral and apical MWIs.

(b) Quantification revealed significant increase

Figure 3.5: Lateral and apical regions of MWI are significantly enriched in actin compared to the interfaces between the cells of same type. In the late stages of cyst formation (54 hours after the heat-shock), the intensity of actin at interfaces between misspecified cells (mis/mis) is also increased, whereas it is comparable to the wild type interfaces (wt/wt) at the early stages of cyst formation.

3.1.4 Clone shape quantifications

Misspecified clones are circular

Concurrent with enrichment in contractile components, we observed significant changes to the shape of interfaces between misspecified and wild type cells. We observed the smoothening of apical interfaces at the level of adherens junction between misspecified cells and wild type cells. While this shortening of common adherens junction between differently fated cells has been described in [78, 79, 73], and a general increase in apical smoothness of misspecified cell populations was quantified in [80], we observed that misspecified clones specifically exhibited smoothing and minimisation of basolateral interface contact area (Fig. 3.6). To quantify the smoothness of clonal interfaces we defined a measure C for the basal circularity, which relates the basal area A and circumference P of a clone:

$$C = 4\pi \frac{\text{Area}}{\text{Perimeter}^2}. \tag{3.1}$$

For a basally perfectly circular clone this measure gives $C = 1$, and it decreases for increasing deviation from the round shape. Fig. 3.6 shows that the basolateral clone circularity increases from 0.32 in wild type clones to 0.76 in *fkh*-expressing clones already early after clone induction. We detected a similar increase in basolateral circularity for clones of wild type cells surrounded by misspecified cells. These results suggest that contractile changes to both apical and basolateral MWI surfaces result in minimisation of the entire lateral contact area between wild type and misspecified cells.

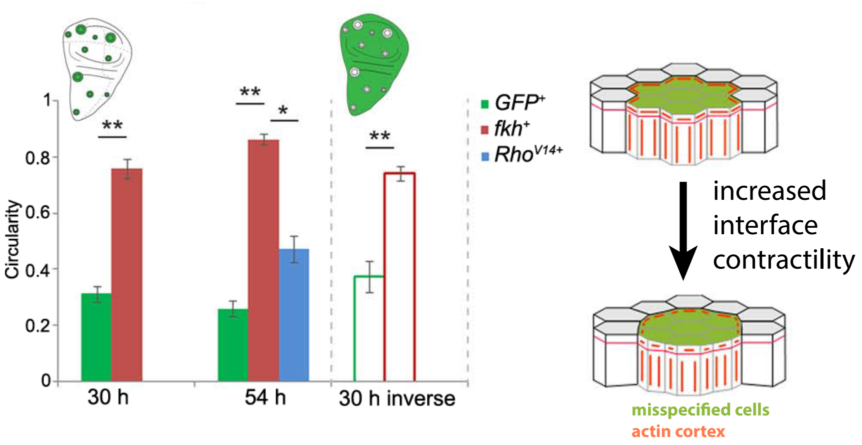

Figure 3.6: Small clones surrounded by cells with a different fate showed a significatn increase in circularity of their basal interface compared to the circularity of GFP-marked wild type clones.

Clone deformation and cyst formation depends on clone size

To study how the clone shape depends on the number of cells in the clone, we quantified the shapes of 79 *fkh*-expressing clones ranging in size from 2 to 120 cells at early stages of cyst formation. In two perpendicular cross-sections of each clone we measured apical and basal clone width w_a and w_b, as well as apical and basal deformation away from the apical and basal surface of the surrounding tissue, u_a and u_b (Fig. 3.7a). As shown in Fig. 3.7, apical indentation u_a and basal deformation u_b are maximal for intermediate clone sizes ($N_c \sim 70$ cells), and minimal for either small or very large clones. Similarly, the relative difference between apical and basal widths w_a and w_b was maximal for intermediate clone sizes, which corresponds to strongly wedge-shaped cysts (Fig. 3.7). The data shows that small and large clones do not undergo strong apical and basal deformations but still experience MWI smoothing.

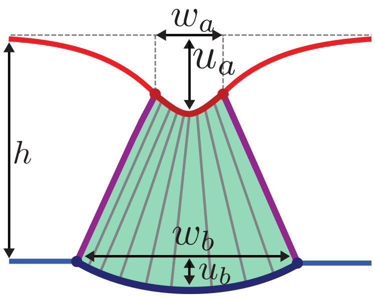

(a) Parametrisation of the cyst shape

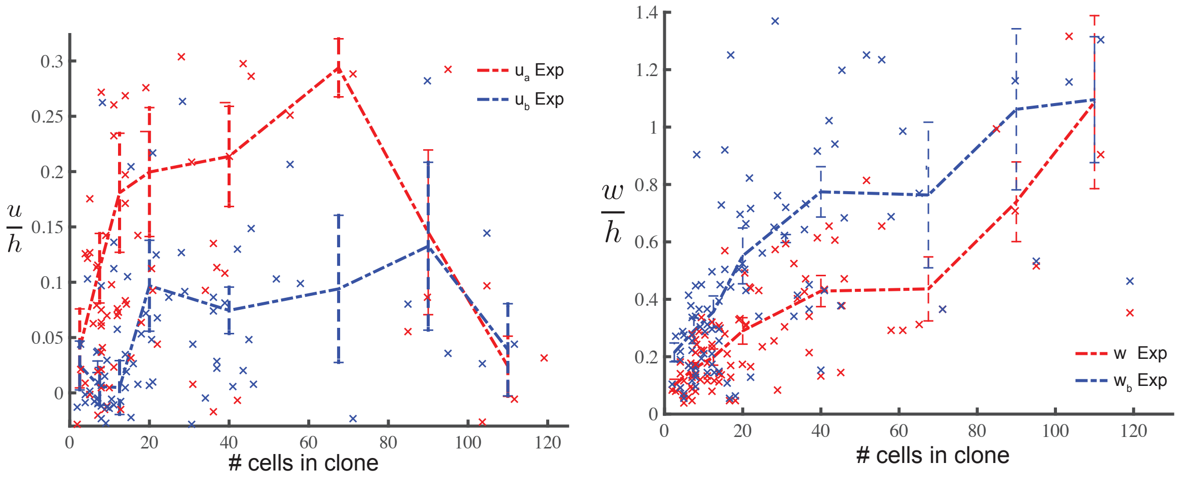

(b) apical and basal indentations

(c) apical and basal widths

Figure 3.7: Clonal shapes as a function of the number of cells in the clone. The graphs show the binned averages and the standard error of the mean. Whereas clones of intermediate size show a distinct formation of cysts, small and large clones barely invaginate.

3.2 The mechanics of cyst formation

3.2.1 The boundary contraction mechanism

The mechanical origins of cyst formation are not yet well established, but different mechanisms have been proposed to be the drivers. The formation of cyst-like structures in homogeneous epithelia was proposed to result from epithelial growth in a confined space and the consequent buckling of the tissue [81, 82]. To test if increased rates of cell proliferation are necessary for cyst initiation our collaborators reduced proliferation inside the misspecified clones (by interfering with the growth-promoting function of the Hippo/Salvador/Warts pathway). These experiments showed that cysts still formed when proliferation was impeded, indicating that the out-of-plane deformation of *Psc-Su(z)2* mutant clones is not a result of spatial constraints imposed on proliferating *Psc-Su(z)2* cells by surrounding wild type cells.

Monier and colleagues showed in [47] that epithelial folding in the *Drosophila* imaginal leg disc is driven by forces generated in apoptotic cells. However, the additional overexpression of apoptosis-inhibitors (*p35*, *dIAP1*) did also not prevent the clones from forming cysts, suggesting that apoptosis is not required for the formation of cysts.

Dahmann and colleagues hypothesised in [70, 83] that a cell-autonomous shape change in the misspecified cells, from columnar to cuboidal, could be responsible for the formation of cysts. Therefore, we aimed to understand if cyst formation can be understood as a cell-autonomous process reflecting altered mechanical cell properties resulting from ectopic target gene activation. Whereas this effect could indeed explain cyst formation, one would expect that it cannot account for the invagination of wildtype cells in the inverse experiments following a long heat shock as shown in Section 3.1.2. To test this hypothesis, our collaborators artificially induced a bulk effect by overexpressing Rho-Kinase mosaically in patches of cells, and found that indeed small clones formed cyst-like structures. However, if small wild type clones were surrounded by misspecified cells the wild type cells did not invaginate but tower over the misspecified cells (data shown in [64]).

In the previous sections we gave different experimentally supported arguments that the MWI experiences an increased contractility along its apical bonds and lateral surfaces. We showed that Actin, Myosin and Moesin are increasingly recruited to the MWI (3.1.3), which correlates well with the increase of their baso-lateral smoothness (3.1.4). Furthermore we showed that also wildtype clones surrounded by misspecified were induced to form cysts, suggesting a mechanism that acts mainly at the MWI, as opposed to a cell-autonomous mechanism where mechanical properties of the misspecified cells are changed.

Consequently, the mechanism we propose for the formation of cysts is that the increase in contractile machinery at the apical and lateral interfaces between differently fated cells leads to an increase in contractile tension. This tension induces a compression of the misspecified clone and the consequent buckling and cyst formation. If this boundary effect is sufficient to induce the formation of cysts, from symmetry arguments it follows immediately that it can also recapitulate the formation of inverse cysts.

In the next sections we will use 3D Vertex Model simulations and the continuum theory introduced in Chapter 2 to show conceptually and quantitatively how the contractile boundary effect can induce the formation of cysts in the observed range of clone sizes.

3.2.2 Cysts are buckled clones

In the previous section we suggested that the formation of cysts is driven by a mechanical boundary effect acting along the interfaces between cells of different fate. In this section we use the continuum theory introduced in Section 2.2.1 to qualitatively show why this boundary mechanism leads to the predominant deformation of intermediately sized clones, which was experimentally quantified in Section 3.1.4.

In a nutshell, this dependency of clone shape and clone size is due to two size dependent effects which are illustrated in Fig. 3.8.

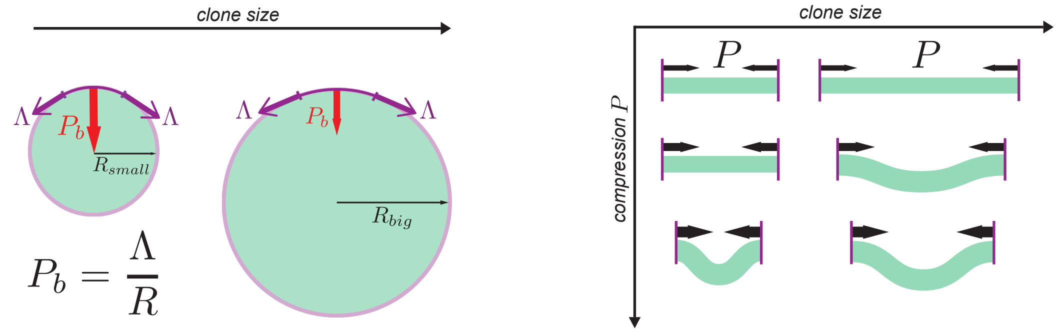

(a) The pressure exerted by the contractile boundary clone decreases with increasing clone size, as predicted by the law of Laplace.

(b) The critical boundary pressure that is required to buckle a clamped clone decreases with increasing clone size.

Figure 3.8: The stability of clones subjected to a contractile boundary is determined by two opposing size-dependent contributions. While the compression due to the boundary contraction decreases with increasing clone size, the pressure required to induce the buckling increases, hence allowing for different regions of stability.

First, the pressure P_b exerted on the clone by the contractile boundary with tension Λ

decreases with increasing clone size R following the law of Laplace and we find:

$$P_b = \frac{\Lambda}{R}. \tag{3.2}$$

Therefore large clones do not feel sufficient boundary compression, and will not be induced to buckle (Fig. 3.8a). The second effect is the size dependency of the buckling pressure of clamped elastic plate: the bigger the piece of material with clamped boundaries, the weaker the required buckling pressure. Therefore, in this simplified view there exist two antithetic contributions that together determine the buckling thresholds of the clone (Fig. 3.8).

In the following sections we will study the buckling transitions of a 2D elastic material subject to a contractile boundary and derive the regions of instability that correspond to the regions of cyst formation in the biological experiments.

Parametrisation and free energy

The epithelium is modelled as a thin elastic layer under compression, which is coupled by elastic links to an underlying solid substrate. Its shape is geometrically represented by the position of the mid-plane through the tissue given by a function $h(x, y)$, that describes the tissue's z-position in the Monge gauge parametrisation:

$$\mathbf{X} = x\,\mathbf{e}_x + y\,\mathbf{e}_y + h(x, y)\mathbf{e}_z. \tag{3.3}$$

A sketch of the parametrisation is shown in Fig. 3.9.

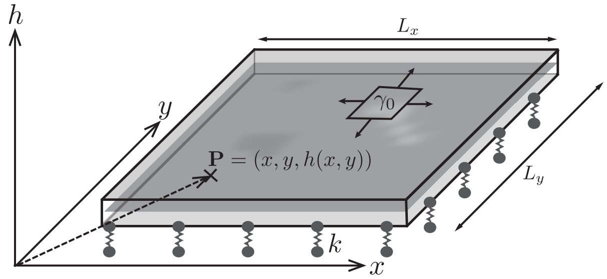

$$W = \int \left(\frac{\kappa}{2}(C - C_0)^2 + \gamma + \frac{k}{2}h^2 \right) dA$$

κ ... bending modulus

C_0 ... instantaneous curvature

γ ... external tension

k ... ECM attachment stiffness

Figure 3.9: The tissue is represented by its mid plane in the Monge gauge. Then an extended free Helfrich energy F of the tissue shapes is defined, which takes into account the bending stiffness, external tension and the ECM attachment.

The tissue has a bending rigidity κ which penalises deviation of the local curvature C from the preferred curvature C_0. In addition, an elastic material with elastic modulus k

is assumed to connect the tissue to the underlying ECM, represented as a flat surface at position $h = 0$, as shown in FIG. 3.9. The corresponding mechanical work for a region of tissue S then reads

$$W = \int_S \left(\frac{\kappa}{2} C^2 - \kappa C_0 C + w_0(\rho) + \frac{k}{2} h^2 \right) dA, \tag{3.4}$$

where $C = \frac{1}{R_1} + \frac{1}{R_2}$ with R_1 and R_2 the two principal radii the mean curvature, ρ is the cell density, and w_0 is the mechanical energy density at zero curvature. In the limit of weak bending $|\nabla h| \ll 1$, the work function reads up to the second order in height deviation

$$W \approx W_0 + \int_S \left(\gamma \frac{(\nabla h)^2}{2} + \frac{\kappa}{2} (\Delta h)^2 - \kappa C_0 \Delta h + \frac{k}{2} h^2 \right) dxdy \tag{3.5}$$

where we have introduced the surface tension $\gamma = d(\rho^{-1} w_0)/d(\rho^{-1})$.

The stability of a flat, homogeneous tissue under compression

In this section we use the continuum model of an epithelium introduced above, to obtain the buckling threshold for a flat, homogeneous tissue under compression.Introducing an effective friction coefficient $\alpha > 0$, the dynamical equation for the tissue height can be derived by taking the functional derivative of Equation 3.5 with respect to the height function $h(.,.)$, which represents the tissue in the Monge gauge:

$$\alpha \partial_t h(\mathbf{x}, t) = -\kappa \Delta^2 h(\mathbf{x}, t) + \gamma \Delta h - k h(\mathbf{x}, t) \tag{3.6}$$

with $\Delta = \partial_x^2 + \partial_y^2$ the Laplacian operator. If the tissue is periodic on $\Omega = [0, L_x] \times [0, L_y]$, the Fourier transform of $h(\mathbf{x}, t)$ on Ω is defined as:

$$\tilde{h}(\mathbf{q}, t) = \int_\Omega h(\mathbf{x}, t) e^{i\langle \mathbf{q}, \mathbf{x} \rangle} d\mathbf{x} \tag{3.7}$$

for $\mathbf{q} \in \tilde{\Omega} = \{\frac{2\pi i}{L_x} : i = 1, 2, ...\} \times \{\frac{2\pi j}{L_y} : j = 1, 2, ...\}$. Note that in general, as the tissue is made of discrete cells, the discrete modes in $\tilde{\Omega}$ are furthermore restricted by the length scale of the cells, but the effect can be neglected for tissues with large numbers of cells. For $|\mathbf{q}| = q$, the dynamic equation (3.6) can be written in Fourier space:

$$\alpha \partial_t \tilde{h}(\mathbf{q}, t) = (-\kappa q^4 - \gamma q^2 - k) \tilde{h}(\mathbf{q}, t), \tag{3.8}$$

and consequently the criterion for mode $\mathbf{q}$ to be stable is

$$\kappa q^4 + \gamma q^2 + k > 0. \tag{3.9}$$

In the limit of an infinite tissue with $L_x \to \infty$ and $L_y \to \infty$ the excitement for all $\mathbf{q}$ (i.e. for all $q > 0$) is allowed, such that an infinite tissue is stable only if the compression does not exceed γ^* which is given by

$$\gamma^* = -2\sqrt{\kappa k}. \tag{3.10}$$

If the tissue is compressed (i.e. $\gamma > 0$) and the compression exceeds $\gamma^* > \gamma$, the infinite flat tissue ceases to be stable and buckles. This implies that a large tissue under compression is never stable, unless the tissue is connected to the ECM with a nonzero attachment stiffness $k > 0$. Using this formalism, the stability of an epithelium represented in the 3D Vertex Model with an external compression has been derived in SECTION 2.2.4 as a function of the microscopic parameters.

A clamped circular tissue region subjected to a contractile boundary

Now we consider a stable tissue under a global tension γ_0, that is we require $\gamma_0 > -2\sqrt{\kappa k}$ according to Eq. 3.10. A circular region of the tissue is surrounded by a contractile boundary exerting a line tension Λ, as shown in FIG. 3.10.
The resulting compression γ_c of the circular region with radius R is the sum of the external compression acting on the tissue and the compression due to the boundary effect:

$$\gamma_c = \gamma_0 - \frac{\Lambda}{R}. \tag{3.11}$$

Now the mechanical properties of the tissue and the clones are set, and we study the stability of the clones as a function of the mechanical parameters and the clone size.

The clone is represented by a circular region of tissue, which is clamped at its boundary and the dynamic equation for the shape of the tissue region is given by Eq. 3.6 with $\gamma = \gamma_c$. In APPENDIX C.1 we derive an exact stability criterion for clones as a function of the mechanical parameters and clone size. FIG. 3.10 shows a resulting phase plot of stability of a clone for varying clone radius R and applied boundary tension Λ. Furthermore, we obtain asymptotical expressions for the lower bound and the upper bound of buckling,

R_{min} and R_{max} respectively, for small ECM attachment stiffness:

$$R_{min} = j_{11}^2 \kappa / \Lambda \tag{3.12}$$

$$R_{max} = \frac{\Lambda}{\gamma_0 + 2\sqrt{k\kappa}}, \tag{3.13}$$

with $j_{11} \approx 3.832$ the first root of the Bessel function J_1. Our theory therefore approximately predicts buckling of flat clones of radius R, only if $R_{min} < R < R_{max}$. This is well in agreement with the experimental observations shown in Fig. 3.7, because the theory predicts correctly that buckling occurs only on an intermediate clone size range, whereas small and large clones remain stable despite the compression of the contractile boundary. This supports the idea that the formation of cysts can be understood as the buckling of a piece of flat tissue due to the compression generated by a contractile boundary around misspecified clones.

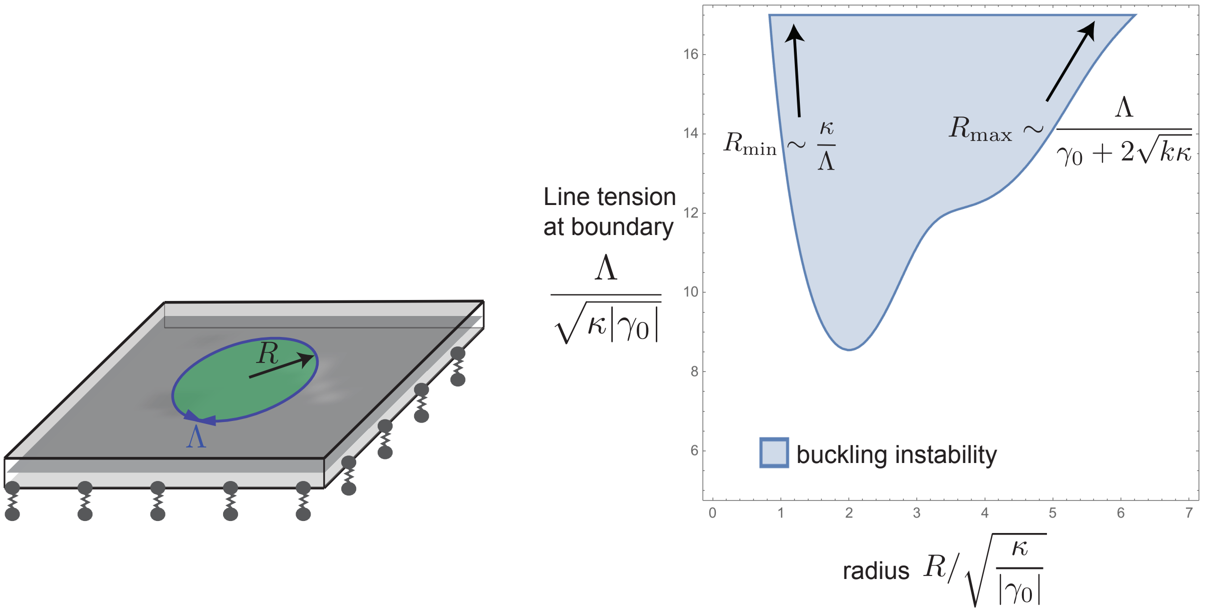

Figure 3.10: Stability of a circular clone with radius R, surrounded by a contractile boundary with line tension Λ. The blue region shows the unstable regime where the clones buckle. R_{min} and R_{max} denote the asymptotical critical radii of clone of buckling for small attachment stiffness k.

3.2.3 Cyst formation in the 3D Vertex Model

We showed in the previous section that cyst formation can be understood qualitatively as the buckling of a clamped circular piece of tissue compressed by a contractile boundary. While this analysis showed that clone formation should be restricted to clones of intermediate size, it could only predict the onset of the instability but not the final clone shape resulting from the contractile boundary mechanism. In this section we use 3D Vertex Model simulations to study the equilibrium shapes of compressed clones, and to identify parameter regimes that quantitatively replicate the experimentally observed size-shape relation of cysts, which was shown in Section 3.1.4.

The wing disc epithelium is represented using the full 3D Vertex Model of simple epithelia, which was introduced and studied in Chapter 2. We start by estimating mechanical parameters of the homogeneous wildtype tissue, by taking into consideration the shape of the wildtype epithelium and we use an experimental setup where the ECM is removed, to estimate the level of compression exerted by the ECM. Then we study the response of clones of different sizes to the contractile boundary effect, in order to match the simulations to the quantifications shown in Fig. 3.7. Thereby we numerically show within the framework of our model that a 3-fold increase in apical line tension and lateral surface tension along the MWI is sufficient to quantitatively capture the observed cyst shapes in experiments.

Constraints on model parameters of the wild type tissue

To represent the wing imaginal disc in the 3D Vertex Model, a number of mechanical parameters have to be determined. If we assume that the cells volume is always constant at V^0, this leaves eight free parameters: the preferred cell volume V_0, the apical, basal and lateral surface tensions (T_a, T_b and T_l respectively), the apical and basal line tensions (Λ_a and Λ_b respectively), the external compression (T_{ext}) and the stiffness of the attachment to the ECM (k_v). Normalisation leaves six independent mechanical parameters to describe the mechanics of ths wild type tissue. In the following we will show how the replication of aspect ratios of wild type tissues in simulations adds two additional constraints on the mechanical parameters, leaving four free mechanical parameters that can be varied independently.

By measuring the average heights and apical areas of cell, we determined the average wild type aspect ratio of the wild type pouch to be $\beta^{wt} \simeq 16.2$. The ECM possibly exerts an external tension T_{ext} on the tissue, and to estimate this tension the relaxation of the tissue after the removal of the ECM was analysed. Fig. 3.11 shows how the treatment of the wing discs with collagenase led to significant ECM removal. In about 10 minutes after the removal, the pouch flattened significantly and the cells changed their aspect ratio (table in Fig. (3.11) without significantly changing their volume. These measurements are in good agreement with the values given by Pastor-Pareja and colleagues in [28]. Assuming that collagenase application only removes the external mechanical constraints imposed by the ECM and does not alter the mechanical properties of the cells, the wing disc expansion following ECM removal indicates that in the wildtype case the ECM exerts compressive stresses onto the epithelium. We showed in Section 2.2.2 how in the 3D Vertex Model the tension generated by a tissue depends on its mechanical parameters and its cell density (Eq. 2.45). For the tissue to be in mechanical equilibrium this tension has to be balanced by the external tension exerted onto the tissue. If the cells' volume is fixed at V_0 the tissue's aspect ratio is related to its cell density by $\rho = (\beta/V_0)^{2/3}$. Denoting T_{ext}^{wt} the compression due to the ECM, and T_{ext}^{coll} the remaining compression after collagenase treatment and removal of the ECM, the following two constraints enforce the right aspect ratios of the mechanically equilibrated tissue:

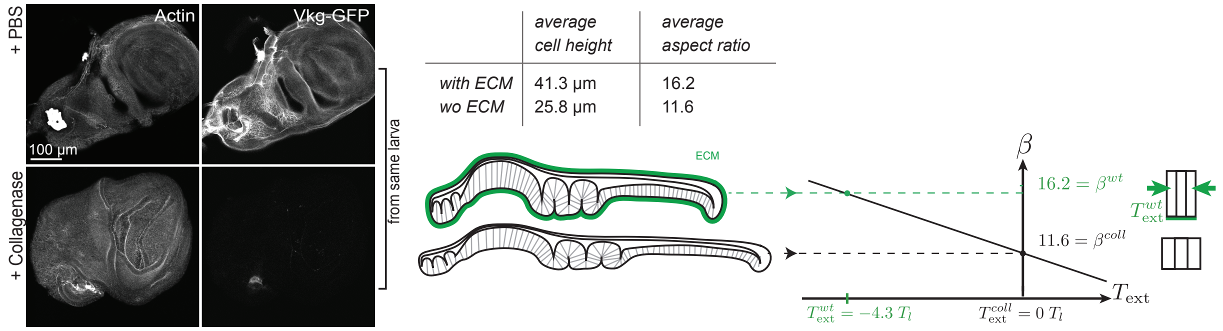

	average cell height	*average aspect ratio*
with ECM	41.3 µm	16.2
wo ECM	25.8 µm	11.6

Figure 3.11: Application of collagenase led to the dissolution of the ECM, and to the consequent expansion of the tissue. The tissues' aspect ratios before and after treatment allow to infer information about the mechanical parameters of the wildtype tissue and the level of compression exerted by the ECM.

$$T_{\text{ext}}^{wt} = \zeta((\beta^{wt}/V_0)^{2/3}) \tag{3.14}$$

$$T_{\text{ext}}^{coll} = \zeta((\beta^{coll}/V_0)^{2/3}). \tag{3.15}$$

Replacing the experimental values of β^{wt} and β^{coll} in equalities 3.14 and 3.15, and assuming that $T_{\text{ext}}^{coll} = 0$ imposes two algebraic constraints on the model parameters that ensure that the wildtype tissue in simulations has the same aspect ratios as in experiments. These constraints will be used in the following section

Contractile bulk versus contractile boundary effect

In Section 3.2.1 we gave general arguments why the contractile boundary effect could induce the formation of cysts and inverse cysts, whereas the contractile bulk mechanism fails to account for the invagination of wildtype cells. To test this hypothesis, we used mechanical tissue parameters fulfilling the relations 3.14 and 3.15 above to recapitulate the wildtype tissue shape, and simulated separately the influence of the bulk and the boundary effects on a patch of 20 cells. Mutant clones have been accounted for in simulations by introducing a set of cells different from wild type cells. An initial clone consisting of N mutant cells is created by assigning mutant properties to the N cells closest to an arbitrarily selected point in the relaxed homogeneous tissue; one initial clone configuration is exemplarily shown in Fig. 3.12A.

To account for the boundary effect the apical line and lateral surface tensions between the two different cell types have been increased, whereas all other mechanical properties of the mutant cells remain unchanged. In the cell autonomous bulk effect, on the other hand, only the lateral surface tensions of the misspecified cells have been increased.

The patch of cells shown in Fig. 3.12A shows an initial equilibrium tissue configuration where all cells are mechanically identical. Fig.s 3.12B&C show the deformation of small wildtype and mutant clones induced by the contractile bulk effect, that is by a threefold increase in lateral tension in all mutant cells. The figure shows that small clones indent apically and form cyst-like structures, resulting from the lateral constriction of cells inside the clone. However, if a patch of wildtype cells is surrounded by misspecified cells that experience the same increased lateral contractility, it will not invaginate and form a cyst, but surmount the surrounding mutant tissue (Fig. 3.12C). These results have been confirmed by the Rho-Kinase experiments discussed in Section 3.2.1. Our simulations therefore demonstrate that the bulk effect alone cannot simultaneously account for both, the formation of cysts and of inverse cysts. However, we found in simulations that the contractile boundary effect with threefold increased tensions at the lateral and apical MWIs as shown in Figs. 3.12D&E, can lead to the apical indentation of both, misspecified and wildtype clones.

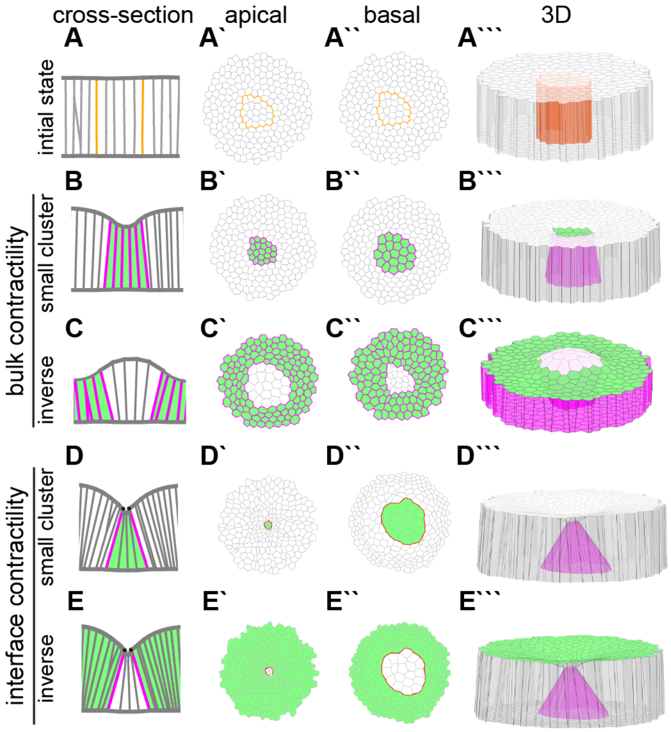

Figure 3.12: Equilibrium tissue shapes for the contractile bulk and the contractile boundary effect. A 3-fold increase in lateral contractility inside the misspecified cells leads to the formation of cysts (B) but fails to explain the occurrence of inverse cysts (C). A 3-fold increase in interface contractility between misspecified and wild type cells can account both for the formation of cysts and the formation of inverse cysts (D and E).

A 3-fold increase in tension recapitulates the observed cyst shapes

We will now use the 3D Vertex Model to show that the contractile boundary mechanism can also account quantitatively for the details of the clone shapes as a function of the clone size, which were quantified in Fig. 3.7. As discussed above, there are four free mechanical parameters in the 3D Vertex Model simulations that can be varied independently while replicating the aspect ratios of wild type epithelium (Eqs. 3.14 and 3.15). In addition, two mechanical parameters are required to describe the strength of the boundary effect acting along the MWIs, namely the increase in apical line tension and the increase in lateral surface tension. This leaves six free parameters to fit the four experimental curves of the apical and basal indentations and widths, shown in 3.7. We performed an extensive parameter search to identify these parameters, which is described in more detail in Appendix C.1.1.

The set of parameters given in Table 3.2 was found to give rise to equilibrium shapes that closely resemble the experimental data, and the comparison of the respective curves in simulations and in experiments is shown in FIG. 3.7. The quantitative agreement between all four curves over the whole range of quantified clone shapes shows how accurately cyst formation can be captured in the 3D Vertex Model. In FIG. 3.13c exemplary images of cysts of different sizes are shown for both experiments and simulations. Note, that to replicate the resulting deformations in simulations, the apical surface and line tensions had to be chosen smaller than the basal tensions, indicating that mechanical stresses generated along the basal tissue surface play an important role in determining the shape of epithelia.

description	**parameter**	**value**
cell volume	V_0/l_0^3	1
lateral surface tension	T_l/T_l	1.0
lateral surface tension around clone	T_l^c/T_l	3.0
apical surface tension	T_a/T_l	3.1
basal surface tension	T_b/T_l	6.95
external compression	T_{ext}/T_l	-4.2
apical line tension	$\Lambda_a/(l_0T_l)$	0.18
apical line tension around clone	$\Lambda_a^c/(l_0T_l)$	0.53
basal line tension	$\Lambda_b/(l_0T_l)$	0.18
stiffness of ECM attachment	k_v/T_l	5.0

Table 3.2: List of parameters obtained from comparison of the vertex model to clone shape measurements as a function of clone size.

To study the dependency of the deformations on the choice of parameters and to henceforth highlight the mechanical key drivers behind the deformations, simulations were run where only single parameters deviated from the preferred set of parameters given in TABLE 3.2. The resulting deformations as a function of the number of cells in the clone are shown in FIG. C.1.

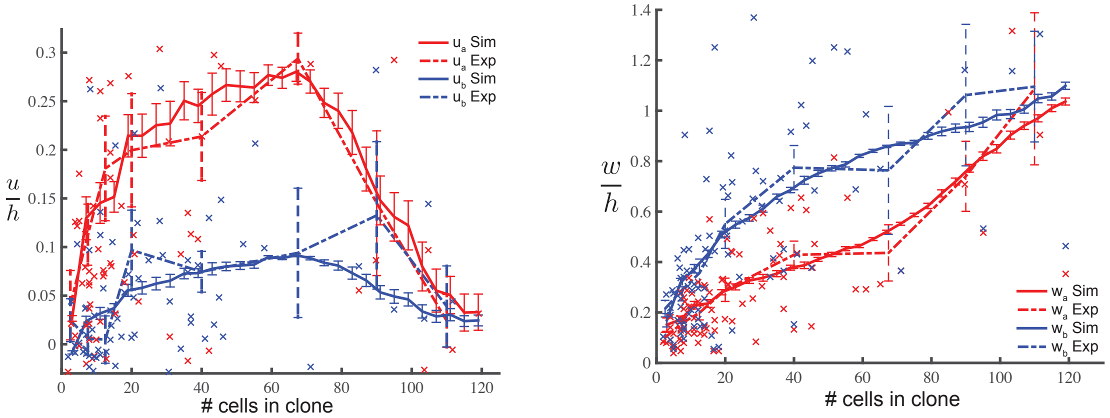

(a) Comparison of apical and basal indentation of clones in simulations and experiments as a function of the clone size.

(b) Comparison of apical and basal widths of clones in simulations and experiments as a function of the clone size.

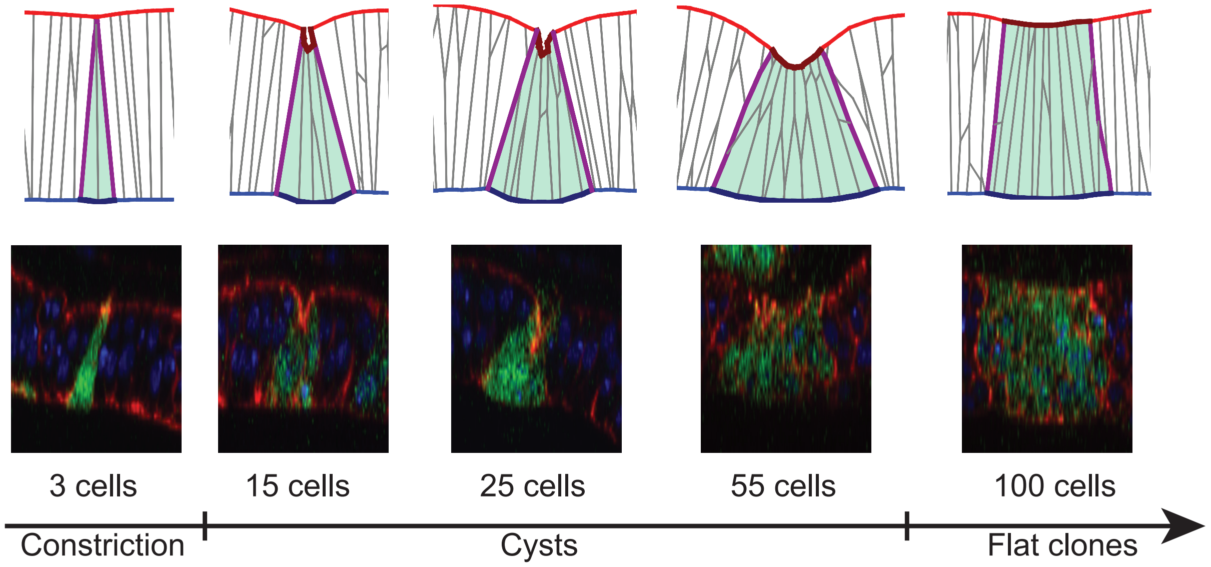

(c) Simulated and experimental cross-sections of clones containing different cell numbers. Apical constriction, cyst formation, or minimal deformations correlate with clone size. Note that cross-section choice results in junctions not spanning apico-basal axis. Scale bars, 25 μm.

Figure 3.13: Comparison of the deformations of clones (parameterised as described in Fig. 3.7a) in experiments and the corresponding deformations in 3D Vertex Model simulations with the optimal parameter set and three-fold increase in tension around the clone. The bars indicate the standard error of the mean of 15 simulations starting from different initial conditions.

3.2.4 Relating the coarse grained theory and the 3D Vertex Model

In Section 3.2.2 we showed, how the contractile boundary in a continuous theory can qualitatively explain cyst formation as the buckling of intermediately sized circular clones due to a contractile boundary. Then we used the 3D Vertex Model simulation framework in Section 3.2.3 to show that an increase of the interface tension by a factor 3 can quantitatively account for the observed cyst shapes over the analysed range of clone sizes. In this section we will make the connection between the two modelling approaches and show that for the mechanical parameters used in the 3D Vertex Model also the continuous theory predicts a buckling in the observed range between 3 and 106 cells.

In Section 2.2.2 we derived how the microscopic mechanical parameters of homogeneous epithelia in the 3D Vertex Model relate to the in-plane tension γ_0 generated by the tissue, to the tissue's bending modulus κ, and to the effective attachment stiffness k:

$$\gamma_0 = T_a + T_b + \frac{3^{1/4}}{\sqrt{2}}\sqrt{\rho_0}(\Lambda_a + \Lambda_b - T_l h) + K_{3D} h_0^2 (\frac{1}{\rho_0} - \frac{V_0}{h_0}) \tag{3.16}$$

$$\kappa = \frac{T_a + T_b}{8} V_0^2 \rho_0^2 + \frac{\sqrt{2}}{8 \cdot 3^{3/4}} T_l V_0 \sqrt{\rho_0} \left(\sqrt{3} - V_0^2 \rho_0^3\right) \tag{3.17}$$

$$k = \frac{6}{3}\frac{k_v}{A_\alpha} = 2k_v\rho. \tag{3.18}$$

The effective additional tension generated by the excess of apical line tension Λ_a^c and lateral surface tension T_l^c around the clone reads

$$\Lambda = \Lambda_a^c + hT_l^c. \tag{3.19}$$

Using these four relations, the corresponding normalised coarse grained mechanical parameters for the set of 3D Vertex Model parameters we used to simulate cyst formation (given in Table 3.2) can be obtained:

$$\kappa/(T_l l_0^2) \simeq\ 0.34 \tag{3.20}$$

$$\gamma_0/T_l \simeq -4.2 \tag{3.21}$$

$$k/\left(T_l/l_0^2\right) \simeq\ 64.0 \tag{3.22}$$

$$\Lambda/(\beta^{2/3} l_0 T_l + \Lambda_a) \simeq\ 2.0. \tag{3.23}$$

The number of cells N in a circular clone and its radius R are related through the cell density ρ:

$$N = R^2 \pi \rho. \tag{3.24}$$

By using the experimental value of the aspect ratio of cells $\beta = h\sqrt{\rho} \approx 16.2$, we find the 2D cell density ρ for a given fixed cellular volume V_0 to be $\rho = (\beta/V_0)^{2/3}$.

After connecting all the parameters and variables, the continuum theory can be used to derive approximate critical buckling radii for the performed simulations by using the expressions given in section 3.2.2 and replacing the continuum theory parameters by the effective parameters obtained from the 3D Vertex Model parameters.

Fig. 3.14 shows the phase diagram of buckling instability for a clone clamped at its boundary, with the parameters obtained above. For the increase in line tension corresponding to a 3-fold increase in apical line tension and lateral surface tension, the linear theory predicts a range of buckling between 3 cells and 106 cells. This is in good agreement with the range of cyst formation observed in simulations, as shown in Fig. 3.13. Note however that the boundary conditions used in this calculation are not identical to the conditions in 3D Vertex Model simulations where the clone is embedded in a deformable tissue.

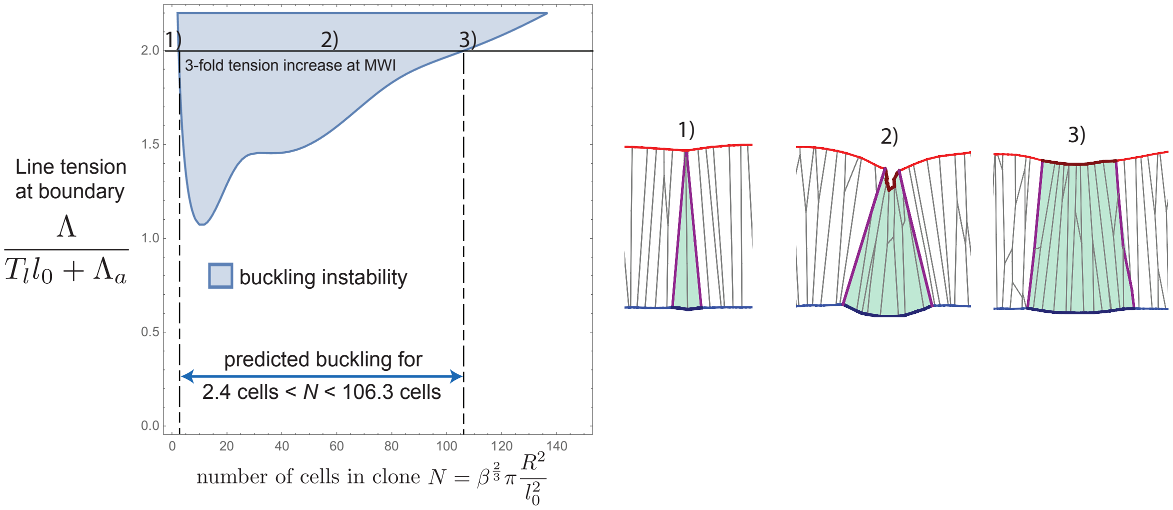

Figure 3.14: Phase plot of clone buckling, for the effective coarse grained parameters derived from optimal set of parameters in simulations. For a three-fold increase in line tension, the continuous theory predicts a buckling of clones containing between ~ 3 and ~ 106 cells. This is in good agreement with the region of strongest deformation in simulations and in experiments shown in Fig. 3.13.

3.3 The function of the contractile boundary mechanism

After identifying the contractile boundary mechanism to be the driver of cyst formation in the wing disc epithelium, we wondered if its existence serves a function, which could represent an evolutionary advantage and explain its existence. In SECTION 3.3.1 we show how the contractile boundary mechanism can lead to the extrusion of small misspecified clones, and we give experimental evidence that these extrusions of small clones happen frequently in the imaginal wing disc. These results suggest that the mechanism could act as a mechanical control that helps maintaining the tissue integrity through the extrusion of misspecified cells, which could otherwise disrupt the delicate epithelial structure. Paradoxically, the formation of disrupting cysts is caused by a failure of the same mechanism to eliminate small-sized cell clusters. In SECTION 3.3.2 we finally show that the contractile boundary mechanism also occurs as a response to a mutation in the potent oncogene *RasV12*, which has a human homologue that plays an important role in many cancers. These findings suggest an important role of the contractile boundary effect in epithelial cancers.

3.3.1 Loss of small misspecified clones

Experimental images and simulations showed that small clones do not form cysts, but experience a significant apical constriction (FIG. 3.13). This apical shrinkage resembles initial stages of cell extrusion events that occur during clearing of apoptotic cells from epithelial tissues or during live cell extrusion initiated by cell crowding [84, 85, 86, 47]. When apically constricted, the cells lose their main adhesion to the surrounding tissue and are consequently removed from the tissue towards the basal side. Our observations therefore suggest that interface contractility may specifically drive elimination of single misspecified cells or small clusters of misspecified cells by promoting apical surface constriction and, potentially, a subsequent basal extrusion.

To test if size-dependent elimination of misspecified cell clusters indeed occurred in the imaginal wing disc, we quantified the distribution of clone sizes and compared clone numbers with wild type phenotype to clones that aberrantly expressed the transcription factor *fkh*. To control the variability in experimental conditions, our collaborators used the Tie-Dye technique to generate clones marked by RFP and wild type clones marked by GFP inside the same wing imaginal disc. In these experiments we quantified clones marked with RFP, that could have four different genotypes: clones with wild type genotype, clones expressing *fkh*, clones expressing the apoptosis inhibitor *dIAP1*, or clones expressing both, *fkh* and *dIAP1*. Images of the experiments are shown in FIG. 3.15a, and in FIG. 3.15 we show how the number of clones of different sizes marked with GFP compares to the number of clones marked with RFP in these 4 distinct experimental setups.

We found that the frequency of RFP and GFP expressing clones is very similar 30 hours after the heat-shock, if the RFP clones have wild type phenotype. However, the additional expression of *fkh* reduced the number of RFP clones significantly compared to the number of GFP clones. The expression of the apoptosis inhibitor *dIAP1* alone in RFP clones did not significantly alter the intrinsic frequency of RFP clones to GFP clones, but also it did not reduce the loss of small clones if combined with *fkh*.
The number of *fkh* clones containing less than 3 cells was reduced by more than 30%, even if addition the cells expressed the inhibitor of apoptosis *dIAP1*. However, expression of *dIAP1* significantly rescued the statistical distribution of large clones sizes back to wild type levels indicating that apoptosis in larger clones is strongly reduced (FIG. 3.15b). Therefore *dIAP1*-expression suppressed apoptosis less effectively in single *fkh*-expressing cells if compared to larger clones. Combined, these experiments suggest that small *fkh*-expressing cell clusters are specifically subjected to strong apoptotic stimuli, which cannot be counteracted by limiting *dIAP1* levels.

We hypothesised that if apoptosis in small misspecified cell clusters is specific to MWI contractility, then apoptosis must also be induced in small wild type cell clusters encircled by misspecified cells. We thus examined wild type clones at early stages after induction of large domains of *fkh*-expressing cells. We indeed observed frequent Dcp-1 activation, which is a marker for apoptotic cells, in small wild type cell clusters. Similarly, when we examined wing discs that ectopically expressed *ey*, we found that apoptosis is repeatedly activated in small wild type cell clones. Combined, these results strongly suggest that MWI contractility may drive cell elimination by specifically inducing apoptosis in small clusters of MWI-encircled cells, following the initial strong apical constriction.

3.3.2 Cyst formation and cancer

The Ras family is a class of related proteins which are ubiquitously expressed in all cell lineages and organs, and which are involved in transmitting signals within cells. Because these signals result in cell growth and division, overactive Ras signaling can ultimately lead to cancer. The Ras genes in humans are the most common oncogenes in human cancer, and mutations that permanently activate Ras are found in 20% to 25% of all human tumours and in up to 90% in certain types of cancer (e.g. pancreatic cancer). It has been shown in [71] that clones overexpressing oncogenic Ras (*RasV12*) experienced significant interface

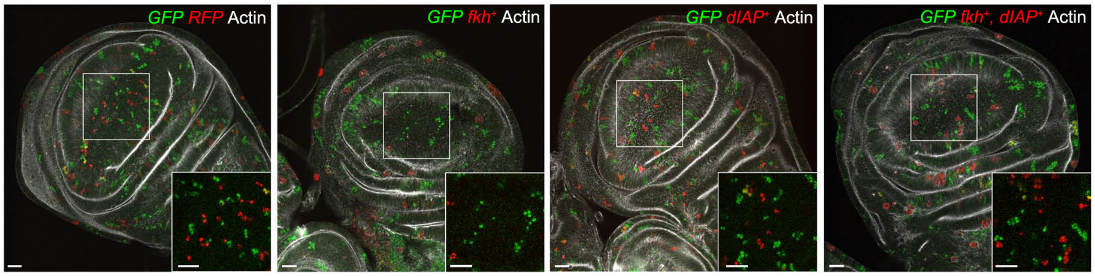

(a) Tie-DYE experiments allow to compare frequencies of GFP and RFP clones, and show that the expression of *fkh* in addition to RFP leads to a significant loss of clones expressing RFP in the pouch, compared to GFP-wildtype clones (images on the left). The number of small clones was still significantly reduced, even if in addition the apoptosis inhibitor *dIAP1* was expressed (images on the right).

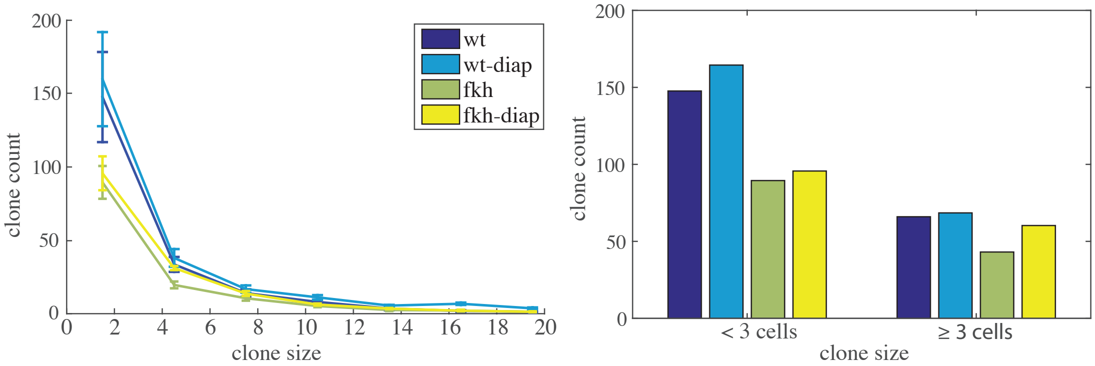

(b) Mean and SEM of number of RFP clones of different sizes, counted in $N \geq 10$ imaginal wing discs 30 hours after a 10 min heat-shock. Small clones expressing fkh are significantly reduced in comparison to wild type clone numbers. Additional expression of the apoptosis inhibitor *dIAP1* in *fkh*-expressing clones can not prevent the loss of small clones, but it recovers the reduction of bigger clones.

Figure 3.15: Small clones expressing the transcription factor *fkh* are lost due to the increased contractility at the MWI. Also the additional inhibition of apoptosis through *dIAP1* did not rescue the number of small *fkh*-expressing clones.

reduction, and we therefore set out to understand if also this smoothening could be driven by increased MWI contractility.

Indeed, our collaborators found that small *RasV12*-expressing clones formed basally extruding cysts in peripheral domains of the wing disc (FIG. 3.16a). Furthermore, they could show that wild type cell patches surrounded by *RasV12*-expressing cells undergo interface smoothening and cyst formation. Following the previous reasoning, these observations suggest that oncogenic Ras promotes cyst formation by inducing increased contractility along the MWI. While we rarely observed apoptosis in wild type GFP-expressing or *RasV12*-transformed cells, we found apoptotic pathways are frequently activated in small wild type cell clusters surrounded by *RasV12*-expressing cells (Fig. 3.16b). Apoptosis in wild type cells occurs almost exclusively in the disc periphery, where also *RasV12*-induced MWI-effects are strongest. Combined, these results reinforce the conclusion that MWI contractility is induced by apposition of cell populations with different fates and that MWI contractility drives cell elimination by activation of apoptosis in small, encircled cell clusters. Based on the presented results, we suggest that the potent human oncogene Ras elicits MWI contractility which leads to cystic deformation of Ras-clones. Indeed, several studies describe altered interface actin dynamics of *RasV12* transformed cells in MDCK monolayers [87, 88, 89, 90].

Strikingly, cystic deformations have also been observed in mouse models of colon cancer upon deregulation of Wnt/APC and TGFβ-signaling [59, 60, 91, 63]). Our work suggests that disruption of Shh/Hh, JAK/STAT, TGFβ/Dpp and Wnt/Wg patterning fields causes cyst formation. These observations emphasise that epithelial cysts may be an early hallmark of tissue disruption in cancer driven by mutagenic changes to differentiation state. Because cysts survive abscission from the surrounding tissue, their formation may promote displacement of cells into new micro-environments and may precede emergence of invasive cell behaviours.

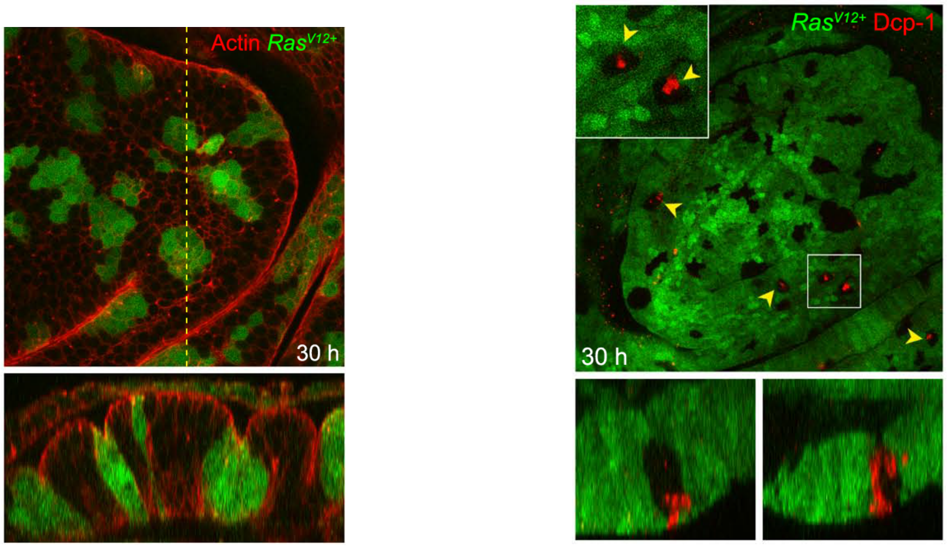

(a) Short heat-shock. **(b)** Long heat-shock + apoptosis marker.

Figure 3.16: Small clones expressing the potent oncogene Ras formed cysts in the periphery of the wing disc (a), whereas they were not significantly different from wild type clusters in the centre of the wing disc. Strikingly, the regions of cyst formation also correspond to the regions where wild type cells surrounded by Ras-expressing cells are undergoing apoptosis (b), indicating that also here the contractile boundary effect at the MWI leads to the elimination of constricted clones.

3.4 Summary

We showed that the formation of epithelial cysts in *Drosophila* imaginal discs is a general response to ectopic expression of transcription factors that specify cell fate. Increased actin accumulation at the interface between differently fated cells precedes the extrusion of small cell clusters, while leading to the bulging out and cystic deformations of intermediate cell clusters. Large misspecified clones only experience interface smoothing.

Based on these observations we suggested a novel mechanism, which is based on an increase in contractility along the apical and lateral interfaces between cells of different fate. We used a generic continuous theory of epithelial sheets, to show that the process of cyst formation can be understood from two simple physical effects that control a buckling instability of surrounded clones: the law of Laplace and the resistance of the tissue to bending. By describing cyst formation as flat clones undergoing a buckling instability, we were able to show why cyst formation is restricted to clones of intermediate sizes. By replicating cyst formation in 3D Vertex Model simulations, we could furthermore show that a 3-fold increase in apical line tension and lateral surface tension at the MWI captures very well the cyst shapes observed in experiments.

Previous studies have highlighted the importance of increased tension at apical adherens junction interfaces and their role in interface morphology [44, 92, 37, 77]. However, cellular forces and deformations associated with interface mechanics in three dimensions have not been explored. Here we showed for the first time that in addition to apical adherens junction, increased actomyosin contractility at basolateral interfaces is extensively regulated and that taking this 3rd dimension of cellular forces into account has crucial consequences for our understanding of 3D tissue morphology. Our experiments and simulations suggest that increased interface contractility induces a repertoire of tissue deformation including cell extrusion and tissue invagination, in addition to interface smoothing. Our simulations showed that an increase in both lateral surface tension and apical line tension by a factor 3 is required to account for these deformations. This increase is similar to the increase in line tensions of a factor 2.5 that has been estimated to act at the interface between developmentally specified compartments [37].

The experimentally observed cyst displayed strong deformations of the apical tissue surfaces compared to the basal surfaces. The 3D Vertex Model simulations only captured this behaviour correctly under the assumption, that the tensions generated along the apical tissue surfaces are smaller than the tensions generated basally. While previous studies focussed on the influence of the apically generated line and surface tensions on epithelial shape, our results suggest that forces generated along the basal surfaces of cells might even be stronger and therefore crucial to understand complex epithelial deformation.

Finally we showed how an increase in interface contractility at the MWI can act as surveillance mechanism by excluding small misspecified clones, but can also drive disease-promoting disruption of epithelial integrity by deforming misspecified cell clusters into cysts. We speculated that interface contractility could have a broader function in driving morphogenesis at the interface between differently fated cells during development.

Our results provide a novel perspective on the morphogenetic mechanisms arising from cell fate heterogeneities within epithelial tissues. It will be interesting to investigate if the cellular mechanisms that drive contractile changes at the interface to misspecified cells and those that drive contractility at the interface between differently specified compartments are alike. Similarly, many developmental invagination processes are driven by cell fate specification of intermediate sized cell clusters and offer therefore an opportunity to understand similarities and differences between morphogenetic behaviours driven by apposition of differently fated cells in development or disease.

CHAPTER 4

Ventral furrow formation through sagittal contraction

4.1 Introduction

In the following chapter we introduce and study a new mechanical driver to play a crucial role in the process of ventral furrow formation at the beginning of the gastrulation process of the fruit fly. This work has been done in collaboration with Matteo Rauzi from the European Molecular Biology Laboratory, Heidelberg.

The morphological event of *Gastrulation* is a fundamental early step in the development of any *Drosophila* fruit fly, which was briefly outlined in Section 1.2. Before being reshaped by gastrulation the undeveloped organism, called *blastula*, is merely an ellipsoidal array of cells surrounding a liquid, without distinct indications pointing to the final shape of the organism. During gastrulation, the progenitor cells of the gut and its appendages (the endoderm), and the progenitors of the organs between gut and outer body wall, such as muscles, blood and heart (the mesoderm) translocate away from the surface of the embryo towards the interior. The cells remaining on the outside of the embryo (the ectoderm) will later outline the body as epidermis and give rise to the nervous system.

Therefore, in some respects gastrulation is the most fundamental morphological transformation, as it leads to the separation of the three germ layers (*endoderm*, *mesoderm* and *ectoderm*) and hence lays out the basic body plan of the adult organism. The words of Lewis Wolpert neatly emphasise the importance of the process: "It is not birth, marriage, or death, but gastrulation, which is truly the most important time in your life." (cited in [93]). The first step of gastrulation is the *ventral furrow formation* during which the mesoderm gets internalised into the blastula, and in this chapter we set out to study this process and put forward a new mechanism that is driving it.

In Sections 4.1.1 the experimental system is introduced, and the characteristics of ventral furrow formation are discussed in detail. Section 4.1.2 gives an overview of existing mechanical models of ventral furrow formation. We suggest that a new model of ventral furrow formation is needed in light of recent observations.

Based on these observations we present a novel mechanical model of ventral furrow formation: the sagittal contraction mechanism (4.2). We use the 3D Vertex Model to simulate a yolk-filled blastula, and show that the proposed mechanism can account for the formation of a significant furrow (4.2.1). Then we demonstrate how to represent the spherical blastula and the sagittal contraction mechanism in the continuum model of epithelial mechanics (4.2.2). By solving for the shape of the epithelium, we hence show that also the continuous theory predicts the formation of a ventral furrow, and we use this analytical approach to identify the mechanical key parameters of the process. We finally show that the complementary approaches agree very well in the respective limits of small deformations, by comparing the predictions of 3D Vertex Model simulations and of the continuum theory (4.2.3). Finally we give an outlook and suggest further directions to explore in terms of experiments and physical modelling (4.3).

4.1.1 The nuts and bolts of mesoderm invagination

The *Drosophila* embryo at the onset of gastrulation, illustrated in FIG. 4.1, consists of roughly 6000 cells forming the columnar epithelium *blastoderm* that encloses a fluid-filled cavity called *blastocoel*. The cells' apical surfaces face the outside of the embryo, whereas the basal sides face the blastocoel. The apical tissue surface is surrounded by the *vitelline membrane* made of stiff, interlinked protein fibres that forms a hard shell around the embryo and does not deform significantly during the whole process of gastrulation [94]. Our quantification showed that the blastula can be approximately described by an ellipsoid with a long axis of ~ 245 μm in length, and two short axes of roughly identical lengths of 90μm as shown in FIG. 4.1. The position of the poles, and of the dorsal and ventral tissues is illustrated in FIG. 4.1. The progenitor cells of the mesoderm, the *mesoderm primordium* (which will be called simply mesoderm from now on) is a $\sim$22-cell-wide band of cells on the ventral side of the blastoderm that encompasses about 19% of the embryo's central dorsal-ventral cross section ([94], FIG. 4.1).

At the onset of gastrulation the ventral epithelium progresses into an inward-fold called *ventral furrow* which consequently deepens and moves inside the epithelium, until finally the adjacent tissues of the mesoderm touch each other and seal off the internalised mesodermal tube. FIG. 4.2 shows how during this folding the ventral-most cells deform from a columnar to a wedge-like shape, and the mesodermal cells undergo a transient lengthening before they return to roughly their initial aspect ratios. The invagination occurs very rapidly in the time course of about 20 minutes, and throughout the whole process the tissue maintains its structure of an epithelial monolayer, the cells do not divide and they do not undergo topological transitions.

While most of the existing insights in the mechanical origins of ventral furrow formation

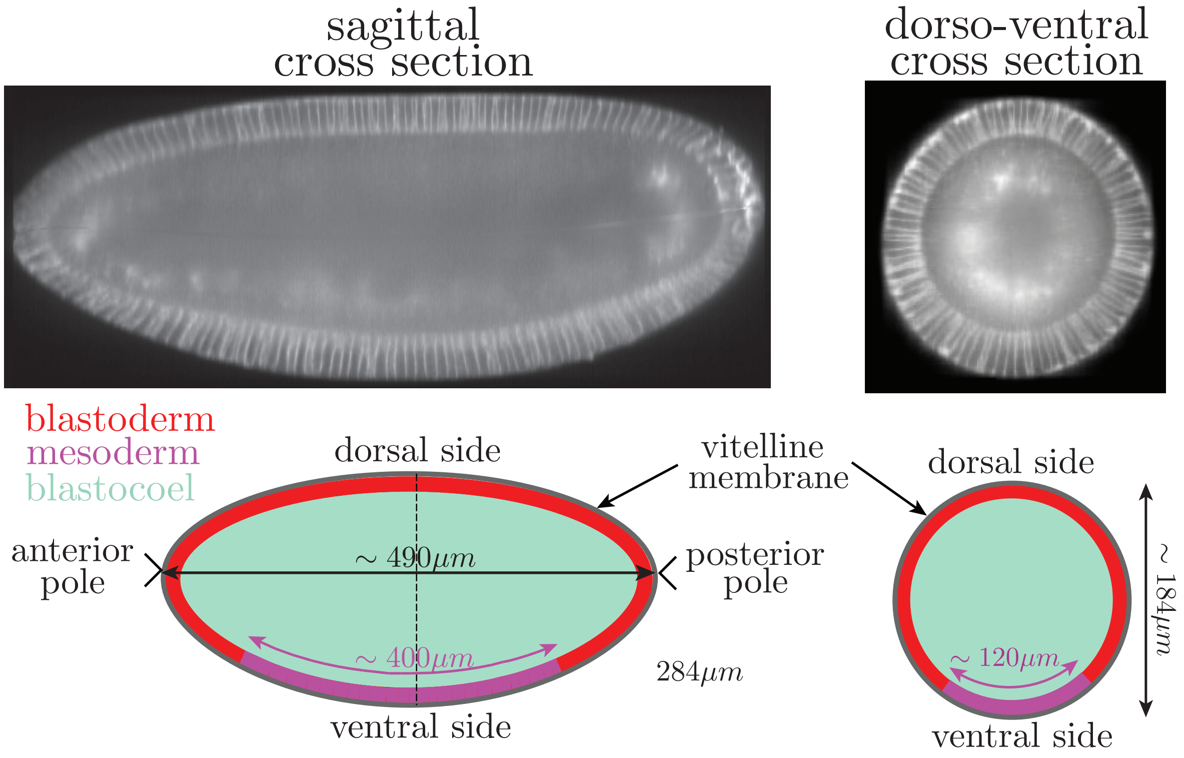
sagittal cross section
dorso-ventral cross section
blastoderm
mesoderm
blastocoel
dorsal side
vitelline membrane
anterior pole
posterior pole
~ 490μm
~ 400μm
284μm
ventral side
dorsal side
~ 184μm
~ 120μm
ventral side

Figure 4.1: The yolk in the blastocoel is surrounded by a simple epithelium, called blastoderm. The sagittal cross section shows the two distinct poles of the blastoderm: the anterior pole (A) and the posterior pole (P). The mesodermal tissue along the ventral region of the blastoderm undergoes invagination during ventral furrow formation. The blastula is completely surrounded by a stiff structure consisting of protein fibres called vitelline membrane (experimental images reproduced courtesy to Matteo Rauzi)

have been obtained through the analysis of the shape changes observed in the dorsal-ventral section through the blastula, new experimental methods, allow for the live imaging of the complete embryo during the duration of gastrulation [97]. The upper image in Fig. 4.3 shows a sagittal cross section through the central embryo at an advanced stage of ventral furrow formation, and underneath the corresponding dorsal-ventral sections are exhibited. Notably, the section of the imaging plane and the mesoderm forms a straight line, which is marked by the dotted white line in the figure.

Laser cutting experiments described by Martin and colleagues suggested that the whole blastoderm is under tension, since ablations of the tissue induced tissue wide epithelial tears [98]. This tension generated by the epithelium must be balanced by fluid pressure exerted by the yolk. In the same paper they showed furthermore that the mesodermal cells undergo waves of apical constriction on the time scale of ~ 1 minute and that they are under stronger tension than the cells outside the mesoderm (Fig. 4.2B).

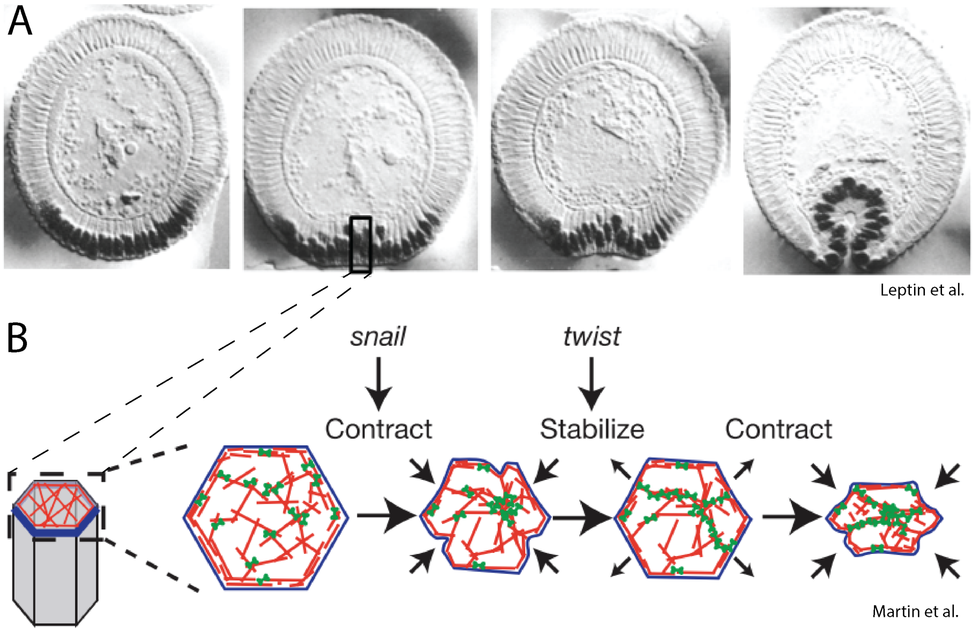

Figure 4.2: A) Four stages of ventral furrow formation shown in the dorsal-ventral section through the centre of the blastula, where cell membranes and nuclei are labelled. In the time course of ~20 min the mesoderm progresses into an inward fold, which deepens and moves inside the epithelium. The images have been taken by Maria Leptin and colleagues and were published in [95]. B) Martin et al. showed in [96] that during ventral furrow formation the cells inside the mesoderm increase their contractility and undergo a series of apical constrictions in the course of which they significantly decrease their apical surface area.

He and colleagues demonstrated in [99] that initial furrow formation occurs even if cellularisation was inhibited, suggesting that forces generated inside the apical surface of the tissue are sufficient to drive the formation of a furrow While therefore not required for initial furrow formation, the cell closure and influence of tensions generated on other than apical cell surfaces is very likely to play an important role in the remaining gastrulation process.

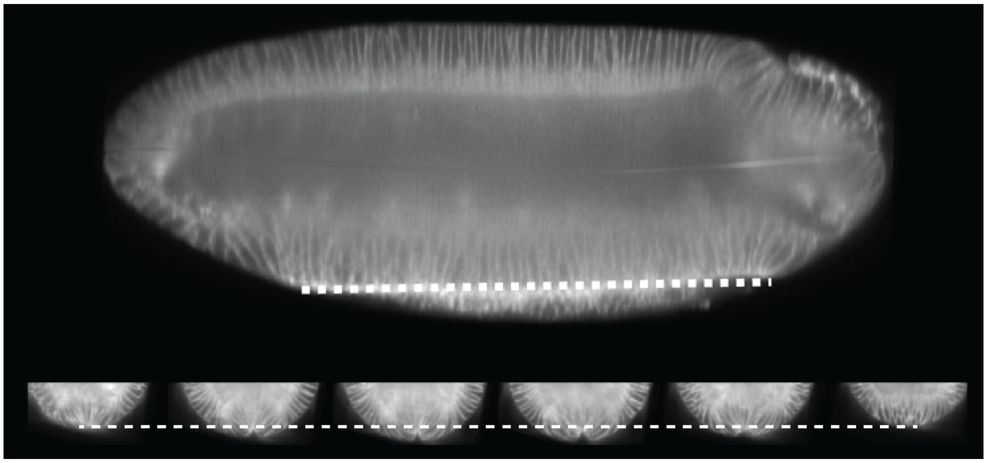

Figure 4.3: The top image shows a sagittal cross section through the blastula during the process of ventral furrow formation; the bottom images show the corresponding dorsal-ventral sections through different positions of that same blastula. Labelled in white is the membrane. The mesoderm straightens in the beginning of ventral furrow formations, and then the mesodermal midline moves in an orchestrated manner into the blastula. All images are replicated with courtesy to Matteo Rauzi.

4.1.2 Mechanical models of ventral furrow formation

Early attempts to understand the mechanical origins of mesoderm invagination date back to Odell and Oster in 1981, where they proposed a purse string mechanism of mesoderm invagination [100]. Following this pioneering work a number of other mechanical models with different assumptions and conclusions have been proposed. The following section will give a short overview of the current literature. For a more comprehensive study of existing models please refer to the review by Rauzi and colleagues [94].

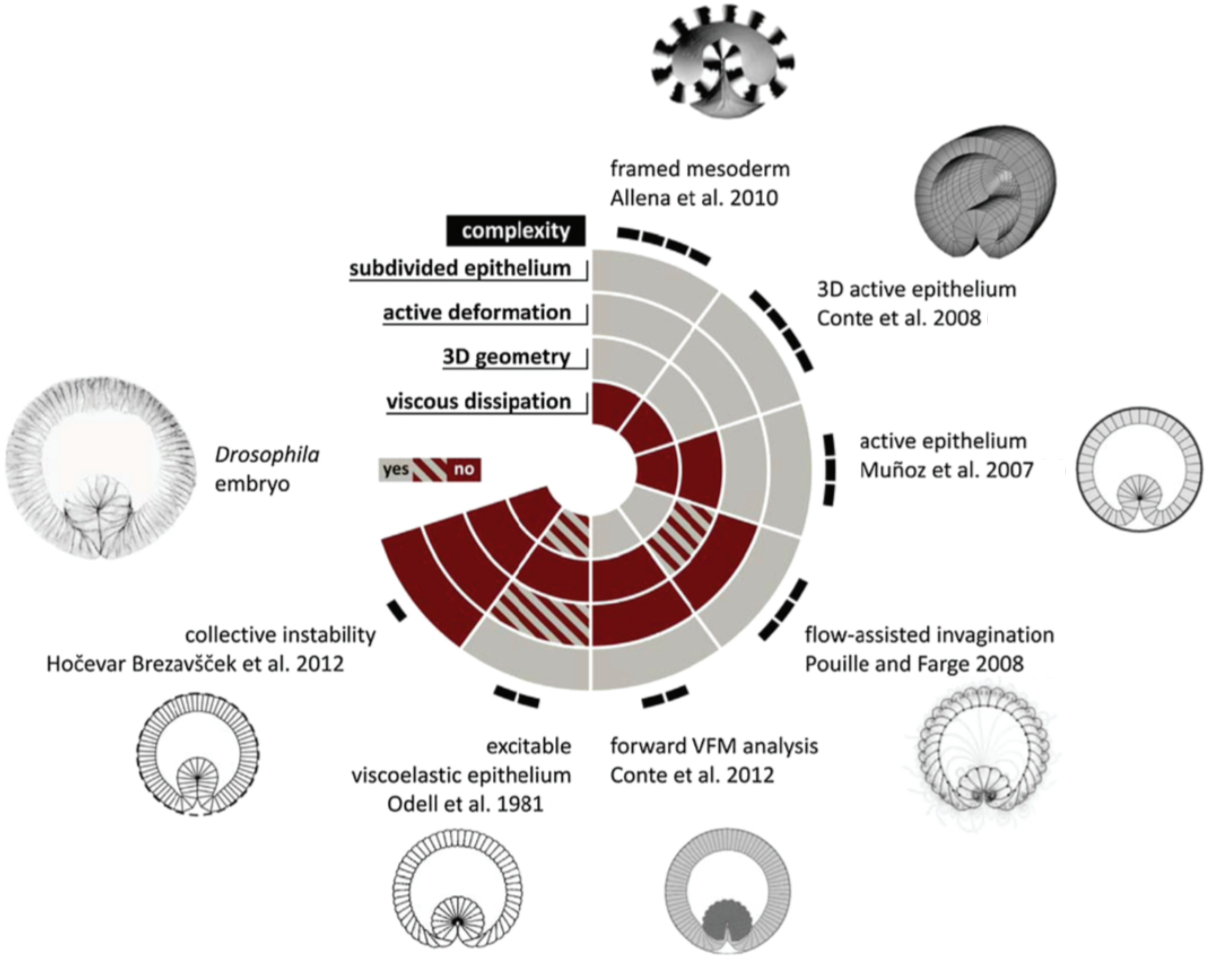
framed mesoderm
Allena et al. 2010
complexity
subdivided epithelium
active deformation
3D geometry
viscous dissipation
yes
no
3D active epithelium
Conte et al. 2008
active epithelium
Muñoz et al. 2007
Drosophila embryo
flow-assisted invagination
Pouille and Farge 2008
collective instability
Hočevar Brezavšček et al. 2012
excitable viscoelastic epithelium
Odell et al. 1981
forward VFM analysis
Conte et al. 2012

Figure 4.4: Overview of the existing mechanical models of mesoderm invagination. Illustration modified from [94].

As suggested in [94], the existing models of ventral furrow formation can be divided into two classes depending on the way they impose the deformations of the mesodermal cells. In the *shape-prescribing models*, the shapes of the mesodermal cells is imposed and the resulting deformations of the blastoderm is obtained [101, 102, 103]. Since these models do not discuss the mechanical drivers of the process, which will want to study in this chapter, we will not further describe these approaches here.

Force-prescribing models, on the other hand, take into account the tensions generated inside the tissue, and the cellular deformations are understood as the results of forces acting inside cells and onto the epithelium [100, 104, 105, 106]. In the seminal paper by Odell et al. [100], the epithelium was represented as a 2D excitable visco-elastic medium. There they showed that a wave of apical constriction of cells propagating through the tissue, together with volume conservation of cells can drive ventral furrow formation. However, while the ideas that were put forward were revolutionary, such a wave of constrictions has not been observed in experiments [94]. After this original demonstration that collective apical constriction of mesodermal cells is sufficient to create a ventral furrow, most of the subsequent physical models focussed on the details of this apical contraction mechanism in the dorsal ventral plane, by using different models such as finite element models and vertex models [101, 102, 107, 103, 108, 109]. All these mechanisms are based on the idea that the mesodermal cells generate a torque in the dorso-ventral cross section, which leads to the subsequent curvature of the cells. However, the furrow formation in acellular embryos [99] suggests that forces generated inside the apical cell surfaces are sufficient for furrowing, and that in fact the torque is not required. The focus of the models on the dorso-ventral sections did not allow these models to investigate the role of apical constriction of the cells in the sagittal direction on the formation of the furrow, and to explain the synchronised formation of the furrow in different dorso-ventral sections.

In 2012, Hocevar Brezavscek and colleagues explored a different approach: they suggested a minimal mechanism, where furrow formation results from a buckling transition of a compressed tissue consisting of identical cells [110]. While the proposed idea is original, it had been shown by Martin et al. in [98] that the blastoderm is under tension rather than compression, which is not compatible with the idea of buckling.

4.2 The sagittal contraction mechanism

In Section 4.1.1 we presented the previous experimental results, which showed that the blastoderm at the onset of gastrulation is under tension [98], that the mesoderm straightens along the sagittal cross section (experiments by Matteo Rauzi, shown in Fig. 4.3) and that ventral furrow formation also takes place when cellularisation is inhibited [99]. Combined, these observations suggest that the existing models do not capture all main aspects of ventral furrow formation, and/or that the assumptions of the models are not fulfilled in the actual biological system. In this thesis we aim to help closing these gaps by introducing a new minimal mechanism for the ventral furrow formation: the sagittal contraction mechanism. We show that this new mechanism leads to the formation of a furrow while at the same time it is in good agreement with the latest experimental observations.

We propose the new mechanism of sagittal contraction is, where ventral furrow formation is driven, or at least enhanced, by the contraction of the mesoderm along the sagittal direction. Due to the curvature of the mesoderm along the sagittal section of the blastula the contraction will generate forces normal to the blastula in the dorsal-ventral sections of the tissue and trigger the indentation. The furrow forms because the increase in tension leads to a straightening of the mesoderm in the sagittal section, which corresponds to a furrow formation if the process is observed in the dorsal-ventral cross section, as shown in Fig. 4.5.

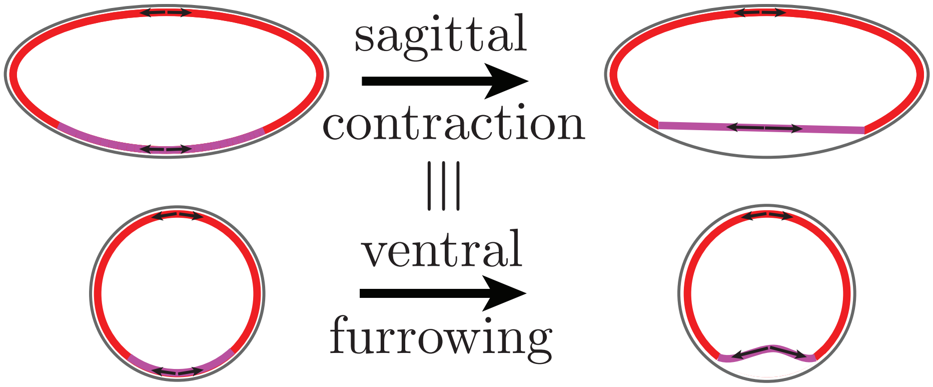

Figure 4.5: An increase in the mesodermal tension leads to a straightening of the mesoderm in the sagittal section of the tissue. This flattening in turn leads to an invagination along the dorsal-ventral cross section of the tissue.

The increase in tension generated along the apical surface of the mesodermal cells has been described by Martin and colleagues in [96], and it leads to a force acting to decrease both the width and the length of the mesodermal tissue. Note that if the cells are able to

maintain their volume and the apical tension in the mesodermal cells is stronger than the basal tension, a torque in the stripe will be generated. While the torque could enhance the formation of the furrow, it seems not to be crucial since it has been shown that the initiation of furrow formation also works if cellularisation has been corrupted [99].
We will show in the following sections how an increased apical tension in the mesodermal cells alone can trigger the formation of a furrow, even in the absence of tensions generated along lateral and basal cell bodies. The mechanism accounts for the observed straightening of the mesoderm along the sagittal section, and it works even if the tissue is under tension.

To put the proposed sagittal contraction mechanism to the test, we model the blastula as a spherical tissue in which a stripe of the tissue (representing the mesoderm) experiences increased contractility. The spherical approximation of the shape has the advantage of being analytically tractable while still capturing the main features of the shape and the process.

By simulating the apical epithelial tissue surface only in the Apical 3D Vertex Model, we demonstrate in SECTION 4.2.1 that an increase in apical tension inside a stripe of cells along the sphere indeed leads to the formation of a ventral furrow. In 4.2.2, we use the continuum theory of simple epithelia introduced in 2 to describe the epithelium as a thin elastic sheet with bulk and shear modulus surrounding a compressible yolk. Using a linear theory we hence show that the response to an increase in tension inside a stripe will induce the formation of a furrow, and that the depth of the furrow is set by the ratio of the tissue's bulk and shear modulus. In SECTION 4.2.3 we use the established relationship between the parameters of the continuum model and the 3D Vertex Model, and show that both theories predict identical deformations for small perturbations away from a homogeneous tension of the tissue.

4.2.1 Sagittal contraction in the Apical 3D Vertex Model

Since it was found that ventral furrow formation happens even if cellularisation has been impaired and consequently all forces are generated apically, we use the Apical 3D Vertex Model (cf. SECTION 2.1.6) to represent the blastoderm at the onset of gastrulation. Here we do not take into account the constraints imposed through the vitelline membrane, to first understand the principles of how the sagittal contraction deforms the tissue. This approach has the further advantage that we can compare the resulting deformations to the analytically obtained deformations in the continuum theory in SECTION 4.2.3. How to include the effects of the vitelline membrane, and to account for the ellipsoidal tissue shape in simulations is discussed in D.2. The blastoderm is assumed to surround a compressible fluid representing the yolk (cf. SECTION 2.3) and is under tension, which is why the equilibrium shape of the mechanically homogeneous blastoderm is a sphere. The work function of the tissue therefore reads

$$W = \sum_{\alpha \in \mathcal{C}} \left(\frac{K_\alpha^{2D}}{2} (A_\alpha - A_\alpha^0)^2 + \Lambda_\alpha \frac{P_\alpha}{2} \right) + \frac{K_y}{2} (V_y^0 - V_y)^2, \tag{4.1}$$

where the sum is over all cells α with apical area A_α and perimeter P_α, preferred area A_α^0, area elasticity K_α^{2D} and apical line tension Λ_α. The yolk has a volume V_y and behaves elastically with bulk elasticity K_y around its preferred volume V_y^0. Note that we assume that a bond between two cells experiences the mean line tensions generated by these cells.

The epithelium is now taken to consist of two different cell types with distinct mechanical properties: mesodermal and non-mesodermal cells. The mechanical description of the epithelium includes a total of eight free non-normalised parameters, which are given in Table 4.1: two parameters for the constraints imposed by the weakly compressible yolk, one parameter for the apical line tension inside each cell type, and two parameters for the area elasticity for each cell type. Normalisation of the parameters, i.e. making them non-dimensional, reduces the number of free independent parameters to six.

After defining the system we use 3D Vertex Model simulations to study how the initially homogeneous and spherical tissue deforms due to an increase in tension inside the mesoderm. We therefore start from a tissue shown in FIG. 4.6 and study the response of the overall tissue shape to an increase in line tension inside this stripe. We introduce the quantity $\delta\Lambda$ to characterise the increase in line tension in the mesoderm, that is $\Lambda_M = \Lambda + \delta\Lambda$.

FIG. 4.7 shows the resulting tissue shapes for varying line tension Λ outside the mesoderm and the relative increase in line tension inside the stripe $\delta\Lambda/\Lambda$. By these simulations we demonstrate that the sagittal contraction mechanism with a twofold increase in line tension

description	**parameter**	**normalisation**
volume yolk	V_y^0	$V_y^0/(l^0)^3 = 1$
bulk modulus yolk	K_y	$K_y/((l^0)^2 K^{2D})$
preferred cell area	A^0	$A^0/(l^0)^2$
apical area elasticity	K^{2D}	$K^{2D}/K^{2D} = 1$
apical line tension	Λ	$\Lambda/(K_{2D}(l^0)^2)$
preferred cell area (mesoderm)	A_M^0	$A_M^0/(l^0)^2$
apical area elasticity (mesoderm)	K_M^{2D}	K_M^{2D}/K^{2D}
apical line tension (mesoderm)	Λ_M	$\Lambda_M/(K^{2D}(l^0)^2)$

Table 4.1: List of mechanical parameters and their normalisation, for furrow formation in the Apical 3D Vertex Model. Two parameters describe external forces from the compressible yolk, and three parameters each describe the mechanical properties of cells inside and outside the mesoderm.

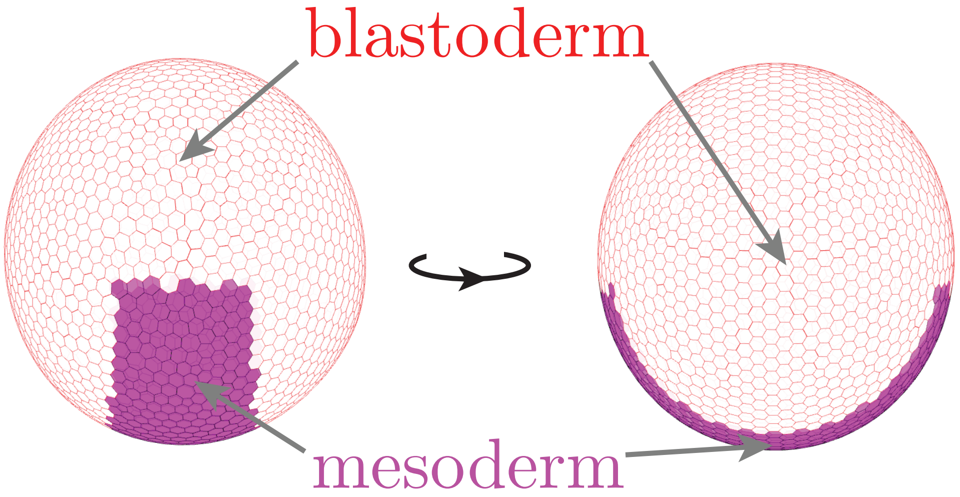

Figure 4.6: An equilibrated spherical blastula in Apical 3D Vertex Model simulations, consisting of 2000 mechanically homogeneous cells with the distinct stripe of the pre-mesodermal cells shown in purple.

inside the mesoderm is sufficient for the formation of a significant furrow even, if the rest if the tissue is under tension. Note, that this folding does not rely on torques being created specifically inside the cells, which could be achieved through differences in apical and basal tensions as we showed in Section 2.2.2. The furrow forms rather due to the shape anisotropy of the contracting stripe, the curvature of the blastula and the resistance of the surrounding tissue to in-plane deformations.

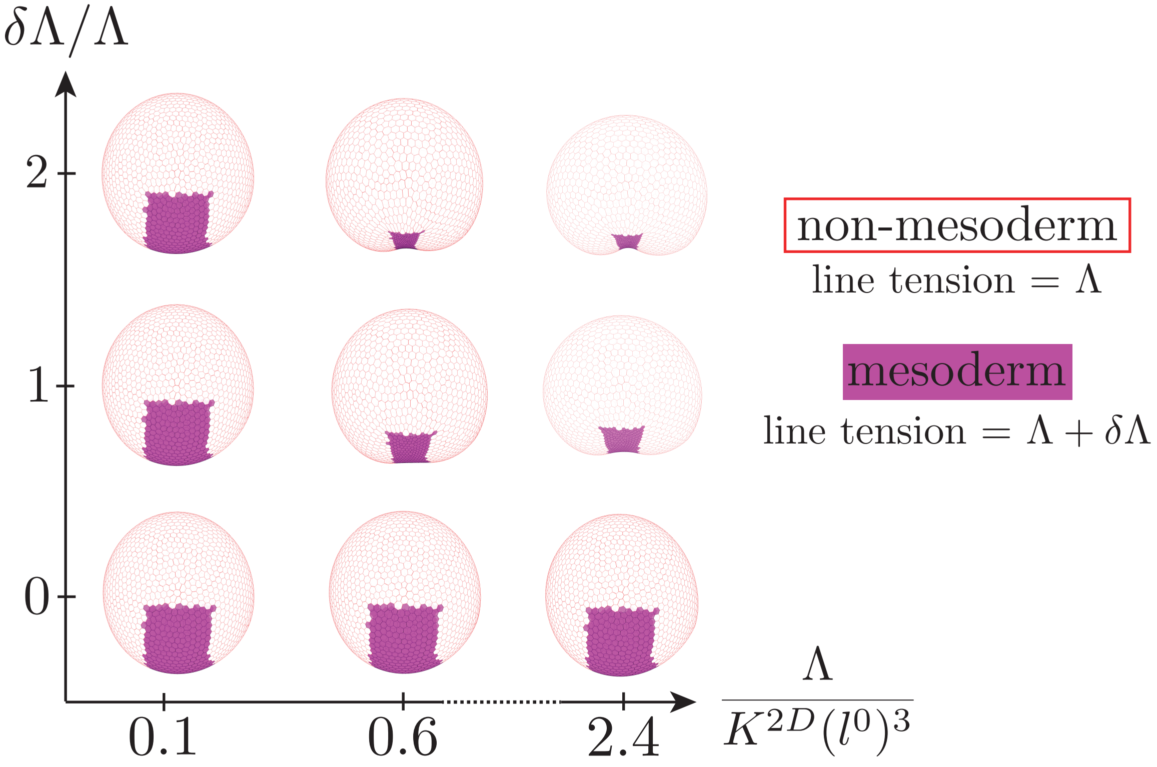
$\delta\Lambda/\Lambda$
2
1
0
0.1
0.6
2.4
$\frac{\Lambda}{K^{2D}(l^0)^3}$
non-mesoderm
line tension $= \Lambda$
mesoderm
line tension $= \Lambda + \delta\Lambda$

Figure 4.7: Simulations of a spherical blastula consisting of 2000 cells with a ventral stripe subjected to an increased contractility. Λ denotes the line tension generated outside the mesoderm and $\delta\Lambda/\Lambda$ denotes the relative difference in active tension between mesodermal and non-mesodermal cells. The equilibrium solutions show qualitatively that the proposed mechanism of sagittal contraction can account for the initiation of furrow formation. Also, the final results show a strong dependency of the final shape on the generated line tensions.

4.2.2 A continuum model for sagittal contraction

Deformations of a sphere in the regime of low tension perturbations

In the previous section we showed in Apical 3D Vertex Model simulations that an increase in line tension in a stripe of cells representing the mesoderm leads to the formation of a significant furrow. In this section we apply the continuous theory introduced in Chapter 2 to a spherical tissue surrounding a compressible fluid, and show analytically how an increase in tension in a stripe of the tissue induces the formation of a furrow.

In Section 2.2.5 we demonstrated that an epithelium in the Apical 3D Vertex Model can be effectively described as a thin elastic plate, with zero bending modulus and bulk and shear moduli that depend on the cellular mechanical parameters. The behaviour of a tissue made of mechanically homogeneous cells in a spherical tissue surrounding a compressible fluid was analysed in Section 2.3. We now additionally include the effect of the contracting mesoderm by increasing the active tension inside a stripe of the tissue, and study the resulting deformation of the epithelial shape.

The local deformations of the tissue on the sphere away from the initial homogeneous state are captured in the strain tensor u_{ij}, while the corresponding stress tensor σ_{ij} describes the stresses induced by the strain. We furthermore introduce an active isotropic field of stress ζ generated locally inside the tissue, which accounts for both the stress on the surface at zero deformation and the perturbation of the stress which leads to deformations. In the case of weak deformations, the relationship between stress and strain is given by the following generalisation of Hooke's Law:

$$\sigma_{ij} = K u_{ll} \delta_{ij} + 2\mu \tilde{u}_{ij} + \zeta \delta_{ij}, \tag{4.2}$$

where u_{ll} and $\tilde{u}_{ij}$ are respectively the trace and the traceless part of the strain tensor u, δ_{ij} is the Kronecker symbol, ζ represents an isotropic active tension, and K and μ are the bulk and shear moduli, respectively.

In the following we parameterise the sphere with the two angles $(\theta, \phi) \in [0, 2\pi] \times [0, \pi]$, where the transformation to the Euclidean space is given by:

$$x = R \cos\theta \sin\phi \tag{4.3}$$

$$y = R \sin\theta \sin\phi \tag{4.4}$$

$$z = R \cos\theta. \tag{4.5}$$

Small deformations away from the sphere can be described by making the radius R a

function of the angles $R(\theta,\phi) = R_0 + \delta R(\theta,\phi)$. In this parametrisation the active isotropic tensions on the sphere are described by $\zeta(\theta,\phi) = \zeta_0 + \delta\zeta(\theta,\phi)$, where ζ_0 is the initial homogeneous tension and $\delta\zeta(\theta,\phi)$ represents an inhomogeneous perturbation. Now we will analytically obtain the deformations of the tissue away from the spherical shape that result from small relative perturbations in the tension $\delta\zeta(\theta,\phi)/\zeta_0 \ll 1$.
For this purpose it is convenient to represent the perturbation $\delta\zeta(\theta,\phi)$ in the basis of spherical harmonics. Any continuous scalar field $f(\theta,\phi)$ on the sphere can be decomposed into spherical harmonics by:

$$f(\theta,\phi) = \sum_{n=0}^{\infty}\sum_{m=-n}^{n} f_{nm} Y_{nm}(\theta,\phi) \tag{4.6}$$

where f_{nm} are the coefficients of the decomposition of the function $f(\theta,\phi)$ in the basis of spherical harmonics. The respective basis $Y_{nm}(\theta,\phi)$ is defined in Appendix D.1.4.
We show in Appendix D.1.4, how this decomposition can be used in Eq. 4.2 to derive the coefficients of the relative radial deformation $(\delta R/R_0)_{nm}$ away from the equilibrium radius R_0 in the spherical harmonics space in terms of the coefficients of the applied perturbation $(\delta\zeta/\zeta_0)_{nm}$:

$$\boxed{\begin{aligned}
(\delta R/R_0)_{00} &= -\frac{1}{\frac{K}{\zeta_0} + 2\pi\frac{K^y R_0^4}{\zeta_0} - 1}\,(\delta\zeta/\zeta_0)_{00} && \text{(4.7a)}\\
(\delta R/R_0)_{1m} &= 0 && \text{(4.7b)}\\
(\delta R/R_0)_{nm} &= \frac{-2}{\frac{K}{\mu}n(n+1) + 2\frac{K}{\zeta_0} + n(n+1) - 2}\,(\delta\zeta/\zeta_0)_{nm} \quad \text{for } n > 1 && \text{(4.7c)}
\end{aligned}}$$

These expressions reveal the role of the three coarse grained parameters K, μ and ζ_0 in the out-of-plane deformation $\delta R/R_0$ of the spherical tissue resulting from the perturbation of the homogeneous tension. The important normalised mechanical parameters governing the deformation are K/μ and K/ζ_0, and an increase in these parameters leads to a decrease in the deformation for fixed relative perturbations of the in-plane tension. In the limit of dominating 2D bulk modulus of the epithelium $K/\mu \gg 1$, $K/\zeta_0 \gg 1$ the sphere does not deform, whereas the deformation is strongest if the bulk modulus is dominated by the initial tension ζ_0 and the shear modulus μ:

$$\lim_{K/\mu, K/\zeta_0 \to \infty} (\delta R/R_0)_{nm} = 0 \text{ for } n > 1 \tag{4.8}$$

$$\lim_{K/\mu, K/\zeta_0 \to 0} (\delta R/R_0)_{nm} = \frac{-2}{n(n+1)-2} (\delta\zeta/\zeta_0)_{nm} \text{ for } n > 1 \tag{4.9}$$

Note that the influence of the ratio of bulk and shear modulus K/μ increases for higher modes $n \gg 1$ since then the prefactor $n(n+1)$ dominates the strength of the deformation.

Numerical solution of furrow formation in the linear theory

The previous calculations allow to obtain the resulting deformation of a tissue for given small perturbations in tension $\delta\zeta/\zeta_0$. To represent the sagittal contraction mechanism, the blastula is now assumed to be under constant tension ζ_0 everywhere other than in the mesoderm where it is set to $\zeta_0 + \delta\zeta$ for constant $\delta\zeta$. Let $\chi^{\mathbb{M}}(\theta, \phi)$ be the characteristic function of the mesoderm, which is one in the region of the mesoderm and zero otherwise and thereby completely describes the position of the mesoderm. If the tension is only increased in the mesoderm, the global tension at the onset of ventral furrow formation can be written:

$$\zeta(\theta, \phi) = \zeta_0 + \delta\zeta\chi^{\mathbb{M}}(\theta, \phi). \tag{4.10}$$

We define the mesoderm to have a shape that covers ~20% of the circle in the dorsal-ventral mid section and ~41% of the circle in the sagittal midsection. The resulting perturbation in tension is shown in Fig. 4.8. By defining the shape of the mesoderm, the bulk and shear moduli (μ and K) and the tension ζ_0 of the tissue, the deformations for small tension perturbations can be obtained through the expressions given above. First the tension perturbations $\delta\zeta\chi^{\mathbb{M}}(\theta, \phi)$ have to be represented in the space of spherical harmonics, then the corresponding spherical coefficients of the radial deformations $\delta R/R_0$ are obtained through Eqs. 4.7a-4.7c, and finally the deformations are transformed back and plotted in Euclidean space.

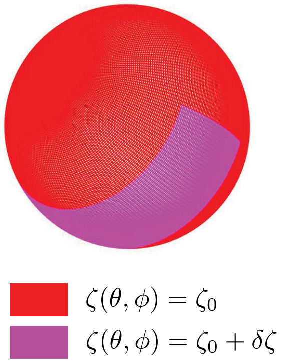
🟥 $\zeta(\theta, \phi) = \zeta_0$
🟪 $\zeta(\theta, \phi) = \zeta_0 + \delta\zeta$

Figure 4.8: Initial tension distribution on surface.

The resulting deformations as a function of the tension increase $\delta\zeta/\zeta_0$ are shown for varying ratios of bulk and shear moduli in Fig. 4.9. The results show consistent with the earlier simulations, that also in the continuum theory an increase in tension inside a stripe of the tissue can trigger the deformation of the sphere and create a furrow along the stripe of increased tension. The extent of furrowing depends on the increase in mesodermal tension, but also on the relative strength of the shear modulus compared to the bulk modulus. Note however, that the results obtained from the continuous calculations are valid only for small tension perturbations $\delta\zeta/\zeta_0$, i.e. in the linear regime, and for larger tensions higher order effects would need to be taken into account. Furthermore, the representation of the perturbation function into spherical harmonics has been done to the 40th degree and on a discrete mesh, which is why the shown results necessarily include small numerical errors.

A comparison of Figs. 4.9 to the equilibrium configurations obtained for the equivalent setup in the Apical 3D Vertex Model, shown in Fig. 4.7, show that both theoretical approaches predict the formation of a significant furrow arising only from an increase of tension inside a stripe of the tissue. These findings suggest that the sagittal contraction mechanism can indeed play an important role in the formation of the ventral furrow in the early gastrulation of *Drosophila*.

The analytical approach introduced in this chapter helped to identify the crucial coarse grained mechanical parameters that govern the strength of the deformation arising from an increase in tension inside a stripe of the tissue. The relevant normalised parameters are namely the ratios between the bulk modulus and the shear modulus K/μ and the ratio between the bulk modulus and the generated tension K/ζ_0. Our results suggest that the furrow formation is strongest, when both these normalised parameters are small and the cells' bulk modulus is dominated by their shear modulus and the tensions generated inside the tissue.

It remains to be determined how well the results of the continuous and the discrete model can be mapped onto each other, which will be the subject of the following section.

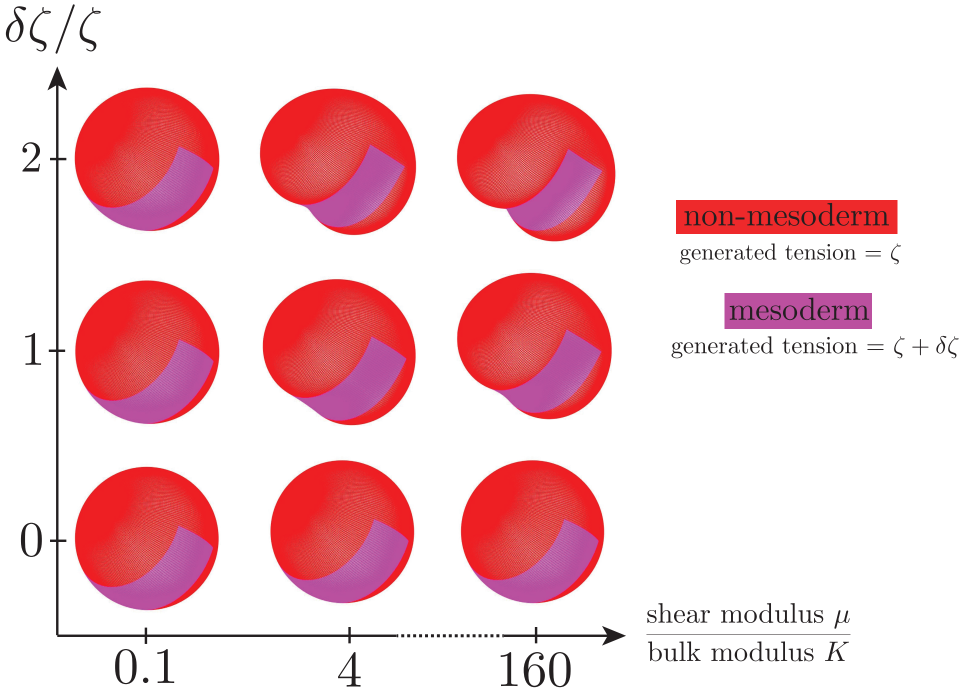
$\delta\zeta/\zeta$
2
1
0
0.1
4
160
$\frac{\text{shear modulus } \mu}{\text{bulk modulus } K}$
non-mesoderm
generated tension = ζ
mesoderm
generated tension = $\zeta + \delta\zeta$

Figure 4.9: Analytical predictions for the deformations of the sphere for varying relative increase in tension in the stripe (shown in FIG. 4.8), and varying bulk and shear modulus.

4.2.3 Bridging the scales between the continuous and the discrete model

In Section 2.2.5 we derived how the coarse grained tension and elastic moduli of an epithelium represented in the Apical 3D Vertex Model depend on the stresses generated inside the cells. The effective active tension ζ, shear modulus μ and bulk modulus K, were given as a function the local cell density ρ by:

$$\zeta = K^{2D}(\frac{1}{\rho} - A^0) + \frac{\sqrt{3}}{2}\sqrt{\rho}\Lambda \tag{4.11}$$

$$\mu = \frac{3^{1/4}}{2^{3/2}}\sqrt{\rho}\Lambda \tag{4.12}$$

$$K = K^{2D}/\rho - \frac{3^{1/4}}{2^{3/2}}\sqrt{\rho}\Lambda, \tag{4.13}$$

where K^{2D} characterises the elasticity of the cells around their preferred area A_0, and Λ the line tensions acting along the apical junctions. Now we proceed to compare resulting deformations due to small perturbations in the mesodermal tension in Apical 3D Vertex Model simulations (4.2.1) and in the corresponding continuum model (4.2.2). These comparisons provide another strong check for the consistency of the discrete and the continuum model, as well as for the correctness of the presented analytical calculations and the 3D Vertex Model simulations.

Comparison of simulations and analytical predictions mode by mode

To perform a mode-wise comparison of the deformations in simulations to the analytical predictions given in Eqs. 4.7a-4.7c, we randomly initiated homogeneous spherical tissues in the Apical 3D Vertex Model, as described in B.1.3, and relaxed them to a regular cell packing on a sphere. Then we perturbed the homogeneous tension ζ_0 by a single spherical harmonic $\delta\zeta(\theta,\phi) = \delta\zeta_p Y_{nm}(\theta,\phi)$ with $\delta\zeta_p/\zeta_0 \ll 1$, by locally changing the line tension of the bonds depending on their position. After relaxing the tissue shape to the nearest equilibrium, we studied the resulting deformations in simulations by decomposing the relaxed shape in spherical harmonics. Figure 4.10a shows an example of the spatial perturbation of the tension by the spherical harmonic $(3,2)$, i.e. $\delta\zeta(\theta,\phi) = 0.002Y_{3,2}(\theta,\phi)\zeta_0$, and the plot of the resulting deformation of the equilibrium shape $\delta R(\theta,\phi)$ in Apical 3D Vertex Model simulations is given in Fig. 4.10.

We obtained the response of the equilibrium shape in Apical 3D Vertex Model simulations resulting from the spherical harmonic perturbations of tensions $\delta\zeta_p Y_{nm}$ $(n \leq 4)$ for

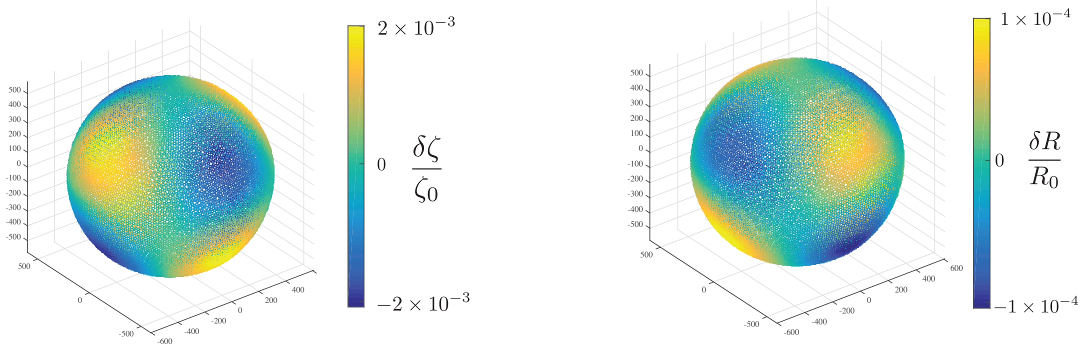

(a) Perturbation of bond tensions in 3D Vertex Model simulations by the spherical harmonic $(3,2)$, such that $\delta\zeta = 0.002 \times Y_{3,2}\zeta_0$

(b) Radial displacement of vertices away from the equilibrium sphere in simulations resulting from tension perturbation shown on the left

Figure 4.10: Spherical harmonic perturbation $\delta\zeta/\zeta_0$ of the tension (left) and the resulting equilibrium deformations in Apical 3D Vertex Model simulations with 6,000 cells (right). Perturbations in pure spherical harmonics allow for a mode-wise comparison of the simulations and the analytical theory, by which we demonstrate the consistency of the two frameworks. The detailed parameters of the shown simulation are given in D.1.6.

several tissues with different cell numbers and mechanical parameters. By relating the coarse grained mechanical parameters to the microscopic parameters in 3D Vertex Model simulations, and using the relations 4.7a-4.7c we then obtained the analytically predicted deformation for the respective parameter sets and compared them to the actual deformations in simulations. Two mode-wise comparisons of simulations and linear theory are shown in Appendix D.1.6.

We found that the relative difference of the deformations in 3D Vertex Model simulations and the analytical prediction was consequently less than 8% for all studied parameter regimes and modes, and in average close to 3%. These observed differences might be due to a variety of reasons. First, the analytical calculations hold true only in the limit of infinitely small cells, which is not the case in simulations and leads to discretisation errors. Secondly, the equilibrated mechanically homogeneous spherical tissues are not completely homogeneous, but have a number of topological defects where the assumption of a hexagonal packing breaks down. Therefore the local coarse grained mechanical properties K, μ and ζ_0, which are based on the assumption of the hexagonal packing, inhibit spatial heterogeneities that are not taken into account in the analytical calculations. The same holds for the perturbation of the line tensions, which lead to small spatial perturbations of the shear modulus μ. Finally, in simulations we also measure higher order effects on the equilibrium shape, which are not taken into account in the analytical calculations, which only hold true in the linear regime of infinitesimal small perturbations.

Taking into account these inherent limitations of the comparison, the 3% difference between analytical results and the complex simulations in the Apical 3D Vertex Model for different tissue sizes, mechanical parameters and all studied modes indicates a very good agreement between the analytical calculations and simulations. To account also for the deformations caused by an increase in tension inside a stripe of the mesoderm, like in the sagittal contraction mechanism, we compare the analytical and simulation results for this setup in Appendix D.2. There we show that also in this case the observed deformations in Apical 3D Vertex Model simulations are close to the analytical predictions. These comparisons once more confirm the good agreement between the two frameworks.

4.3 Outlook

After showing that the proposed minimal mechanism of sagittal contraction can qualitatively account for the formation of a furrow, it will be very interesting to analyse if the proposed mechanism can also account for the details of the process of furrow formation observed in experiments. To that end the cellular flows and deformations in both simulations and experiments can be compared, in order to identify a parameter regime where experiments and simulations match. To achieve this correspondence it might be required to account for constraints imposed by the vitelline membrane. Details of how the vitelline membrane can be included in 3D Vertex Model simulations are given in Appendix D.2.

As stated above, the sagittal contraction mechanism constitutes a minimal model of ventral furrow formation and while it can explain the onset of furrow formation even in the acellular embryo it might not be sufficient to explain the whole furrowing in the wildtype embryos, because other important contributions have been neglected. If for instance, cells are able to control their volume, an increase in apical tension in the mesoderm would also lead to the generation of a torque inside the mesodermal cells favouring the formation of a furrow. Also, it was observed in experiments that the basal surfaces of the mesodermal cells are depleted of Myosin II during the first steps of ventral furrow formation, which could generate an additional talk enhancing the formation of a furrow. Using 3D Vertex Model simulations, it will be interesting to study how the combination of both effects, i.e. the contraction in the sagittal section and the generated torque in the ventral direction, will influence the formation of the furrow. Active torques generated inside the tissue could also be included in the continuous theory of epithelial mechanics discussed in this chapter. This extension could allow the application of the continuous model to other phenomena of epithelial deformation such as fold formation, which are not purely relying on apical force generation, and again the analytical predictions could be compared to simulations of full epithelia in the 3D Vertex Model.

Another promising branch of future research includes experiments where the *Drosophila* embryo is modified, to test predictions derived from the sagittal contraction model. In one potential experiment one could try to flatten the mesoderm along the sagittal section (by squeezing the embryo), which should inhibit the formation of the furrow if the sagittal contraction mechanism is a necessary driver of furrow formation. In another possible experimental setup the mesoderm is locally stitched to the vitelline membrane before the onset of gastrulation, the tissue shapes can be compared to simulations in the 3D Vertex Model where also the position of a set of cells has been fixed. The sagittal contraction model would suggest that this leads to a significant reduction of furrow formation.

4.4 Summary

In this chapter we presented the sagittal contraction mechanism, and suggested that it plays an important role in the formation the ventral furrow in the gastrulation of *Drosophila*. The underlying idea of the mechanism is the following: a stripe of cells along the sagittal section of the blastoderm, namely the mesoderm, experiences an increased contractility along their apical surfaces and this contraction in the sagittal section leads to the formation of a furrow in the ventral section of the embryo.

Using Apical 3D Vertex Model simulations we showed that a 2-fold increase of line tension in the mesoderm can account for the formation of a significant furrow, suggesting that our model represents a possible minimal mechanism for the initiation of ventral furrow formation. Using a continuum model where the epithelium is represented by a thin shell on a sphere with elastic bulk and shear moduli, we showed analytically that an increase in active tension inside a stripe along the sphere can lead to the formation of a furrow along the stripe. The strength of the deformation is mainly determined by the ratio between the tissue's shear and bulk modulus: the larger this ratio becomes, the stronger the tissue is deformed and the deeper the resulting furrow. A comparison of the two approaches showed quantitatively that both models predict the same deformation for a given perturbation in tension, underlining the consistency of the two frameworks. Whereas the continuum framework helped to identify the key mechanical parameter, the 3D Vertex Model framework was used to identify equilibrium tissue configurations far from the regime of linear tension perturbations. Furthermore, the 3D Vertex Model can be used to simulate more complex tissue geometries and for instance to take into account constraints imposed by the vitelline membrane, or the influence of more than two cell types.

The discussed mechanism of sagittal contraction purely relies on tensions generated along the apical surfaces of the cells, it also leads to furrow formation if the blastoderm is under tension and it leads to the straightening of the mesoderm in the sagittal section. Thereby it can account for several recent experimental findings that were not considered in previous models, and provides new perspectives on the mechanical drivers of ventral furrow formation.

The combination of the Apical 3D Vertex Model and the emerging continuum theory provides a set of tools, which can be used in the future to gain an even better understanding of the details of gastrulation process. Possible ways to pursue this aim have been presented in the Outlook section 4.3 of this chapter.

CHAPTER 5

Conclusions

5.1 Two complementary approaches to 3D epithelial mechanics

In present thesis we introduced and combined two approaches to study the interplay between the mechanical stresses generated inside cells and the complex 3D shape of simple epithelia: a 3D Vertex Model and a continuum model for epithelial mechanics. Both models have different complementary advantages as we discussed in Section 1.5.3, and in this thesis we showed how to make use of them to research the shapes, properties and morphogenetic deformations of simple epithelia.

The 3D Vertex Model describes the epithelial shape through networks of apical and basal vertices, which in turn define discrete bonds, surfaces and cells. In the continuum model the epithelium is described as a thin sheet and represented by the position of the tissue mid-plane as a 2D manifold in 3D space. Effective work functions have been introduced in both models representing the underlying mechanical assumptions. In the 3D Vertex Model the mechanical work function depends on the position of vertices, the length of bonds, the area of surfaces and the volume of cells. The respective work contributions result from a spring like attachment of the vertices (representing coupling to the basement membrane), line and surface tensions (representing the contractility of the acting cortex) and volume pressure (representing cell volume control). In the continuum model the work function depends on the in-plane deformation of the tissue through a bulk and shear modulus, the distance to an underlying material through a spring-like potential and the curvature of the mid-plane through a preferred curvature and bending modulus. Forces in the 3D Vertex Model are derived from differentiating the mechanical work function with respect to vertex positions, whereas in the continuum description force densities are given by the functional derivative of the work function with respect to the local tissue shape.

Then we combined the two approaches through a mapping between their mechanical parameters, hence showing how coarse grained mechanical parameters of epithelia in the continuum model depend on the locally generated active stresses inside the cells in the 3D Vertex Model. Assuming a hexagonal packing of cells we derived the corresponding mechanical parameters in the continuum theory, namely the effective tension, shear modulus, bulk modulus, bending modulus and preferred curvature, as functions of the cell density, the stresses generated inside the cells and the external forces. A numerical study using the 3D Vertex Model showed that the obtained coarse grained parameters are valid approximations of the elastic properties, both in ordered and in disordered tissues.

In the remainder of the thesis we applied the two methods to derive properties of flat and spherical epithelia, and to get a deeper understanding of two processes in the morphogenesis of the model system *Drosophila melanogaster*: cyst formation in the wing imaginal disc and ventral furrow formation at the onset of gastrulation.

5.2 Applications

5.2.1 Shapes and stability of simple epithelia

Starting from the 3D Vertex Model we first analysed how the aspect ratio of cells in flat epithelia depends on the distribution of tensions generated inside the cells and on the external forces. Thereby we showed how cells can control their shapes by adapting their relative lateral surface tensions compared to the tensions generated apically and basally. Then we used the continuum model to study the influence of external compression on the stability of flat epithelia. We found that a flat epithelium under compression can lose its stability in two ways: in 1) cells obtain a negative bending modulus which gives rise to short wave length undulations, whereas in 2) the bending modulus remains positive and the tissue undergoes buckling on long wave lengths to decrease its total surface area. The analytical predictions were verified quantitatively in 3D Vertex Model simulations, indicating the consistency of the two approaches in the studied limits.

Then we used both approaches to derive equilibrium shapes of spherical epithelia surrounding a compressible fluid. We hence showed how the radius of the sphere and the height of the cells depend on the total tension generated inside the epithelium, but also on the difference between the apical and basal tensions. A comparison of the analytical predictions from the continuum theory and 3D Vertex Model simulations again yielded a very good agreement between the two methods.

5.2.2 Cyst formation

We then proceeded to apply the 3D Vertex Model and the continuum theory to study the formation of epithelial cysts in the wing imaginal disc in a collaboration with Christina Bielmeier and Anne Classen. We found that cysts, clusters of epithelial cells that bulge out from the epithelium, are a general response to aberrant expression of cell fate specifying transcription factors in patches of cells. By combining experiments and physical modelling, we showed that cyst formation is mechanically driven by an increased contractility around misspecified clones. In the framework of the continuum model, cyst formation can be understood as the buckling of a clamped, circular piece of tissue under compression following the law of Laplace. We hence showed that the formation of cysts should be restricted to an intermediate range of clone sizes, which was confirmed through quantifications of clone shapes in experiments. Then we went beyond the linear stability analysis by using 3D Vertex Model simulations and demonstrated that a three-fold increase in lateral surface tension and apical line tension around the clones accounts also quantitatively for the cyst shapes observed in experiments. We then verified that the regions of cyst formation in simulations concur well with buckling regions in the continuum theory for the corresponding set of coarse grained parameters.

Simulations showed that the boundary effect leads to a strong apical constriction of small clones, which was often observed to precede cellular extrusion. The consequent hypothesis that small clones are extruded from the tissue was confirmed by a statistical analysis of clone size distributions in experiments. Therefore we suggested that the discovered boundary mechanism could act as a potential error correction mechanism to maintain epithelial integrity, by mechanically extruding misspecified cells or clones from the tissue.

5.2.3 Ventral furrow formation by a sagittal contraction mechanism

We finally studied the ventral furrow formation initiating the gastrulation of *Drosophila* in a collaboration with Matteo Rauzi. During ventral furrow formation a region of the blastoderm, the mesoderm, undergoes apical constriction and subsequently forms a furrow and invaginates into the blastula. As a new minimal model for ventral furrow formation we suggest the sagittal contraction mechanism, where ventral furrow formation is driven by the constriction of the mesoderm along its curved sagittal cross section. This mechanism does not rely on the generation of local torques in the mesoderm and leads to a straightening of the mesoderm along the sagittal cross section, which is both in good agreement with recent experimental observations. By 3D Vertex Model simulations we showed that the proposed mechanism can indeed trigger the formation of a significant ventral furrow along the constricting mesoderm on a spherical blastula. Using the continuum theory we then demonstrated that the strength of the deformation of the sphere for a small increase in tension inside the mesoderm depends mainly on the ratio between the tissue's bulk and shear modulus. This prediction was quantitatively verified by numerical experiments in the 3D Vertex Model, and the comparison to the analytical predictions.

We therefore showed that the sagittal contraction mechanism constitutes a minimal model to drive the formation of a ventral furrow, and suggested that this previously neglected mechanism plays an important role as a driver of the process. Our findings can help elucidate why ventral furrow formation even occurs even if cellularisation has been inhibited, and explain the flattening of the mesoderm in the course of the process along the sagittal cross section. Finally we discussed possible directions of future research into the mechanics of the gastrulation process in *Drosophila* that involve modelling, experiments and the combination of both.

5.3 Outlook

In this thesis we developed a framework to study the mechanics of simple epithelia that combines the computational advantages of a 3D Vertex Model with the generic features and analytical approachability of a continuum theory. In future research, these models can be further analysed and adapted, their mechanical assumptions can be tested in more detail, and due to their generality they can be applied to shed light on the relation between mechanics and shape of simple epithelia.

Starting from the mechanical assumptions of the 3D Vertex Model, we derived expressions for the shape of cells in flat and spherical epithelia and for the coarse grained mechanical tissue properties, as a function of the stresses generated on the level of cells and external forces. Experimental measurements of the distribution of active stresses inside cells could be used to make predictions about the cell shapes and the coarse grained mechanical properties of the tissue. These predictions could then be compared to the actual cell shapes, and to the measurable coarse grained mechanical tissue parameters (obtained for instance in [26]). This way experiments can help to verify, or correct, the mechanical assumptions made in the construction of the models.

Importantly, in addition to the already discussed phenomena, the general frameworks for epithelial mechanics introduced in this thesis can be applied to a variety of fascinating phenomena in morphogenesis that involve the deformation of simple epithelia. A glimpse at the development of wing imaginal disc of *Drosophila* reveals that even in this intensely studied system, the mechanical drivers of many morphogenetic events are not well understood. Newly developed (live) imaging techniques and experimental methods, together with the mechanical modelling techniques discussed in this thesis can help to shed light on these phenomena. In a collaboration with Liyuan Sui and Christian Dahmann (TU Dresden) we combine 3D Vertex Model simulations with biological experiments to elucidate the role of novel mechanisms in the formation of folds between the hinge and the pouch region. In this research we confirm once more the importance of basally and laterally generated active tensions inside epithelial cells, which play an important role in the 3D Vertex Model and have rarely been discusses in previous studies. In another collaboration with Maria del Carmen Diaz de la Loza and Barry Thompson (The Francis Crick Institute) we apply the introduced frameworks to study the forces that drive the expansion of the imaginal wing disc shortly after pouch eversion.

At first sight, understanding the development of a fruit fly's wing might not seem relevant for medical research. However, we suggest that our fundamental research helps to reveal general relationships between the forces generated inside and applied onto epithelial cells and the 3D shape of simple epithelia, which can be applied to elucidate the origins of other developmental and disease-related epithelial deformations that have not be addressed previously.

For instance, the research on cyst formation in *Drosophila* presented in this thesis, brought to light a potential mechanism of how epithelia can mechanically remove misspecified (and cancerous) cells and hence maintain their genetical integrity. Future studies could focus on the potential role of this stress-based repair mechanism in adult tissues. Furthermore, cysts play an important role in the etiology of many human diseases, such as cancer where they have been proposed to play a role in metastasis [59, 60, 61, 62, 63, 111, 112], polycystic kidney disease [113] and polycystic ovary syndrome [114]. The mechanical drivers of cyst formation in these contexts could be very similar to the formation of cysts in the wing imaginal discs. Further studies of diseases that give rise to cyst-like-structures, could build on our research of cyst formation in flies, to gain important insights into their possible mechanical origins and might finally help to improve the diagnosis and treatment.

In a collaboration with Hendrik Messal and Axel Behrens (The Francis Crick Institute) we explored in a similar direction of research by studying the initial steps of pancreatic cancer in mice. We combine 3D Vertex Model simulations with in-vitro and in-vivo experiments to estimate the mechanical changes that occur in cancerous cells, and to analyse their influence on the cylindrical shape of the surrounding pancreatic epithelium.

The field of epithelial mechanics is a very versatile ground of research with many open questions and interesting applications. Through this thesis we hope to contribute to it through a combination of novel computational and analytical modelling approaches, and we hope that it will find further applications to shed more light on the complex mechanics of simple epithelia in 3D.

Appendices

APPENDIX A

Introduction

A.1 List of vertex models for epithelial mechanics

Table A.1 contains a list of previously published studies that used vertex models to describe epithelial mechanics, sorted by the year of publication. The second column denotes the type of the vertex models and if vertex positions in the models are in 2D or in 3D. Apical vertex models were discussed in more detail in Section 1.5.1, whereas lateral vertex models were introduced in 4.1.2. The abbreviations IWD, PWD and ILD represent the *imaginal wing disc*, *imaginal pupal disc* and *imaginal leg disc* of the *Drosophila* embryo, respectively.

Study	**Model type**	**Phenomenon**	**Organism**
Farhadifar et al. [35]	2D apical	cell packing	*Drosophila* IWD
Nagai et al. [36]	2D apical	wound healing	*Xenopus*
Landsberg et al. [37]	2D apical	compartment boundaries	*Drosophila* IWD
Aigouy et al. [38]	2D apical	planar cell polarity	*Drosophila* IWD
Staple et al. [39]	2D apical	cell packing	*Drosophila* IWD
Wartlick et al. [40]	2D apical	tissue size control	*Drosophila* IWD
Trichas et al. [41]	2D apical	cell migration, rosettes	Mouse
Aegerter-Wilmsen et al. [42]	2D apical	tissue size control	*Drosophila* IWD
Salbreux et al. [43]	2D apical	retina patterning	zebrafish
Aliee et al. [44]	2D apical	compartment boundaries	*Drosophila* IWD
Osterfield et al. [45]	3D apical	appendage formation	*Drosophila* egg
Murisic et al. [46]	3D apical	tissue buckling	None
Monier et al. [47]	3D apical	fold formation	*Drosophila* ILD
Odell et al. [100]	2D lateral	gastrulation, tube formation	*Drosophila*
Munoz et al. [101]	2D lateral	gastrulation	*Drosophila*
Brezavscek et al. [110]	2D lateral	gastrulation	*Drosophila*
Rauzi et al. [109]	2D lateral	gastrulation	*Drosophila*

Table A.1: List of previously published vertex models for epithelial mechanics.

APPENDIX B

The 3D Vertex Model

B.1 The implementation

B.1.1 Obtaining the cell volume and surface areas from the vertex positions

In the 3D Vertex Model a cell's geometry is defined by a set of apical, basal and lateral triangles, that by construction completely define the cell's volume. A cell α which is enclosed by M_α apical and basal vertices, has an apical and a basal surface consisting of M_α triangles each. The apical and the basal surface areas A^a_α and A^b_α are the sum of the areas of the corresponding triangles. The area of a triangle Δ that is given by the by the convex hull of its corner points $\mathbf{X}_{\Delta_1}, \mathbf{X}_{\Delta_1}, \mathbf{X}_{\Delta_1}$, reads:

$$A_\Delta = \frac{1}{2}||(\mathbf{X}_{\Delta_1} - \mathbf{X}_{\Delta_2}) \times (\mathbf{X}_{\Delta_1} - \mathbf{X}_{\Delta_3})||, \tag{B.1}$$

with '×' denoting the crossproduct of two vectors. Furthermore the cell has M_α lateral surfaces connecting it to its neighbours, each consisting of 4 triangles. The lateral area A_l is the sum of the areas of the $4M_\alpha$ lateral triangles. The apical and basal perimeter, P^a_α and P^b_α respectively, are defined to be the lengths of the apical and the basal circumference. In order to calculate the volume of cell α it is crucial to take into consideration the orientation of each triangle of the surface towards the cell's inside. A triangle $\Delta^\alpha_n = (\mathbf{X}^\alpha_{n,1}, \mathbf{X}^\alpha_{n,2}, \mathbf{X}^\alpha_{n,3})$ is defined to be oriented counterclockwise towards cell α, if an infinitesimal movement along $\mathbf{V}^\alpha_n = \overrightarrow{\mathbf{X}^\alpha_{n,1}\mathbf{X}^\alpha_{n,2}} \times \overrightarrow{\mathbf{X}_{n,1}\mathbf{X}_{n,3}}$ leads into the cell volume, and otherwise it is oriented clockwise. Following this logic we can define an *orientation function* O for each triangle towards the cell α:

$$O(\Delta^\alpha_n) = \begin{cases} 1 & \text{if } \Delta^\alpha_n \text{ is oriented clockwise towards cell } \alpha \\ -1 & \text{else.} \end{cases} \tag{B.2}$$

The outer surface of each cell α is made of $6M_\alpha$ triangles (four for each edge are contributing to the lateral surfaces, and two to the cell's apical and basal basal surface), numbered

$\Delta^\alpha_1, ..., \Delta^\alpha_{6M_\alpha}$. Then the volume of cell α is given by:

$$V_\alpha = \sum_{i=1}^{6M_\alpha} \frac{1}{6} < \overrightarrow{\mathbf{X}^\alpha_{i,1}\mathbf{X}^\alpha_{i,2}} \times \overrightarrow{\mathbf{X}^\alpha_{i,1}\mathbf{X}^\alpha_{i,3}}, \mathbf{X}^\alpha_{i,1} > O(\Delta^\alpha_i) \tag{B.3}$$

where by '$< .,. >$' we denote the scalar product of the Euclidean vector space. Note that

$$V_{\text{Tetra}}(\mathbf{X}_1, \mathbf{X}_2, \mathbf{X}_3) = \frac{1}{6} < \overrightarrow{\mathbf{X}^1\mathbf{X}_2} \times \overrightarrow{\mathbf{X}_1\mathbf{X}_3}, \mathbf{X}_1 > \tag{B.4}$$

is the signed volume of the tetrahedron defined between the triangle $(\mathbf{X}_1, \mathbf{X}_2, \mathbf{X}_3)$ and the origin. The validity of the algorithm can be shown by the application of the theorem of Gauß to the characteristic function of the polyhedron, where the integral over the volume is first replaced by the integral of the normal along the surface, which then can be replaced by the summation over the triangles of the surface. For details of the derivation please refer for instance to [116].

B.1.2 Forces acting on the periodic box

We can give analytical expressions for the tensions exerted on the periodic boundaries by using the basic geometrical constituents of the tissue: lines, triangles and tetrahedrons. Let $\Delta \in \mathcal{T}$ be a triangular surface part of the tissue, given by the convex hull of its corner points $\mathbf{X}_{\Delta_1}, \mathbf{X}_{\Delta_2}, \mathbf{X}_{\Delta_3}$. The normal of triangle Δ is given by the cross product

$$N_\Delta = (\mathbf{X}_{\Delta_1} - \mathbf{X}_{\Delta_2}) \times (\mathbf{X}_{\Delta_1} - \mathbf{X}_{\Delta_3}), \tag{B.5}$$

and the direction of line l by:

$$d_l = \mathbf{X}_{l_1} - \mathbf{X}_{l_2}. \tag{B.6}$$

The tension on line l is denoted by Λ_l, the surface tension on triangle Δ by T_Δ and the volume and pressure of cell α again by V_α and P_α. Then the force exerted on the periodic boundaries reads:

$$F_{L_x} = \frac{\partial W}{\partial L_x} = \frac{1}{L_x} \left(\sum_{\alpha \in \mathcal{T}} P_\alpha V_\alpha + \sum_{\Delta \in \mathcal{T}} T_\Delta \frac{N^2_{\Delta,y} + N^2_{\Delta,z}}{||N_\Delta||} + \sum_{l \in \mathcal{L}} \Lambda_l \frac{d^2_{l,x}}{|d_l|} \right) - T_{ext} L_y \tag{B.7}$$

$$F_{L_y} = \frac{\partial W}{\partial L_y} = \frac{1}{L_y} \left(\sum_{\alpha \in \mathcal{T}} P_\alpha V_\alpha + \sum_{\Delta \in \mathcal{T}} T_\Delta \frac{N^2_{\Delta,x} + N^2_{\Delta,z}}{||N_\Delta||} + \sum_{l \in \mathcal{L}} \Lambda_l \frac{d^2_{l,y}}{|d_l|} \right) - T_{ext} L_x \tag{B.8}$$

The corresponding tensions acting on the periodic box can be derived by dividing the forces by the box size:

$$\zeta_{xx} = -\frac{1}{L_y}\frac{\delta W}{\delta L_x},\ \zeta_{yy} = -\frac{1}{L_x}\frac{\delta W}{\delta L_y}. \tag{B.9}$$

B.1.3 Initial tissue configurations

The study of equilibrium shapes of tissues in simulations requires the creation of initial tissue configurations, which are then relaxed to determine the equilibrium. Here we describe how different types of starting conditions for epithelia in simulations have been created for the use of this thesis. We used three different ways to create initial conditions: in the first one, the apical and basal sides of the tissue are assumed to have a regular hexagonal packing of cells. The apical and basal $x-y-$position of each vertex are identical, and the difference in $z-$positions establishes the initial tissue height. The size of the periodic box has to match the periodicity of the regular hexagonal packing. This regular configuration can then also be used to create irregularly packed tissue by continuously enforcing cell divisions of randomly chosen cells, and then relax the tissue to the next equilibrium. These regular hexagonal packings can also be randomised by performing random cell divisions, let the tissue relax and repeat the process until the desired tissue size is reached. Random initial tissue configurations can also be created by calculating a 2D Voronoi tessellation of randomly distributed points in a periodic box of size $L_x^0 \times L_y^0$. Apical and basal vertices are then again assigned the same $x-$ and $y-$coordinates, but different $z-$coordinates. Tissues that are randomly generated in this way tend to be highly irregular and therefore far from an equilibrium solution. An example of such an initial condition and the relaxed tissue after minimising the work function with respect to vertex position, size of the periodic box and tissue topology are shown in Fig. 2.7. To also account for epithelial tissues with a spherical topology that for instance surround a cavity, we propose and provide two methods to create initial configurations for them. Both methods are based on the positioning of the apical cell centres on the sphere with radius R_a, and then defining the cells by the Voronoi tessellation on the surface of the sphere. The basal vertex positions are the projection of the apical vertex positions onto the sphere with radius R_b. If the apical surface of the tissue is to face the outside, the apical radius has to be chosen bigger than the basal one $R_a > R_b$ and likewise $R_b > R_a$ if the apical cell surfaces are facing the cavity.

Two ways have been used to initially distribute the apical cell centres on the sphere that give rise to a random and a regular initial configuration, which are exemplarily shown in Fig. B.1. In B.1d the points are distributed randomly on the sphere which gave rise to a highly disordered initial tissue. To distribute cell midpoints as regular as possible on the sphere, we implemented an EQ sphere algorithm approach in Matlab, which is based on the method proposed in [117]. In this case the initial topology of the tissue is already close to a hexagonal packing and therefore it is closer to an equilibrium configuration than the random packing. An example of such an initial configuration is shown in Fig. B.1d.

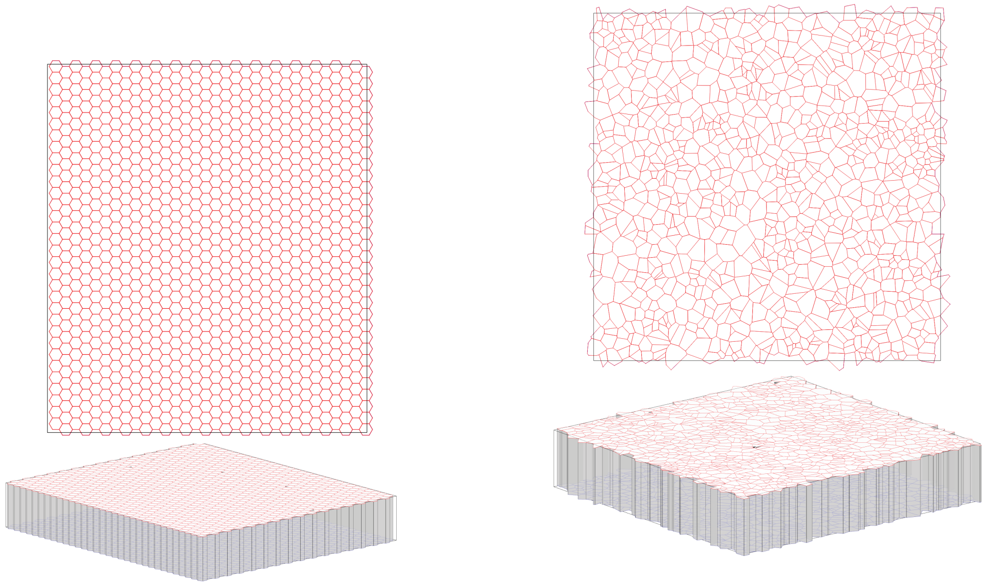

(a) Periodic hexagonal packing, made of 32x32 regular hexagonal tissue

(b) Random tissue configuration of 1000 cells created by a 2D Voronoi tessellation around randomly distributed points.

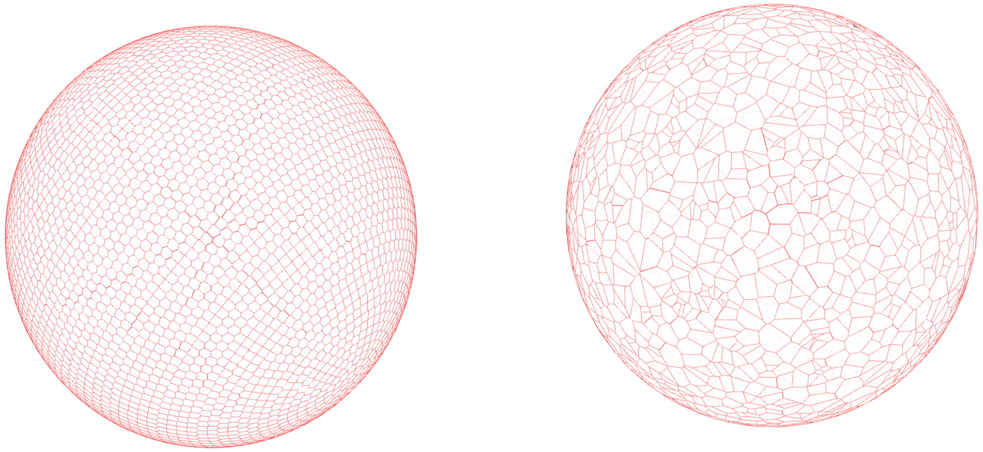

(c) Regular configuration of 5000 cells, generated by using an EQ partition method.

(d) Random tissue configuration of 2000 cells created by a Voronoi tessellation on a sphere around randomly distributed points.

Figure B.1: Creation of initial configurations of ordered and disordered tissues, both for periodic flat and spherical tissues.

B.2 Mechanical Properties

B.2.1 Geometrical quantities of regular hexagonal tissues

The epithelium consists of n_x cells along the x-direction and n_y cells along the y-direction. The apical and basal surfaces of the cells are identical hexagons with height h, and are described by their in-plane extensions l_x and l_y. The tissue has a total volume of $L_x \times L_y \times h$ and the cell density is denoted by $\rho = n_x n_y / L_x L_y$. All cells have identical apical and basal areas A, lateral surface area A_l, equal apical and basal perimeter p and volume V, which in the terms of the parametrisation (l_x, l_y, h) are given by:

$$A = l_x l_y \tag{B.10}$$

$$A_l = 2(l_x + \frac{\sqrt{3}}{2} l_y)h \tag{B.11}$$

$$P = 2(l_x + \frac{\sqrt{3}}{2} l_y) \tag{B.12}$$

$$V = l_x l_y h \tag{B.13}$$

B.2.2 Parametrisation of curved tissues

If a regular hexagonal cell is described by its height h, and its apical and basal radii, R_a and R_b, as shown in Fig. 2.11, the apical, basal and lateral surface areas, apical and basal perimeters and cell volume are given respectively through the following relations:

$$A_a = \frac{3\sqrt{3}}{2} R_a^2 \tag{B.14}$$

$$A_b = \frac{3\sqrt{3}}{2} R_b^2 \tag{B.15}$$

$$A_l = 3\left(R_a + R_b\right)\sqrt{h^2 + \frac{3}{4}(R_a - R_b)^2} \tag{B.16}$$

$$P_a = 6R_a \tag{B.17}$$

$$P_b = 6R_b \tag{B.18}$$

$$V = \frac{\sqrt{3}}{2} h \left(R_a^2 + R_b^2 + R_a R_b\right). \tag{B.19}$$

B.2.3 Mechanical properties of epithelia in the Apical 3D Vertex Model

In A-Model epithelia, introduced in SECTION 2.1.6, cells have zero volume elasticity, no basal and lateral tensions, but experience apical surface elasticity. These tissues are effectively 2D manifolds defined by the positions of the apical vertices, since the work function W^A which was given in Equation 2.26 does not depend on the position of the basal vertices. Each cell α is assumed to have a preferred area A^0_α, and the apical surface tension T_α as a function of the cell area A_α reads:

$$T_\alpha(A_\alpha) = K^{2D}_\alpha (A_\alpha - A^0_\alpha). \tag{B.20}$$

Let Λ_α be the line tension acting on the cell's perimeter P_α; then the total internal work of the tissue can be written:

$$W^A_i = \sum_\alpha \left(\frac{K^{2D}_\alpha}{2} (A_\alpha - A^0_\alpha)^2 + \frac{\Lambda_\alpha}{2} P_\alpha \right). \tag{B.21}$$

We start the analysis by restricting to mechanically homogeneous tissues, where all cells have the same mechanical properties ($K^{2D}_\alpha = K^{2D}, A^0_\alpha = A^0, \Lambda_\alpha = \Lambda, \Lambda_\alpha = \Lambda$ for all α), and the regular hexagonal packing is a stable equilibrium. The tissue is aligned along the x and y-axis and consists of n_x cells in x-direction and n_y cells along y-direction, with corresponding extensions l_x and l_y. Furthermore we require that all angles in the tissue are 120°, which is enforced by the force balance condition for the case of non-zero line tension. The parametrisation is similar to the one chosen in SECTION 2.2.2 and sketched in FIG. B.2. The apical area A and perimeter P of all cells are henceforth given by:

$$A = l_x l_y,\ P = l_x + \frac{\sqrt{3}}{2} l_y. \tag{B.22}$$

With this the internal work for the tissue reads

$$W^A_i = n_x n_y \left(\frac{K^{2D}}{2} (\frac{L_x}{n_x} \frac{L_y}{n_y} - A^0)^2 + \frac{\Lambda}{2} (\frac{L_x}{n_x} + \frac{\sqrt{3}}{2} \frac{L_y}{n_y}) \right) \tag{B.23}$$

We study the tissue's mechanical properties around the equilibrium cell density ρ_0, and derive the generated tension as well as the effective shear and bulk moduli. Note that if all mechanical forces are acting along apical tissue surfaces there is no cost in bending the tissue, which results in a zero bending modulus.

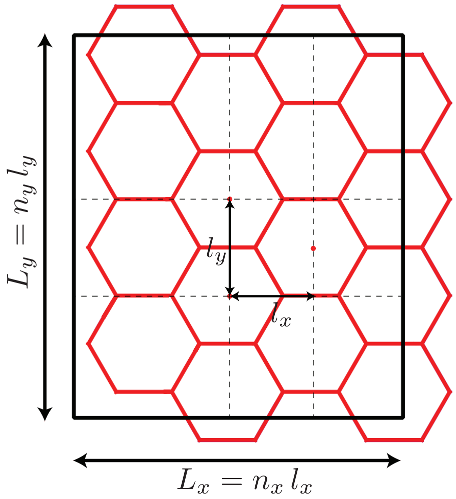

Figure B.2: Apical configuration of $n_x \times n_y$ cells, in a hexagonal packing with periodic boundary conditions. The configuration is uniquely described by their extensions l_x and l_y.

Tension generated inside the tissue.

The tensions generated inside the tissue acting on the periodic box are given by

$$\sigma_{xx} = -\frac{1}{L_y}\frac{\partial W_{int}}{\partial L_x} = K^{2D}(\frac{L_x L_y}{n_x n_y} - A^0) + \frac{1}{2}\frac{n_y}{L_y}\Lambda \tag{B.24}$$

$$\sigma_{yy} = -\frac{1}{L_x}\frac{\partial W_{int}}{\partial L_y} = K^{2D}(\frac{L_x L_y}{n_x n_y} - A^0) + \frac{\sqrt{3}}{4}\frac{n_x}{L_x}\Lambda. \tag{B.25}$$

If the external tension is isotropic, the hexagons are regular and the tissue is completely described by its cell density ρ. Then the tension as a function of the cell density reads:

$$\zeta = K^{2D}(\frac{1}{\rho} - A^0) + \frac{3^{1/4}}{2\sqrt{2}}\Lambda\sqrt{\rho}. \tag{B.26}$$

For the tissue to be in equilibrium the internal tension has to be balanced by the external tension T_{ext} that is acting on the epithelium, giving rise to the following force balance condition

$$\zeta(\rho_0) = T_{ext}. \tag{B.27}$$

Bulk and shear modulus

As explained in Section 2.2.2, the bulk modulus is a coarse grained property of a 2D material that describes the elastic response of the material to an infinitesimal bulk deformation. Similarly, the shear modulus characterises the response to a shear deformation, which preserves the total area but shears the tissue. Both types of deformations are illustrated for a Type II tissue in Fig. B.3. The precise definition of bulk and shear modulus are given in Section 2.2.2, and also the derivation of the expressions is analogous to the case of the Type I tissues. Therefore we just give the results here. The bulk modulus of a tissue with equilibrium cell density ρ_0 reads:

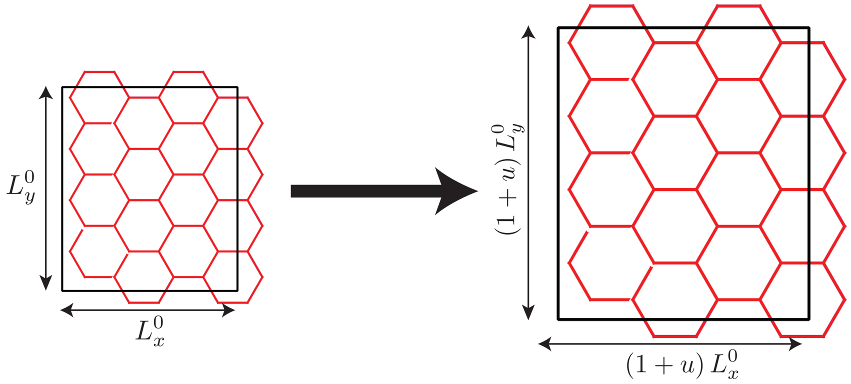

(a) Bulk deformation with scaling factor u.

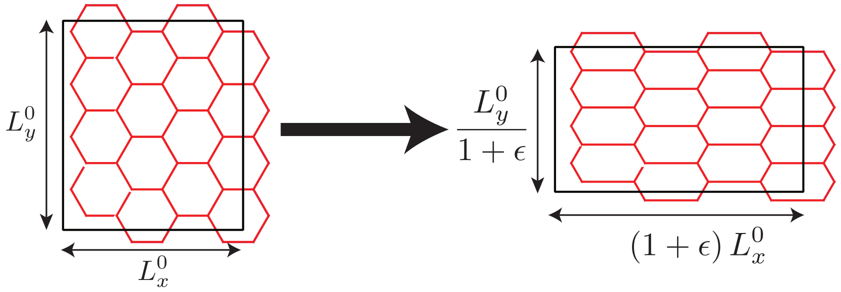

(b) Shear deformation with scaling factor ϵ.

Figure B.3: Shear and bulk deformation of a flat tissue.

$$K = \frac{K_{2D}}{\rho_0} - \frac{3^{1/4}}{2^{3/2}}\Lambda\sqrt{\rho_0}. \tag{B.28}$$

The bulk modulus increases with increasing surface elasticity, and is negatively correlated with the line tensions generated by the cells. The corresponding shear modulus reads

$$\mu = \frac{3^{1/4}}{2^{3/2}} \sqrt{\Lambda} \sqrt{\rho_0}, \tag{B.29}$$

meaning that line tensions are required for the tissue to have a non-zero shear modulus, and that the area elasticity does not influence the shear modulus explicitly, which is a consequence of the area conserving property of the shear deformation. Note however that for fixed external tension the variation of the area elasticity will lead to a change in cell density and consequently will alter the shear modulus.

Equilibrium cell density of epithelia in the Apical 3D Vertex Model

For completeness we will now derive the equilibrium cell density of an A-Model tissue under external tension. In equilibrium at the cell density ρ_0, the external and the internal tensions have to balance, which is ensured by the force balance Equation B.27:

$$T_{ext} = K^{2D}(\frac{1}{\rho_0} - A^0) + \frac{3^{1/4}}{2\sqrt{2}} \Lambda \sqrt{\rho_0} \tag{B.30}$$

The tissue has an equilibrium cell density only under the following condition:

$$T_{ext} > \frac{3^{7/6}}{2^{5/2}} (K_{2D}\Lambda^2)^{1/3} - K_{2D}A_0. \tag{B.31}$$

The corresponding phase space for the existence of an equilibrium cell density in terms of the only dimensionless parameters $T_{ext}/(K_{2D}A_0)$ and $\Lambda/(K_{2D}A_0^{3/2})$ is shown in Fig. B.4). In the presence of positive line tensions $\Lambda > 0$ there will always exist an upper bound of the cell density beyond which the tissue will collapse to a single point.

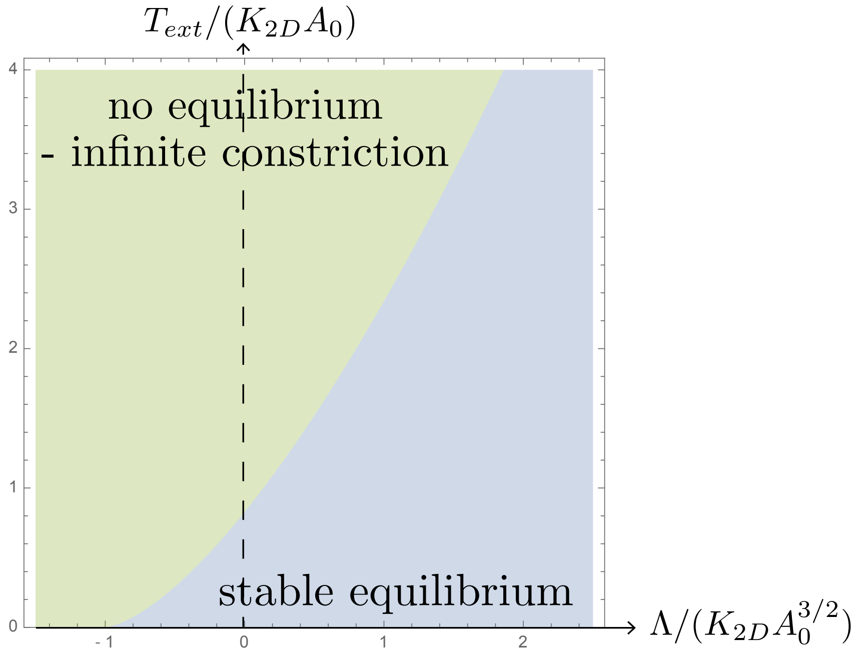

Figure B.4: Existence of a stable equilibrium cell density as a function of the only dimensionless quantities $T_{ext}/(K_{2D}A_0)$ and $\Lambda/(K_{2D}A_0^{3/2})$.

B.3 Mechanical parameters in 3D Vertex Model simulations

Throughout the thesis many simulations have been run using the 3D Vertex Model. The corresponding parameter set are referenced at the respective positions in the text and specified in the following section.

B.3.1 Simulation parameters for 3D Vertex Model simulations of homogeneous, planar tissues

#	**Section & Figure**	T_a	T_b	Λ_a	Λ_b	T_l	V^0	K^{3D}	T_{ext}	k
A	2.4.1, Fig. 2.17	5	5	10	10	1	25980	0.01	V	0
B	2.4.1, Fig. 2.17	5	5	10	10	V	25980	0.01	0	0
C	2.4.1, Fig. 2.18	5	5	10	10	1	25980	0.01	V	0
D	2.4.1, Fig. 2.18	5	5	10	10	V	25980	0.01	0	0
E	2.4.2, Fig. 2.19	2	2	V	V	1	25980	0.01	0	0
F	2.4.2, Fig. 2.19	V	V	10	10	1	25980	0.01	0	0
G	2.4.3, Fig. 2.20a	2	2	10	10	V	25980	0.01	0	0
H	2.4.3, Fig. 2.20b	2	2	V	V	1	25980	0.01	0	0
I	2.4.4, Fig. 2.21	V	V	0	0	1	25980	0.01	0	0
J	2.4.4, Fig. 2.21	0	0	V	V	1	25980	0.01	0	0
K	2.4.5, Fig. 2.22	0.5	0.5	0	0	1	25980	0.01	V	V

Table B.1: The mechanical parameters denote the apical and basal surface tensions (T_a and T_b) and line tensions (Λ_a and Λ_b), the lateral surface tension (T_l), the preferred cell volume (V^0) and the cells' volume elasticity (K^{3D}). The external compression is given by T_{ext} and the attachment stiffness to the vitelline membrane by k. If one or more parameter is varied in the set of simulations shown in the main text of the thesis, it is replaced by V.

B.3.2 Simulation parameters for simulations of homogeneous, spherical epithelia

The following parameter set has been used to simulate a epithelium on a sphere in 2.4.6, to compare simulation results to analytical predictions. The results of the simulations are shown in Fig. 2.23.

- respective apical and surface tensions T_a and T_b are specified in the graph

- lateral surface tension $T_l = 1$
- line tensions $\Lambda_a = \Lambda_b = 0$
- preferred cell volume $V^0 = 25980$
- cell bulk modulus $K^{3D} = 10^{-3}$
- basally volume, of basally enclosed cavity $V_y^0 = 257553800$
- volume elasticity of enclosed volume: $K^y = 10^{-10}$

The following set of mechanical parameters has been used to simulate an Apical 3D Vertex Model epithelium on a sphere in 2.4.6. The results are shown in FIG. 2.24.

- preferred volume of sphere: $V_y^0 = 4/3\pi R_0^3 = 14137170$
- volume elasticity of sphere: $K_y = 10^{-6}$
- area elasticity of cells $K_{2D} = 5$
- the respective cell area A_0 and apical line tension Λ are specified in the graph

APPENDIX C

Cyst Formation

C.1 Buckling instability of a spherical clone under compression

Here we derive the stability of a flat rotational symmetric clone with radius R that is clamped at its boundaries subjected to a compression γ_c. The constitutive dynamical equation is given by:

$$\alpha \partial_t h(\mathbf{x}, t) = -\kappa \Delta^2 h(\mathbf{x}, t) + \gamma \Delta h - k h(\mathbf{x}, t) \tag{C.1}$$

Let now r denote the radial coordinate of the rotational symmetric clone. The clamped boundary conditions are enforced by requiring

$$h(R) = 0 \tag{C.2}$$

$$\partial_r h(R) = 0. \tag{C.3}$$

Introducing the Laplace transform of the height function $\tilde{h}(r, s)$

$$\tilde{h}(r, s) = \int_{-\infty}^{\infty} h(r, t) e^{st} dt, \tag{C.4}$$

Eq. C.1 can be rewritten

$$-\kappa \Delta_r^2 \tilde{h}(r) + \gamma_c \Delta_r \tilde{h}(r) - (k + \alpha s) \tilde{h}(r) = 0, \tag{C.5}$$

where Δ_r is the Laplacian in polar coordinates with rotational symmetry

$$\Delta_r = \frac{\partial^2}{\partial r^2} + \frac{1}{R_0} \frac{\partial}{\partial r}. \tag{C.6}$$

The solution of Eq. C.5 reads

$$\tilde{h}(r, s) = A J_0(\lambda_+(\alpha s) r) + B J_0(\lambda_-(\alpha s) r) + C Y_0(\chi_+(\alpha s) r) + D Y_0(\chi_-(\alpha s) r), \tag{C.7}$$

where we have introduced 4 unknown constants A, B, C, D which have to be specified by the boundary conditions; $J_0(x)$ and $Y_0(x)$ are Bessel functions of the first and second type. Because $Y_0(x)$ diverges for $x \to 0$ and the height function must stay finite for $r \to 0$ we can infer $C = D = 0$. The two inverse length scales $\lambda_\pm(s) > 0$ are solutions of the polynomial equation

$$\kappa\lambda_\pm^4 + \gamma_c\lambda_\pm^2 + (k + \alpha s) = 0, \tag{C.8}$$

which can be obtained from the relations

$$\Delta_r J_0(\lambda r) = -\lambda^2 J_0(\lambda r) \tag{C.9}$$

$$\Delta_r Y_0(\lambda r) = -\lambda^2 Y_0(\lambda r). \tag{C.10}$$

Solving Eq. C.8, we find the following expressions for λ_+ and λ_-:

$$\lambda_\pm(s, R) = \sqrt{-\frac{\gamma_c(R)}{2\kappa} \pm \sqrt{\frac{\gamma_c(R)^2}{4\kappa^2} - \frac{k + \alpha s}{\kappa}}}. \tag{C.11}$$

Imposing the boundary conditions (C.2)-(C.3) then results in the following two relations

$$AJ_0(\lambda_+ R) + BJ_0(\lambda_- R) = 0 \tag{C.12}$$

$$A\lambda_+ J_1(\lambda_+ R) + B\lambda_- J_1(\lambda_- R) = 0, \tag{C.13}$$

which have a non-zero solution for A and B provided that

$$F(s) = \lambda_- J_0(\lambda_+ R)J_1(\lambda_- R) - \lambda_+ J_0(\lambda_- R)J_1(\lambda_+ R) = 0 \tag{C.14}$$

where in addition the trivial solution $\lambda_+ = \lambda_-$ can be discarded as it leads to a zero deformation. Eq. C.14 yields the solution for the rates of growth of perturbations of the shape of the circular region. Stability of the circular tissue region requires that all these solutions verify $Re(s) < 0$. The stability threshold of the clone can be found by solving the equation $F(0) = 0$. In Supplementary Figures S8(E-F), we solve this equation numerically to obtain a phase diagram as a function of R and Λ/γ_0.

We now give analytical expressions for the boundaries of the stability diagram in simple limits. We first note that in the limit of a large tissue region $R \to \infty$, the stability criterion converges to the stability threshold of an infinite tissue, $\gamma_c > -2\sqrt{\kappa k}$ (Eq. 3.10). As a result, for large R the circular tissue region is unstable for

$$R < \frac{\Lambda}{\gamma_0 + 2\sqrt{k\kappa}}. \tag{C.15}$$

Subsequently we find the stability line in the limit where there is no elastic attachment to the ECM, $k = 0$. The stability threshold then reads simply

$$J_1\left(\sqrt{\frac{-\gamma_c}{\kappa}}R\right) = 0, \tag{C.16}$$

which has solution only for $\gamma_c < 0$, as the region is always stable for $\gamma_c > 0$. Denoting $j_{11} \simeq 3.832$ the first zero of the Bessel function J_1 and using Eq. 3.11, the condition for the circular region to be unstable can be rewritten

$$\gamma_0 R^2 - \Lambda R + j_{11}^2\kappa < 0 \tag{C.17}$$

such that the sizes of unstable circular region are given for $k = 0$ by

$$\frac{\Lambda}{2\gamma_0} - \sqrt{\left(\frac{\Lambda}{2\gamma_0}\right)^2 - \frac{j_{11}^2\kappa}{\gamma_0}} < R < \frac{\Lambda}{2\gamma_0} + \sqrt{\left(\frac{\Lambda}{2\gamma_0}\right)^2 - \frac{j_{11}^2\kappa}{\gamma_0}} \qquad \text{for } \gamma_0 > 0 \tag{C.18}$$

$$R > \frac{j_{11}^2\kappa}{\Lambda} \qquad \text{for } \gamma_0 = 0 \tag{C.19}$$

$$R > \frac{\Lambda}{2\gamma_0} + \sqrt{\left(\frac{\Lambda}{2\gamma_0}\right)^2 - \frac{{j_{11}}^2\kappa}{\gamma_0}} \qquad \text{for } \gamma_0 < 0. \tag{C.20}$$

The lower limit for all values of γ_0 is $R > j_{11}^2\kappa/\Lambda$ for large $\Lambda \gg \sqrt{\kappa|\gamma_0|}$. An upper limit to stability exists only for positive tension $\gamma_0 > 0$; for negative tension $\gamma_0 < 0$ an infinite tissue is unstable, such that for $R \to \infty$ the circular region is always unstable when $k = 0$. The asymptotic stability criterion C.15 indicates however that for $k > 0$ and $\gamma_0 < 0$, a region of large stable tissue sizes arises at large R when the attaching spring elasticity is large enough, $k > \gamma_0^2/(4\kappa)$. In FIG. 3.10 we show the phase space of the buckling region of a clone as the function of the boundary contraction and the clone size.

C.1.1 Details of the parameter search

To account for the dependence of the final clone shape on the initial tissue configuration, the minimisation process was run for 15 random initial configurations of 2000 cells for each parameter set and each clone size. Then the same measurements of clone shape were done as in experiments and the results were compared.

In the 3D Vertex Model description of both the wild type tissue and the boundary effect there are 8 free mechanical parameters that had to be determined - they are given with their normalisation in Table 3.2.

The two constraints, given in Equations 3.14 and 3.14, enforce the right aspect ratios of the wild type tissue and reduce the number of free mechanical parameters to 6. Then a parameter search was performed by varying independently each of these free six parameters. For each set of tested parameters, 60 simulations with 30 cyst sizes and 15 different initial tissue configurations were run and for every mechanical equilibrium in simulations the same quantities describing the shape of the cysts as in the experimental quantification, shown in Fig. 3.7a, have been extracted and the respective averages and standard deviations were calculated. These curves were generated for ~ 200 different parameter sets. The set of parameters that resembles the experimental data the most closely is given in Table 3.2.

C.1.2 Parameter variation for cyst simulations in the 3D Vertex Model

In Section 3.2.3 we presented a set of parameter of the 3D Vertex Model, for which the equilibrium tissue shapes nicely capture the properties of the clone size dependency of cyst shapes observed in experiments. To test the sensitivity of the deformations in simulations with respect to changes in single parameters, we individually varied parameters around the parameters fitted to experimental observations.

The mechanical parameters for each set of simulations are the same as in Table 3.2, except for indicated parameter changes and values marked by an asterisk in equations below. Graphs show mean and standard error of the mean of 15 simulations per clone size. Graphs illustrate experimental (dotted line) and simulated (continuous line) deformation of apical (red) or basal (blue) cyst surfaces with respect to clone size. Parameters u_a, u_b, w_a and w_b are illustrated in Fig. 3.7a, and normalised with the height h of the surrounding tissue. The results are shown in Fig. C.1 and in the following we will give the respective parameter changes and comment briefly on the results.

(A) Original parameter set as given in Table 3.2 with a 3-fold increase in apical line and lateral surface tension at the MWI.
(B) Simulations of contractile bulk effect with 3-fold increased lateral surface tension in misspecified cells only. Large clones are strongly deformed by such a perturbation, in disagreement with experimental observations.

$(T_l^{mut-mut,*} = 3T_l,\ T_l^{c,*} = 2T_l)$

(C) Simulations with increased apical line and lateral surface tensions at the MWI by a factor of 2. The clone deformation is weaker than observed in experiments.

$(T_l^{c,*} = 2T_l,\ \Lambda_a^{c,*} = 2\Lambda_a)$

(D) Simulations with increased apical line and lateral surface tensions at the MWI by a factor of 4. The clone deformation is larger than observed in experiments.

$(T_l^{c,*} = 4T_l,\ \Lambda_a^{c,*} = 4\Lambda_a)$

(E-F) Simulations with 3 and 10 fold increased apical line tension alone at the MWI, and no increase in lateral surface tension. Experimentally observed apical indentation is not recapitulated in these conditions. This suggests that the contribution of contractility at basolateral interfaces is necessary to describe the observed clone shapes.

(E: $T_l^{c,*} = T_l,\ \Lambda_a^{c,*} = 3\Lambda_a;$
$F : T_l^{c,*} = T_l,\ \Lambda_a^{c,*} = 10\Lambda_a)$

(G) Simulations with 3-fold increase in lateral surface tension at the MWI, and no increase in apical line tension. Experimentally observed apical indentation and apicobasal asymmetry is not recapitulated in these conditions.This indicates that the additional symmetry breaking by the increase in apical line tension at the MWI is required to explain the observed deformations.

$(T_l^{c,*} = 3T_l,\ \Lambda_a^{c,*} = \Lambda_a)$

(H) Simulations with increased stiffness of attachment to the ECM. With increasing attachment stiffness the apical and basal surfaces deform less.

$(k^* = 2k)$

A Original parameter set

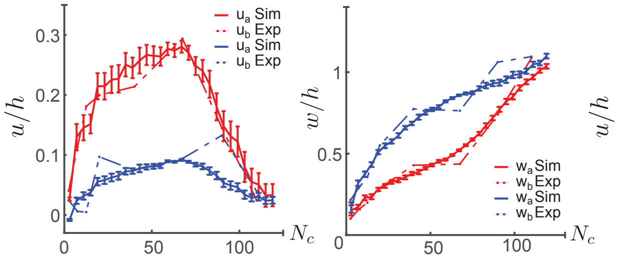

B Bulk contractility

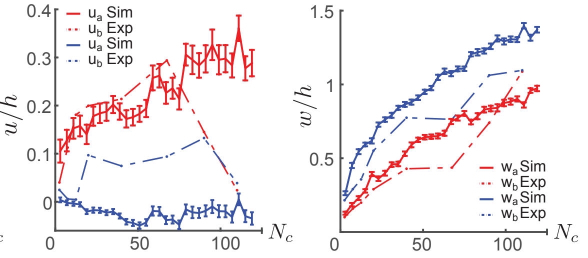

C 2-fold contractility increase: apical & lateral MWI

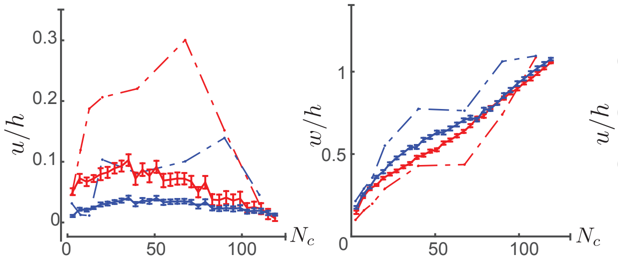

D 4-fold contractility increase: apical & lateral MWI

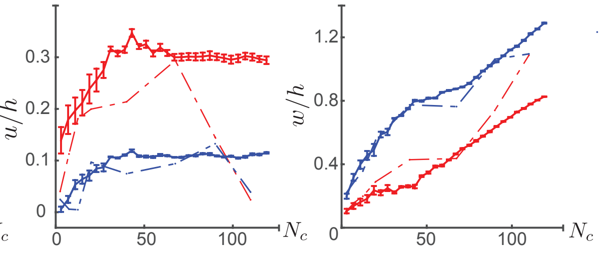

E 3-fold contractility increase: apical MWI only

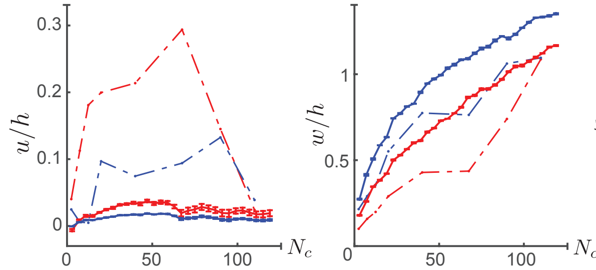

F 10-fold contractility increase: apical MWI only

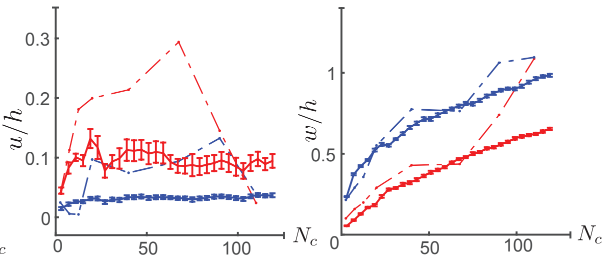

G 3-fold contractility increase: lateral MWI only

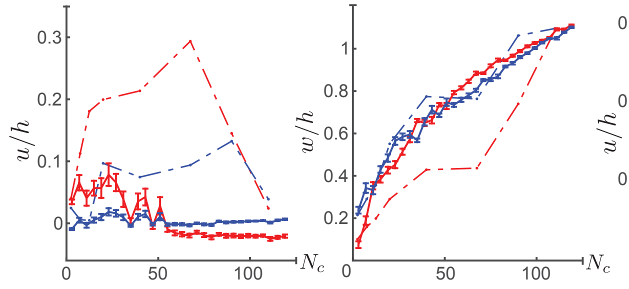

H Increased ECM stiffness

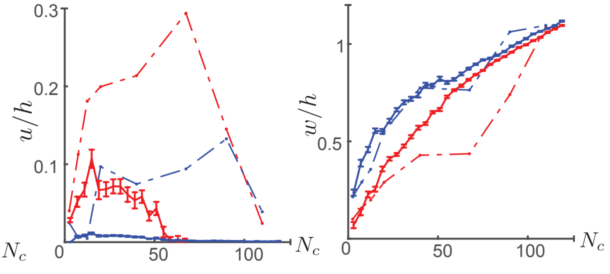

Figure C.1: The variation of single parameters around the set given in 3.2 shows their individual influence on the shapes of the cysts.

APPENDIX D

Ventral furrow formation through sagittal contraction

D.1 Solving the stress equation on a sphere

The derivations in this section have been originally carried out by Guillaume Salbreux and are taken from his notes. Here we study a thin elastic sheet whose reference state has a spherical shape. The elastic material has a 2D bulk modulus K and 2D shear modulus μ. The inner volume of the sphere exerts a pressure P on the two-dimensional elastic sheet, while the outside pressure is set to 0. We derive here the deformations of the tissue resulting from perturbations in active tensions generated in the sheet.

As prerequisites we start by deriving important quantities of the differential geometry for a slightly deformed sphere.

D.1.1 Differential geometry of the sphere

We choose the spherical coordinates (θ, ϕ), with the three associated vectors

$$\mathbf{u}_r = \sin\theta\cos\phi\mathbf{u}_x + \sin\phi\sin\theta\mathbf{u}_y + \cos\theta\mathbf{u}_z \tag{D.1}$$

$$\mathbf{u}_\theta = \cos\theta\cos\phi\mathbf{u}_x + \cos\phi\sin\theta\mathbf{u}_y - \sin\theta\mathbf{u}_z \tag{D.2}$$

$$\mathbf{u}_\phi = -\sin\phi\mathbf{u}_x + \cos\phi\mathbf{u}_y \tag{D.3}$$

We consider a slightly deformed sphere perturbed around the radius R_0. A position $\mathbf{X}$ on the sphere is located at coordinates θ, ϕ, such that

$$\mathbf{X}(\theta, \phi) = [R_0 + \delta R(\theta, \phi)]\,\mathbf{u}_r. \tag{D.4}$$

The tangent vectors to the deformed sphere are

$$\mathbf{e}_\theta = \partial_\theta\mathbf{X} = (R_0 + \delta R)\mathbf{u}_\theta + \partial_\theta\delta R\mathbf{u}_r \tag{D.5}$$

$$\mathbf{e}_\phi = \partial_\phi\mathbf{X} = (R_0 + \delta R)\sin\theta\mathbf{u}_\phi + \partial_\phi\delta R\mathbf{u}_r \tag{D.6}$$

The normal vector reads

$$\mathbf{n} = \frac{1}{\sqrt{1 + (\frac{\partial_\theta \delta R}{R_0})^2 + (\frac{\partial_\phi \delta R}{R \sin\theta})^2}} \left[\mathbf{u}_r - \frac{\partial_\theta \delta R}{R_0} \mathbf{u}_\theta - \frac{\partial_\phi \delta R}{R_0 \sin\theta} \mathbf{u}_\phi \right], \tag{D.7}$$

and to lowest order in $\frac{\delta R}{R_0}$

$$\mathbf{n} \approx \mathbf{u}_r - \frac{\partial_\theta \delta R}{R_0} \mathbf{u}_\theta - \frac{\partial_\phi \delta R}{R_0 \sin\theta} \mathbf{u}_\phi. \tag{D.8}$$

The associated metric on the deformed reads

$$g_{ij} = R_0^2 \begin{pmatrix} (1 + \frac{\delta R}{R_0})^2 + (\frac{\partial_\theta \delta R}{R_0})^2 & \frac{\partial_\theta \delta R \partial_\phi \delta R}{R_0^2} \\ \frac{\partial_\theta \delta R \partial_\phi \delta R}{R_0^2} & (1 + \frac{\delta R}{R_0})^2 \sin^2\theta + (\frac{\partial_\phi \delta R}{R_0})^2 \end{pmatrix}, \tag{D.9}$$

which to lowest order in $\frac{\delta R}{R_0}$ becomes

$$g_{ij} \approx R_0^2 \begin{pmatrix} 1 + 2\frac{\delta R}{R_0} & 0 \\ 0 & \sin^2\theta (1 + 2\frac{\delta R}{R_0}) \end{pmatrix}, \; g^{ij} \approx R\frac{1}{R^2} \begin{pmatrix} 1 - 2\frac{\delta R}{R_0} & 0 \\ 0 & \frac{1}{\sin^2\theta}(1 - 2\frac{\delta R}{R_0}) \end{pmatrix} \tag{D.10}$$

and the infinitesimal area element is given by $\sqrt{g} d\theta d\phi = R_0^2 (1 + 2\frac{\delta R}{R_0}) \sin\theta d\theta d\phi$.
We also introduce the Levi-civita tensor on the sphere

$$\varepsilon_{ij} = \begin{pmatrix} 0 & 1 \\ -1 & 0 \end{pmatrix} \tag{D.11}$$

The curvature tensor reads to first order in $\frac{\delta R}{R_0}$

$$C_{ij} = -(\partial_i \mathbf{e}_j).\mathbf{n} \approx -R_0 \begin{pmatrix} -1 - \frac{\delta R}{R_0} + \frac{\partial_\theta^2 \delta R}{R_0} & -\frac{\cos\theta \partial_\phi \delta R}{R_0 \sin\theta} + \frac{\partial_\theta \partial_\phi \delta R}{R_0} \\ -\frac{\cos\theta \partial_\phi \delta R}{R \sin\theta} + \frac{\partial_\theta \partial_\phi \delta R}{R_0} & -(1 + \frac{\delta R}{R_0}) \sin^2\theta + \cos\theta \sin\theta \frac{\partial_\theta \delta R}{R_0} + \frac{\partial_\phi^2 \delta R}{R_0} \end{pmatrix}$$

or

$$C_i^{\,j} \approx -\frac{1}{R_0} \begin{pmatrix} -1 + \frac{\delta R}{R_0} + \frac{\partial_\theta^2 \delta R}{R_0} & \frac{1}{\sin^2\theta} \left(-\cot\theta \frac{\partial_\phi \delta R}{R_0} + \frac{\partial_\theta \partial_\phi \delta R}{R_0} \right) \\ -\cot\theta \frac{\partial_\phi \delta R}{R_0} + \frac{\partial_\theta \partial_\phi \delta R}{R_0} & -1 + \frac{\delta R}{R_0} + \cot\theta \frac{\partial_\theta \delta R}{R_0} + \frac{\partial_\phi^2 \delta R}{R \sin^2\theta} \end{pmatrix} \tag{D.12}$$

The covariant derivative ∇_i of a vector field $\mathbf{u}$ is defined by the tangential portion of the usual derivative

$$\nabla_i \mathbf{u} = \left(\frac{\partial u^i}{\partial x^j} + u^k {\Gamma^i}_{jk} \right) \mathbf{e}_i, \tag{D.13}$$

where the Christoffel symbol Γ is defined by

$$g_{kl} {\Gamma^k}_{ij} = \frac{1}{2} \left(\frac{\partial g_{jl}}{\partial x^i} + \frac{\partial g_{li}}{\partial x^j} - \frac{\partial g_{ij}}{\partial x^l} \right). \tag{D.14}$$

Note that $\nabla_i g^{kl} = 0$ and $\nabla_i \varepsilon^{kl} = 0$.

Finally, we denote $\tilde{A}$ the traceless part of a tensor A, defined by $\tilde{A}_{ij} = A_{ij} - \frac{1}{n}\delta_{ij} A_{ll}$ where n denotes the dimension of A.

D.1.2 Constitutive equations and force balance

The total deformation vector of the sphere $\mathbf{u}$, has both a tangential and normal contribution:

$$\mathbf{u} = u^i \mathbf{e}_i + u^n \mathbf{n} \tag{D.15}$$

The covariant constitutive equation for an active elastic material reads

$$\sigma_{ij} = 2\mu \tilde{u}_{ij} + K {u_l}^l g_{ij} + \zeta_{ij} \tag{D.16}$$

where the elastic deformation tensor u_{ij} reads

$$u_{ij} = \frac{1}{2}(\nabla_i u_j + \nabla_j u_i) + u^n {C_k}^k g_{ij} \tag{D.17}$$

and the tensor ζ_{ij} corresponds to the active stress generated in the material.

The tangential and normal force balance equations on the sphere read respectively

$$\nabla_i \sigma^{ij} = 0 \tag{D.18}$$

$$\sigma^{ij} C_{ij} = \Delta P \tag{D.19}$$

D.1.3 Solving the force balance equations

We start from an undeformed sphere with radius R_0, which is subjected to an isotropic active tension ζ_0. The pressure inside the sphere is denoted P_0. The force balance equation then reduces to:

$$P_0 = \frac{2\zeta_0}{R_0}. \tag{D.20}$$

We now study deformations away from the undeformed sphere. The normal deformation tensor u^n the corresponds to δR defined in Eq. D.4. The active stress tensor is taken here isotropic, $\zeta_{ij} = \zeta g_{ij}$. The deformations, elastic tensions and active tensions following the deformation are described by

$$R = R_0 + \delta R \tag{D.21}$$

$$P = P_0 + \delta P \tag{D.22}$$

$$\sigma^{ij} = \sigma_0^{ij} + \delta\sigma^{ij} \tag{D.23}$$

$$\zeta = \zeta_0 + \delta\zeta. \tag{D.24}$$

The resulting tensions read to linear order in $(u_i, \delta R)$:

$$\delta\sigma_{ij} \simeq 2\mu\tilde{u}_{ij} + K {u_l}^l g_{ij} + \delta\zeta g_{ij} \tag{D.25}$$

$$= \delta\sigma^e_{ij} + \delta\zeta g_{ij}. \tag{D.26}$$

with $\tilde{u}_{ij}$ the traceless part of the planar deformation tensor u, and $\delta\sigma^e_{ij}$ the elastic stress.

The tangential force balance equation D.18 can be decomposed into two scalar equations by contraction with the covariant derivatives:

$$\nabla_i \nabla_j \sigma^{ij} = 0 \tag{D.27}$$

$${\varepsilon_j}^k \nabla_k \nabla_i \sigma^{ij} = 0. \tag{D.28}$$

Using this development to linear order, these two equations can be rewritten...

The normal force balance equation D.19 can be rewritten

$$\zeta_0 \delta {C_k}^k + \frac{1}{R_0} \delta {\sigma_k}^k = \delta P, \tag{D.29}$$

D.1.4 Spherical harmonics

Scalar spherical harmonics

The spherical harmonics expansion of a scalar field f on a sphere reads

$$f(\theta,\phi)=\sum_{n=0}^{\infty}\sum_{m=-n}^{n} f_{nm}Y_{nm}(\theta,\phi) \tag{D.30}$$

Note that in the following we will use the shorthand notation $\sum_{n=0}^{\infty}\sum_{m=-n}^{n}\equiv\sum_{n,m}$. The spherical harmonics

$$Y_{nm}(\theta,\phi)=\alpha_{nm}P_n(\cos\theta)e^{im\phi} \tag{D.31}$$

are eigenfunctions of the Laplace equation on the sphere:

$$\nabla_i\nabla^i Y_{nm}=-n(n+1)Y_{nm} \tag{D.32}$$

where the Laplace operator reads

$$\nabla_i\nabla^i f=\partial_\theta^2 f+\cot\theta\partial_\theta f+\frac{1}{\sin^2\theta}\partial_\phi^2 f. \tag{D.33}$$

α_{nm} are normalisation coefficients, given by

$$\alpha_{nm}=\sqrt{\frac{2n+1}{4\pi}\frac{(n-m)!}{(n+m)!}} \tag{D.34}$$

such that the orthonormality condition

$$\int_{\theta=0}^{\theta=\pi}\int_{\phi=0}^{\phi=2\pi} Y_{nm}{Y_{n'm'}}^{*}\sin\theta d\theta d\phi=\delta_{nn'}\delta_{mm'} \tag{D.35}$$

is fulfilled.

Vectorial spherical harmonics

A vectorial field can represented in spherical harmonics, by considering it to be the gradient field of a scalar field, and thus it can be obtained by differentiating a field of scalar spherical harmonics [118]. For vectors one can define $\mathbf{s}^1_{nm}\equiv\partial_i Y_{nm}\mathbf{e}^i$, with $\mathbf{e}^i$ the tangent vectors of the undeformed sphere:

$$\begin{aligned}
\mathbf{s}^1_{nm} &= \partial_\theta Y_{nm}\mathbf{e}^\theta + \partial_\phi Y_{nm}\mathbf{e}^\phi && \text{(D.36)}\\
&= \alpha_{nm}\left[\partial_\theta(P_n(\cos\theta))e^{im\phi}\mathbf{e}^\theta + \alpha_{nm} imP_n(\cos\theta)e^{im\phi}\mathbf{e}^\phi\right] && \text{(D.37)}\\
&= \alpha_{nm}\partial_\theta(P_n(\cos\theta))e^{im\phi}\mathbf{e}_\theta + \alpha_{nm}\frac{1}{\sin^2\theta}imP_n(\cos\theta)e^{im\phi}\mathbf{e}_\phi && \text{(D.38)}\\
&= \alpha_{nm}\partial_\theta(P_n(\cos\theta))e^{im\phi}\mathbf{u}_\theta + \alpha_{nm}im\frac{1}{\sin\theta}P_n(\cos\theta)e^{im\phi}\mathbf{u}_\phi && \text{(D.39)}
\end{aligned}$$

and $\mathbf{s}^2_{nm} \equiv \mathbf{n}\times\mathbf{s}^1_{nm}$:

$$\begin{aligned}
\mathbf{s}^2_{nm} &= \alpha_{nm}\frac{1}{\sin\theta}imP_n(\cos\theta)e^{im\phi}\mathbf{e}^\theta - \alpha_{nm}\sin\theta\partial_\theta(P_n(\cos\theta))e^{im\phi}\mathbf{e}^\phi && \text{(D.40)}\\
&= \alpha_{nm}\frac{1}{\sin\theta}imP_n(\cos\theta)e^{im\phi}\mathbf{e}_\theta - \alpha_{nm}\frac{1}{\sin\theta}\partial_\theta(P_n(\cos\theta))e^{im\phi}\mathbf{e}_\phi && \text{(D.41)}\\
&= \alpha_{nm}im\frac{1}{\sin\theta}P_n(\cos\theta)e^{im\phi}\mathbf{u}_\theta - \alpha_{nm}\partial_\theta P_n(\cos\theta)e^{im\phi}\mathbf{u}_\phi. && \text{(D.42)}
\end{aligned}$$

Tensorial spherical harmonics

To obtain tensorial spherical harmonics, two traceless tensors $\mathbf{S}_1^{(n,m)}$ and $\mathbf{S}_2^{(n,m)}$ can be constructed [119]:

$$\begin{aligned}
S_1^{(n,m)^{ij}} &= \left[\nabla^i\nabla^j - \tfrac{1}{2}\nabla_k\nabla^k\right]Y_{nm} && \text{(D.43)}\\
S_2^{(n,m)^{ij}} &= \tfrac{1}{2}\left[\varepsilon^{ik}\nabla^j\nabla_k + \varepsilon^{jk}\nabla^i\nabla_k\right]Y_{nm}. && \text{(D.44)}
\end{aligned}$$

By making use of the eigenfunction property (Eq. D.32) one can show that the following identities hold:

$$\begin{aligned}
\nabla_i\nabla_j S_1^{(n,m)}{}_i^j &= \frac{n(n+1)}{2}\left[n(n+1)-2\right]Y_{nm} && \text{(D.45)}\\
\varepsilon_j{}^k\nabla_k\nabla^i S_1^{(n,m)}{}_i^j &= 0 && \text{(D.46)}\\
\nabla_i\nabla_j S_2^{(n,m)}{}_i^j &= 0 && \text{(D.47)}\\
\varepsilon_j{}^k\nabla_k\nabla^i S_2^{(n,m)}{}_i^j &= \frac{n(n+1)}{2}\left[n(n+1)-2\right]Y_{nm}. && \text{(D.48)}
\end{aligned}$$

D.1.5 Deformations resulting from small perturbations in the active tension

The stress tensor

The deformation field is a vector field on the sphere, which can be decomposed in vectorial spherical harmonics:

$$\mathbf{u} = \sum_{n,m} \left[A_{nm}\mathbf{s}^1_{nm} + B_{nm}\mathbf{s}^2_{nm}\right] \tag{D.49}$$

Using this notation together with the relations D.43-D.48, the elastic stress tensor, given in Eq. D.25, becomes

$$\begin{aligned}
\delta\sigma^e_{ij} &= \mu(\nabla^i u^j + \nabla^j u^i - \nabla_k u^k g^{ij}) + K(\nabla_k u^k + \frac{\delta R}{R_0})g^{ij} \\
&= \sum_{n,m} A_{nm}\left[2\mu\nabla^i\nabla^j Y_{nm} + (K-\mu)\nabla_k\nabla^k Y_{nm} g^{ij}\right] \\
&\quad + B_{nm}\left[\mu\varepsilon^{jk}\nabla^i\nabla_k Y + \varepsilon^{ik}\nabla^j\nabla_k Y_{nm} + (K-\mu)\nabla_k\varepsilon^{kl}\nabla_l Y_{nm} g^{ij}\right] + K\frac{\delta R_{nm}}{R_0}Y_{nm}g^{ij} \\
&= \sum_{n,m} A_{nm}\left[2\mu\nabla^i\nabla^j Y_{nm} + (K-\mu)\nabla_k\nabla^k Y_{nm} g^{ij}\right] + B_{nm}\left[\mu(\varepsilon^{jk}\nabla^i\nabla_k Y_{nm} + \varepsilon^{ik}\nabla^j\nabla_k Y_{nm})\right] \\
&\quad + K\frac{\delta R_{nm}}{R_0}Y_{nm}g^{ij} \\
&= \sum_{n,m} K(\frac{\delta R_{nm}}{R_0} - A_{nm}n(n+1))Y_{nm}g^{ij} + 2\mu A_{nm}\left[\nabla^i\nabla^j Y_{nm} - \frac{1}{2}\nabla_k\nabla^k Y_{nm} g^{ij}\right] \\
&\quad + 2\mu B_{nm}\frac{\varepsilon^{jk}\nabla^i\nabla_k Y_{nm} + \varepsilon^{ik}\nabla^j\nabla_k Y_{nm}}{2}
\end{aligned}$$

The isotropic perturbation of the active stress, which can be decomposed into the homogeneous contribution ζ_0 and the perturbation $\delta\zeta$, reads if represented in spherical harmonics:

$$\zeta^{ij}(\theta,\phi) = (\zeta_0 + \delta\zeta(\theta,\phi))\, g^{ij} = \left(\zeta_0 + \sum_{n,m}\delta\zeta_{nm}Y_{nm}(\theta,\phi)\right) g^{ij}$$

Force balance

The force balance equations D.29-D.28 can then be used together with the relations D.45-D.48, to obtain relations relating coefficients of the deformation and active stress in the spherical harmonics expansion:

$$-n(n+1)K\frac{\delta R_{nm}}{R_0} + A_{nm}K(n(n+1))^2 + A_{nm}2\mu\frac{n(n+1)}{2}(n(n+1)-2) - \delta\zeta_{nm}n(n+1) = 0$$

$$B_{nm}\mu\frac{n(n+1)}{2}(n(n+1)-2) = 0$$

$$2K(\frac{\delta R_{nm}}{R_0} - n(n+1)A_{nm}) = R_0\delta P_{nm} - 2\delta\zeta_{nm} + \zeta_0(2-n(n+1))\frac{\delta R_{nm}}{R_0}.$$

These equations can be solved for R_{nm}, A_{nm} and B_{nm} to obtain the resulting deformations for a given perturbation ζ_{nm}.
For the zeroth mode $n = m = 0$ the deformation corresponds to a change in radius:

$$\frac{\delta R_{00}}{R_0} = -\frac{1}{\frac{K}{\zeta_0} + 2\pi\frac{K^y R_0^4}{\zeta_0} - 1}\frac{\delta\zeta_{00}}{\zeta_0} \tag{D.50}$$

$$A_{00} = \frac{1 - 2\pi\frac{K^y R_0^4}{\zeta_0}}{2\frac{\mu}{\zeta_0}(\frac{K}{\zeta_0} + 2\pi\frac{K^y R_0^4}{\zeta_0} - 1)}\frac{\delta\zeta_{00}}{\zeta_0} \tag{D.51}$$

$$B_{00} = 0 \tag{D.52}$$

The first modes $n = 1$ leads only to a translation of the sphere, and the resulting deformations consequently read

$$\frac{\delta R_{00}}{R_0} = 0 \tag{D.53}$$

$$A_{1m} = \frac{\delta\zeta_{1m}}{2K}, \tag{D.54}$$

and for modes $n > 1$ one finds the following in-plane and radial deformations

$$\frac{\delta R_{nm}}{R_0} = \frac{-2}{\frac{K}{\mu}n(n+1) + 2\frac{K}{\zeta_0} + n(n+1) - 2}\frac{\delta\zeta_{nm}}{\zeta_0} \tag{D.55}$$

$$A_{nm} = \frac{\zeta_0}{Kn(n+1) + 2\frac{K\mu}{\zeta_0} + (n(n+1)-2)\mu}\frac{\delta\zeta_{nm}}{\zeta_0} \tag{D.56}$$

$$B_{00} = 0. \tag{D.57}$$

D.1.6 Mode-wise comparison of Apical 3D Vertex Simulations and analytical calculations

In section 4.2.3 we discuss how to compare the analytically obtained spherical deformations to equilibrium shapes obtained in Apical 3D Vertex Model simulations, by perturbing the homogeneous tension with pure spherical harmonics. Here we give the resulting deformations for two tissues consisting of 6,000 cells, to show the good match between the continuous and the 3D Vertex Model framework. The tables below show the values for the ratio between the spherical harmonics coefficients of the relative deformation and the relative perturbations in tension $\left(\delta R/R_0\right)_{nm} / \left(\delta R/\delta_0\right)_{nm}$ obtained, both from simulations and from analytical predictions given in Eqs. 4.7a-4.7c.

The mechanical parameters for the results shown in table 4.10 have been chosen as follows:

$$V_y^0 = 875958700 \tag{D.58}$$

$$K_y = 10^{-6} \tag{D.59}$$

$$\Lambda = 12000 \tag{D.60}$$

$$K_a = 1 \tag{D.61}$$

$$A_a^0 = 575.959. \tag{D.62}$$

The resulting coarse grained mechanical parameters of the equilibrated tissue made of 6,000 cells with mean radius $R_0 = 593.307$ read

$$\zeta_0 = 593.28 \tag{D.63}$$

$$K = 531.879 \tag{D.64}$$

$$\mu = 205.608. \tag{D.65}$$

For a perturbation $\delta\zeta(\phi,\theta) = 0.002\zeta_0 Y_{nm}(\phi,\theta)$ around the homogeneous tension ζ_0, the resulting deformations are shown in the following table together with the predictions from the analytical theory given in Eqs. 4.7a-4.7c.

Table D.1: Comparison of the quantity $\left(\delta R/R_0\right)_{nm} / \left(\delta R/\delta_0\right)_{nm}$ for modes $n, m \leq 4$ obtained from simulations and from analytical calculations with the mechanical parameters given above.

n/m	0	1	2	3	4	analytical predictions
0	-6.9 e-05					-7.4e-05
1	3.8e-06	2.06 e-06				0
2	-0.089	-0.091	-0.093			-0.094
3	-0.045	-0.045	-0.047	-0.049		-0.047
4	-0.027	-0.027	-0.028	-0.028	-0.029	-0.028

As additional test we repeated the test with a different set of mechanical parameters as follows:

$$V_y^0 = 875958700 \tag{D.66}$$

$$K_y = 10^{-6} \tag{D.67}$$

$$\Lambda = 15000 \tag{D.68}$$

$$K_a = 1 \tag{D.69}$$

$$A_a^0 = 575.959. \tag{D.70}$$

The resulting coarse grained mechanical parameters of the equilibrated tissue made of 6,000 cells with mean radius $R_0 = 593.0$ read

$$\zeta_0 = 680.96 \tag{D.71}$$

$$K = 479.792 \tag{D.72}$$

$$\mu = 257.111. \tag{D.73}$$

Also for this equilibrium setup we studied the deformations of the epithelium resulting from a perturbation of the homogeneous tension ζ_0 by $\delta\zeta(\phi,\theta) = 0.002\zeta_0 Y_{nm}(\phi,\theta)$ for modes $n, n \leq 4$. The resulting normalised deformations are given in the following table together with the predictions from the analytical theory derived above and given in Eqs. 4.7a-4.7c.

Table D.2: Comparison of the quantity $(\delta R/R_0)_{nm} \,/\, (\delta R/\delta_0)_{nm}$ for modes $n, m \leq 4$ obtained from simulations and from analytical calculations with the mechanical parameters given above.

n/m	0	1	2	3	4	analytical predictions
0	-9.1e-05					-8.7e-05
1	1.4e-05	2.0e-05				0
2	-0.115	-0.114	-0.129			-0.120
3	-0.054	-0.060	-0.057	-0.063		-0.059
4	-0.035	-0.034	-0.035	-0.035	-0.037	-0.035

Both tables D.1 and D.2 show a good agreement between the analytical solution and the simulation results over all studied modes of perturbations. The average errors lie well within a 5% margin, and the possible reasons for these deviations are discussed in section 4.2.3.

Comparison of deformations in simulations and analytical predictions for sagittal contraction mechanism

After showing the good agreement of the deformations between simulations and analytical results for spherical harmonic perturbations in tension mode by mode, we next simulated an epithelium consisting of 10,000 cells in the Apical 3D Vertex Model and studied the deformation resulting from an increase in tension along a stripe of the tissue. As in 4.6 all cells inside a rectangular stripe along the surface of the sphere were defined as mesodermal cells. For the continuum calculations, the equivalent region has been defined to be the mesoderm on a discretised sphere as described in 4.2.2. Both initial configurations of the tissue and the region of the mesoderm are shown in Fig. D.1a. We then defined a measure of the deviation of the tissue's shape from a perfect sphere, to compare the results of the two theories. We therefore chose the spherical presentation where the distance of the epithelium from its midpoint is given as a function of the angles $R(\theta, \phi)$, and defined the measure of deformation D per unit increase in tension inside the stripe:

$$D = \frac{\partial \Big(\mathrm{std}(R(\theta,\phi)) / < R(\phi,\zeta) > \Big)}{\partial(\delta\zeta/\zeta_0)}. \tag{D.74}$$

$< R(\theta, \phi) >$ and $\mathrm{std}(R(\theta, \phi))$ are the mean and standard deviation of the distance of all cellular midpoints in the Apical 3D Vertex Model, and of the discrete points from the

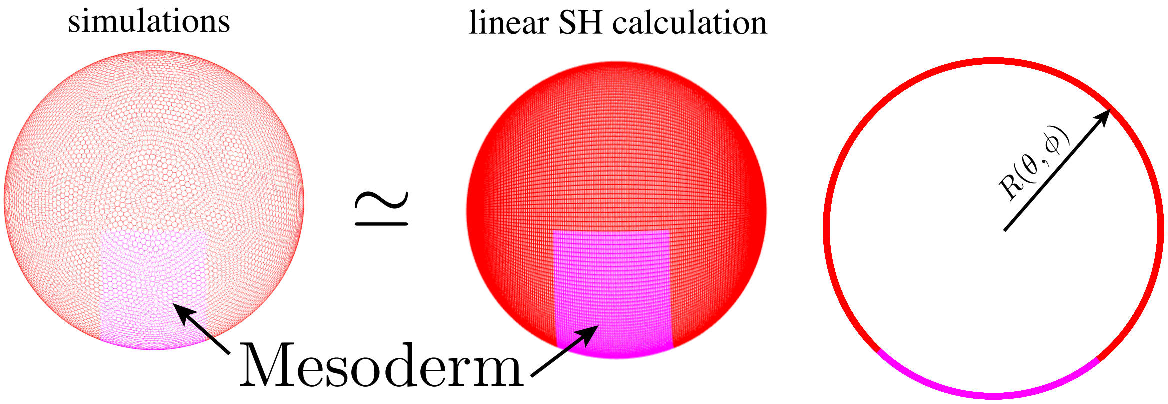

(a) Initial configurations **(b)** Parametrisation.

Figure D.1: a) To compare simulations and continuous calculations, equivalent initial configurations of the blastula have been created made of 10,000 cells in simulations and of 40,000 grid points on a sphere for the spherical harmonics calculation. b) A parametrisation of the blastula in spherical coordinates $R(\theta, \phi) = R_0 + \delta R(\theta, \phi)$ was used.

centre of the epithelium in the continuous theory. Note that this measure was found to be better suited for the comparison, since it is less dependent on local inhomogeneities than for instance measuring the maximal and the minimal distance of points from the midpoint of the sphere. The resulting deviations obtained in both models for varying K/μ are shown in Fig. D.2.

The graph shows clearly that in the studied range of parameters, both models predict the same response of the tissue shape to an increase in tension, for corresponding mechanical parameters. From these findings we conclude that the models are equivalent in the studied regime of weak perturbations, and that the continuum model can be seen as the limit of the 3D Vertex Model simulations. The initial deformations of the tissue do not depend on the detailed shape of the cells, but can be predicted only by knowing the coarse grained shape and the cell densities.

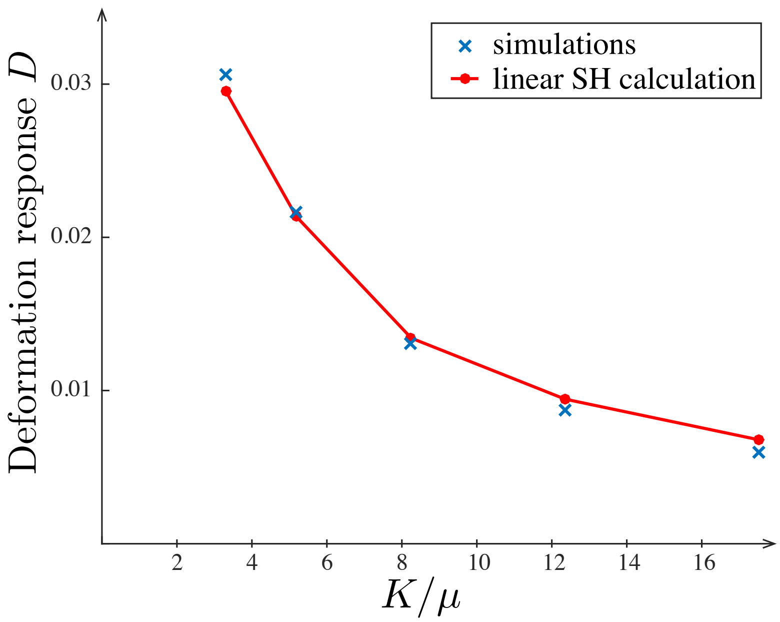

Figure D.2: Deformations resulting from small increase in tension in the mesoderm obtained in 3D Vertex Model simulations of blastula and by using linear response theory. The deformation of the tissue is measured by the standard deviation of the vertex distances (in simulations) or grid points (in the linear theory) from the tissue midpoint, and presented as a function of the ratio of bulk and shear modulus.

D.2 The vitelline membrane in the 3D Vertex Model

In order to quantitatively model the details of the process it is required to take into account the mechanical constraints imposed by the vitelline membrane on the blastula. The vitelline membrane is represented by a 2D manifold, which is an ellipsoid centred at the Cartesian origin and the axes of the ellipsoid are aligned with the axes of the Cartesian coordinate system. The length of the corresponding half-axes are given by $L_x^{\mathbb{M}}$, $L_y^{\mathbb{M}}$ and $L_z^{\mathbb{M}}$ and the vitelline membrane is defined by the equation

$$\mathbb{M} = \{(x,y,z) : \left(\frac{x}{L_x^{\mathbb{M}}}\right)^2 + \left(\frac{y}{L_y^{\mathbb{M}}}\right)^2 + \left(\frac{z}{L_z^{\mathbb{M}}}\right)^2 = 1\}. \tag{D.75}$$

A point (x, y, z) that is not part of $\mathbb{M}$ lies in the interior of the vitelline membrane if $(x/L_x)^2 + (y/L_y)^2 + (z/L_z)^2 < 1$ and outside otherwise.

With this definition the vitelline membrane can be taken into account by writing the mechanical work function of the epithelium as follows:

$$W = \sum_{\alpha\in\mathcal{C}} \left(\frac{K_\alpha^{2D}}{2}(A_\alpha - A_\alpha^0)^2 + \frac{\Lambda_\alpha}{2} P_\alpha \right) + \sum_{v\in\mathcal{V}} (1-\delta_v^{\mathbb{M}}) \frac{k^{\mathbb{M}}}{2}(d_v^{\mathbb{M}})^2 + \frac{K_y}{2}(V_y - V_y^0)^2 \qquad \text{(D.76)}$$

where $\delta_v^{\mathbb{M}} = 1$ only if the vertex v lies in the interior of the vitelline membrane, and d_v^M denotes the shortest cartesian distance of v to $\mathbb{M}$. The mechanical parameter $k^{\mathbb{M}}$ is the spring constant of the spring like force experienced by the vertices once they leave the interior of the vitelline membrane. The ellipsoidal vitelline membrane is required in the model to account for the non-spherical shape of the tissue if the tissue is considered to be spatially homogeneous. The volume elasticity of the blastocoel is represented by the preferred volume V_y^0 and the volume elasticity K_y. An example of a homogeneous tissue under tension surrounding the blastocoel and confined inside the vitelline membrane is shown in Fig. D.3.

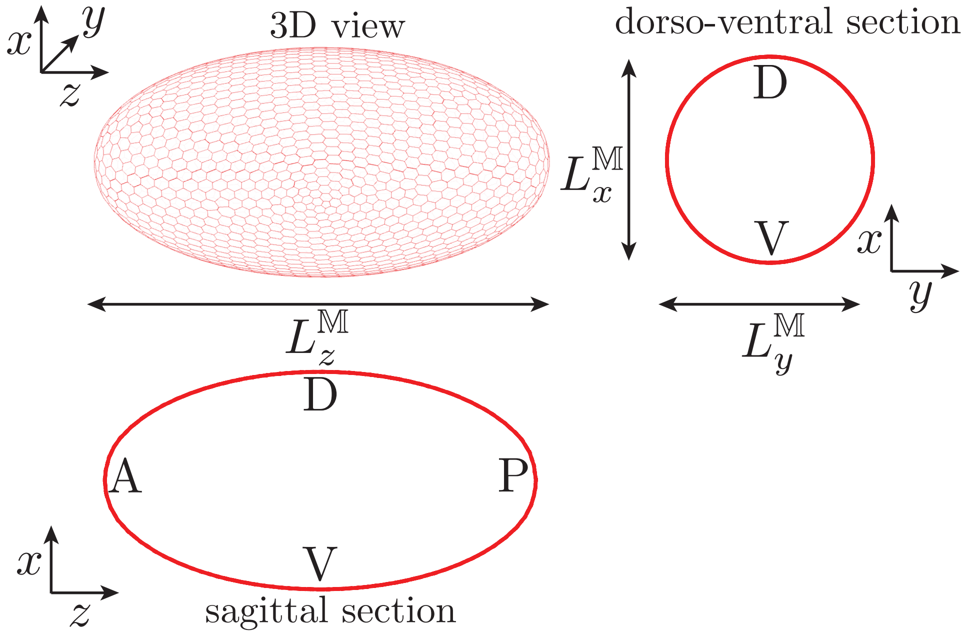

Figure D.3: The blastoderm in the 3D Vertex Model is a 2D manifold enclosing the blastocoel which exerts a pressure onto the tissue. All forces are assumed to act in the apical surface of the tissue. The vitelline membrane surrounding the tissue is represented by an ellipsoid with short axes $L_x^{\mathbb{M}}$ and $L_y^{\mathbb{M}}$, and long axis $L_z^{\mathbb{M}}$, which exerts a springlike force upon penetration by the vertices.

Bibliography

[1] Eva Bianconi et al. “Annals of Human Biology An estimation of the number of cells in the human body”. In: 4460.January 2016 (2013). DOI: `10.3109/03014460.2013.807878`.

[2] Calvin B Bridges, Alfred Henry Sturtevant, and Thomas Hunt Morgan. *Contributions to the Genetics of Drosophila Mel’anogaster.* Gibson Brothers, 1919.

[3] Thomas Hunt Morgan. *The physical basis of heredity.* JB Lippincott, 1919.

[4] J W Fristrom. “The developmental biology of Drosophila.” In: *Annual review of genetics* 4.12 (1970), pp. 325–346. ISSN: 0066-4197. DOI: `10.1146/annurev.ge.04.120170.001545`.

[5] Ka Ketchum et al. “The genome sequence of Drosophila melanogaster”. In: *Science* 287.March (2000), pp. 2185–2195. ISSN: 0036-8075. DOI: `10.1126/science.287.5461.2185`.

[6] José A Campos-Ortega and Volker Hartenstein. *The embryonic development of Drosophila melanogaster.* Springer Science & Business Media, 2013.

[7] Lewis Wolpert, Cheryll Tickle, and Alfonso Martinez Arias. *Principles of development.* Oxford university press, 2015.

[8] Antoon Moorman et al. “Development of the Heart : (1) Formation of the Cardiac Chambers and Arterial Trunks”. In: 1 (2003). ISSN: 0007-0769. DOI: `10.1136/heart.89.7.806`.

[9] Carmen Hagios, André Lochter, and Mina J Bissell. “Tissue architecture: the ultimate regulator of epithelial function?” In: *Philosophical Transactions of the Royal Society of London B: Biological Sciences* 353.1370 (1998), pp. 857–870.

[10] Darcy Wentworth Thompson et al. “On growth and form.” In: *On growth and form.* (1942).

[11] Matthew C Gibson et al. “The emergence of geometric order in proliferating metazoan epithelia”. In: 442.August (2006), pp. 2–5. DOI: `10.1038/nature05014`.

[12] Reza Farhadifar. “Dynamics of Cell Packing and Polar Order in Developing Epithelia”. In: (2009).

[13] Frank Jülicher et al. “Modeling molecular motors”. In: *Reviews of Modern Physics* 69.4 (1997), pp. 1269–1282. ISSN: 0034-6861. DOI: `10.1103/RevModPhys.69.1269`.

[14] Guillaume Salbreux, Guillaume Charras, and Ewa Paluch. "Actin cortex mechanics and cellular morphogenesis". In: *Trends in Cell Biology* 22.10 (2012), pp. 536–545. ISSN: 09628924. DOI: `10.1016/j.tcb.2012.07.001`.

[15] F Hanakam et al. "Myristoylated and non-myristoylated forms of the pH sensor protein hisactophilin II: intracellular shuttling to plasma membrane and nucleus monitored in real time by a fusion with green fluorescent protein." In: *The EMBO journal* 15.12 (1996), pp. 2935–2943. ISSN: 0261-4189.

[16] Andrew G. Clark, Kai Dierkes, and Ewa K. Paluch. "Monitoring actin cortex thickness in live cells". In: *Biophysical Journal* 105.3 (2013), pp. 570–580. ISSN: 00063495. DOI: `10.1016/j.bpj.2013.05.057`.

[17] S. J. Winder. "Actin-binding proteins". In: *Journal of Cell Science* 118.4 (2005), pp. 651–654. ISSN: 0021-9533. DOI: `10.1242/jcs.01670`.

[18] E Evans and a Yeung. "Apparent viscosity and cortical tension of blood granulocytes determined by micropipet aspiration." In: *Biophysical journal* 56.1 (1989), pp. 151–160. ISSN: 00063495. DOI: `10.1016/S0006-3495(89)82660-8`.

[19] Jean-Yves Tinevez et al. "Role of cortical tension in bleb growth." In: *Proceedings of the National Academy of Sciences of the United States of America* 106.44 (Nov. 2009), pp. 18581–6. ISSN: 1091-6490. DOI: `10.1073/pnas.0903353106`.

[20] Olivier Thoumine, Olivier Cardoso, and Jean Jacques Meister. "Changes in the mechanical properties of fibroblasts during spreading: A micromanipulation study". In: *European Biophysics Journal* 28.3 (1999), pp. 222–234. ISSN: 01757571. DOI: `10.1007/s002490050203`.

[21] Robert M. Hochmuth. "Micropipette aspiration of living cells". In: *Journal of Biomechanics* 33.1 (2000), pp. 15–22. ISSN: 00219290. DOI: `10.1016/S0021-9290(99)00175-X`.

[22] E C Schwarz et al. "Dictyostelium myosin IK is involved in the maintenance of cortical tension and affects motility and phagocytosis." In: *Journal of cell science* 113 (Pt 4 (2000), pp. 621–633. ISSN: 0021-9533.

[23] J Dai et al. "Myosin I contributes to the generation of resting cortical tension." In: *Biophysical journal* 77.2 (1999), pp. 1168–1176. ISSN: 00063495. DOI: `10.1016/S0006-3495(99)76968-7`.

[24] Michael A Gelbart et al. “Volume conservation principle involved in cell lengthening and nucleus movement during tissue morphogenesis.” In: *Proceedings of the National Academy of Sciences of the United States of America* 109.47 (2012), pp. 19298–303. ISSN: 1091-6490. DOI: `10.1073/pnas.1205258109/-/DCSupplemental.www.pnas.org/cgi/doi/10.1073/pnas.1205258109`.

[25] David E. Breen et al. “Epithelial cell reconstruction and visualization of the developing Drosophila wing imaginal disc”. In: *2012 IEEE Symposium on Biological Data Visualization (BioVis)* (Oct. 2012), pp. 77–84. DOI: `10.1109/BioVis.2012.6378596`.

[26] Andrew R Harris et al. “Characterizing the mechanics of cultured cell monolayers.” In: *Proceedings of the National Academy of Sciences of the United States of America* 109.41 (Oct. 2012), pp. 16449–54. ISSN: 1091-6490. DOI: `10.1073/pnas.1213301109`.

[27] Raghu Kalluri. “Basement membranes: structure, assembly and role in tumour angiogenesis.” In: *Nature reviews. Cancer* 3.June (2003), pp. 422–433. ISSN: 1474175X. DOI: `10.1038/nrc1094`.

[28] José Carlos Pastor-Pareja and Tian Xu. “Shaping cells and organs in Drosophila by opposing roles of fat body-secreted Collagen IV and perlecan.” In: *Developmental cell* 21.2 (Aug. 2011), pp. 245–56. ISSN: 1878-1551. DOI: `10.1016/j.devcel.2011.06.026`.

[29] Howard A. Schneiderman Clifton A. Poodry. “Intercellular adhesivity and pupal morphogenesis inDrosophila melanogaster”. In: 9 (1971), pp. 1–9.

[30] Xuejun Chen and Barry M Gumbiner. “Crosstalk between different adhesion molecules”. In: (2006), pp. 572–578. DOI: `10.1016/j.ceb.2006.07.002`.

[31] Paloma Domínguez-Giménez, Nicholas H Brown, and María D Martín-Bermudo. “Integrin-ECM interactions regulate the changes in cell shape driving the morphogenesis of the Drosophila wing epithelium”. In: (2007). DOI: `10.1242/jcs.03404`.

[32] Liyuan Sui, Gert O Pflugfelder, and Jie Shen. “The Dorsocross T-box transcription factors promote tissue morphogenesis in the Drosophila wing imaginal disc.” In: *Development (Cambridge, England)* 139.15 (Aug. 2012), pp. 2773–82. ISSN: 1477-9129. DOI: `10.1242/dev.079384`.

[33] Hisao Honda. “Geometrical models for cells in tissues”. In: *International review of cytology* 81 (1983), pp. 191–248.

[34] Hisao Honda, Masaharu Tanemura, and Tatsuzo Nagai. "A three-dimensional vertex dynamics cell model of space-filling polyhedra simulating cell behavior in a cell aggregate." In: *Journal of theoretical biology* 226.4 (Feb. 2004), pp. 439–53. ISSN: 0022-5193. DOI: `10.1016/j.jtbi.2003.10.001`.

[35] Reza Farhadifar et al. "The influence of cell mechanics, cell-cell interactions, and proliferation on epithelial packing." In: *Current biology : CB* 17.24 (Dec. 2007), pp. 2095–104. ISSN: 0960-9822. DOI: `10.1016/j.cub.2007.11.049`.

[36] Tatsuzo Nagai and Hisao Honda. "Computer simulation of wound closure in epithelial tissues: Cell-basal-lamina adhesion". In: *Physical Review E - Statistical, Nonlinear, and Soft Matter Physics* 80.6 (Dec. 2009), pp. 1–12. ISSN: 15393755. DOI: `10.1103/PhysRevE.80.061903`.

[37] Katharina P Landsberg et al. "Increased cell bond tension governs cell sorting at the Drosophila anteroposterior compartment boundary." In: *Current biology : CB* 19.22 (Dec. 2009), pp. 1950–5. ISSN: 1879-0445. DOI: `10.1016/j.cub.2009.10.021`.

[38] Benoît Aigouy et al. "Cell Flow Reorients the Axis of Planar Polarity in the Wing Epithelium of Drosophila". In: *Cell* 142.5 (2010), pp. 773–786. ISSN: 00928674. DOI: `10.1016/j.cell.2010.07.042`.

[39] D B Staple et al. "Mechanics and remodelling of cell packings in epithelia." In: *The European physical journal. E, Soft matter* 33.2 (Oct. 2010), pp. 117–27. ISSN: 1292-895X. DOI: `10.1140/epje/i2010-10677-0`.

[40] O Wartlick et al. "Dynamics of Dpp signaling and proliferation control." In: *Science (New York, N.Y.)* 331.6021 (2011), pp. 1154–1159. ISSN: 0036-8075. DOI: `10.1126/science.1211373`.

[41] Georgios Trichas et al. "Multi-Cellular Rosettes in the Mouse Visceral Endoderm Facilitate the Ordered Migration of Anterior Visceral Endoderm Cells". In: *PLoS Biology* 10.2 (2012), e1001256. ISSN: 1545-7885. DOI: `10.1371/journal.pbio.1001256`.

[42] T. Aegerter-Wilmsen et al. "Integrating force-sensing and signaling pathways in a model for the regulation of wing imaginal disc size". In: *Journal of Cell Science* 125.17 (2012), e1–e1. ISSN: 0021-9533. DOI: `10.1242/jcs.120758`.

[43] Guillaume Salbreux et al. "Coupling Mechanical Deformations and Planar Cell Polarity to Create Regular Patterns in the Zebrafish Retina". In: *PLoS Computational Biology* 8.8 (2012), e1002618. ISSN: 1553-7358. DOI: `10.1371/journal.pcbi.1002618`.

[44] Maryam Aliee et al. “Physical mechanisms shaping the Drosophila dorsoventral compartment boundary”. In: *Current Biology* 22.11 (2012), pp. 967–976. ISSN: 09609822. DOI: `10.1016/j.cub.2012.03.070`.

[45] Miriam Osterfield et al. “Three-Dimensional Epithelial Morphogenesis in the Developing Drosophila Egg”. In: *Developmental Cell* 24.4 (2013), pp. 400–410. ISSN: 15345807. DOI: `10.1016/j.devcel.2013.01.017`.

[46] Nebojsa Murisic et al. “From Discrete to Continuum Models of Three-Dimensional Deformations in Epithelial Sheets”. In: *Biophysical Journal* 109.1 (2015), pp. 154–163. ISSN: 00063495. DOI: `10.1016/j.bpj.2015.05.019`.

[47] Bruno Monier et al. “Epithelium Folding”. In: *Nature* 518.7538 (2015), pp. 245–248. ISSN: 0028-0836. DOI: `10.1038/nature14152`.

[48] Douglas B Staple. “Understanding Mechanics and Polarity in Two-Dimensional Tissues”. In: *Dissertation MPI PKS* (2011).

[49] M S Steinberg. “Mechanism of tissue reconstruction by dissociated cells. II. Time-course of events.” In: *Science (New York, N.Y.)* 137.X 127 (1962), pp. 762–763. ISSN: 0036-8075. DOI: `10.1126/science.137.3532.762`.

[50] Malcolm S. Steinberg. “on the Mechanism of Tissue Reconstruction By Dissociated Cells, I. Population Kinetics, Differential Adhesiveness, and the Absence of Directed Migration*”. In: *Proceedings of the National Academy of Sciences of the United States of America* 48 (1962), pp. 1577–1582. ISSN: 0027-8424. DOI: `10.1073/pnas.48.9.1577`.

[51] Malcolm S. Steinberg. “on the Mechanism of Tissue Reconstruction By Dissociated Cells, Iii. Free Energy Relations and the Reorganization of Fused, Heteronomic Tissue Fragments*”. In: *Proceedings of the National Academy of Sciences of the United States of America* 48 (1962), pp. 1769–1776. ISSN: 0027-8424. DOI: `10.1073/pnas.48.10.1769`.

[52] Jonas M Ranft. “Physique théorique Mechanics of Growing Tissues : A Continuum Description Approach”. In: (2012), p. 162.

[53] K Kruse et al. “Generic theory of active polar gels: a paradigm for cytoskeletal dynamics.” In: *The European physical journal. E, Soft matter* 16.1 (Jan. 2005), pp. 5–16. ISSN: 1292-8941. DOI: `10.1140/epje/e2005-00002-5`.

[54] J. F. Joanny et al. “Hydrodynamic theory for multi-component active polar gels”. In: *New Journal of Physics* 9 (2007), pp. 1–17. ISSN: 13672630. DOI: `10.1088/1367-2630/9/11/422`.

[55] Sriram Ramaswamy. “The Mechanics and Statistics of Active Matter”. In: *Annual Review of Condensed Matter Physics* 1.1 (2010), pp. 323–345. ISSN: 1947-5454. DOI: `10.1146/annurev-conmatphys-070909-104101`.

[56] A C Callan-Jones and F Jülicher. “Hydrodynamics of active permeating gels”. In: *New Journal of Physics* 13.9 (2011), p. 093027. ISSN: 1367-2630. DOI: `10.1088/1367-2630/13/9/093027`.

[57] M. C. Marchetti et al. “Hydrodynamics of soft active matter”. In: *Reviews of Modern Physics* 85.3 (2013), pp. 1143–1189. ISSN: 00346861. DOI: `10.1103/RevModPhys.85.1143`.

[58] Numerical Methods and That Work. “10 . 6 Conjugate Gradient Methods in Multidimensions”. In: *Numerical Recipes* i (1990), pp. 420–425.

[59] Nick Barker et al. “Crypt stem cells as the cells-of-origin of intestinal cancer.” In: *Nature* 457.7229 (2009), pp. 608–611. ISSN: 0028-0836. DOI: `10.1038/nature07602`.

[60] Eduard Batlle et al. “β-catenin and TCF mediate cell positioning in the intestinal epithelium by controlling the expression of EphB/EphrinB”. In: *Cell* 111.2 (2002), pp. 251–263. ISSN: 00928674. DOI: `10.1016/S0092-8674(02)01015-2`.

[61] Graham P. Bell and Barry J. Thompson. “Colorectal cancer progression: Lessons from Drosophila?” In: *Seminars in Cell and Developmental Biology* 28 (2014), pp. 70–77. ISSN: 10963634. DOI: `10.1016/j.semcdb.2014.02.007`.

[62] John Farley, Laurent L Ozbun, and Michael J Birrer. “Genomic analysis of epithelial ovarian cancer.” In: *Cell research* 18.5 (2008), pp. 538–548. ISSN: 1001-0602. DOI: `10.1038/cr.2008.52`.

[63] Daniel Pinto and Hans Clevers. “Wnt control of stem cells and differentiation in the intestinal epithelium”. In: *Experimental Cell Research* 306.2 (2005), pp. 357–363. ISSN: 00144827. DOI: `10.1016/j.yexcr.2005.02.022`.

[64] Christina Bielmeier et al. “Interface Contractility between Differently Fated Cells Drives Cell Elimination and Cyst Formation”. In: *Current Biology* (2016). DOI: `10.1016/j.cub.2015.12.063`.

[65] D Beuchle, G Struhl, and J Müller. “Polycomb group proteins and heritable silencing of Drosophila Hox genes.” In: *Development (Cambridge, England)* 128.6 (2001), pp. 993–1004. ISSN: 0950-1991.

[66] Pierre Gandille et al. "Mutations in the polycomb group gene polyhomeotic lead to epithelial instability in both the ovary and wing imaginal disc in Drosophila." In: *PloS one* 5.11 (Jan. 2010), e13946. ISSN: 1932-6203. DOI: `10.1371/journal.pone.0013946`.

[67] N Azpiazu and G Morata. "Function and regulation of homothorax in the wing imaginal disc of Drosophila." In: *Development (Cambridge, England)* 127.12 (2000), pp. 2685–2693. ISSN: 0950-1991.

[68] J Wu and S M Cohen. "Proximal distal axis formation in the Drosophila leg: distinct functions of teashirt and homothorax in the proximal leg." In: *Mechanisms of development* 94.1-2 (2000), pp. 47–56. ISSN: 0925-4773. DOI: `10.1016/S0925-4773(00)00311-7`.

[69] X Liu, M Grammont, and K D Irvine. "Roles for scalloped and vestigial in regulating cell affinity and interactions between the wing blade and the wing hinge." In: *Developmental biology* 228.2 (2000), pp. 287–303. ISSN: 00121606. DOI: `10.1006/dbio.2000.9939`.

[70] Thomas J Widmann and Christian Dahmann. "Dpp signaling promotes the cuboidal-to-columnar shape transition of Drosophila wing disc epithelia by regulating Rho1." In: *Journal of cell science* 122 (2009), pp. 1362–1373. ISSN: 0021-9533. DOI: `10.1242/jcs.044271`.

[71] D a Prober and B a Edgar. "Ras1 promotes cellular growth in the Drosophila wing." In: *Cell* 100.4 (2000), pp. 435–446. ISSN: 00928674. DOI: `10.1016/S0092-8674(00)80679-0`.

[72] Melanie I Worley, Linda Setiawan, and Iswar K Hariharan. "TIE-DYE: a combinatorial marking system to visualize and genetically manipulate clones during development in Drosophila melanogaster." In: *Development (Cambridge, England)* 140.15 (2013), pp. 3275–84. ISSN: 1477-9129. DOI: `10.1242/dev.096057`.

[73] Sandra G. Zimmerman et al. "Apical constriction and invagination downstream of the canonical Wnt signaling pathway require Rho1 and Myosin II". In: *Developmental Biology* 340.1 (2010), pp. 54–66. ISSN: 00121606. DOI: `10.1016/j.ydbio.2010.01.021`.

[74] Matthew C Gibson and Norbert Perrimon. "Extrusion and death of DPP/BMP-compromised epithelial cells in the developing Drosophila wing." In: *Science (New York, N.Y.)* 307.5716 (Mar. 2005), pp. 1785–9. ISSN: 1095-9203. DOI: `10.1126/science.1104751`.

[75] Jie Shen and Christian Dahmann. "Extrusion of cells with inappropriate Dpp signaling from Drosophila wing disc epithelia." In: *Science (New York, N.Y.)* 307.5716 (Mar. 2005), pp. 1789–90. ISSN: 1095-9203. DOI: `10.1126/science.1104784`.

[76] Li-Hsun Chang et al. "Differential adhesion and actomyosin cable collaborate to drive Echinoid-mediated cell sorting." In: *Development (Cambridge, England)* 138.17 (2011), pp. 3803–3812. ISSN: 0950-1991. DOI: `10.1242/dev.062257`.

[77] Robert J Major and Kenneth D Irvine. "Influence of Notch on dorsoventral compartmentalization and actin organization in the Drosophila wing." In: *Development (Cambridge, England)* 132.17 (2005), pp. 3823–3833. ISSN: 0950-1991. DOI: `10.1242/dev.01957`.

[78] C Dahmann and K Basler. "Opposing transcriptional outputs of Hedgehog signaling and engrailed control compartmental cell sorting at the Drosophila A/P boundary." In: *Cell* 100.4 (2000), pp. 411–422. ISSN: 00928674. DOI: `10.1016/S0092-8674(00)80677-7`.

[79] Katja Röper. "Anisotropy of Crumbs and aPKC Drives Myosin Cable Assembly during Tube Formation". In: *Developmental Cell* 23.5 (2012), pp. 939–953. ISSN: 15345807. DOI: `10.1016/j.devcel.2012.09.013`.

[80] Jie Shen, Christian Dahmann, and Gert O Pflugfelder. "Spatial discontinuity of optomotor-blind expression in the Drosophila wing imaginal disc disrupts epithelial architecture and promotes cell sorting." In: *BMC developmental biology* 10 (2010), p. 23. ISSN: 1471-213X. DOI: `10.1186/1471-213X-10-23`.

[81] E. Hannezo, J. Prost, and J. F. Joanny. "Instabilities of monolayered epithelia: Shape and structure of villi and crypts". In: *Physical Review Letters* 107.7 (2011), pp. 1–5. ISSN: 00319007. DOI: `10.1103/PhysRevLett.107.078104`.

[82] Amy E Shyer et al. "Villification: how the gut gets its villi." In: *Science (New York, N.Y.)* 342.6155 (2013), pp. 212–8. ISSN: 1095-9203. DOI: `10.1126/science.1238842`.

[83] Thomas J Widmann and Christian Dahmann. "Wingless signaling and the control of cell shape in Drosophila wing imaginal discs." In: *Developmental biology* 334.1 (Oct. 2009), pp. 161–73. ISSN: 1095-564X. DOI: `10.1016/j.ydbio.2009.07.013`.

[84] George T Eisenhoffer et al. "Crowding induces live cell extrusion to maintain homeostatic cell numbers in epithelia." In: *Nature* 484.7395 (Apr. 2012), pp. 546–9. ISSN: 1476-4687. DOI: `10.1038/nature10999`.

[85] George T. Eisenhoffer and Jody Rosenblatt. “Bringing balance by force: Live cell extrusion controls epithelial cell numbers”. In: *Trends in Cell Biology* 23.4 (2013), pp. 185–192. ISSN: 09628924. DOI: `10.1016/j.tcb.2012.11.006`.

[86] Eliana Marinari et al. “Live-cell delamination counterbalances epithelial growth to limit tissue overcrowding.” In: *Nature* 484.7395 (Apr. 2012), pp. 542–5. ISSN: 1476-4687. DOI: `10.1038/nature10984`.

[87] Catherine Hogan. “Impact of interactions between normal and transformed epithelial cells and the relevance to cancer”. In: *Cellular and Molecular Life Sciences* 69.2 (2012), pp. 203–213. ISSN: 1420682X. DOI: `10.1007/s00018-011-0806-3`.

[88] Catherine Hogan et al. “Characterization of the interface between normal and transformed epithelial cells.” In: *Nature cell biology* 11.4 (Apr. 2009), pp. 460–7. ISSN: 1476-4679. DOI: `10.1038/ncb1853`.

[89] Jennifer S. Liu et al. “Programmed Cell-to-Cell Variability in Ras Activity Triggers Emergent Behaviors during Mammary Epithelial Morphogenesis”. In: *Cell Reports* 2.5 (2012), pp. 1461–1470. ISSN: 22111247. DOI: `10.1016/j.celrep.2012.08.037`.

[90] Selwin K Wu et al. “Cortical F-actin stabilization generates apical-lateral patterns of junctional contractility that integrate cells into epithelia.” In: *Nature cell biology* 16.2 (2014), pp. 167–78. ISSN: 1476-4679. DOI: `10.1038/ncb2900`.

[91] Anna-Pavlina G Haramis et al. “De novo crypt formation and juvenile polyposis on BMP inhibition in mouse intestine.” In: *Science (New York, N.Y.)* 303.5664 (2004), pp. 1684–1686. ISSN: 0036-8075. DOI: `10.1126/science.1093587`.

[92] Maryam Aliee. “Dynamics and mechanics of compartment boundaries in developing tissues”. In: *Dissertation* (2013).

[93] Jonathan Michael Wyndham Slack. *From egg to embryo: determinative events in early development*. Ed. by 13. 2nd ed. Cambridge University Press, 1991.

[94] Matteo Rauzi et al. “Physical models of mesoderm invagination in Drosophila embryo.” In: *Biophysical journal* 105.1 (July 2013), pp. 3–10. ISSN: 1542-0086. DOI: `10.1016/j.bpj.2013.05.039`.

[95] M Leptin and B Grunewald. “Cell shape changes during gastrulation in Drosophila.” In: *Development (Cambridge, England)* 110.1 (1990), pp. 73–84. ISSN: 0950-1991.

[96] Adam C Martin, Matthias Kaschube, and Eric F Wieschaus. “Pulsed contractions of an actin-myosin network drive apical constriction.” In: *Nature* 457.7228 (Jan. 2009), pp. 495–9. ISSN: 1476-4687. DOI: `10.1038/nature07522`.

[97] Uros Krzic et al. “Multiview light-sheet microscope for rapid in toto imaging”. In: *Nature Methods* 9.7 (2012), pp. 730–733. ISSN: 1548-7091. DOI: `10.1038/nmeth.2064`.

[98] Adam C Martin et al. “Integration of contractile forces during tissue invagination.” In: *The Journal of cell biology* 188.5 (Mar. 2010), pp. 735–49. ISSN: 1540-8140. DOI: `10.1083/jcb.200910099`.

[99] Bing He et al. “Apical constriction drives tissue-scale hydrodynamic flow to mediate cell elongation.” In: *Nature* 508.7496 (Apr. 2014), pp. 392–6. ISSN: 1476-4687. DOI: `10.1038/nature13070`.

[100] G M Odell et al. “The mechanical basis of morphogenesis. I. Epithelial folding and invagination.” In: *Developmental biology* 85.2 (1981), pp. 446–462. ISSN: 00121606. DOI: `10.1016/0012-1606(81)90276-1`.

[101] J. Muñoz, K. Barrett, and M. Miodownik. “Gradient decomposition method for the mechanical analysis of morphogenesis”. In: *Journal of Biomechanics* 39.June 2006 (2006), S641. ISSN: 00219290. DOI: `10.1016/S0021-9290(06)85673-3`.

[102] Vito Conte, José J Muñoz, and Mark Miodownik. “A 3D finite element model of ventral furrow invagination in the Drosophila melanogaster embryo.” In: *Journal of the mechanical behavior of biomedical materials* 1.2 (Apr. 2008), pp. 188–98. ISSN: 1878-0180. DOI: `10.1016/j.jmbbm.2007.10.002`.

[103] R Allena, A-S Mouronval, and D Aubry. “Simulation of multiple morphogenetic movements in the Drosophila embryo by a single 3D finite element model.” In: *Journal of the mechanical behavior of biomedical materials* 3.4 (May 2010), pp. 313–23. ISSN: 1878-0180. DOI: `10.1016/j.jmbbm.2010.01.001`.

[104] R Allena, J J Muñoz, and D Aubry. “Diffusion-reaction model for Drosophila embryo development.” In: *Computer methods in biomechanics and biomedical engineering* 16.3 (2013), pp. 235–48. ISSN: 1476-8259. DOI: `10.1080/10255842.2011.616944`.

[105] Jose J. Munoz, Vito Conte, and Mark Miodownik. “Stress-dependent morphogenesis: Continuum mechanics and truss systems”. In: *Biomechanics and Modeling in Mechanobiology* 9.4 (2010), pp. 451–467. ISSN: 16177959. DOI: `10.1007/s10237-009-0187-9`.

[106] Ashok Ramasubramanian and Larry A. Taber. “Computational modeling of morphogenesis regulated by mechanical feedback”. In: *Biomechanics and Modeling in Mechanobiology* 7.2 (2008), pp. 77–91. ISSN: 16177959. DOI: `10.1007/s10237-007-0077-y`.

[107] Philippe-Alexandre Pouille et al. "Mechanical signals trigger Myosin II redistribution and mesoderm invagination in Drosophila embryos." In: *Science signaling* 2.66 (Jan. 2009), ra16. ISSN: 1937-9145. DOI: `10.1126/scisignal.2000098`.

[108] Vito Conte et al. "A Biomechanical Analysis of Ventral Furrow Formation in the Drosophila Melanogaster Embryo". In: *PLoS ONE* 7.4 (2012), e34473. ISSN: 1932-6203. DOI: `10.1371/journal.pone.0034473`.

[109] Matteo Rauzi et al. "Embryo-scale tissue mechanics during Drosophila gastrulation movements". In: *Nature Communications* 6 (2015), p. 8677. ISSN: 2041-1723. DOI: `10.1038/ncomms9677`.

[110] Ana Hočevar Brezavšček et al. "A model of epithelial invagination driven by collective mechanics of identical cells." In: *Biophysical journal* 103.5 (Sept. 2012), pp. 1069–77. ISSN: 1542-0086. DOI: `10.1016/j.bpj.2012.07.018`.

[111] Julie Adam et al. "Renal Cyst Formation in Fh1-Deficient Mice Is Independent of the Hif/Phd Pathway: Roles for Fumarate in KEAP1 Succination and Nrf2 Signaling". In: *Cancer Cell* 20.4 (2011), pp. 524–537. ISSN: 15356108. DOI: `10.1016/j.ccr.2011.09.006`.

[112] William R. Brugge et al. "Diagnosis of Pancreatic Cystic Neoplasms: A Report of the Cooperative Pancreatic Cyst Study". In: *Gastroenterology* 126.5 (2004), pp. 1330–1336. ISSN: 00165085. DOI: `10.1053/j.gastro.2004.02.013`.

[113] Patricia D. Wilson. "Polycystic Kidney Disease". In: *The new england journal of medicine* (2004), pp. 151–164.

[114] David A Ehrmann. "Polycystic ovary syndrome". In: *The new england journal of medicine* 1.2 (2005), pp. 60–63. ISSN: 16089677. DOI: `1043-2760(89)90003-9[pii]`.

[115] Raphaël Etournay et al. "Interplay of cell dynamics and epithelial tension during morphogenesis of the Drosophila pupal wing." In: *eLife* 4 (2015), e07090. ISSN: 2050-084X. DOI: `10.7554/eLife.07090`.

[116] Robert Nürnberg. "Calculating the area and centroid of a polygon". In: *wwwf.imperial.ac.uk/˜rn/centroid.pdf* 2.C (2013), pp. 3–5.

[117] Paul Leopardi. "A partition of the unit sphere into regions of equal area and small diameter". In: *Electronic Transactions on Numerical Analysis* 25 (2006), pp. 309–327. ISSN: 10689613. DOI: `10.1.1.90.2213`.

[118] E. L. Hill. "The Theory of Vector Spherical Harmonics". In: *American Journal of Physics* 22.4 (1954), p. 211. ISSN: 00029505. DOI: `10.1119/1.1933682`.

[119] Michael Freeden, Willi and Schreiner. “Tensor Spherical Harmonics”. In: *Spherical Functions of Mathematical Geosciences*. Springer, 2009, pp. 273–337.

Versicherung

Hiermit versichere ich, dass ich die vorliegende Arbeit ohne unzulässige Hilfe Dritter und ohne Benutzung anderer als der angegebenen Hilfsmittel angefertigt habe; die aus fremden Quellen direkt oder indirekt übernommenen Gedanken sind als solche kenntlich gemacht. Die Arbeit wurde bisher weder im Inland noch im Ausland in gleicher oder ähnlicher Form einer anderen Prüfungsbehörde vorgelegt.
Die vorliegende Arbeit wurde am Max-Planck-Institut für Physik komplexer Systeme (Dresden), und am Francis Crick Institute Limited (London) angefertigt und von Prof. Dr. Frank Jülicher und Dr. Guillaume Salbreux betreut. Meine Person betreffend erkläre ich hiermit, dass keine früheren erfolglosen Promotionsverfahren stattgefunden haben. Ich erkenne die Promotionsordnung der Fakultät für Mathematik und Naturwissenschaften, Technische Universität Dresden an.

Silvanus Alt, London der 12.03.2016